ATTENTION: The Singapore Copyright Act applies to the use of this document. Nanyang Technological University Library
0416234

Fabrication and Characterization of Austenitic Stainless Steel – Nitrogen Films

Kappaganthu Sri Ramakanth

NANYANG TECHNOLOGICAL UNIVERSITY
12 JUL 2006
LIBRARY

School of Materials Science & Engineering

A thesis submitted to the Nanyang Technological University
in fulfilment of the requirement for the degree of
Doctor of Philosophy

2006

TA
418.9
.T45
K17
2006

ATTENTION: The Singapore Copyright Act applies to the use of this document. Nanyang Technological University Library

ACKNOWLEDGMENTS

I would like to take this moment to acknowledge the support and assistance provided to me by some wonderful persons during my research work.

I am greatly indebted to my thesis advisor, Associate Professor Sun Yong, whose guidance and support has always been a source of inspiration and motivation to me throughout this work. In more than three years of working with him, I learned to explore new ideas and to trust my abilities and intuition. He rendered an encouraging and productive atmosphere for me by accommodating sufficient space for my individualistic decisions. My research would have been different without his support. During the period of invaluable studentship under him I got opportunity to work with variety of advanced processes and characterization equipment, analyze the results and also learnt about publication of the research results. I take this opportunity to express that my gratitude towards him will remain afresh forever.

I also wish to thank Nanyang Technological University and School of Materials Science and Engineering for providing financial support and studentship during the course of this study.

I thank my colleagues Mr. Nurot Panich and Mr.Dangeti SivaRamakrishna for their invaluable support and care throughout my doctoral work and Mr.Nagasekhar for his relentless support during the editing of the final manuscript. I am thankful to my senior Dr. Cheng Hao who helped me in the initial days. I sincerely acknowledge to A/P Cheng Zhong, A/P Sam Zhang, A/P Raju V.Ramanujan, A/P Timothy John White, A/P Ashraff Uddin, Dr. Cheng Hao, Dr. Zhou Weihua, Dr. Sun Deen and SE Lab lab-mates

I take this opportunity to thank once again my parents, sister, relatives and friends without whom I would not be what I am now.

ATTENTION: The Singapore Copyright Act applies to the use of this document. Nanyang Technological University Library

TABLE OF CONTENTS

ACKNOWLEDGMENTS i

TABLE OF CONTENTS ii

ABSTRACT vii

LIST OF FIGURES ix

LIST OF TABLES xvii

LIST OF NOTATIONS xviii

LIST OF PUBLICATIONS xx

Chapter 1 INTRODUCTION 1

1.1 BACKGROUND 1

1.2 OBJECTIVES OF THE RESEARCH WORK 4

1.3 ORGANIZATION OF THE THESIS 4

Chapter 2 LITERATURE SURVEY 5

2.1 SPUTTER DEPOSITION PROCESS 5

2.1.1 History of Sputter Deposition Process 5

2.1.2 Principles of Sputter Deposition 6

2.1.2.1 The Glow Discharge 6

2.1.2.2 The Thornton Model of Film Structure 9

2.1.3 Reactive Sputter Deposition 11

2.1.4 Target Poisoning and Arcing 12

2.1.5 Sputter Deposition Process Parameters 15

2.1.5.1 Pressure and Total Gas Flow Rate 15

2.1.5.2 Substrate Temperature and Control 16

2.1.5.3 Current and Voltage 16

2.2 THE STAINLESS STEEL – NITROGEN SYSTEM 17

ATTENTION: The Singapore Copyright Act applies to the use of this document. Nanyang Technological University Library

2.2.1 Bulk Nitrogen-Bearing Stainless Steels 17
2.2.2 Low Temperature Nitriding of Austenitic Stainless Steels 19
2.2.2.1 Introduction 19
2.2.2.2 Structural Studies on Low Temperature-Nitrided Stainless Steels 21
2.2.3 Magnetic Studies on Bulk Nitrided Stainless Steel 25
2.3 STAINLESS STEEL – NITROGEN FILMS 26
2.3.1 Fabrication and Structure of SS-N Films 26
2.3.2 Mechanical Properties of SS-N Films 28
2.3.3 Corrosion Resistance of SS-N Films 30
2.3.4 Magnetic Properties of SS-N Films 31
2.4 THE FE-N PHASE DIAGRAM 31
2.5 THE NEW FeN PHASE 33
Chapter 3 EXPERIMENTAL PROCEDURES 35
3.1 SUBSTRATE MATERIALS AND PREPARATIONS 35
3.2 THE SPUTTERING TARGET MATERIALS 35
3.3 FILM FABRICATION 37
3.3.1 The Sputtering Deposition System 37
3.3.2 Deposition of SS-N Films 39
3.4 PHASE IDENTIFICATION AND LATTICE PARAMETER DETERMINATION BY X-RAY DIFFRACTION 41
3.5 SECONDARY ELECTRON IMAGING (SEI) 43
3.6 SIZE DETERMINATION OF SURFACE GRANULAR FEATURES 45
3.7 ELEMENTAL ANALYSIS BY SPECTROSCOPIC TECHNIQUES 46
3.7.1 Energy Dispersive X-ray Spectroscopy 46
3.7.2 X-ray Photoelectron Spectroscopy 47

ATTENTION: The Singapore Copyright Act applies to the use of this document. Nanyang Technological University Library

3.8 ATOMIC FORCE MICROSCOPIC CHARACTERIZATION 47

3.9 CHARACTERIZATION WITH TRANSMISSION ELECTRON MICROSCOPY 48

3.10 DETERMINATION OF MAGNETIZATION BY VIBRATING SAMPLE MAGNETOMETER 50

3.11 MECHANICAL PROPERTY CHARACTERIZATION 52

3.11.1 Nanoindentation 52

3.11.2 Microscratch 53

Chapter 4 RESULTS 54

4.1 NITROGEN CHEMICAL COMPOSITION 54

4.1.1 Nitrogen Incorporation in SS Films Deposited On Unheated Substrates 54

4.1.2 Nitrogen Incorporation In SS Films Deposited at 300 °C 56

4.1.3 Effect of Deposition Power Density On Nitrogen Incorporation 57

4.2 PHASE EVOLUTION IN SS-N FILMS INVESTIGATED BY DIFFRACTION TECHNIQUES 59

4.2.1 SS-N Films On Unheated Substrates 59

4.2.2 SS-N Films Deposited on Substrates Heated to 300 °C 64

4.2.3 Effect of Substrate Temperature on γ_N Phase Formation 74

4.2.4 Effect of Substrate Temperature on MN Phase Formation 75

4.2.5 Effect of Deposition Power Density on γ_N Phase Formation 78

4.2.6 Effect of Deposition Power Density on MN Phase Formation 79

4.2.7 Effect of Target-Substrate Distance on Phase Evolution 80

4.2.8 Effect of Substrate Bias on MN Phase Formation 81

4.2.9 Phase Evolution in the Annealed Films 82

4.3 DEPOSITION RATE 84

ATTENTION: The Singapore Copyright Act applies to the use of this document. Nanyang Technological University Library

4.4 FILM MORPHOLOGIES DETERMINED BY ELECTRON MICROSCOPY 86
4.5 CROSS SECTIONAL TEM EXAMINATION 92
4.6 MECHANICAL PROPERTIES OF SS-N FILMS 95
4.6.1 Hardness & Reduced-Modulus Values of SS-N Films 95
4.6.2 Mechanical Properties of MN Phase 96
4.6.3 Adhesion Properties of SS-N Films 97
4.7 MAGNETIZATION VALUES OF SS-N FILMS AT ROOM TEMPERATURE 99
Chapter 5 DISCUSSION 102
5.1 NITROGEN INCORPORATION AND PHASE EVOLUTION 102
5.1.1 Nitrogen Incorporation 102
5.1.2 Phase Evolution 102
5.2 NATURE OF THE γ_N AND MN PHASES 106
5.2.1 Lattice parameter and Nitrogen Concentration 108
5.2.2 Lattice Distortion 110
5.2.3 Analysis of Chemical States by XPS 113
5.2.4 Summary 115
5.3 FACTORS AFFECTING THE FORMATION OF γ_N AND MN PHASES 117
5.3.1 Influence of Substrate Temperature on γ_N Phase Formation 118
5.3.2 Influence of Target-substrate Distance on Phase Formation 119
5.3.3 Influence of Deposition Power Density on γ_N Phase Formation 120
5.3.4 Influence of Substrate Temperature on MN Phase Formation 121
5.3.5 Influence of Substrate Bias on the MN Phase Formation 123
5.4 THERMAL STABILITY OF THE γ_N AND MN PHASES 124

ATTENTION: The Singapore Copyright Act applies to the use of this document. Nanyang Technological University Library

5.5 DEPOSITION RATE, TEXTURE AND MORPHOLOGY OF SS-N FILMS 125
5.5.1 Deposition Rate 125
5.5.2 Texture in SS-N Films 127
5.5.3 Surface Morphological Features 132
5.6 PROPERTY – STRUCTRE RELATIONSHIP 134
5.6.1 Hardness and Reduced-Modulus of SS-N Films 134
5.6.2 Adhesion Properties 137
5.7 SATURATION MAGNETIZATION OF SS-N FILMS 138
Chapter 6 CONCLUSIONS AND SUGGESTIONS FOR FUTURE WORK 140
6.1 CONCLUSIONS 140
6.2 SUGGESTIONS FOR FUTURE WORKS 142
Appendix OTHER RELATED STUDIES ON FE–N FILMS 144
A.1 XRD STUDIES ON PHASE EVOLUTION 144
A.1.1 Pure Fe Film 144
A.1.2 Fe-N Films Produced at Various N_2/Ar Flow Rates 145
A.1.3 Fe-N Films Produced at Various Temperatures 148
A.2 DISCUSSION 150
A.3 FESEM OF FE-N FILMS 150
A.4 ATOMIC FORCE MICROSCOPIC STUDIES ON FE-N FILMS 151
A.5 PROBLEMS ENCOUNTERED WITH FE-N FILMS 152
REFERENCES 156

ATTENTION: The Singapore Copyright Act applies to the use of this document. Nanyang Technological University Library

ABSTRACT

In the present work, the Fe-N based film systems fabricated by reactive magnetron sputtering were investigated, with particular emphasis on the stainless steel-nitrogen (SS-N) system. For the purpose of understanding the phase evolution and various structural and compositional features of the films as a function of nitrogen doping and deposition parameters, a series of SS-N films were prepared under various deposition conditions. Structural characterization was conducted by a variety of experimental and analytical techniques, including grazing angle incidence X-ray diffraction, secondary electron imaging, energy dispersive spectroscopy, high resolution field emission scanning electron microscopy, transmission electron microscopy, and X-ray photoelectron spectroscopy. The mechanical properties of the films were evaluated by nanoindentation and microscratch tests. In addition, the room temperature magnetization behavior of the films was measured by the vibrating sample magnetometry technique.

These efforts have facilitated a better understanding of the phase evolution and structural and properties characteristics of the resultant films. It was found that although sputtering of the austenitic stainless steel target with face centred cubic structure in pure argon atmosphere resulted in the formation of a ferrite film with body centred cubic structure, doping of the film with nitrogen by sputtering in argon and nitrogen gas mixtures led to a series of structural changes in the film. With increasing amount of nitrogen doping, the crystalline structure of the films changed from bcc ferrite (α), to a mixture of bcc ferrite and expanded fcc austenite (γ_N) supersaturated with nitrogen, and to the MN (metal nitride) type nitride phase. Subtle differences in phase evolution depended on % N_2, power density and the substrate temperature. This MN type phase, where M represents all the metallic elements in the stainless steel, i.e. M=Fe+Cr+Ni+Mo, has a face-centered cubic structure and equiatomic (M/N=l) stoichiometry.

Further studies were conducted to investigate the influence of various deposition parameters such as nitrogen gas composition in the sputtering gas mixture,

ATTENTION: The Singapore Copyright Act applies to the use of this document. Nanyang Technological University Library

substrate temperature, sputtering power density, target-to-substrate distance, and substrate biasing.

Properties characterization revealed that nitrogen doping can effectively enhance the hardness of the stainless steels films, but reduce the reduced-modulus of elasticity. Thus the nitrogen doped expanded austenite films and MN films are more elastic than the pure stainless steel film. There exists a correlation between film hardness and nitrogen content in the expanded austenite films. The MN phase possesses the highest hardness among all the films fabricated in this work. Magnetization measurements showed that the ferrite film is ferromagnetic, and the saturation magnetization of the film decreases with increasing amount of nitrogen doping until a single fcc expanded austenite phase is formed. The measurements further revealed that the fcc expanded austenite phase and the MN phase are non-magnetic.

The results of this work have demonstrated that a series of SS-N films with controlled phase constituents and structural features can be fabricated by magnetron sputtering. These films possess promising mechanical and magnetic properties, and thus should have potentials for tribological, anti-corrosion, and magnetic device applications.

ATTENTION: The Singapore Copyright Act applies to the use of this document. Nanyang Technological University Library

LIST OF FIGURES

2.1 Cross-sectional view of glow discharge..... 7

2.2 Schematic of I-V characteristics of DC glow discharge..... 9

2.3 Thornton's model of thin film morphology..... 11

2.4 Schematic variation of (a) deposition rate and (b) working pressure with respect to reactive gas partial pressure..... 14

2.5 Scanning electron micrograph of the low temperature as-nitrided AISI 316 steel surface showing surface relief, shearing, and deformation..... 22

2.6 True profile of textured expanded austenite shown in comparison to the calculated profile of a randomly oriented bulk sample..... 23

2.7 Fourier filtered HRTEM image of nitrided austenite layer showing antiphase boundary..... 24

2.8 Lattice parameters calculated from fixed incident angle scanning and symmetric scanning..... 25

2.9 Ratio of interplanar spacing of (200) to (111) in the bulk expanded austenite plotted against nitriding temperature showing deviation from ideal fcc structure..... 25

2.10 Ferromagnetic domains imaged by magnetic force microscopy in bulk expanded austenite..... 26

2.11 Lattice parameter of S phase versus nitrogen content in the SS-N films..... 27

2.12 Nitrogen content and hardness of the SS-N films plotted against N_2 flow rate..... 29

2.13 Hardness and modulus values, of various SS-N films against at.% N..... 30

2.14 Metastable phase diagram of Fe-N system..... 32

3.1 XRD plot of the 316L stainless steel target..... 36

3.2 XRD plot of Fe target..... 37

3.3 Photograph showing the MSS3 diode planar magnetron sputtering machine. 38

3.4 Schematic showing the sputter deposition process..... 38

3.5 Diffraction geometries of (a) Bragg Brentano and (b) GIXD methods..... 41

3.6 Rigaku Dmax 2200 XRD used for the GIXD analysis of the Fe-N based 43

ATTENTION: The Singapore Copyright Act applies to the use of this document. Nanyang Technological University Library

films.....

3.7 Schematic profile of primary electron inside the sample..... 45

3.8 FESEM used for the characterization of the Fe-N based films..... 45

3.9 Electron ray diagram showing the focusing of (a) diffraction pattern in the diffraction mode and (b) bright field image in the image mode..... 49

3.10 Transmission Electron Microscope (Jeol JEM 2010) used for characterization of stainless steel-nitrogen films..... 50

3.11 Schematic diagram of the VSM..... 51

3.12 Vibrating sample magnetometer (Lakeshore 736) used for determining the room temperature magnetization values of various SS-N films..... 51

3.13 NanoTest nanoindentor machine of Micromaterials Ltd used for mechanical characterization of SS-N films..... 52

4.1 XPS detailed spectrum of the SS-N film deposited at 300 °C with 0% N_2 and 2.2Wcm^{-2}, and 7 cm target-substrate distance 55

4.2 Nitrogen content in the SS-N films, deposited with various nitrogen gas compositions on unheated substrates with 2.2Wcm^{-2} and 7 cm target-substrate distance, as determined by EDS. 56

4.3 Nitrogen concentration in SS-N films, deposited at 300 °C, 2.2Wcm^{-2}, and 7 cm target-substrate distance as a function of nitrogen gas composition in the sputtering gas mixture, determined by EDS 57

4.4 Nitrogen content versus power density versus power density, of SS-N films deposited on unheated substrates with 2.2Wcm^{-2} and 7 cm target-substrate distance and (a) 25% N_2 and (b) 100% N_2..... 58

4.5 Nitrogen contents and lattice parameters plotted for various substrate temperatures of the films deposited with 25% N_2..... 59

4.6 GIXD pattern of the pure stainless steel film, deposited on unheated substrate with 2.2Wcm^{-2} and 7 cm target-substrate distance, obtained with 2° glancing angle of incidence 60

4.7 GIXD patterns of SS-N films deposited on unheated substrate with (a) 5%, (b) 10%, and (c) 15% N_2 in the gas mixture, 2.2Wcm^{-2} and target-substrate distance of 7 cm 61

4.8 GIXD pattern of SS-N film deposited on unheated substrate with 25% N_2, 62

ATTENTION: The Singapore Copyright Act applies to the use of this document. Nanyang Technological University Library

	$2.2Wcm^{-2}$ and 7 cm target-substrate distance.....	
4.9	GIXD pattern of SS-N film deposited on unheated substrate with 30% N_2, $2.2Wcm^{-2}$ and 7 cm target-substrate distance	62
4.10	GIXD pattern of SS-N film deposited on unheated substrate with 40% N_2 $2.2Wcm^{-2}$ and 7 cm target-substrate distance	63
4.11	GIXD pattern of SS-N film deposited on unheated substrate with 50% N_2 $2.2Wcm^{-2}$ and 7 cm target-substrate distance	63
4.12	GIXD pattern of SS-N film deposited on unheated substrate with 100% N_2 $2.2Wcm^{-2}$ and 7 cm target-substrate distance	64
4.13	GIXD pattern with 2° glancing angle of incidence obtained for stainless steel films deposited with (a) 0% and (b) 4% N_2 at 300 °C with $2.2Wcm^{-2}$ and 7 cm target-substrate distance	65
4.14	(a) Plan view bright field image and (b) Electron Diffraction Pattern of the SS film deposited at 300 °C with 0% N_2, $2.2Wcm^{-2}$ and 7 cm target-substrate distance	65
4.15	GIXD pattern of SS-N film deposited at 300 °C, $2.2Wcm^{-2}$, 7 cm target-substrate distance and with 10% N_2.....	66
4.16	TEM bright field image (a) and SAD pattern (b) from the γ_N film produced with 10%N_2 in the gas mixture at 300 °C, 2.2 Wcm^{-2} and 7 cm target-substrate distance	67
4.17	GIXD pattern of SS-N film deposited at 300 °C & $2.2Wcm^{-2}$, 7 cm target-substrate distance and with (a) 25% N_2, (b) 30% N_2 and (c) 37% N_2	69
4.18	(a) Bright field image and (b) Electron Diffraction Pattern of the SS-N film deposited at 300 °C with 25% N_2, $2.2Wcm^{-2}$ and 7 cm target-substrate distance	70
4.19	(a) Plan view bright field image, (b) Electron Diffraction and (c) Nanobeam electron diffraction patterns obtained from the same SS-N film deposited at 300 °C with 37% N_2, $2.2Wcm^{-2}$ and 7 cm target-substrate distance	71
4.20	GIXD pattern of SS-N film deposited at 300 °C with 45% N_2, $2.2Wcm^{-2}$ and 7 cm target-substrate distance.....	72
4.21	(a) Cross sectional bright field image and (b) Electron Diffraction Pattern	72

ATTENTION: The Singapore Copyright Act applies to the use of this document. Nanyang Technological University Library

of the SS-N film deposited at 300 °C with 45% N_2, 2.2Wcm^{-2} and 7 cm target-substrate distance.....

4.22 GIXD pattern of SS-N film deposited at 300 °C with 50% N_2, 2.2Wcm^{-2} and 7 cm target-substrate distance..... 73

4.23 (a) Cross sectional bright field image and (b) electron diffraction pattern of the SS-N film deposited at 300 °C with 50% N_2, 2.2Wcm^{-2} and 7 cm target-substrate distance 73

4.24 GIXD pattern of SS-N film deposited at 300 °C with 75%, 2.2Wcm^{-2} and 7 cm target-substrate distance 74

4.25 GIXD pattern of various γ_N films deposited with different substrate temperatures, 2.2Wcm^{-2} and 7 cm target-substrate distance 75

4.26 (a) Cross sectional bright field image and (b) Electron Diffraction pattern of the SS-N film deposited at 150 °C with 25% N_2, 2.2Wcm^{-2} and 7 cm target-substrate distance 75

4.27 GIXD pattern of SS-N film deposited at 400 °C with 50% N_2, 2.2Wcm^{-2} and 7 cm target-substrate distance 76

4.28 GIXD pattern of SS-N film deposited at 450 °C with 50% N_2, 2.2Wcm^{-2} and 7 cm target-substrate distance..... 76

4.29 GIXD pattern of SS-N film deposited at 500 °C with 50% N_2 2.2Wcm^{-2} and 7 cm target-substrate distance..... 77

4.30 (a) Cross sectional bright field image and (b) Electron Diffraction Pattern of the SS-N film deposited at 500 °C with 50% N_2, 2.2Wcm^{-2} and 7 cm target-substrate distance..... 77

4.31 Plots of nitrogen content versus substrate temperature of the films deposited with 50% N_2, 2.2Wcm^{-2} and 7 cm target-substrate distance..... 78

4.32 GIXD patterns of SS-N films deposited on unheated substrate with 25% N_2, 7 cm target-substrate distance & various power densities 79

4.33 GIXD patterns of SS-N films deposited on unheated substrate with 100% N_2, 7 cm target-substrate distance & various power densities..... 79

4.34 GIXD patterns of SS-N films deposited with (a) 25% & (b) 40% N_2 at 300 °C, 2.2Wcm^{-2} & 4 cm target-substrate distance 80

4.35 GIXD patterns of SS-N films deposited with (a) 50% & (b) 75% N_2 at 300 °C, 2.2Wcm^{-2} & 4 cm target-substrate distance..... 81

ATTENTION: The Singapore Copyright Act applies to the use of this document. Nanyang Technological University Library

4.36 GIXD patterns of SS-N films deposited at 300 °C with 50% N_2, 2.2Wcm^{-2}, 7 cm target-substrate distance and various RF substrate bias powers 82

4.37 GIXD pattern of MN film annealed for 500 °C-3 hours after depositing on unheated substrate with 50 % N_2, 2.2Wcm^{-2} and 7 cm target-substrate distance 83

4.38 GIXD pattern of SS-N film deposited on unheated substrate with 9.9Wcm^{-2}, 7 cm target-substrate distance power, and 25% N_2 and annealed for 500 °C-3 hours. The film contains pure γ_N phase with nitrogen content insufficient for Cr_2N precipitation..... 83

4.39 GIXD pattern of SS-N film annealed for 500 °C-3 hours after depositing on unheated substrate with 100 % N_2 & 6.6Wcm^{-2} and 7 cm target-substrate distance 84

4.40 GIXD pattern of SS-N film annealed for 500 °C-3 hours after deposited at 300 °C with 75% N_2 & 2.2Wcm^{-2}..... 84

4.41 Deposition rate as a function of nitrogen gas composition in the gas mixture, on unheated substrates, 2.2Wcm^{-2} and 7 cm target-substrate distance..... 85

4.42 Deposition rate versus power density, of pure γ_N films deposited with (a) 25% N_2 and (b) 50% N_2 on unheated substrate, 2.2Wcm^{-2} and 7 cm target-substrate distance..... 86

4.43 FIELD EMISSION SEM micrographs showing the fractured cross section morphology of the films deposited on unheated Si substrates 2.2Wcm^{-2}, 7 cm target-substrate distance and with various % N_2 in the gas mixture. (a) 0% N_2; (b) 15% N_2; (c) 30% N_2; (d) 40% N_2; (e) 50% N_2..... 87

4.44 Field Emission Scanning Electron (FESEM) Microscope micrographs showing the fractured cross section morphologies of the films deposited on the Si substrates heated to 300°C, 2.2Wcm^{-2}, 7 cm target-substrate distance and with various % N_2 in the gas mixture. (a) 0% N_2; (b) 10% N_2; (c) 25% N_2; and (d) 50% N_2..... 88

4.45 FIELD EMISSION SEM micrographs showing the surface morphology of the films deposited on the unheated Si substrates, 2.2Wcm^{-2}, 7 cm target- 90

ATTENTION: The Singapore Copyright Act applies to the use of this document. Nanyang Technological University Library

substrate distance and with various % N_2 in the gas mixture. (a) 0% N_2; (b) 5% N_2; (c) 10% N_2; (d) 25% N_2; (e) 50% N_2.....

4.46 FIELD EMISSION SEM micrographs showing the surface morphologies of the films deposited on the Si substrates heated to 300°C with 2.2Wcm^{-2}, 7 cm target-substrate distance and various % N_2 in the gas mixture. (a) 0% N_2; (b) 5% N_2; (c) 10% N_2; (d) 25% N_2; (e) 45% N_2 and (f) 50% N_2..... 91

4.47 Bright field image of cross sectional view of the film deposited at 500 °C with 2.2 Wcm^{-2}, 7 cm target-substrate distance and (a) 25% N_2 in gas mixture at 150 °C, (b) 50% N_2, (c) 50% N_2 at 300 °C, and (d) the same as that of (c)..... 92

4.48 Bright field image of cross sectional view of the film deposited at 500 °C with 2.2 Wcm^{-2}, 7 cm target-substrate distance (a) 50% N_2 and (b) HREM image of the same film as (a)..... 94

4.49 HREM image of the film deposited with 50% N_2, 2.2 Wcm^{-2}, 7 cm target-substrate distance at 300 °C 94

4.50 Hardness of the SS-N films deposited on mild steel substrates with different % N_2 in the sputtering gas mixture at 300 °C & with 2.2 Wcm^{-2}, 7 cm target-substrate distance 96

4.51 Load versus depth of indentation done on various MN films 97

4.52 Friction versus load curves of the microscratch tests performed on various SS-N films 101 98

4.53 Magnetic moment (emu) vs magnetic Field (Oe) curves measured at room temperature for (a) Bare Holder, (b) 0, (c) 8, (d) 37, (e) 45, (f) 50, and on unheated substrates with % N_2 of (g) 10, and (h) 50..... 100

4.54 Initial permeability plot of the SS-N films deposited with (a) 4% N_2 and (b) 8% N_2 in gas mixture 101

5.1 Relative XRD peak intensities of various constituent phases in the film deposited with 25% N_2 on unheated substrates..... 104

5.2 Schematic showing qualitatively the relative positions of various zones in the film deposited with 25% N_2 on unheated substrates..... 104

5.3 Variation of lattice parameter with nitrogen concentration in the FCC γ_N and MN phases formed in the SS-N films deposited at 300 °C, 100W and 7 109

ATTENTION: The Singapore Copyright Act applies to the use of this document. Nanyang Technological University Library

cm target-substrate distance.....

5.4 Plot of a_{hkl} versus $\cos^2\theta/\sin\theta$ of γ_N and MN phases from selected films..... 111

5.5 XPS spectra of (a) Cr2p 2/3 and (b) N1s from various phases indicated. The pure SS film was produced on unheated substrates with pure argon, and the γ_N and MN phases were produced at 300 °C with 25%N_2 and 50%N_2, respectively..... 115

5.6 GIXD patterns of SS-N films deposited on various substrates at 300 °C with 50% N_2 & 100W..... 117

5.7 Nitrogen contents and lattice parameters plotted for various substrate temperatures of the films deposited with 25% N_2..... 119

5.8 GIXD pattern obtained with 3.5° glancing angle for the film deposited at 500° C with 50% N_2, 2.2Wcm^{-2} and 7 cm target-substrate distance..... 123

5.9 Schematic showing angle between the diffracting plane and the surface of the sample as $90° - (\theta + \alpha)$..... 128

5.10 Tilt of (111) plane about the surface (degree) in the SS-N film containing expanded austenite deposited with 30% N_2 at 300 °C..... 129

5.11 GIXD pattern, of pure stainless steel film deposited at 300 °C & with 100W, obtained with glancing angle of incidence of 44°..... 132

5.12 Average asperity size measured by FESEM for various stainless steel based films deposited at 300 °C and on unheated substrates..... 131

5.13 FIELD EMISSION SEM micrographs showing the surface morphology of the films deposited at 300 °C with 50% N_2 in the gas mixture, for (a) 45 minutes (135 nm thick) and (b) 75 minutes (225 nm thick)..... 133

5.14 Variation of hardness and modulus of the SS-N films deposited with at.% N in the SS-N films deposited at 300 °C & with 100W..... 136

5.15 Optical micrographs of micro scratch tracks on various SS-N films..... 137

5.16 Saturation magnetization on unheated substrates of SS-N films with varying % N_2..... 139

A.1 XRD plot of the film deposited with 0% N_2 gas mixture and at 100° C..... 144

A.2 XRD plot of the film deposited with (a) 0.05%, (b) 0.11% &, and (c) 0.33% N_2 in gas mixture and at 100° C..... 147

A.3 XRD plot of the film deposited on unheated substrate and with 50% N_2 gas 148

ATTENTION: The Singapore Copyright Act applies to the use of this document. Nanyang Technological University Library

mixture.....

A.4 XRD plot of the film deposited with 50% N_2 in gas mixture and at 150 °C... 149

A.5 XRD plot of the film deposited with 50% N_2 gas mixture and at 300 °C..... 149

A.6 FESEM micrographs of Fe-N films deposited at various conditions..... 149

A.7 AFM pictures of films deposited at temperatures with 50% N_2 in sputtering gas mixture, along with the respective R_a values in nm..... 154

A.8 AFM pictures of the films deposited at 100 °C with various % N_2 in sputtering gas mixture, along with the respective R_a values in nm..... 155

ATTENTION: The Singapore Copyright Act applies to the use of this document. Nanyang Technological University Library

LIST OF TABLES

2.1 Details of FeN phase obtained in the sputter deposited Fe-N films.... 34

3.1 Specifications of the substrates used for depositions of the Fe-N based films..... 35
3.2 Composition of AISI 316L target..... 36
3.3 Conditions of deposition process at which all the sets of SS-N films.. 40
3.4 Salient differences between GIXD and Bragg-Brentano mode of XRD analysis..... 42
3.5 Details of indentation experiments carried out with NanoTest..... 53
3.6 Details of microscratch experiments carried out with NanoTest..... 53

4.1 Elemental composition of pure stainless steel film 55
4.2 Hardness & Reduced-Modulus values of various SS-N films deposited with varying % N_2 in sputtering gas mixture at 300 °C..... 95
4.3 Hardness values of various SS-N films..... 96

5.1 Phase constituents in various SS-N films deposited on Si (100) with varying % N_2, with 100W on unheated substrates 106
5.2 Bragg angles diffraction peaks corresponding to γ_N and the MN phases..... 107
5.3 Lattice Distortion Index for various SS-N films 113
5.4 Summary of binding energy or Cr2p 2/3 and N1s, and possible bonding state Cr and N in pure SS, γ_N and MN phases 114
5.5 Texture Index in terms of (111) plane parallel to the surface for SS-N Films..... 130
5.6 Critical loads of adhesive failure of the SS-N films deposited with various % N_2 in gas mixture at 300°C 137

ATTENTION: The Singapore Copyright Act applies to the use of this document. Nanyang Technological University Library

LIST OF NOTATIONS

AFM	Atom force microscope
at.	Atomic
Ar	Argon
Bcc	Body centered cubic
Bct	Body centered tetragonal
B_s	Saturation magnetic induction
C	Carbon
At.% N	Concentration of nitrogen
Cr	Chromium
d	Crystal lattice spacing
Emu	Electromotive unit
Fcc	Face centered cubic
Fe	Iron
G	Gauss
K	Kilo
k	Boltzman constant
M_s	Saturation magnetization
M	Alloying element
Mg	Magnesium
mTorr	Milli Torr
N	Nitrogen
Ni	Nickel
nm	Nanometer
O	Oxygen
Pa	Pascal
RF	Radio frequency
RT	Room temperature
Sccm	Standard cubic centimeter per minute
SEM	Scanning electron microscope
SS	Stainless steel

ATTENTION: The Singapore Copyright Act applies to the use of this document. Nanyang Technological University Library

Si	Silicon
Ta	Tantalum
T_e	Electron temperature
Ti	Titanium
T_{sub}	Substrate temperature
W	Watt
XRD	X-ray diffraction
Zr	Zirconium
θ	Angle of incidence of X-ray
^oC	Degree centigrade
μ_B	Bohr magneton
%	Percentage

ATTENTION: The Singapore Copyright Act applies to the use of this document. Nanyang Technological University Library

LIST OF PUBLICATIONS

1. S. R. Kappaganthu and Y. Sun, "Influence of Deposition Conditions on the Production of MN-Type Cubic Nitride Films by Reactive Sputter Deposition of a Stainless Steel Target", Surface and Coatings Technology, 198, 59-63, 2005
2. S.R. Kappaganthu and Y. Sun, "Studies on Structure and Morphology of Sputter Deposited Stainless Steel – Nitrogen Films ", Applied Physics A, 81 (4), 737-744 Sep., 2005
3. Nurot Panich, S. R. Kappaganthu and Y. Sun, "Polytetrafluoroethylene Doped MoS_2 Films for Precision Engineering Applications", International Conference on Precision Engineering, Singapore, 2004
4. S. R. Kappaganthu and Y. Sun, "Formation of a MN-Type Cubic Nitride Phase in Reactively Sputtered Stainless Steel-Nitrogen Films", Journal of Crystal Growth, 267/1-2, 385-393, 2004
5. Y. Sun and S. R. Kappaganthu, "Effect of Nitrogen Doping on Sliding Wear Behaviour of Stainless Steel Coatings ", Tribology Letters, 17, No.4, November, 2004
6. S. R. Kappaganthu and Y. Sun, "Effect of Nitrogen Partial Pressure and Temperature on RF Sputtered Fe-N Films", Surface and Coatings Technology, 167, 165-9, 2003
7. S. R. Kappaganthu and Y. Sun, "Mechanical integrity of nitrogen doped stainless steel stainless steel coatings", International Conference on Advances in Surface Treatment: Research and Applications", Hyderabad, 2003
8. S. R. Kappaganthu and Y. Sun, "Magnetic Properties of Sputter Deposited Stainless Steel-Nitrogen Films", International Conference on Materials of Advanced Technology", Singapore, 2003
9. D. Siva Rama Krishna, S.R. Kappaganthu and Y. Sun, "Thermal Oxidation of Titanium Coatings on Stainless Steel for Potential Tribological Applications", International Conference on Advances in Surface Treatment: Research and Applications", Hyderabad, 2003

ATTENTION: The Singapore Copyright Act applies to the use of this document. Nanyang Technological University Library

Chapter 1

INTRODUCTION

1.1 BACKGROUND

The iron-nitrogen system is one of the most widely studied binary system due to the existence of several interesting stable and metastable phases which can offer a range of interesting mechanical, chemical and magnetic properties. These phases include N-incorporated martensite (α'), austenite (γ), γ'-Fe_4N nitride, ϵ-$Fe_{2-3}N$ nitride and ordered α''-$Fe_{16}N_2$ nitride. More recently, a new mestastable phase FeN with equiatomic stoichiometry has also been discovered in iron nitride films by reactive sputtering of an iron target. The study on the Fe-N system during the past five decades has been based on surface reactions and nitridation. Recently there have been increasing interests in studying this Fe-N system by thin film deposition. In particular among many phases in the Fe-N system, the metastable and ordered nitride, α''-$Fe_{16}N_2$, has been found to possess a giant magnetic moment of 2.8 μ_B per iron atom. This value is not only larger than that of bulk iron (2.2 μ_B), but also larger than that of the $Fe_{65}Co_{35}$ alloy (2.5 μ_B), which has the greatest saturation magnetization in iron-based substitutional alloys [1]. However, due to poor thermal stability of the α''-$Fe_{16}N_2$ phase which can only be formed below 200 °C [2], it is not possible to produce a pure α''-$Fe_{16}N_2$ phase by nitriding and difficult to produce a single α''-$Fe_{16}N_2$ film by film fabrication. Further efforts are required to study the evolution of various phases in magnetron sputtered Fe-N film as a function of deposition parameters.

Apart from the above discussed Fe-N films, applications and research on nitrogen doped iron based materials is of scientific interest since the early days of nitridation of stainless steels which was first developed in the twenties of the last century. The nitridation of stainless steel was developed initially for facilitating the incorporation of nitrogen atoms to the near surface region of the steel to form a hardened case. Since then nitrogen has been discovered to be an important solute inclusion in stainless steel for imparting interesting properties. Various studies

ATTENTION: The Singapore Copyright Act applies to the use of this document. Nanyang Technological University Library

have been done on the effect of nitrogen on various mechanical properties like elastic modulus [3], hardness [4], thermal aging [5, 6 and 7], corrosion resistance [8], and magnetization [9, 10, 11 and 12]. It was found that the strong affinity between chromium and nitrogen was the cause for increase in yield strength and thermal stability of austenite structure [4], and that nitrogen brings up on ferromagnetic behavior of austenite phase as determined by magnetic force microscope [11]. Many differences between the influences of carbon and nitrogen as interstitial elements on stainless steels were discovered. Most of the differences were ascribed to the differences in electronegativities and the ionic radii [2, 7 and 13].

Application of conventional nitridation of steels has been in existence due to the increase in case hardness owing to the affinity between Cr-N [3 and 4]. Nevertheless, the corrosion resistance properties of such nitrided surfaces were found to deteriorate [14]. Interestingly, in the case of low temperature nitridation, improvement in mechanical strength of stainless steels [15] could be achieved differently through the formation of expanded austenite, γ_N (also known as S phase). It was also found that the corrosion properties of the case hardened surface produced by low temperature nitriding are as good as untreated stainless steels. The studies were carried out in detail by many investigations [16 and 17], the discussion of which is outside the scope of this report.

Regarding the magnetic properties of the expanded austenite phase (γ_N), only limited studies, by means of magnetic force microscope and Mossbauer spectroscopy have taken place. The studies indicated that the bulk γ_N phase, formed by low temperature nitriding, is a ferromagnetic phase, although fcc austenite is paramagnetic. It has been found that low energy, high current density ion-beam processing of fcc austenitic stainless steel surfaces could alter the magnetic properties of the material. The incorporation of more than 20% nitrogen in the fcc austenite surface resulted in a ferromagnetic behavior caused either by tetragonal distortion of the lattice [12] or by means of lattice expansion [10] or by defect density [11]. This further highlights the unique role of nitrogen in the Fe-based system. Further investigation is however required to clarify this unusual magnetic behavior in fcc austenite films, in particular when doped with nitrogen.

ATTENTION: The Singapore Copyright Act applies to the use of this document. Nanyang Technological University Library

More recently, there have been growing interests in the fabrication of stainless steel films doped with nitrogen (SS-N) on various substrates, due to the application potential of such films as wear resistant, corrosion resistant coatings. The microstructure and properties of SS-N films are dependent on deposition process conditions. Various amounts of nitrogen content, variety of texture, morphologies and properties are possible in the SS-N films. Due to the increased popularity of the low temperature nitridation, majority of the recent studies focused on the S phase (or γ_N phase), formed in SS-N films, which displays a range of attractive mechanical and corrosion properties and interesting magnetic properties.

However, previous works [7-13], involving fabrication of nitrogen doped stainless steel films, only dealt with characterization of the S phase films. The optimization of mechanical properties was attempted with no attention to the phase evolution in the SS-N films. Only vague knowledge is available about the factors that determine the mechanical properties of the SS-N films. The properties are influenced by microstructural aspects like residual stress, grain-size distribution and phase composition. Further, despite the dependence of the microstructure on conditions of the physical vapor deposition technique employed, negligible efforts were made to understand the influence of various deposition process parameters.

On the other hand, reactive sputter deposition, over the other thin film fabrication techniques, has the advantages such as the potential in yielding new phases, producing expanded austenite with minimal dislocation density and strain, incorporation of a range of nitrogen contents in the films. The combined understanding on the influence of each of the deposition process parameters can provide improved insight into the nature of formation of the various phases and the film growth. Even though it was discussed in the preceding paragraphs that expanded austenite offers improved mechanical and interesting magnetic properties, attempts to understand the relation between microstructure and deposition process have not been made in sufficient amounts. Thus, there is a need for emphasizing holistic studies to be conducted on reactive sputter deposition of stainless steel films doped with various amounts of nitrogen.

ATTENTION: The Singapore Copyright Act applies to the use of this document. Nanyang Technological University Library

1.2 OBJECTIVES OF THE RESEARCH WORK

This project involves the fabrication and characterization of two kinds of films, i.e. nitrogen doped stainless steel films (SS-N) and Fe-N films by magnetron sputtering and various experimental and analytical techniques. Based on the above discussion, it was decided to conduct studies with the following specific research objectives:

1. To investigate and understand the role of reactive sputter deposition process conditions in phase evolution in stainless steel – nitrogen (SS-N) films.

2. To study various structural, morphological and compositional features of the resultant films.

3. To explore and investigate the mechanical and magnetic properties of the stainless steel – nitrogen films.

4. To characterize the Fe-N based thin films deposited by RF- magnetron reactive sputtering and evaluate the possibility of forming single α''-$Fe_{16}N_2$ phase with polycrystalline microstructure.

1.3 ORGANIZATION OF THE THESIS

Chapter 1 introduces the field of iron-nitrogen based material system, discusses the advantages and interests in the research and concludes by highlighting the need for further work and with proposition of objectives of the work. Chapter 2 attempts for detailed review on various aspects of the Fe-N based system, like phase diagram, crystallography, nitridation of stainless steel and properties of the nitrided steels. It also covers fundamentals of sputtering and reactive sputter deposition. Chapter 3 details about various sets of samples produced, and details of characterization techniques used for the proposed studies. In chapter 4, results of various experiments on SS-N films are consolidated and further analyzed and discussed in detail in chapter 5. Finally chapter 6 summarizes the results obtained, conclusions drawn along with suggestions for further research.

ATTENTION: The Singapore Copyright Act applies to the use of this document. Nanyang Technological University Library

Chapter 2

LITERATURE SURVEY

2.1 SPUTTER DEPOSITION PROCESS

2.1.1 History of Sputter Deposition Process

Sputtering was first observed in a dc glow discharge tube by Grove in 1852 [18]. Following the discovery of the phenomenon it was widely used as a method for coating mirrors. But the invention of much faster process, "vacuum evaporation", decades later caused sputtering to be largely discarded by workers in the thin film field. It was in the 1920s that the pioneering work of Irwin Langmuir laid the foundation for modern plasma physics and led to a much better understanding of the gas discharge environment in which sputtering operates [18]. Increasing interest in refractory-metal films for microelectronics and cryogenic applications has caused many workers to take a second look at sputtering. With the development of radio frequency (RF) sputtering and other variants of sputtering systems, it has become one of the versatile techniques in thin film deposition

ATTENTION: The Singapore Copyright Act applies to the use of this document. Nanyang Technological University Library

2.1.2 Principles of Sputter Deposition

2.1.2.1 The Glow Discharge

If a dc voltage is applied between two electrodes spaced some distance apart in a low pressure gas, the current flow will be negligibly small unless some minimum value, called breakdown voltage is used. However, if the cathode is made to emit electrons (for example, by irradiating it with ultraviolet light), a small current flows between the electrodes.

This current, which is immediately extinguished when the source of emission at the cathode is removed, can be observed to increase with increasing electrode spacing, provided the applied voltage exceeds the ionization potential of the gas concerned. The increase in current with spacing occurs because at a given pressure, electrons on their way from the cathode to the anode make a fixed number of ionizing collisions per unit length so that the longer the distance they travel the

ATTENTION: The Singapore Copyright Act applies to the use of this document. Nanyang Technological University Library

as negative glow region where the number of ions and electrons is nearly the same. At the anode-side edge of the negative glow, the electrons must have lost energies (due to their collision history) required for the ionization and so a electrons-accumulated dark space forms, which is called "Faraday's dark space". Electrons, after passing through the Faraday's dark space by diffusion, are accelerated by electric field in front of anode and start ionizing the gas. This region extending until the anode is called "anode glow" or "positive column". Figure 2.1 shows schematically various regions along with the potentials across the discharge column.

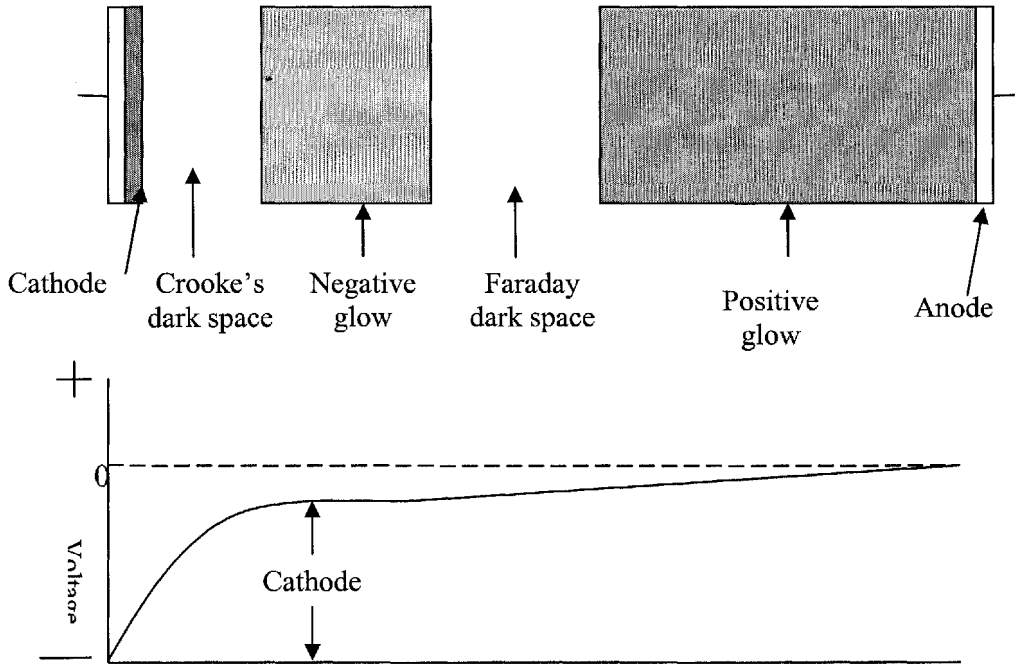


Figure 2.1: Cross-sectional view of glow discharge [19]

For a given external applied voltage, the ion density determines the thickness of the dark space. The lesser the thickness, the more is the electric field in the Crooke's space, and the efficiencies of electrons to ionize the atoms in the glow region and ions to generate secondary electrons at the cathode increase, causing breakdown with applied voltage. Once breakdown occurs, the number of secondary electrons produced at the cathode is sufficient to maintain the discharge glow and thus it is said to be self-sustained.

At relatively low voltages the cross sectional area will be less than the available cathode area and thus the cathode surface is only partially covered with the glow.

ATTENTION: The Singapore Copyright Act applies to the use of this document. Nanyang Technological University Library

This arises because the glow requires a minimum current density to produce sufficient secondary electrons for self-sustenance. When only a small amount of power is available, the cross sectional area of the glow is reduced until this minimum current density is attained. If additional power is applied to the discharge tube, the glow adjusts to this by increasing its cross sectional area, thus raising the total current but keeping the current density constant.

As long as this current density does not increase, neither does the voltage across the dark space. This minimum voltage drop needed to maintain the glow is called the normal cathode fall and the corresponding glow is referred to as the 'normal glow". When the power to the discharge tube is increased above the point where the glow covers the entire available cathode area, the current density at the cathode must increase. The glow can do this only by increasing the number of secondary electrons coming out of the cathode, which requires an increase in the cathode fall. A glow discharge operating in this mode is referred to as "abnormal glow".

Figure 2.2 shows a schematic of the I-V characteristics of DC glow discharge. In practice this abnormal glow is the only mode of interest for the deposition of films by sputtering. Sputtering experiments are performed with glows that are strongly abnormal. This is primarily because the current density in the normal glow is too low for atoms to be sputtered out of the cathode at useful rates and also because the voltage drops in the normal glow is quite low so that sputtering yields are similarly low. For optimum sputtering rate, the anode should not be inside the glow, so that full glow-length can be used for the build up of plasma density, by ionization-collisions of electrons [20].

ATTENTION: The Singapore Copyright Act applies to the use of this document. Nanyang Technological University Library

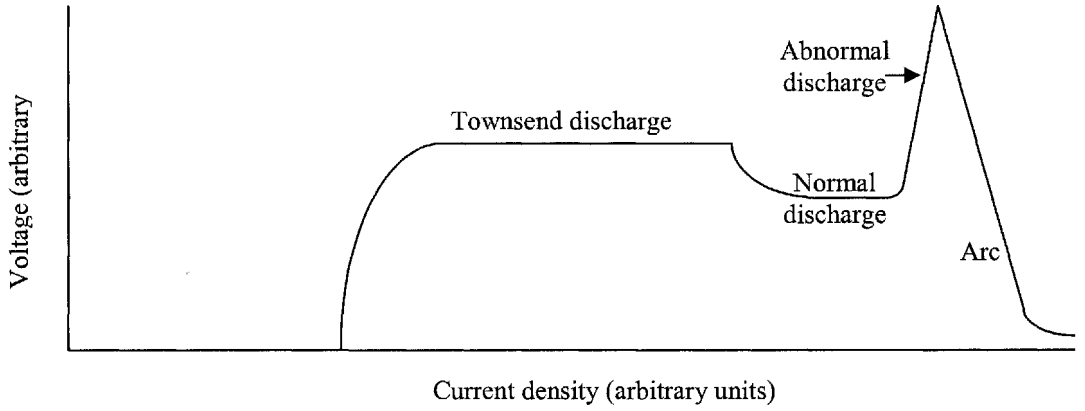


Figure 2.2: Schematic of I-V characteristics of DC glow discharge [21]

2.1.2.2 The Thornton Model of Film Structure

PVD processes normally involve three steps, namely the generation of metal vapor, transportation of the vapor, and condensation of the coating atoms onto the substrate surface. The condensation of the coating atoms can be pictured as occurring in the following three steps.

1. Incident atoms transfer kinetic energy to the lattice and become loosely bonded "adatoms".
2. These adatoms diffuse over the surface, exchanging energy with the lattice and other adsorbed species until they become trapped at low energy lattice sites.
3. The incorporated atoms readjust their position within the lattice by bulk diffusion processes.

The most significant factors influencing the adatom surface mobility are the deposition temperature and the kinetic energy of the incident atoms. One can expect a dense and better microstructure at higher deposition temperature with incident atoms of greater kinetic energy.

Movchan and Demchishin, developed a structural zone model of deposited materials at different temperatures, which is based on the studies of thick coatings of Ti, Ni, W, ZrO and Al_2O_3 deposited by vacuum evaporation. The model describes the type of coating structure formed as a function of the ratio of

ATTENTION: The Singapore Copyright Act applies to the use of this document. Nanyang Technological University Library

deposited temperature (T) to the melting point of the deposited material (T_m), i.e. (T/T_m).

Zone I (T/T_m) < 0.3, a low temperature zone, consists of tapered crystals with a domed surface appearance. It contains longitudinally oriented porosity between the tapered crystals, the internal structure of the crystals has a high dislocation density and is poorly defined. Zone I structures result when adatom diffusion is insufficient to overcome the effects of "shadowing" i.e. the high points of the growing surface receiving more coating flux than the valleys do, resulting in open boundaries between crystals.

Zone II ($0.3 < (T/T_m) < 0.5$), consists of columnar grains which are separated by distinct, dense, inter-crystalline boundaries. The surface has a smooth appearance and the dislocations are primarily in boundary regions and grain size increases with (T/T_m). This is the result of surface diffusion, which occurs during the deposition process, redistributing the coating flux and producing the coalescence of differently oriented islands with the formation of a more ordered surface with a preferred orientation.

Zone III (T/T_m)> 0.5, a high temperature zone, consists of equiaxed grains with a bright surface. Bulk diffusion and recrystallization dominate in zone III and the structure and properties of the coating correspond to a fully annealed metal.

Thornton in a study of the sputter deposition of Ti, Cr, Fe, Cu, Mo and Al thick coatings, found that the working gas pressure (Ar) had a strong influence on the formation of zone I structure. He found that increasing gas pressure promoted the formation of zone I structure and that a transition zone T existed between zone I and II. This transition zone consisted of a dense array of poorly defined fibrous grains without voided boundaries.

The properties of the coating appear to depend principally on the coating structure. It is seen that the hardness of pure metal and alloy coatings decreases with increasing deposition temperature, whilst for compound materials; the hardness tends to increase with increasing deposition temperature. In general, as the coating

ATTENTION: The Singapore Copyright Act applies to the use of this document. Nanyang Technological University Library

structure changes from zone I through zone III, the hardness of the coating increases, with maximum hardness being obtained for zone III structures. This is due to the fact that the strength of ceramic materials is very adversely affected by flaws produced at low temperatures. At higher deposition temperatures the occurrence of these flaws is markedly reduced, producing a more perfect material which results in high hardness.

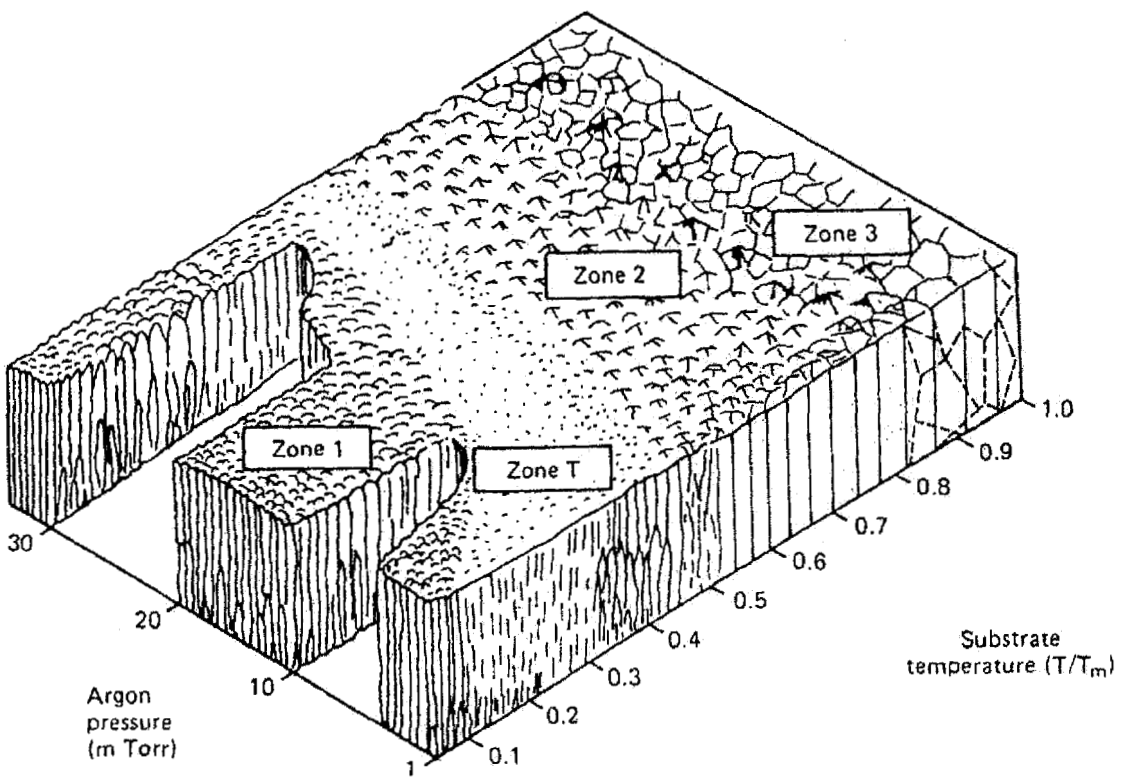


Figure 2.3: Thornton's model of thin film morphology [22]

2.1.3 Reactive Sputter Deposition

Compound films deposited by sputtering a compound target by an inert gas may not have the same composition or stoichiometry as that of the target. This happens due to selective sputtering of different elements in the compound target. Such a non-stoichiometry becomes more serious when one of the constituent elements of the target is non-metallic. Depositing an insulating film from the same material-target by RF sputter deposition often causes uncontrollable heating of the target as the sputtering phenomenon is energy inefficient. Poor conductivity and insufficient target cooling generate thermal stresses, and eventual cracking of the target.

ATTENTION: The Singapore Copyright Act applies to the use of this document. Nanyang Technological University Library

Reactive sputtering was developed to combat such undesirable problems. The popularity of reactive sputtering can also be attributed to [23]:

(1) Capability of producing thin compound films of controllable stoichiometry and composition,

(2) Higher deposition rates compared to the sputter deposition of compound targets on an industrial scale,

(3) Lower secondary electron heating of the substrates compared to the compound targets,

(4) Elemental targets of high purity are achievable, and can be machined and bonded more easily than compound targets,

(5) Relatively superior electrical conductivity of elemental targets over rule the requirement of RF sputtering for the deposition of insulating compound targets, and

(6) Elemental targets are thermally conductive, which makes the cooling of the targets more efficient.

There are two forms of reactive sputtering, both of which use reactive gases. In one form, the target is a nominally pure metal or alloy which is desired to synthesize into a compound by sputtering in a pure reactive gas or an inert gas-reactive gas mixture. The second form of reactive sputtering involves a compound that chemically decomposes substantially during inert gas-ion bombardment, resulting in a film deficient in one or more constituents of the target. Reactive gases containing the relevant species are used to restore the stoichiometry of the resultant film. A large number of reactive gases have been used to synthesize compounds from metal targets or to maintain the stoichiometry in the case of decomposition: air, O_2, or H_2O (oxides), N_2 or NH_3 (thin conducting nitride films), $O_2 + N_2$ (oxynitrides) etc.

2.1.4 Target Poisoning and Arcing

Target poisoning is a non-linear, complex, formidable and severe problem in reactive sputtering, involving many interdependent parameters. It refers to the reaction of the reactive gas with the target to form a compound at the target surface such that further sputtering occurs on the compound rather than on the initial pure metal. The degree of target poisoning depends mainly on the partial pressure of the

ATTENTION: The Singapore Copyright Act applies to the use of this document. Nanyang Technological University Library

reactive gas and the sputtering rate of the target. At very low reactive gas partial pressures and high target sputtering rate, all of the compound synthesis occurs at the substrate and that the stoichiometry of the film depends on the relative rates of arrival at the substrate of sputtered-target atoms and the reactive gas. Under these conditions the rates of removal and/or decomposition of compounds at the target surface are far faster than the rate of formation at the target surface and thus target poisoning is minimized. As the reactive gas partial pressure is increased and/or the target-sputtering rate is decreased, a threshold is reached at which the rate of target-compound formation exceeds the removal rate of compounds [24] and the target is poisoned continuously. These cathode reactions increase suddenly at a critical rate of reactive gas flow or reactive partial pressure.

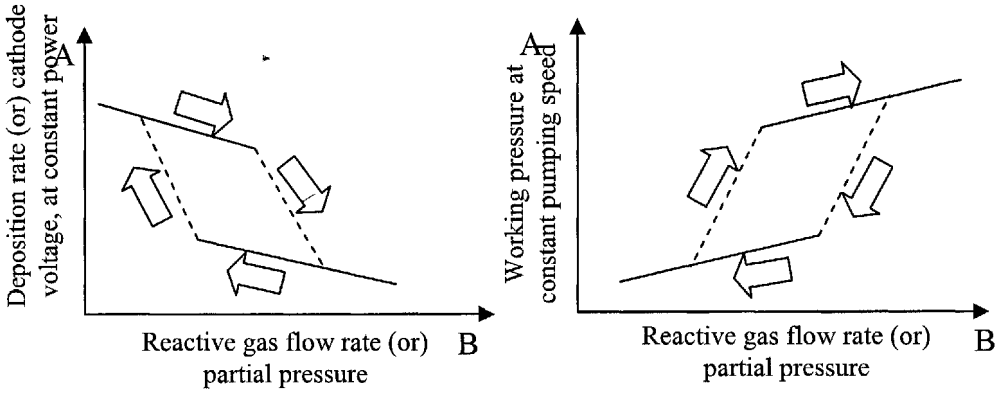
When the reaction product is insulating, a region of the target surface remains covered with the poisoning-product. This insulating region is subject to ion-bombardment and gets highly charged due to charge accumulation or through secondary electron emission. This leads to arcing and instability arising from rapid localized discharges, which disrupt the sputtering discharge and causes arc evaporation from regions of the target, with particle spitting and subsequent contamination of the film [25].

Target poisoning poses serious drawbacks to the application of reactive sputtering for compound-film deposition. Problems due to target poisoning are instability in the sputtering discharge, poor control over the composition of the film, reduced deposition rate, limited range of compositions of the films, inability to form of sub oxides; sub nitrides etc., spitting defects in the film due to arc evaporation, and reduced target lifetime.

The trend in variation of the above mentioned parameters, with the reactive gas flow rate and/or reactive gas partial pressure is shown schematically in Figure 2.4 (a and b). A-axis in Figure 2.4 (a) represents either deposition rate (or) cathode voltage (at constant current), and B-axis represents reactive gas flow rate (or) reactive gas partial pressure. In figure 2.4 (b) A-axis represents reactive gas consumption (whose change is shown by change in total working pressure) and B-axis represents reactive gas flow rate. From Figure 2.4 it is clear that target

ATTENTION: The Singapore Copyright Act applies to the use of this document. Nanyang Technological University Library

poisoning causes the sputtering parameters to show hysteresis behavior with respect to reactive gas flow rate. The reasons for the hysteresis effects of target poisoning are discussed below. Gradual decrease in the sputtering rate with increase in reactive gas flow rate (at a constant power) is due to less efficient sputtering by reactive-gas ions than by inert-gas ions. As the flow rate is increased beyond a critical value, deposition rate abruptly decreases due to the lower sputtering yields of compounds (formed on the target surface) than metals, as extra ion-bombarding energy is required for breaking the bonds of the compounds. This corresponds to the occurrence of target poisoning.



2.4: Schematic variation of (a) deposition rate and (b) working pressure with respect to reactive gas partial pressure

The sudden decrease in the cathode voltage, for a constant power is due to the rapid increase in the discharge current owing to the greater secondary-electron emission yields of compounds than metals. Accordingly, more of the energy of incoming ions is used to produce and accelerate secondary electrons. In the case of working pressure versus reactive gas flow rate (at constant inert gas flow rate), the former increases abruptly as the rate of consumption of reactive gas decreases due to the decrease in the metallic reactant species after the target is poisoned. During the process of gradual decrease in the reactive gas flow, the process of attaining the original sputtering parameters (sputtering conditions existing before the onset of target poisoning) is delayed beyond the critical flow rate. This is because the compound already formed on the target surface requires finite drop in the reactive gas partial pressure for its dissociation.

ATTENTION: The Singapore Copyright Act applies to the use of this document. Nanyang Technological University Library

On the onset of poisoning, the decrease in the consumption of reactive gas (due to lesser sputtered-metal atoms) increases the net reactive gas partial pressure, thereby further accelerating the poisoning process more rapidly. This uncontrolled effect (analogous to avalanche-effect [25-27]) goes until the whole target surface is covered with the poisoning-product. The critical reactive partial pressure depends on the discharge conditions like power, target area [28], type of reactive gas [27], working pressure [28], temperatures of cathode and the substrate [18], and kinetics of compound formation on the target surface [20]. The techniques proposed and/or implemented for the control of target poisoning [23, 24, 28] are maintaining a gradient in the composition of reactive gases, pulsed biasing of the target, increasing the reactivity at the substrate by intensifying the plasma adjacent to the substrate, with the help of a positively biased anode near the substrate, increasing the pumping speed, obstructing the reactive gas flow to the target, pulsed reactive gas flow, plasma emission monitoring, voltage control etc.

2.1.5 Sputter Deposition Process Parameters

2.1.5.1 Pressure and Total Gas Flow Rate

Working pressure during the sputter deposition has significant effect on the deposition rate and quality of the film. Some of the consequences of increasing the sputtering gas pressure are the increase in discharge current; the increase in back scattering; contamination of the films by inert gas; and the low energy of sputtered atoms (by inelastic collisions) thereby causing poor adhesion of the films. The first two effects compete largely and determine deposition rates, as the first effect increases the total number of sputtered atoms while the latter effect scatters the sputtered atoms away from their original direction. The third effect can be used to minimize or maximize the energy of particles incident on substrates. Other effects of high working pressure are poorly defined energies and angles of deposition of sputtered atoms, which make studies on the sputtering phenomena difficult. Increased working pressure can cause voids and pin holes in the films, owing to the poor mobility (energy loss due to multiple collision) of sputtered atoms and self-shadowing effect arising from multiple collisions with gas atoms which cause pronounced angular incidence of the sputtered atoms onto the substrate. It has been

stated that low working pressures cause higher area inhomogeneties of sputtered atoms in the film [29], in case of alloy or compound film.

Pressure in the chamber can play a vital role in target poisoning during reactive sputtering, for a given reactive gas partial pressure. The increase in pressure aggravates the avalanche-effect, during target poisoning on the surface of the target, and brings down the critical reactive flow rate of the onset of target

ATTENTION: The Singapore Copyright Act applies to the use of this document. Nanyang Technological University Library

increasing working pressure, increasing the distance between the cathode and the anode, thermionic emission of electrons at the cathode and usage of magnetron targets etc.

2.2 THE STAINLESS STEEL – NITROGEN SYSTEM

2.2.1 Bulk Nitrogen-Bearing Stainless Steels

Among the several major types of stainless steels, austenitic stainless steels are the most widely used type in industry due to their excellent corrosion resistance and good fabricability such as formability and weldability. Austenitic stainless steels contain mainly 16 – 25 % of Cr required for corrosion resistance and 8 – 15 % of Ni for austenitic phase stabilization. Other alloy elements can be added for structural and properties modification and enhancement, such as Mo for corrosion resistance enhancement, Ti and Nb for structural stabilization and reduction in the tendency towards sensitization.

Sensitization imposes a serious limit to the application of austenitic stainless steels in industry and fusion-weld joining. It occurs at temperatures between 425 and 750 °C or when cooling slowly across this temperature range, where $Cr_{23}C_6$ type carbides form at austenitic grain boundaries, leading to the deterioration of inter-granular corrosion of the stainless steel. Two remedies can be used to alleviate the sensitization problem of austenitic stainless steels [30]. One is by lowering the carbon content in the steel below 0.03 wt %, but this is at the expense of the strength of the steel. Another approach is to add small amounts of such alloy elements as Ti and Nb, which have higher affinity with carbon than that of Cr with carbon, and thus help to avoid the formation of the $Cr_{23}C_6$ carbide.

When austenitic stainless steels are cooled rapidly from high temperature, e.g. 1100 °C, to room temperature, no martensitic phase transformation takes place and the austenitic structure is retained because the martensitic transformation starting temperature (M_s) is well below room temperature due to the large mount of alloy elements in the steel which are effective M_s-reducers, as expressed below [30].

ATTENTION: The Singapore Copyright Act applies to the use of this document. Nanyang Technological University Library

$M_s = 502 - 810\ C - 1230N - 13\ Mn - 13Ni - 12Cr - 54\ Cu - 6\ Mo$----------(1)

Austenitic stainless steels thus can not be hardened by martensitic phase transformation. The most important hardening techniques for austenitic stainless steels are solid-solution hardening by the alloying elements and strain hardening. The later is not only very effective for hardening but in many cases can induce martensitic formation. But strain hardening is normally accompanied with the reduction in corrosion resistance. Therefore, solid-solution hardening becomes the major technique of hardening austenitic stainless steels without impairing the corrosion resistance.

It has been found that nitrogen is the most effective solid-solution hardening element in austenitic steels. This has led to the development of a series of nitrogen-bearing steels, which possess many superior mechanical and chemical properties over the conventional nitrogen-free stainless steels [4]. These include

(1) Stabilization of austenitic structure because nitrogen is an extremely effective austenitic-stabilizer and M_s-reducer as can be seen from equation (1).
(2) Enhancement in mechanical strength because of the strong dislocation-pinning ability of nitrogen when dissolved in the austenite lattice. This requires that the amount of nitrogen added to the steel must be controlled properly followed by heat treatment to ensure that the nitrogen is dissolved in the austenite. Too much nitrogen and improper heat treatment will result in the formation of chromium nitride precipitates and deterioration in corrosion resistance and weldability of the steel. So far the amount of nitrogen that can be added to the austenitic stainless steels has been limited to about 0.3 wt %. When residing in the interstitial sites, nitrogen causes symmetric expansion of the face centered cubic (fcc) austenitic lattice. It has been established that the austenite lattice in the austenitic stainless steels expands with increase in nitrogen content as follows [4]

$a\ (nm) = a_o + 0.000861\ .\ X_N$, where X_N is nitrogen atomic fraction----(2-2)

This expression is similar to that established by Jack [2] for nitrogen in fcc iron:

ATTENTION: The Singapore Copyright Act applies to the use of this document. Nanyang Technological University Library

$a\ (nm) = a_o + 0.0078\ .\ X_N$, where X_N is nitrogen atomic fraction ----------(2-3)

The increase in yield strength due to the nitrogen dissolution is about 5.5 to 6.2 MPa, for each 0.01 % nitrogen i.e.

$$\sigma\ (MPa) = \sigma_0 + (550 \sim 620)\ x\ wt\ \%\ N \text{----------(2-4)}$$

where σ_0 is the yield strength of the corresponding nitrogen-free steel.

(3) Improvement in pitting and crevice corrosion resistance. This is a well-established fact although the reasons behind this beneficial effect have not been fully understood. Several empirical equations have been established to relate the pitting resistance of austenitic stainless steel to nitrogen content and other major alloying elements. One of such expressions is given as follows:

$$\text{Pitting resistance} \propto \%Cr + 3.3\%\ Mo + 16\%\ N \text{---------(2-5)}$$

It can be seen that the beneficial effect of nitrogen in increasing the pitting corrosion resistance is more significant than the other major alloying elements such as Cr and Mo. This may count for the observed increase in the pitting resistance by low temperature nitriding of the austenitic stainless steels as discussed below.

2.2.2 Low Temperature Nitriding of Austenitic Stainless Steels

2.2.2.1 Introduction

Although austenitic stainless steels can be strengthened by the addition of nitrogen as discussed above, the overall strengthening effect is rather limited due to the limit in nitrogen level that can be incorporated in the steel in the bulk form. Attempts have thus been made for alloying the surfaces of austenitic stainless steels using nitrogen as the major surface alloying element. Several commercial nitriding methods were accordingly applied to austenitic stainless steels, including salt bath nitriding, gaseous nitriding and glow discharge plasma nitriding. The latter is the most effective for stainless steels because the bombardment by

ATTENTION: The Singapore Copyright Act applies to the use of this document. Nanyang Technological University Library

energetic positive ions on the component surface helps to remove the native oxide film on stainless steel surface and then accelerates the nitrogen mass transfer from the plasma medium to the component surface.

Conventionally, nitriding of the austenitic stainless steels is carried out at high temperatures between 500 and 700 °C for times up to several tens of hours. This results in the formation of a nitrided case up to 200 μm thick which possesses a very high hardness up to 1200 HV and much improved wear resistance under aggressive conditions. In such a temperature range, due to the strong affinity of nitrogen with Cr in stainless steels, chromium nitrides, CrN and Cr_2N, form in the nitrided case during nitriding. This on the one hand results in the significant increase in hardness of the case by precipitation hardening, but on the other hand leads to the depletion of free Cr in the austenite matrix in the nitrided case. Since the corrosion resistance of stainless steels is provided by the free-Cr, the reduction in free-Cr inevitably results in deterioration in corrosion resistance of the stainless steel surface. Thus, conventional nitriding of stainless steels at temperatures above 500 °C, despite its wide applications in industry for many years, is always accompanied by a significant reduction in corrosion resistance which is not desirable in many engineering applications.

To tackle the problem of deterioration in corrosion resistance arising from conventional nitriding, attempts were made in the mid of 1980s to lower the nitriding temperature. This led to the development of the low temperature nitriding technique for austenitic stainless steels. Zhang and Bell [31] were the first to discover that at the temperature of 400 °C, the resultant nitrided layer, which is about 20 μm thick, is free from chromium nitride precipitates, and is not only hard but also corrosion resistant. The same phenomenon was also found by Ichii [32] independently. Dearnley [33] further studied the variation of a nitrided structure with nitriding temperature and confirmed the formation of a hard and corrosion resistant layer in austenitic stainless steels at temperatures below 450 °C. Since then significant progress has been made in terms of process investigation, structural and properties characterization. Since the structure of the low temperature nitrided layer in austenitic stainless steels is highly relevant to the

ATTENTION: The Singapore Copyright Act applies to the use of this document. Nanyang Technological University Library

present work, more detailed discussion in the structural characterization, resulting from this novel process, is given in the following sections.

2.2.2.2 Structural Studies on Low Temperature-Nitrided Stainless Steels

It has been established that at sufficiently low temperature (less than 450 °C), the formation of Cr nitrides in the nitrided case in austenitic stainless steels is suppressed and the nitrided layer possesses excellent corrosion resistance in particular pitting corrosion resistance, probably arising from the fact that no free-chromium depletion is experienced in the case. A question arose as where does the nitrogen, as high as 30 at.% [34] reside in the nitrided case and about the nature of the layer. Initially, the structure of the low temperature nitrided layer in austenitic stainless steels was mistakenly regarded as being the γ'-Fe_4N [31]. But Ichii [32] found that such a layer has a single phase, which is fcc, similar to the substrate fcc austenite but with an extended lattice up to 0.39 nm in comparison to 0.36 nm of austenite. Ichii regarded this as a new phase, and termed it as the "S" phase. Further studies [12] by others found that the S phase is of fcc austenitic nature, with lattice expansion due to supersaturation of nitrogen in the fcc lattice. The S phase is thus also termed as "expanded austenite" or "γ_N" by others [9 and 10]. Several detailed studies have been conducted recently on the nature of the S phase, the main results of which are summarized below.

It has been found that the expanded austenite phase, also known as the S phase, has predominant cubic structure but with tetragonal distortion due to the stresses generated by virtue of the concentration gradient across the depth [35], the presence of stacking faults generated [36 and 37] and the epitaxial relation [38] of the phase with the unexpanded austenite substrate. Nitriding of austenitic stainless steels at low temperature is accompanied by the generation of large stresses in the lattice which is evident from the stress relief by shearing and deformation as observed on the as-nitrided surface by Sun and Li (Figure 2.5).

ATTENTION: The Singapore Copyright Act applies to the use of this document. Nanyang Technological University Library

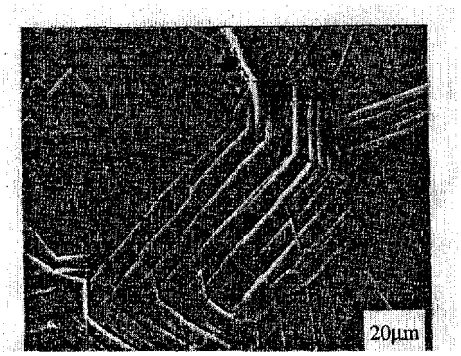


Figure 2.5: Scanning electron micrograph of the low temperature as-nitrided AISI 316 steel surface showing surface relief, shearing, and deformation [113]

Marchev et al (1999) [38] studied the crystal structure of expanded austenite, ion-nitrided under mild conditions and the orientation relation between the nitride layer and textures of austenitic substrate. Studies were carried out with the help of symmetric X-ray diffraction scanning and pole figure diffraction. Apart from interpreting the crystal structure of the expanded austenite to be face centered tetragonal (FCT) they also showed that the phase has preferred orientation with (111) plane being parallel to the substrate. The preferred orientation of the nitride layer can be noticed from the deviation of the symmetric XRD pattern from the calculated one (Figure 2.6). The peak corresponding to planes (222), despite being the fourth strongest one in the calculated pattern, was found to be the third strongest peak. This supports preferred orientation of the (111) planes, which are parallel to (222). It is to be noted that the XRD pattern is not very much identical to that expected for a purely tetragonal crystal structure. This can be understood from the absence of peaks corresponding to planes belonging to the same family of indices.

Jiang et al (2000) studied the microstructure of the low temperature nitrided layer of austenitic stainless steels. The stainless steels were nitrided by intensified plasma assisted processing after smooth polishing and ultrasonic and sputter cleaning. Plasma nitriding was carried out in a mixture of 80% N_2 and 20% Ar at 400 °C. The microstructural studies were carried out by cross sectional and high resolution transmission microscopy. They interpreted that the nitrided austenite lattice attained simple cubic structure with a lattice constant of 3.78 Å and the evolution of the nitride phase is preceded by lattice expansion and formation of

ATTENTION: The Singapore Copyright Act applies to the use of this document. Nanyang Technological University Library

anti phase boundaries and stacking faults (Figure 2.7). It was found that the lattice constant decreases with depth in conjunction with the decrease in nitrogen profile. This suggests the lattice parameter of expanded austenite decreases with decreasing nitrogen concentration. The same phenomenon has also been observed

ATTENTION: The Singapore Copyright Act applies to the use of this document. Nanyang Technological University Library



ATTENTION: The Singapore Copyright Act applies to the use of this document. Nanyang Technological University Library

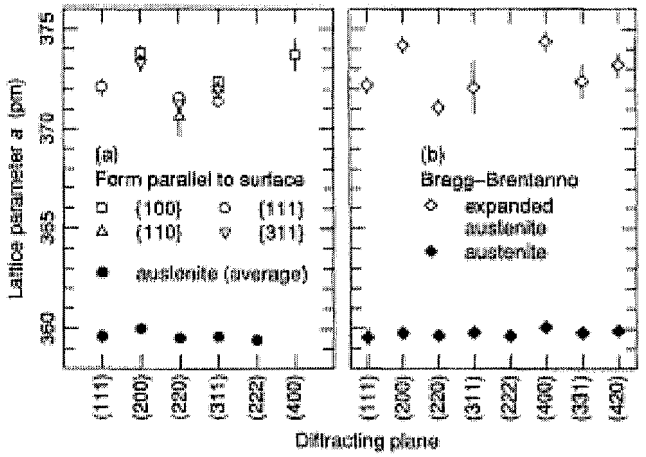


Figure 2.8: Lattice parameters calculated from fixed incident angle scanning and symmetric scanning [12]

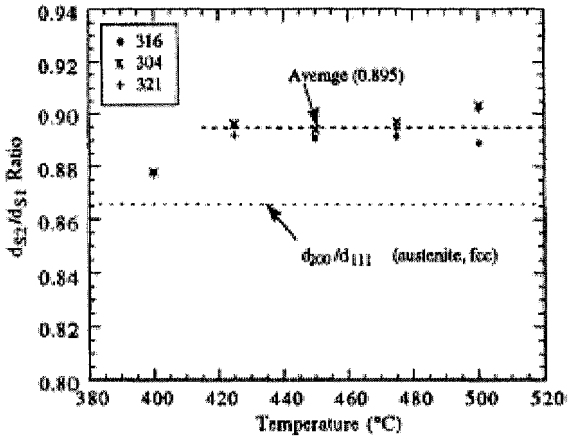


Figure 2.9: Ratio of interplanar spacing of (200) to (111) in the bulk expanded austenite plotted against nitriding temperature showing deviation from ideal fcc structure [36]

2.2.3 Magnetic Studies on Bulk Nitrided Stainless Steel

Nitrided austenitic stainless steels were found to form ferromagnetic nitrogen-supersaturated expanded austenite or the S phase. Indeed, nitrogen incorporated expanded austenite in the nitrided layer with high nitrogen content showed ferromagnetic behavior. Figure 2.10 shows the ferromagnetic domains in the expanded austenite of a bulk nitrided sample imaged with the help of magnetic force microscope. It is also found that the thickness of the ferromagnetic layer increased with increase in the amount of nitrogen incorporation into the nitrided

ATTENTION: The Singapore Copyright Act applies to the use of this document. Nanyang Technological University Library

layer. The ferromagnetic nature was also observed with the help of Mossbauer spectroscopy [34, 42, 43, 45] as well as magnetic force microscope [33].

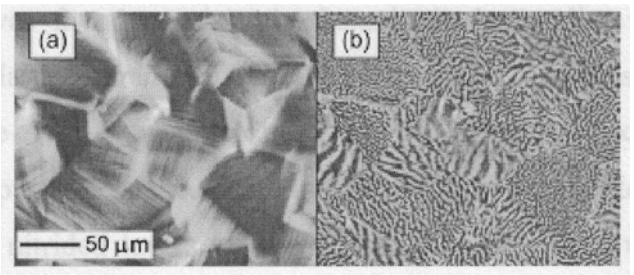


Figure 2.10: Ferromagnetic domains imaged by magnetic force microscopy in bulk expanded austenite [12]

The ferromagnetic behavior of the expanded austenite was initially assumed to be due to strain induced by lattice expansion [43] or dislocation density [44 and 45]. However, neither the lattice expansion [33] nor the dislocation density [46] proved to be the sole reason for inducing ferromagnetism in the expanded austenite. Nitrogen incorporated stainless steel was also studied [47] for the possibility and potential in the application as magnetic recording media.

2.3 STAINLESS STEEL – NITROGEN FILMS

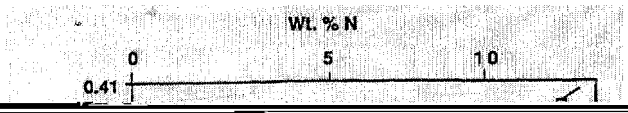
Stainless steel (SS) and stainless steel – nitrogen (SS-N) thin films have been studied over the last one and half decades especially to know their potential as protective coatings on various substrates. While metastable phases in bulk materials form as intermediate/transition phases during annealing, phases formed due to thin film formation differ in many aspects. Phase evolution, surface diffusion and substrate epitaxy have significant effect in films. In addition, formation of metastable phases and diversity of metastable phases are possible in thin films.

2.3.1 Fabrication and Structure of SS-N Films

Bourjot et al (1990) [48] studied the properties of austenitic stainless steel coatings doped with nitrogen on planar steel substrates deposited by sputtering in the nitrogen reactive atmosphere and at a temperature of 300 °C. The growing film was subjected to ion bombardment with current density of 0.5 mA/cm^{-2} and voltage of -100 V. Samples were prepared similarly by Saker et al (1991) [49] and

ATTENTION: The Singapore Copyright Act applies to the use of this document. Nanyang Technological University Library

were studied in comparison to the low temperature plasma nitrided layers of austenitic steels. Films as thick as 10-15 μm were deposited by d.c. triode magnetron reactive sputtering on well prepared and negatively biased steel substrates. It was found consistently from both the studies that the nitrogen content and the lattice parameter increased linearly with increase in the nitrogen proportion in the Ar + N_2 gas mixture (Figure 2.11). The maximum amount of nitrogen in the sputter deposited films (at. % of 42) was found to be much higher than that of the nitrided layers (at. % of 24). Similar results were obtained by Shedden et al [50] for the samples prepared by reactive magnetron sputter deposition. They obtained maximum nitrogen content in the SS-N films of 40 at.% where the nitrogen content increased linearly with N_2 flow rate.



ATTENTION: The Singapore Copyright Act applies to the use of this document. Nanyang Technological University Library

be attributed to the change in metallic regime of sputtering to compound regime in which sputtering rate is lower [20].

A metal nitride phase, MN, was also discovered [33, 48] in this work, where M represents all the metallic elements in stainless steel i.e. M = Fe + Cr + Ni + Mo. This new MN phase is different from the established expanded austenite phase; γ_N in that the MN phase is stoichiometric nitride with cubic structure and characteristic XRD pattern, while the γ_N phase is a solid solution with distorted fcc lattice.

2.3.2 Mechanical Properties of SS-N Films

Mechanical strength of pure and nitrogen incorporated stainless steel coatings on stainless steel substrates have been studied [49] and was found that the hardness of the coatings with pure expanded austenite phase increases with increase in nitrogen content. The mechanical properties, apart from depending on the nitrogen content, also depend on deposition process conditions and morphology of the coatings. Reactive sputter deposition of the SS-N films on various substrates has also been studied in terms of improvement in corrosion resistance and wear resistance [54].

Bourjot et al (1990) [52] determined the microhardness of the SS-N films with various nitrogen contents. The microhardness of pure stainless steel films was found to be 0.7 GPa. It increased linearly with nitrogen content up to 20 % to as high as 15 GPa and decreased to 12 GPa for further increase in nitrogen content (Figure 2.12). While the nitrogen content showed monotonic linear increase, the variations in microhardness could not be exclusively correlated with variations in size of the nanograins. It is to be noted from the results that the hardness of the amorphous phase kept on decreasing with increase in nitrogen content. This supports the requirement of pure crystalline S phase formation with optimal microstructure for enhanced mechanical properties. Adhesion strength of the films on the steel substrates was found to decrease after a certain nitrogen content of 30 % in the films.

ATTENTION: The Singapore Copyright Act applies to the use of this document. Nanyang Technological University Library

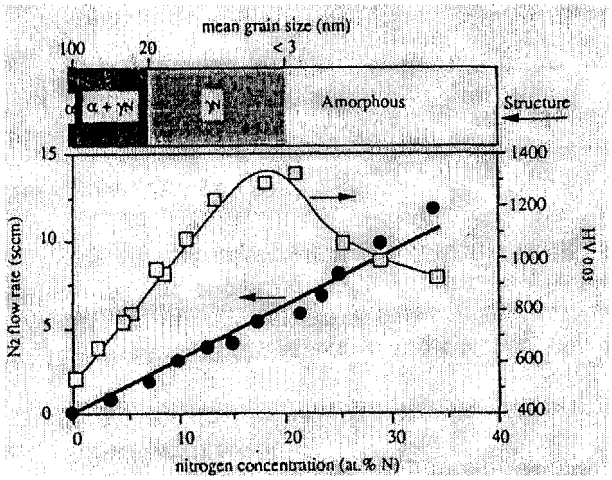


Figure 2.12: Nitrogen content and hardness of the SS-N films plotted against N_2 flow rate [52]

Von Stebut et al (1993) [49] studied in the SS-N films for their mechanical properties in order to optimize the strength of magnetron sputtered nitrogen-doped austenitic stainless steels. The hardness values obtained for uncoated substrates were about 2.2 GPa while the purse stainless steel film on the substrates showed the hardness as high as 4.5 GPa and the hardness increased to about 9.5 GPa with nitrogen doping. This clearly suggests the role of sputter deposition and nitrogen in increasing the mechanical properties of the films.

Dearnley et al (2004) [55] analysed the hardness and modulus values of the SS-N films in relation to the phases formed and the nitrogen content in the films. Figure 2.13 shows the variation of hardness and modulus of SS-N films with respect to the nitrogen content. Metastable ferrite films showed hardness of 18 GPa but the hardness reduced to 10 GPa as the proportion of the austenitic phase increased with increase in nitrogen content. But with the incorporation of nitrogen in the austenite lattice, the hardness again increased to as high as 20 GPa. With the further increase in nitrogen content, the hardness of the film decreased to about 13 GPa due to the presence of other nitride phases, not mentioned. This shows the role of phase constitution and the requirement of microstructural modification for optimal mechanical properties. The films showed similar trend of variation of modulus values with respect to the nitrogen content.

ATTENTION: The Singapore Copyright Act applies to the use of this document. Nanyang Technological University Library

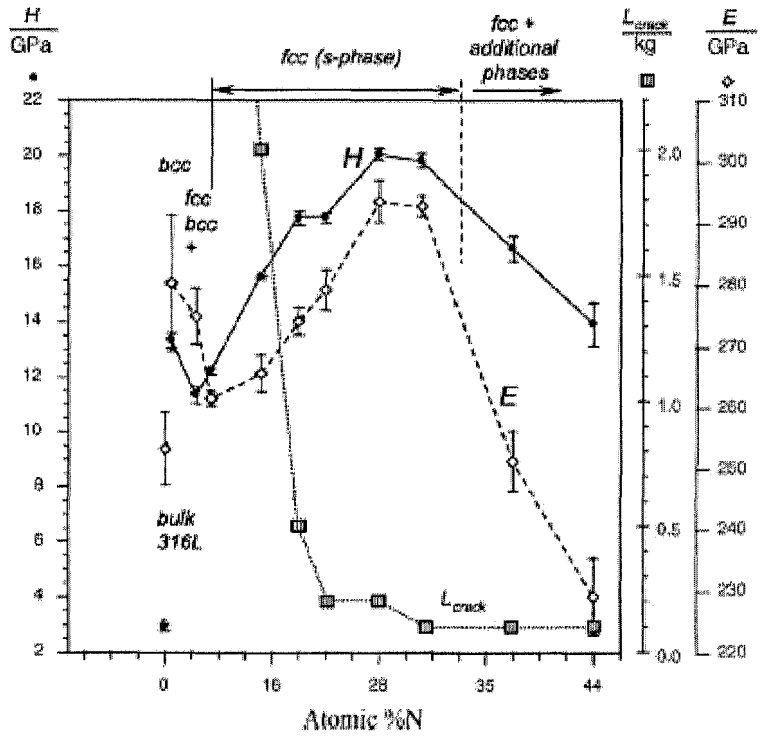


Figure 2.13: Hardness and modulus values, of various SS-N films, plotted against at.% N [55]

From the above, it is clear that the hardness of the films incorporated with nitrogen is much higher than that of pure stainless steel films [49, 52, 53, 56, 57]. The increase in hardness can be either due to the increase in the bond strength or interstitial solid solution strengthening or due to both. But it has also been noticed that the hardness is decreased beyond certain nitrogen content in the film [53, 56]. The reasons behind this are not fully understood.

2.3.3 Corrosion Resistance of SS-N Films

SS-N films deposited by filtered cathodic vacuum arc deposition on low carbon steel also showed improved corrosion resistance [57] tested in 1 N H_2SO_4 solution. Study [58] of the corrosion behaviour of sputter deposited austenitic stainless steel coating showed improvement in corrosion resistance with respect to the bulk stainless steel. Increase in film thickness and nitrogen content lowered the corrosion current density. The improvement in corrosion resistance could be due to the beneficial effect of nitrogen dissolved in the fcc lattice of the phase because studies on nitrogen bearing steel proved that the dissolved nitrogen has a strong repassivation capacity [59].

ATTENTION: The Singapore Copyright Act applies to the use of this document. Nanyang Technological University Library

2.3.4 Magnetic Properties of SS-N Films

It is worth noting that the SS-N films [60] dc-magnetron sputter deposited on low carbon steels showed ferromagnetism when nitrogen gas composition in the sputtering gas mixture was below 25 %. But for higher nitrogen gas composition the nitrogen content in the films achieved was as high as 40 % and the film was paramagnetic. Besides, it is also worth to study the effect of nitrogen on enhancement of the magnetization of the BCC martensite and on the production of ferromagnetic austenite preferentially.

2.4 THE FE-N PHASE DIAGRAM

Iron is known to be one of the strongest, abundantly available engineering materials. The wide application of iron is due to tailorability of its properties during the making or heat treatment. Carbon and nitrogen dissolved in iron are primary elements that impart strength to iron. Furthermore, other properties like corrosion resistance, fatigue, creep, wear-resistance are also influenced by the amount of carbon and nitrogen and the associated heat treatment. Nitrides of iron are known for decades in the context of nitridation of steels. As the formation of each phase imparts different properties, it is necessary to have good knowledge about the Fe-N phase diagram. This also helps in optimizing the properties by careful design and control of the process.

Figure 2.14 shows the Fe-N phase diagram from P. Schaaf [60]. There are salient

ATTENTION: The Singapore Copyright Act applies to the use of this document. Nanyang Technological University Library

that the decreased electronegativity difference between iron and nitrogen atoms in comparison to the iron carbon atoms, increases the directional covalent bond nature in the nitrides [2 and 61].

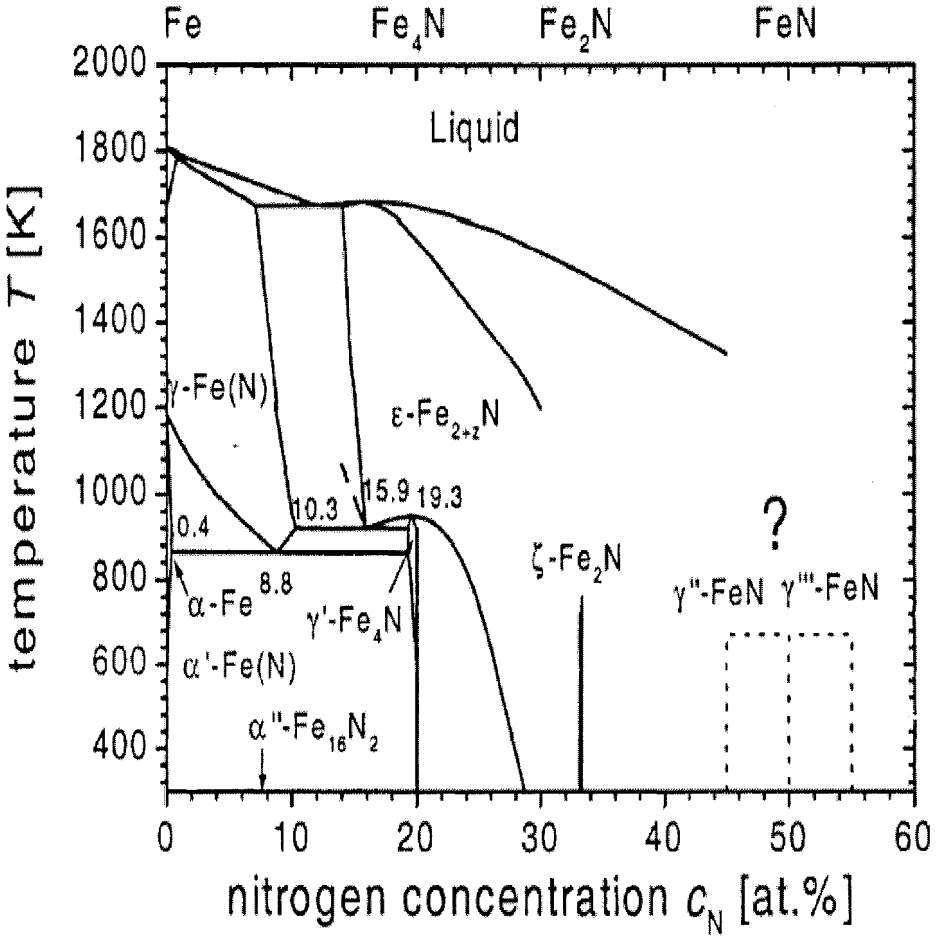


Figure 2.14: Metastable phase diagram of Fe-N system [60]

Solid solution of nitrogen in Fe is stable in equilibrium with nitrogen gas (of 1 bar pressure) at all temperatures above room temperature. γ-Fe_4N and ε-$Fe_{2-3}N$ are metastable with respect to Fe and N_2, whereas nitrogen martensite (α'-$Fe_{16}N_2$); and ordered nitrogen martensite (α''-$Fe_{16}N_2$) are metastable with respect to Fe and Fe_4N [62].

The nitrogen rich phase, ϵ-Fe_2N, has been found to be a transition phase which forms before the more stable phase, γ'-Fe_4N, nucleates [63]. The relative stabilities of the iron nitride phases in bulk form were studied in relation to the action of ammonia and hydrogen [2]. The Fe-N phase diagram was extended because a new FeN phase was discovered in films having approximate stoichiometry and cubic

ATTENTION: The Singapore Copyright Act applies to the use of this document. Nanyang Technological University Library

structure [64, 65]. The dotted lines in the phase diagram represent the uncertainty in the range of nitrogen concentration that restores the NaCl (γ'") or ZnS (γ') structure of the 1: 1 stoichiometric FeN Phase. This is discussed in more detail in section 2.5.

2.5 THE NEW FeN PHASE

The FeN phase was observed first in magnetron sputter deposited FeN films and its formation in the bulk form has not been reported so far. The FeN phase can be present in two different crystalline forms, γ'" (with NaCl structure) and γ' (with ZnS structure), having two different bond natures and valencies as observed with the help of Mossbauer spectroscopy [66]. The FeN phase reported earliest was γ'"-FeN, which has a lattice parameter of 4.52-4.55 Å [67] in contrast to the 4.35 Å [68] of γ'-FeN found later on. There can be deviation of the stoichiometry to either side of the 1:1 stoichiometry of the FeN phase. Nitrogen rich FeN forms the γ'"-FeN [67] while Fe rich phase forms γ'-FeN films [69]. The stoichiometric deviation of the FeN phase is due to the predominant ionic nature of the phase, which allows for ionic vacancies.

Microstructure of the Fe-N films is sensitive to the deposition process parameters as can be understood from the previous section. Difficulty was found in obtaining pure nitrogen rich crystalline FeN phase [70]. Process parameters, both deposition temperature and nitrogen proportion, were proved to play an important role in the microstructure development. The formation of the FeN phase depends on the nitrogen proportion and substrate temperature. It was found that the cubic FeN phase is stable up to 610 K in sputtered Fe-N films. Above 610 K, ϵ-Fe_2N phase starts to form [70]. Nevertheless it has not been studied if the FeN phase forms along with ϵ-Fe_2N or the latter phase forms exclusively for the deposition temperatures above a particular temperature. Furthermore, pure FeN phase in the films could not be achieved completely due to the contamination of the films with C, H and O elements from the chamber walls.

It was found that the ratio of γ'"-FeN to γ'-FeN in the sputter deposited films was non- linear [70] from the correlations with nitrogen/argon flow rate ratio. Even

ATTENTION: The Singapore Copyright Act applies to the use of this document. Nanyang Technological University Library

though pure γ'-FeN has been reported to have formed, the presence of γ'''-FeN in the film cannot be ruled out. The factors favoring one form of FeN phase over the other have not been understood properly even though pure FeN phase with tetragonal structure and lattice parameter (4.28 Å) close to that of γ'-FeN was found to have formed in the plasma-gas-condensed films [71]. It is also worth noting that the phase has been found only in the sputter deposited FeN [70] and plasma-gas condensed [71] films, with average grain size of 5 nm-30 nm, but not in the bulk form.

Table 2.1 furnishes the outcome of various magnetic studies on FeN phase along with the lattice parameters. Results of both, theoretical [72 and 73] and experimental works [74 and 75] showed that γ'''-FeN is ferromagnetic and antiferromagnetic, respectively. While γ'-FeN has been found consistently to be non-magnetic with the help of Mossbauer spectroscopy [74 and 75] and thermomagnetic curves [71].

Table 2.1: Details of FeN phase obtained in the sputter deposited Fe-N films

FeN Phase	Crystal structure type	Lattice parameter (Å)	Magnetic property
γ'''	NaCl	4.52 - 4.55	Ferromagnetic
γ'	ZnS	4.28 - 4.35	Nonmagnetic

ATTENTION: The Singapore Copyright Act applies to the use of this document. Nanyang Technological University Library

Chapter 3

EXPERIMENTAL PROCEDURES

3.1 SUBSTRATE MATERIALS AND PREPARATIONS

The substrate materials used in this work are P-type, boron-doped Si (100) wafer of 4-inch diameter, and amorphous silica glass slides. Table 3.1 lists the specifications of these two materials. The Si (100) wafer, which was mainly used for nitrogen doped stainless steel film deposition, was cut into 2 cm x 2 cm pieces for film deposition, whilst the glass slides were 2.2 cm x 2.2 cm. Before the film depositions, the substrates were cleaned ultrasonically for not less than 20 minutes in an acetone bath, followed by cleaning in ethanol bath and finally subjecting to a jet of pressurized nitrogen gas.

Table 3.1: Specifications of the substrates used for depositions of the Fe-N based films

Substrate	**Si (100)**	**Si (111)**	**Glass**
Specifications	P/Boron, 500-550 micron	P/Boron, 500-550 micron	Deckglaser
Size	1 cm x 1 cm	1 cm x 1 cm	2.2 cm x 2.2 cm

3.2 THE SPUTTERING TARGET MATERIALS

Two types of targets were used to fabricate two different kinds on Fe-N based films, i.e. a pure iron target for Fe-N films and a AISI 316L stainless steel target for stainless steel-nitrogen (SS-N) films. The stainless steel target was machined from a hot-rolled AISI 3126L steel bar into a disc of 76 mm in diameter and 4 mm in thickness. Table 3.2 gives the chemical composition of the stainless steel target. XRD analysis (Figure 3.1) showed that the target had an fcc austenitic structure. The targets were periodically cleaned by manual grinding with P1000 emery paper, followed by ultrasonic cleaning in deionized water and acetone. The pure iron

ATTENTION: The Singapore Copyright Act applies to the use of this document. Nanyang Technological University Library

target was purchased commercially from Pure-Tech Pte Ltd., which has a purity of 99.95% and a dimension of 76 mm in diameter and 6mm in thickness. Figure 3.2 shows the XRD pattern generated from the Fe target. The XRD plot suggests that the target is polycrystalline bcc α-Fe with powder-like orientation of the grains, as the relative intensities of the peaks resemble that of standard powder XRD data.

Table 3.2: Specification of AISI 316L material [76]

Element	Proportion (in Wt. %)
Cr	16-18
Ni	10-14
Mo	2-3
Mn	2
P	0.045
S	0.03
C	0.03
Si	1
Fe	Balance

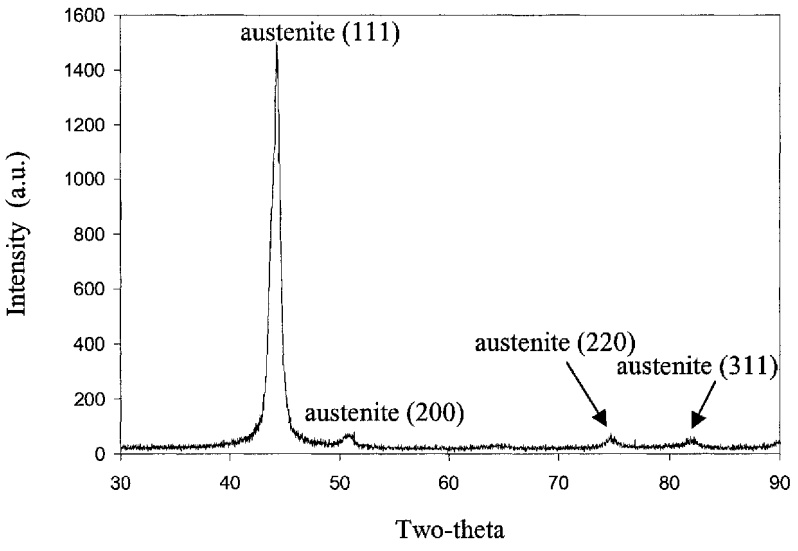


Figure 3.1: XRD plot of the 316L stainless steel target

ATTENTION: The Singapore Copyright Act applies to the use of this document. Nanyang Technological University Library

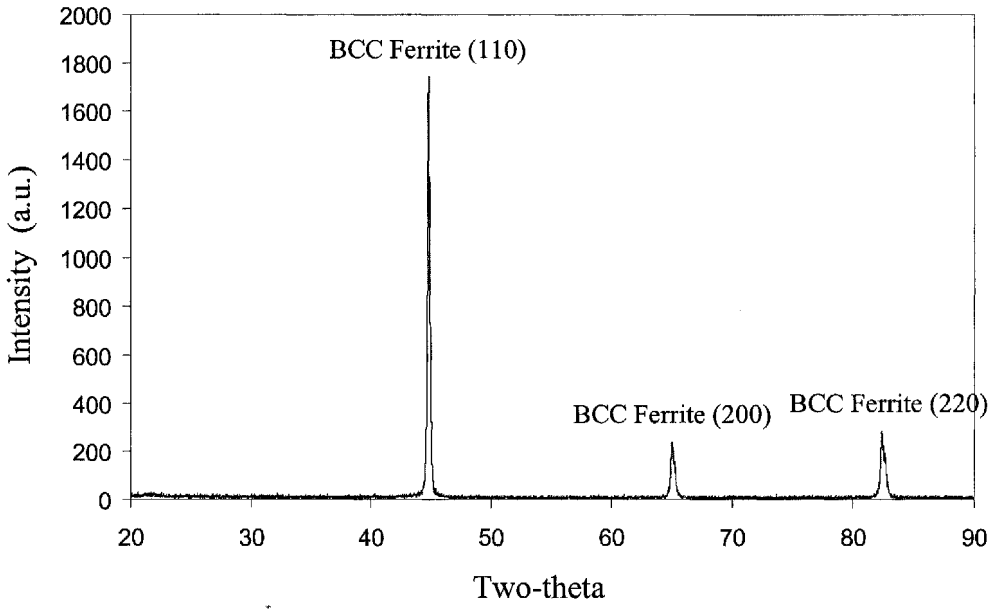


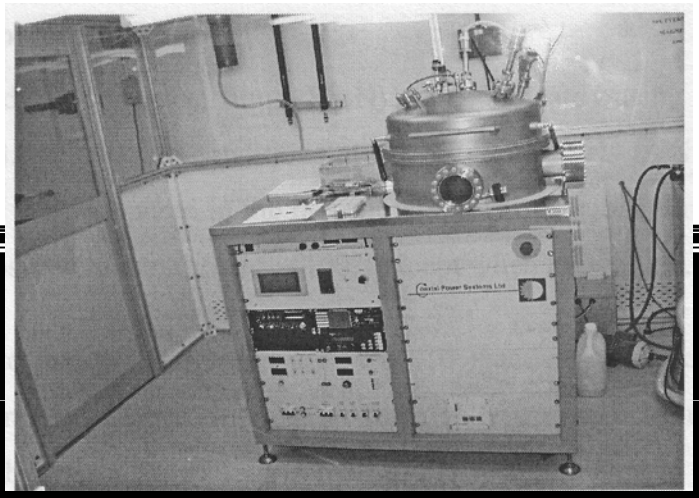
Figure 3.2: XRD plot of Fe target

3.3 FILM FABRICATION

3.3.1 The Sputtering Deposition System

An MSS3 type planar magnetron sputtering system, manufactured by Coaxial Power System Ltd (UK), was used to deposit Fe-N based films in this work. A photograph of the system is shown in Figure 3.3. The system employs a simple chamber with two water-cooled 3 inch planar magnetron target holders. Sputtering can be carried out in both the DC and RF modes. Only RF sputtering was used in this work. The sputtering system has the ability to reach a base pressure of 10^{-5} Pa with the mechanical rotary pump and the turbo molecular pump. The maximum RF power that can be employed is 600 W (13.58 Wcm^{-2}). The system is also equipped with a substrate holder of 170 mm diameter made of molybdenum, which can rotate at 0 to 40 rpm speed. Below the substrate holder is a graphite heating element capable of heating the substrate from 50 to 800 ^{o}C. A thermocouple placed near to the substrate holder without directly contacting the samples, monitors the working temperature. Figure 3.4 shows the schematic of the sputter deposition process inside the chamber.

ATTENTION: The Singapore Copyright Act applies to the use of this document. Nanyang Technological University Library



ATTENTION: The Singapore Copyright Act applies to the use of this document. Nanyang Technological University Library

3.3.2 Deposition of SS-N Films

Nitrogen doped stainless steel films (SS-N) were fabricated using the AISI 316L target. Table 3.3 shows the conditions at which various sets of Stainless steel – Nitrogen films were prepared in the present work. Target-substrate distance was 7 cm and the substrate material was Si (100), except when mentioned.

Total flow rate and working pressure were 10 standard cubic centimeters per minute and 5 mTorr, respectively. SS-N films were prepared by reactive sputter deposition in the present work as per the sample sets tabulated in Table 3.3. The parameters of variation for each set of SS-N films were judiciously prioritized in order based on the cumulative comprehensions made on the influence of the process conditions on the microstructure development. Such an investigation can be subsequently applied qualitatively for the deposition of SS-N films with desired microstructure, disregard of the geometrical design of the reactive sputter deposition chamber.

ATTENTION: The Singapore Copyright Act applies to the use of this document. Nanyang Technological University Library

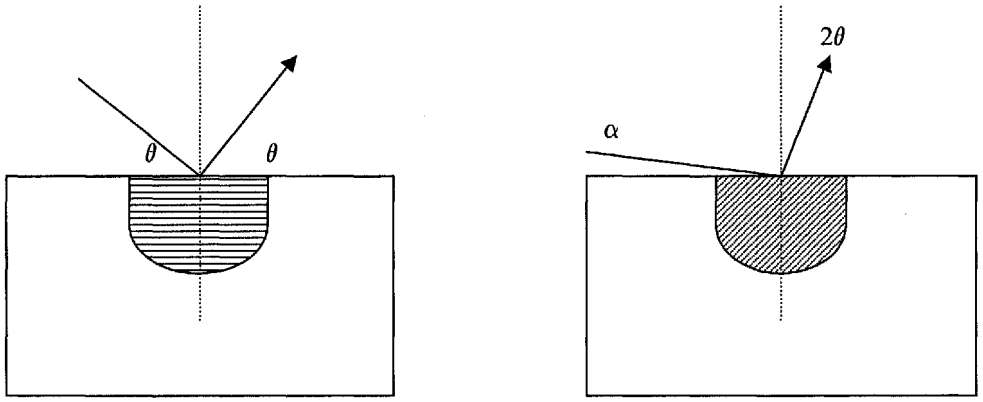
Table 3.3: Conditions of deposition process at which all the sets of SS-N films were prepared

$T_{Substrate}$ (°C)	$\%N_2$	Power Density (Wcm^{-2})	Target-Substrate Distance (cm)	RF substrate Bias (W)
Unheated	0	2.2	7	0
	5			
	10			
	15			
	25			
	40			
	50			
	100			
300	0	2.2	7	0
	5			
	10			
	25			
	30			
	37			
	45			
	50			
	100			
Unheated	25	2.2	7	0
150				
300				
400				
500				
300	50	2.2	7	0
400				
450				
500				
Unheated	25	2.2	7	0
		6.6		
		9.9		
Unheated	100	2.2	7	0
		6.6		
		9.9		
Unheated	25	2.2	4	0
	40			
	50			
	75			
300	50	2.2	7	100
				200
				300

ATTENTION: The Singapore Copyright Act applies to the use of this document. Nanyang Technological University Library

3.4 PHASE IDENTIFICATION AND LATTICE PARAMETER DETERMINATION BY X-RAY DIFFRACTION

Both θ-2 θ mode (Bragg-Brentano) and the grazing angle incidence 2 θ mode (GIXD) X-ray diffraction has been used for phase identification of the resultant thin films. In this section the application of the two methods on thin film is briefly described. Figure 3.5 shows the diffraction geometry of the two methods. Table 3.4 enlists a few of the primary differences between GIXD and Bragg-Brentano modes of XRD analyses.



a) Bragg-Brentano b) GIXD

Figure 3.5: Diffraction geometries of (a) Bragg Brentano and (b) GIXD methods

In the case of conventional θ-2 θ scanning method, the specimen is rotated so that the incident angle of the specimen of the x-ray is θ. The crystal plane that causes diffraction is parallel to the surface of the specimen. Consequently, for a specimen that has a certain lattice plane that is strongly oriented with respect to the surface of the specimen, the peak from the crystal plane is very strong. On the contrary, a very weak peak indicates that the crystal plane is not oriented to the surface of the specimen. Since sputtered films usually have preferred orientation, this method is extremely valuable for studying the film orientation. In the grazing incidence (GIXD) method, the glancing angle, α, is fixed and only the detector scans, hence the crystal plane that satisfies diffraction conditions is inclined at an angle of exactly (θ- α) with respect to the surface of the specimen. Consequently this method is not suitable for studying the crystal planes parallel to the surface.

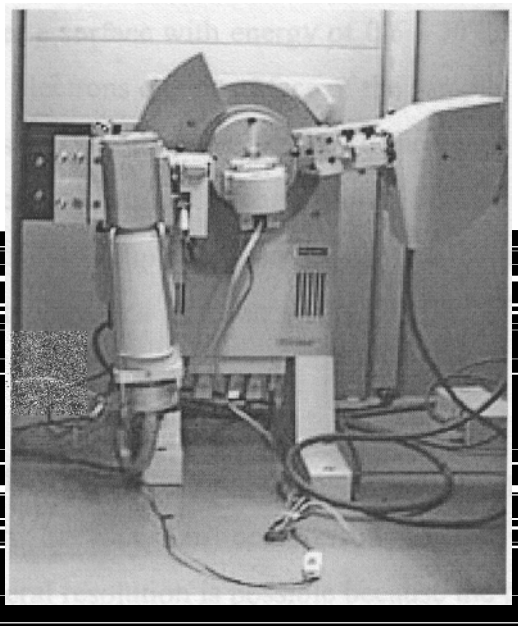
ATTENTION: The Singapore Copyright Act applies to the use of this document. Nanyang Technological University Library

Table 3.4: Salient differences between GIXD and Bragg-Brentano mode of XRD analysis

ϑ (GIXD)	**ϑ-2ϑ (Bragg-Brentano)**
X-rays are incident at constant glancing angle and detector alone moves across the 2ϑ angle.	Source and detector of X-rays make equal angles with the normal to the sample's surface through the rotation of sample holder at the half the speed of that of the detector
Background signal from the substrate is reduced, thereby increasing the sensitivity of phase identification.	Sensitivity is poorer compared to GIXD, as background signal from the substance is not reduced comparatively.
Collimated incident beam and soller-slits are used which do not contribute to the instrumental peak broadening	Incident beam, having finite divergence, is focused on to the substrate because of which instrumental peak broadening is comparatively more.
Grains, corresponding to each of the diffraction peak, are different and are oriented differently with respect to the surface	All the grains corresponding to different diffraction peaks are different and parallel to the surface
Phase profile across the depth is possible to determine, while the relative intensities do not give texture information directly	Texture information can be determined directly while phase profile across the depth can not be derived directly.
Rietveld analysis for structure refinement and quantitative phase analysis is not much established	Rietveld analysis is a common technique for structure refinement and quantitative phase analysis

But there are few advantages of this method in this study: 1) by increasing the incident angle in GIXD method, the X-ray penetration depth can be increased; 2) with a fixed glancing angle, the penetration depth will not change with change in 2 θ. Thus the depth profile of the near surface microstructure can be obtained by this way; 3) the grazing incidence can also increase the volume of material detected by the X-ray penetration depth in the film, which induces higher diffraction intensity. This method is extremely useful in studying multi-layer structures. The samples for the present work were analyzed with the help of Rigaku Dmax 2200 XRD (Figure 3.5) diffractometer in GIXD mode. Copper target with K-alpha radiation of 1.54046 °A wavelength was used.

ATTENTION: The Singapore Copyright Act applies to the use of this document. Nanyang Technological University Library



ATTENTION: The Singapore Copyright Act applies to the use of this document. Nanyang Technological University Library

primary electrons enter a surface with energy of 0.5 - 30 keV, and generate many low energy secondary electrons on the surface of the sample. The intensity of these secondary electrons is largely governed by the surface topography of the sample. They are produced near the surface of the sample, from a small area around the beam tip. An image of the sample surface can thus be constructed by measuring secondary electron intensity as a function of the position of the scanning primary electron beam [78].

The benefits of SEM over conventional optical microscopy include very high resolution and depth of focus in comparison to the conventional optical microscopes. High lateral resolution is possible because the primary electron beam can be focused to a very small spot (< 10 nm). Primary electrons, after impinging on the sample, are scattered with a profile schematically shown in Figure 3.7. From the figure it is clear that the volume of the sample over which secondary electrons are generated is a function of diameter of the incident beam of primary electrons.

Variants of SEM are present depending on the source of primary electrons, thermionic (W, LaB_6) or field emission (sharp tips subjected to electric field). In the case of thermionic sources, in order to narrow the beam size, accelerating voltage of the primary electrons is increased. This increase in primary-electron beam energy causes destruction to the sample as well as increases the surface charging of poorly conducting samples. In the case of field emission SEM, the brightness of the primary electron source is comparatively high, which avoids the necessity of using high accelerating voltages for improved lateral resolution as well as charging of poorly conducting samples. FESEM provides greater spatial resolution in comparison to the thermionic SEM due to the decrease in scattering volume on account of lower demanding accelerating voltages. Also greater depths of field can be achieved with FESEM due to the decrease in numerical aperture of the electron probe. Further, chromatic aberration is minimal in the case of FESEM due to decreased energy spread of the electrons and better quality of the images can be obtained due to increased signal to noise ratio due to increased electron intensity. Figure 3.8 shows the JSM-6340F FESEM used for the present work. The accelerative voltage used for the imaging of the SS-N films is 3 kV.

ATTENTION: The Singapore Copyright Act applies to the use of this document. Nanyang Technological University Library

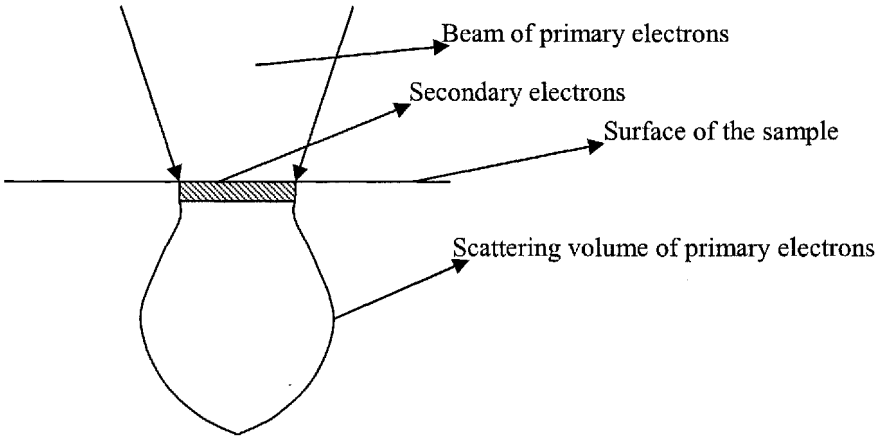
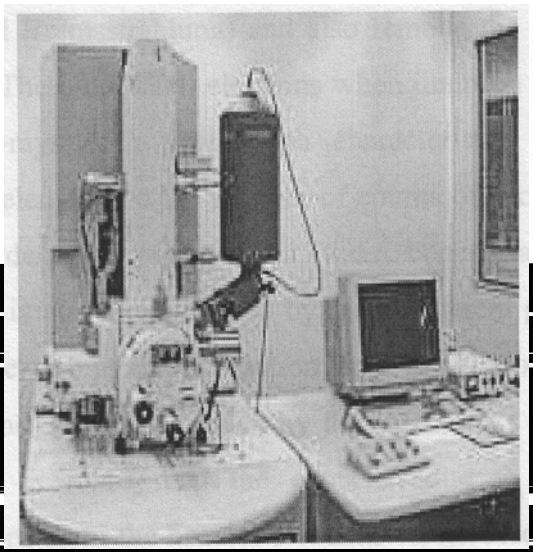


Figure 3.7: Schematic profile of primary electron inside the sample [79]



ATTENTION: The Singapore Copyright Act applies to the use of this document. Nanyang Technological University Library

formula, $\sqrt{s(s-a)(s-b)(s-c)}$, where s = ½(sum of all the edge lengths of each triangle and a, b and c are sides of the triangles). Average grain area for each micrograph was determined by taking into account of fixed number of grains located at random placed. The diameter of an imaginary circle whose area is equal to the average grain area was treated as average grain size.

3.7 ELEMENTAL ANALYSIS BY SPECTROSCOPIC TECHNIQUES

3.7.1 Energy Dispersive X-ray Spectroscopy

Energetic electrons on impinging on the surface of the sample emit continuous radiation (also called Bremsstrahlung) and also remove the electrons in the core shells of the atoms. The outer shell electrons when jump on to the newly vacated inner shell emit x-rays with wavelength characteristic to the element. By determining the wavelength and the number of counts of such X-rays, constituent elements can be identified along with their concentration. However, the quantitative analysis is non-linearly erred by three different phenomena occurring during the electron beam-material interaction, such as (1) atomic weight effect, by virtue of which the net counts/sec given by the low atomic weight elements (for example nitrogen) is more than the expected due to greater amounts of backscattered electrons from the heavier elements which also contribute to the X-ray emission from the lighter elements, (2) absorption effect, by virtue of which characteristic X-rays with different wavelengths do not represent the true relative intensities due to difference in absorption coefficients, and (3) fluorescence effect, where characteristic X-rays from heavier elements can excite the emission of characteristic X-rays from the lighter elements, without the need for electron beam.

Elemental identification and composition were carried out by X-ray spectroscopy facility equipped with the Jeol JSM 6360 scanning electron microscope. Li doped Si solid state detector (Si-Li) separates the characteristic X-rays with different energies and measures the counts per second. Inbuilt standard sample used for calibration of the EDS analysis. With electron beam accelerating voltage of 20 kV, a spot size of 40 nm, and a working distance of 15 mm was maintained through out

ATTENTION: The Singapore Copyright Act applies to the use of this document. Nanyang Technological University Library

the characterization process. Measurements on the samples were done by averaging the values determined at 5 different places on the surface.

3.7.2 X-ray Photoelectron Spectroscopy

The presence of nitrogen was also re-confirmed with the X-ray photoelectron spectroscopy. Film composition was obtained by X-ray photoelectron spectroscopy (XPS) analysis using a Kratos-Axis spectrometer with monochromatic Al Kα (1486.71 eV) X-ray radiation (15 kV and 10 mA) and hemispherical electron energy analyser. The base vacuum of the chamber was 2×10^{-9} Torr. The survey spectra in the range of 0 - 1100 eV were recorded in 1 eV step for each sample, followed by high-resolution spectra over different element peaks in 0.1 eV step, from which the detailed composition was calculated.

3.8 ATOMIC FORCE MICROSCOPIC CHARACTERIZATION

AFM technique is a powerful tool to study the surface topography of materials, and is known for its high spatial and depth resolution. In an AFM instrument, a sharp tip is attached to a flexible cantilever. As the tip is scanned over the surface, the cantilever will deflect up and down across the surface features. By monitoring the cantilever movement, the surface structure is mapped. The deflection of the cantilever can be monitored by optical, interferometry and tunneling method. A dimensional ™ 3100 series scanning probe microscope was employed in this study and operated at tapping mode. The results obtained not only include the topographic images of the surface, but also include the quantitative surface roughness parameter, such as R_a value. In the present studies tapping mode scanning was used where the tip is in the repulsive regime of the tip-sample spacing. The image contrast was obtained by measuring the change in force required to keep the tip at a constant height above the surface, with a feed back loop in order to safeguard the tip from damaging due to the surface roughness.

Mean line: The mean line is commonly used in surface texture measurement and it is based on least square method. It is a line which bisects the profile such that the areas above it and below it and above it are equal and minimum.

ATTENTION: The Singapore Copyright Act applies to the use of this document. Nanyang Technological University Library

Roughness average (R_a): R_a is the arithmetic mean of the departures of the profile from the mean line [80].

3.9 CHARACTERIZATION WITH TRANSMISSION ELECTRON MICROSCOPY

The results obtained for phase identification, by grazing angle incidence X-ray diffraction (GIXD) technique, and for film morphology and structure done by Field Emission Scanning Electron Microscope (FESEM), for the iron-nitrogen based films were further confirmed with the help of transmission electron microscope. Electron beam accelerated by voltages of 200 kV were made to pass through samples thinned down to less than 100 nm and the transmitted electrons were analyzed in order to study the diffraction characteristics and morphology of various samples. Diffraction patterns were obtained with camera length of 30 cm by focusing the image on the backfocal plane (Figure 3.9(a)) of the objective lens on to the image plane of the intermediate lens and is further magnified and projected on to a screen by projector lens. Defocused beam of coherent electrons was diffracted by the periodically arranged atoms in crystallites of various phases. These diffraction patterns were then indexed based on the knowledge on d-spacings of each of the identified phases. On the other hand, bright field images were obtained by focusing the image on the image plane (Figure 3.9(b)) of the objective lens on to the image plane of the intermediate lens and further magnified by projector lens. Image carries the net contrast in the intensity caused in the transmitted electron beam. The intensity-contrast is due to the variation in spatial distribution of scattered electrons. The differences in distribution of scattered electrons are due to the change in lattice spacing with the phase or defects in the crystalline atomic arrangement.

ATTENTION: The Singapore Copyright Act applies to the use of this document. Nanyang Technological University Library

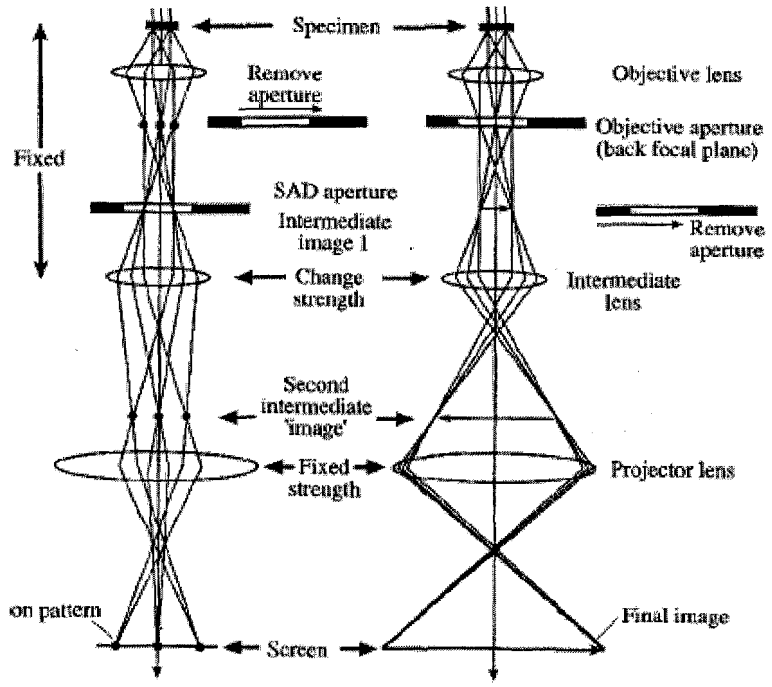


Figure 3.9: Electron ray diagram showing the focusing of (a) diffraction pattern in

ATTENTION: The Singapore Copyright Act applies to the use of this document. Nanyang Technological University Library

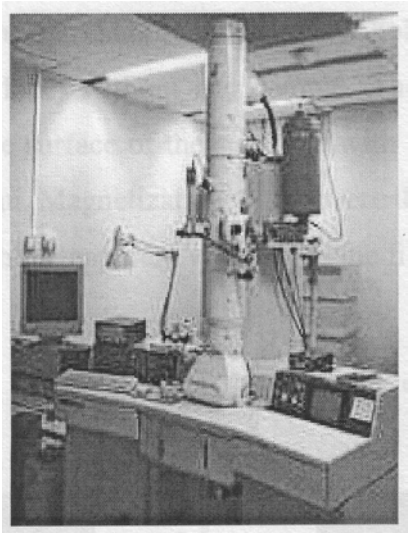


Figure 3.10: Transmission Electron Microscope (Jeol JEM 2010) used for characterization of stainless steel-nitrogen films

3.10 DETERMINATION OF MAGNETIZATION BY VIBRATING SAMPLE MAGNETOMETER

Magnetization values at room temperature for the stainless steel – nitrogen films with varying amounts of nitrogen content and with different phases were determined with the help of vibrating sample magnetometer (VSM). In the following paragraph details [82] of working of VSM are explained. Measurements were done by placing the same number of samples, with similar size and shape (4mm x 5 mm), and at the same place of the sample holder.

If a material is placed within a uniform magnetic field H, a magnetic moment is induced in the sample. In a VSM, a sample is placed within suitably placed sensing coils, and is made to undergo sinusoidal motion, i.e., mechanically vibrated (82 Hz). The resulting magnetic flux changes induce a voltage in the sensing coils that is proportional to the magnetic moment of the sample. The magnetic field may be generated by an electromagnet, or a superconducting magnet. Figure 3.11 shows the schematic of determination of magnetic moment by VSM. Figure 3.12 shows the vibrating sample magnetometer (VSM-Lakeshore 736) used for the determination of magnetization values of various SS-N films at room temperature. The field was ramped between -2000 to +2000 G with ramp rate of 13.6 G/sec and with step of 135 G while the time constant chosen was 0.1 second. All the experiments were carried out after sufficient time for warming up and magnetic

ATTENTION: The Singapore Copyright Act applies to the use of this document. Nanyang Technological University Library

moment gain calibration by using the substrate holder (of material Kel-F, PolyChloroTriFluoroEthylene) without any sample. The external magnetic field was applied parallel to the surface of the substrate with a minimum detection coil sensitivity of 50 x 10^{-3} emu. Magnetization values were then calculated by dividing the magnetic moment with the apparent volumes of the films.

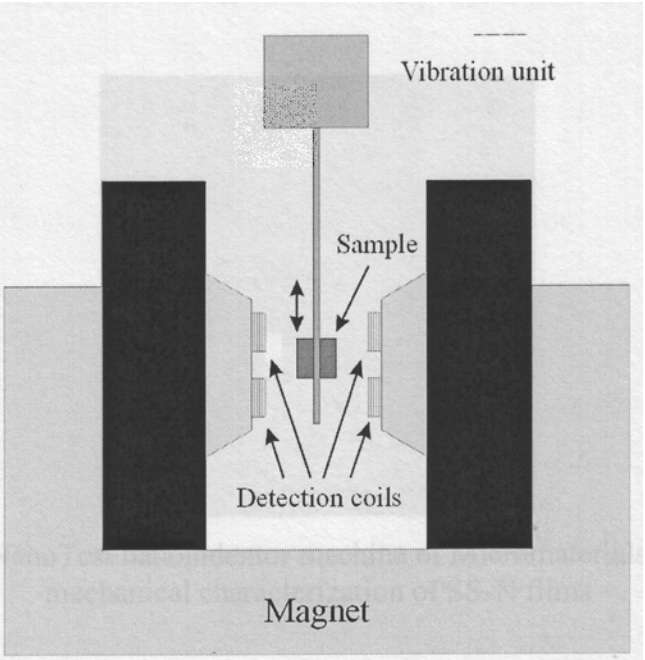


Figure 3.11: Schematic diagram of the VSM [83]

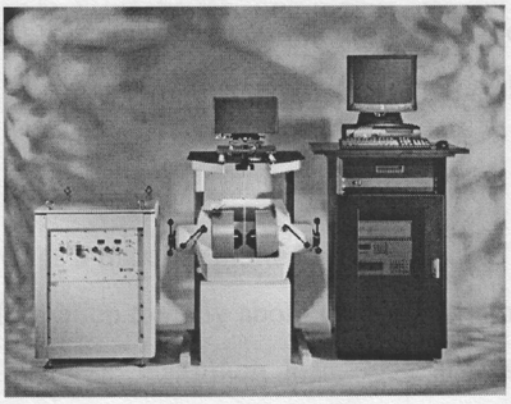


Figure 3.12: Vibrating sample magnetometer (Lakeshore 736) used for determining the room temperature magnetization values of various SS-N films

ATTENTION: The Singapore Copyright Act applies to the use of this document. Nanyang Technological University Library

3.11 MECHANICAL PROPERTY CHARACTERIZATION

3.11.1 Nanoindentation

Figure 3.13 shows the NonoTest nanoindentor of Micromaterials Ltd, UK. Table 3.6 shows the details of the Nanoindentation experiments carried out with the NanoTest.

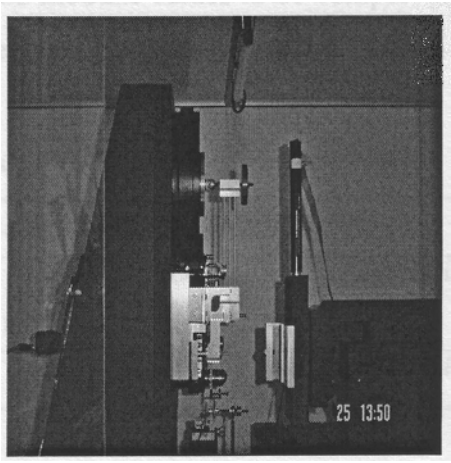


Figure 3.13: NanoTest nanoindentor machine of Micromaterials Ltd used for

ATTENTION: The Singapore Copyright Act applies to the use of this document. Nanyang Technological University Library

contact area as a function of depth of penetration. It can also be obtained empirically by extrapolating the initial portion of the unloading curve to zero-load and using the extrapolated depth with the indenter shape function [87].

Table 3.5 shows the details of experiments carried out with a Berkovich (square based pyramidal diamond with depth to area ratio same as Vicker's) indentor. In order for the hardness and modulii values to be comparable with each other, depth of penetration was chosen to be around one tenth of the film with lowest thickness.

Table 3.5: Details of indentation experiments carried out with NanoTest

Nanoindentation test				
No. of indentations	Depth of penetration	Loading rate	Unloading rate	Indenter
5	50 nm	0.5 mN/s	0.5 mN/s	Berkovich

3.11.2 Microscratch

Scratch test on the sample induces controlled stress and strain to the surface coating via a diamond stylus from which the mechanical response can be measured by simultaneously recording friction transients, acoustic emissions and changes in surface morphology. In the microscratch test, the normal load, tangential load, scratch length, and acoustic emission are monitored simultaneously during an entire scratch process for the purposes of measuring the critical load and studying

ATTENTION: The Singapore Copyright Act applies to the use of this document. Nanyang Technological University Library

Chapter 4

RESULTS

In this chapter, experimental results on nitrogen doped stainless steel (SS-N) films are presented in terms of nitrogen chemical composition, phase evolution, microstructure, morphology and properties. Interpretation and discussion of the results are present in the next chapter. Unless otherwise specified, the films discussed were produced without substrate biasing at a power density of 2.2 Wcm^{-2} and a constant target-to-substrate distance of 7 cm.

4.1 NITROGEN CHEMICAL COMPOSITION

Efforts of this work were primarily focused on studying the process of sputter deposition in nitrogen reactive environment for obtaining expanded austenite with optimal nitrogen content. The degree of nitrogen incorporation can depend on various process parameters like proportion of nitrogen gas in the sputtering gas

ATTENTION: The Singapore Copyright Act applies to the use of this document. Nanyang Technological University Library

Table 4.1: Elemental composition of pure stainless steel film

Element	At.%
Fe	66
Cr	18
Ni	12
Mo	1.5
Mn	2

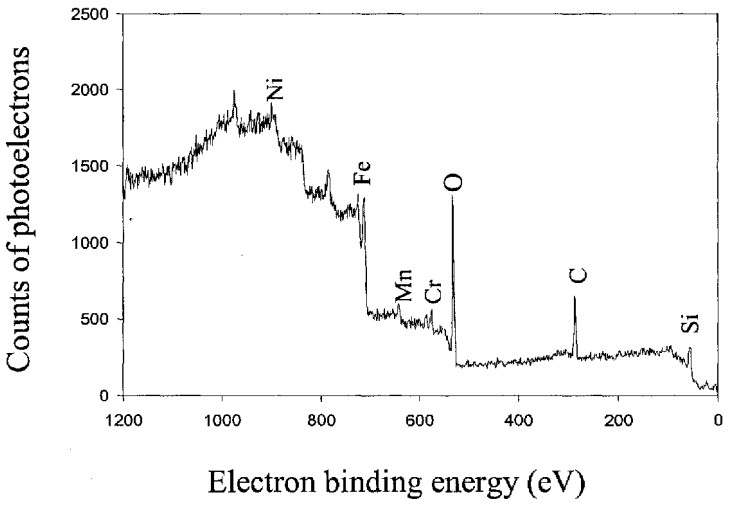


Figure 4.1: XPS detailed spectrum of the SS-N film deposited at 300 °C with 0% N_2 and 2.2Wcm^{-2}, and 7 cm target-substrate distance

Sputtering in Ar + N_2 gas mixtures resulted in the incorporation of nitrogen in the stainless steel films. Figure 4.2 shows the measured nitrogen concentration in the film as a function of nitrogen gas composition in the gas mixture. It can be seen that the relationship between at.% N in the film and nitrogen gas composition in the sputtering atmosphere can be divided into three regions. In region I, between 0 and 7% N_2 in the atmosphere, nitrogen atoms could not be incorporated in the film, below the limits detected by EDS. In region II, between 10% and 40% N_2 in the atmosphere, the at.% N in the film increases continually with the increase in nitrogen gas composition. In region III with the nitrogen gas composition above 40% N_2, the at.% N in film remains nearly constant at a value about 50 at.%.

ATTENTION: The Singapore Copyright Act applies to the use of this document. Nanyang Technological University Library

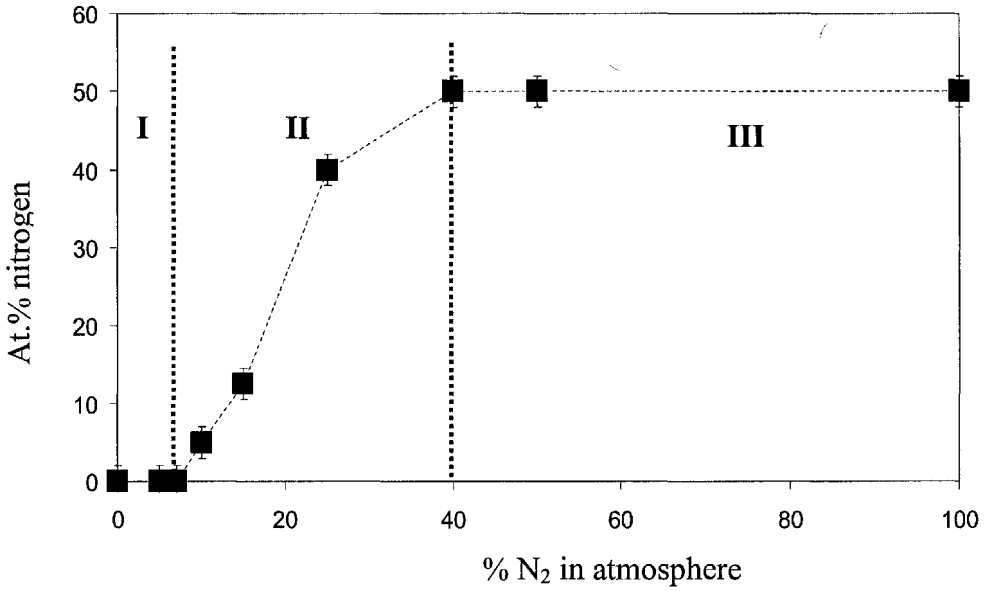


Figure 4.2: Nitrogen content in the SS-N films, deposited with various nitrogen gas compositions on unheated substrates with 2.2Wcm^{-2} and 7 cm target-substrate distance, as determined by EDS. Scatter bar represents the scatter in the values taken over 5 different points

4.1.2 Nitrogen Incorporation In SS Films Deposited at 300 °C

Figure 4.3 shows the nitrogen concentration in the films deposited on Si at elevated temperature of 300 °C as a function of nitrogen gas composition in the sputtering atmosphere. The curve shown in Figure 4.3 for films deposited at 300 °C is similar to that shown in Figure 4.2 for films deposited on unheated substrates, and can also be divided into 3 regions. It can be seen that the nitrogen concentration in the film is negligible when the % N_2 in the atmosphere is less than 5%. This corresponds to region I, where a ferrite phase film is formed, as discussed in detail later. The nitrogen concentration in the film then increases with increase in % N_2 in the atmosphere in region II, until reaching about 45 at.% N in the film, then becomes saturated at 50 at.% N with further increase in % N_2 in the atmosphere to 50%, 75% and 100%.

ATTENTION: The Singapore Copyright Act applies to the use of this document. Nanyang Technological University Library

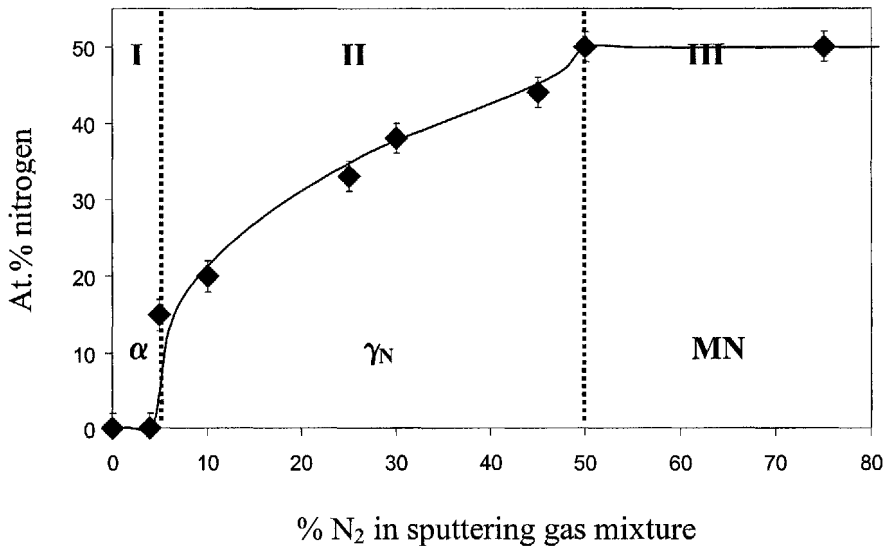


Figure 4.3: Nitrogen concentration in SS-N films, deposited at 300 °C, 2.2Wcm^{-2}, and 7 cm target-substrate distance as a function of nitrogen gas composition in the sputtering gas mixture, determined by EDS

4.1.3 Effect of Deposition Power Density On Nitrogen Incorporation

The variation of nitrogen content in films with varying sputtering power density was studied by deposition on unheated substrates with two constant nitrogen gas

ATTENTION: The Singapore Copyright Act applies to the use of this document. Nanyang Technological University Library

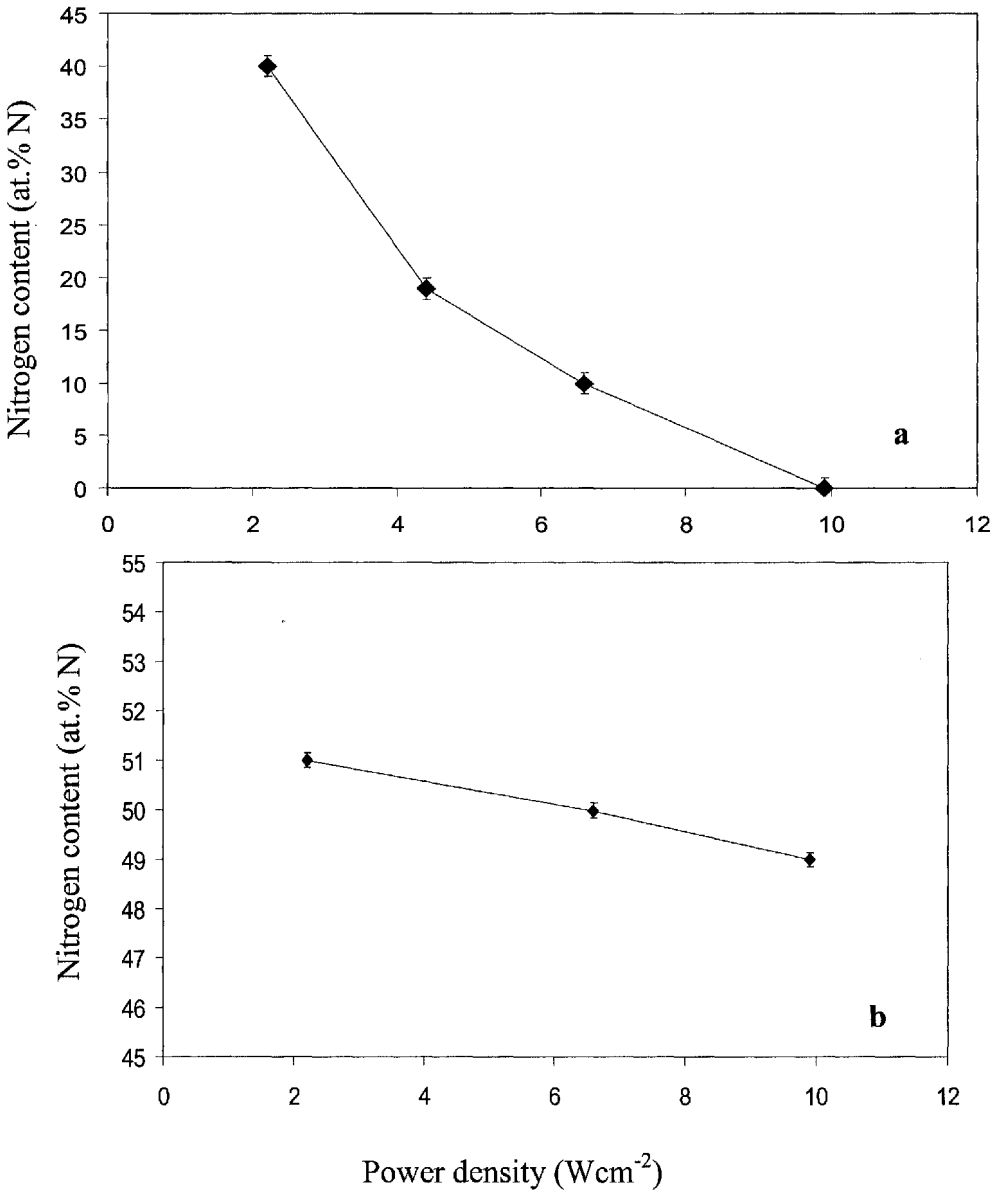


Figure 4.4: Nitrogen content versus power density versus power density, of SS-N films deposited on unheated substrates with 2.2Wcm^{-2} and 7 cm target-substrate distance and (a) 25% N_2 and (b) 100% N_2

4.1.4 Effect of Deposition Temperature On Nitrogen Incorporation

The effect of deposition temperature on nitrogen content in the films was further studied (Figure 4.5) by varying the substrate temperature from unheated to 500 °C. In the films deposited with 25% N_2, the nitrogen content decreased gradually with increasing temperature from about 40 at.% at 150 °C to 29 at.% at 500 °C. However, in the films deposited with 50% N_2, the nitrogen content is almost constant at 50 at.% for temperature upto 300 °C, above which significant decrease in nitrogen content with further increasing temperature was observed. As discussed

ATTENTION: The Singapore Copyright Act applies to the use of this document. Nanyang Technological University Library

later, such variation in nitrogen content and the difference observed for these two sets of films are associated with the nature of the predominant phase and phase decomposition in the films.

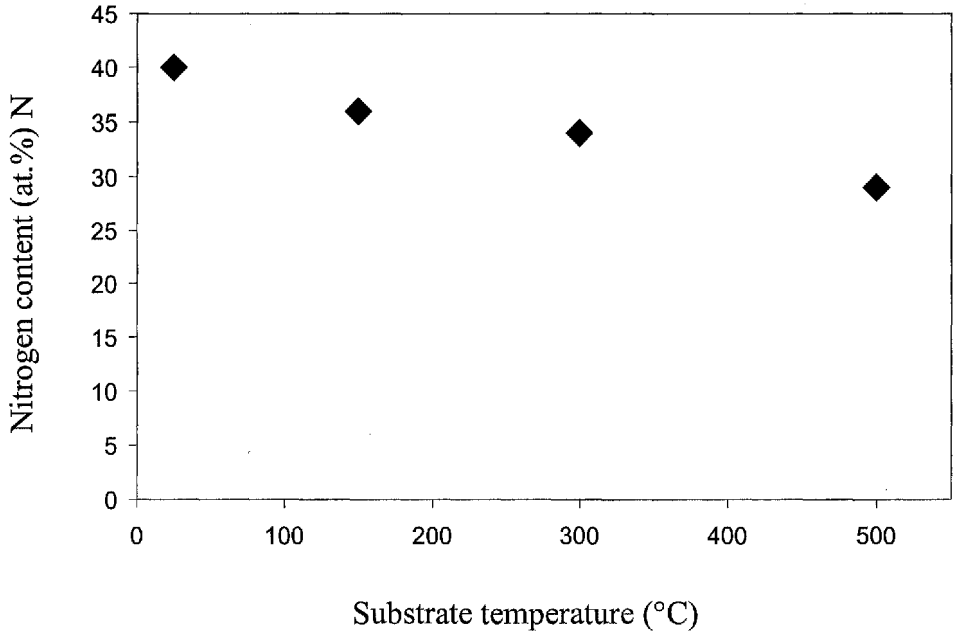


Figure 4.5: Nitrogen contents and lattice parameters plotted for various substrate temperatures of the films deposited with 25% N_2

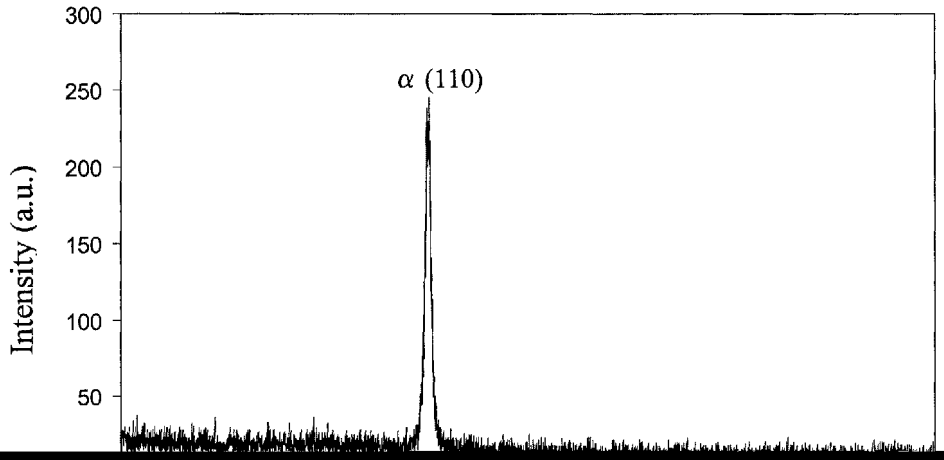
4.2 PHASE EVOLUTION IN SS-N FILMS INVESTIGATED BY DIFFRACTION TECHNIQUES

Glancing angle X-ray diffraction (GIXD) was mainly used to study the evolution of phase in the resultant SS-N films. Selected samples were also studied by TEM and electron diffraction. This section describes the observed variation of phase evolution with various deposition parameters.

4.2.1 SS-N Films On Unheated Substrates

Figure 4.6 shows the GIXD pattern of the film deposited with 0% N_2 on unheated substrate in the sputtering gas mixture. The film gave only a diffracting peak corresponding to (110) plane of BCC ferritic stainless steel. Such single peak pattern of the film is characteristic of well-defined texture in the film. The only one peak, obtained in the GIXD within the Bragg angle range, predicates the absence of random orientation of grains.

ATTENTION: The Singapore Copyright Act applies to the use of this document. Nanyang Technological University Library



ATTENTION: The Singapore Copyright Act applies to the use of this document. Nanyang Technological University Library

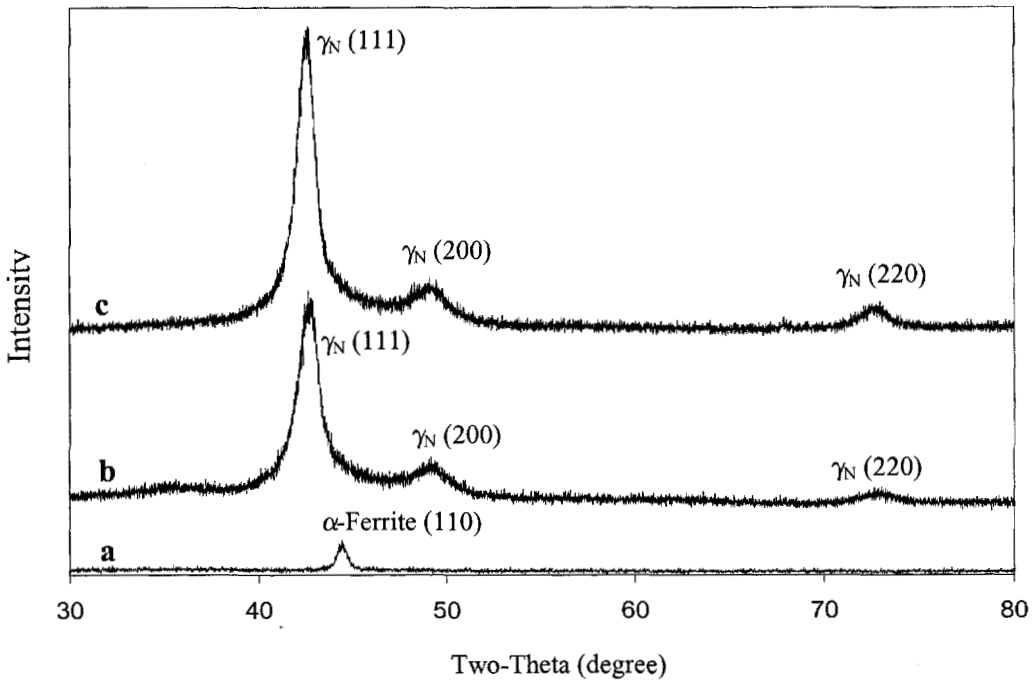


Figure 4.7: GIXD patterns of SS-N films deposited on unheated substrate with (a) 5%, (b) 10%, and (c) 15% N_2 in the gas mixture, 2.2Wcm^{-2} and target-substrate distance of 7 cm

A similar GIXD pattern was obtained for the SS-N film deposited with 15% N_2 in the atmosphere (Figure 4.7(c)). This film also contains the same expanded austenite, γ_N phase, with increased lattice parameter and nanocrystalline structure as evident by the broad diffraction peaks.

Nanocrystallite size of the expanded austenite phase (γ_N) is asserted by the peak broadening, which is typical of crystallite sizes less than 100 °A [89], especially for the employed high resolution GIXD instrumentation and the scanning step (0.008°). Thus, the broader diffracting peaks from the 10% and the 15% films suggest nanocrystalline nature of the film with considerable grain boundary volume. Drastic change in phase evolution was noticed in the film deposited with 25% N_2 on the unheated substrate. A very prominent amorphous hump can be seen from the GIXD pattern as shown in Figure 4.8. Besides the amorphous phase, two

ATTENTION: The Singapore Copyright Act applies to the use of this document. Nanyang Technological University Library

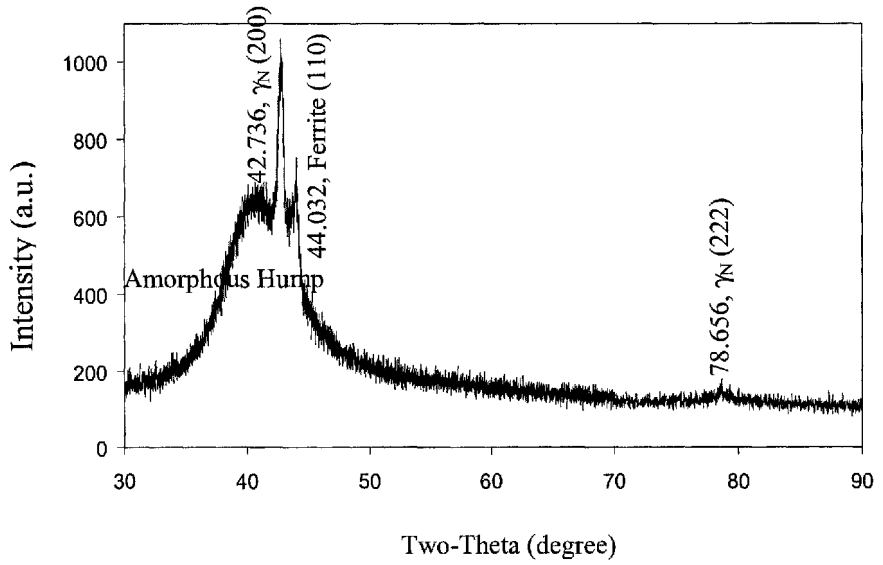


Figure 4.8: GIXD pattern of SS-N film deposited on unheated substrate with 25% N_2, 2.2Wcm^{-2} and 7 cm target-substrate distance

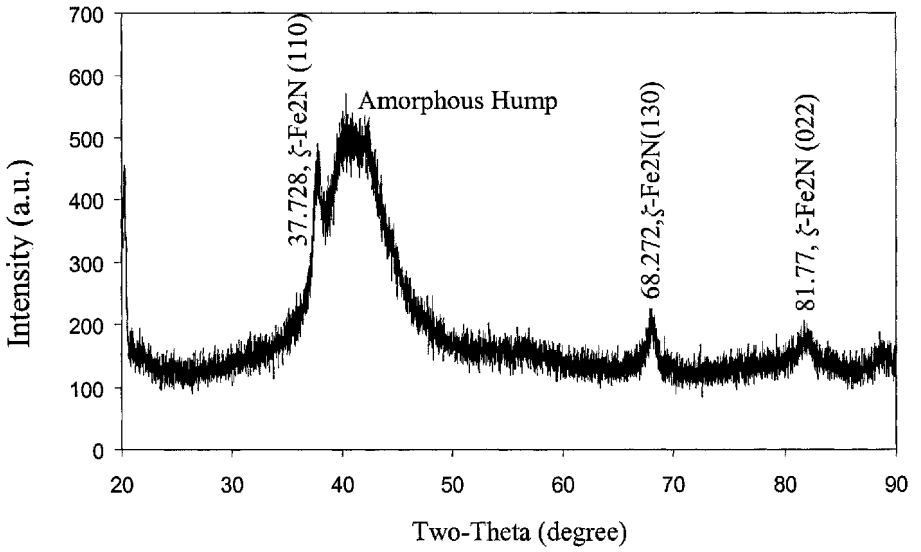


Figure 4.9: GIXD pattern of SS-N film deposited on unheated substrate with 30% N_2, 2.2Wcm^{-2} and 7 cm target-substrate distance

Further, with the increase in the nitrogen gas composition to 40% in the atmosphere, the film became more crystalline-like with diffraction peaks higher than the amorphous hump (Figure 4.10). Formation of crystalline ζ-Fe_2N phase is also evident for the case of 40% N_2. Apart from this, another crystalline phase with characteristic FCC diffraction peaks of γ_N can be found in the film.

ATTENTION: The Singapore Copyright Act applies to the use of this document. Nanyang Technological University Library

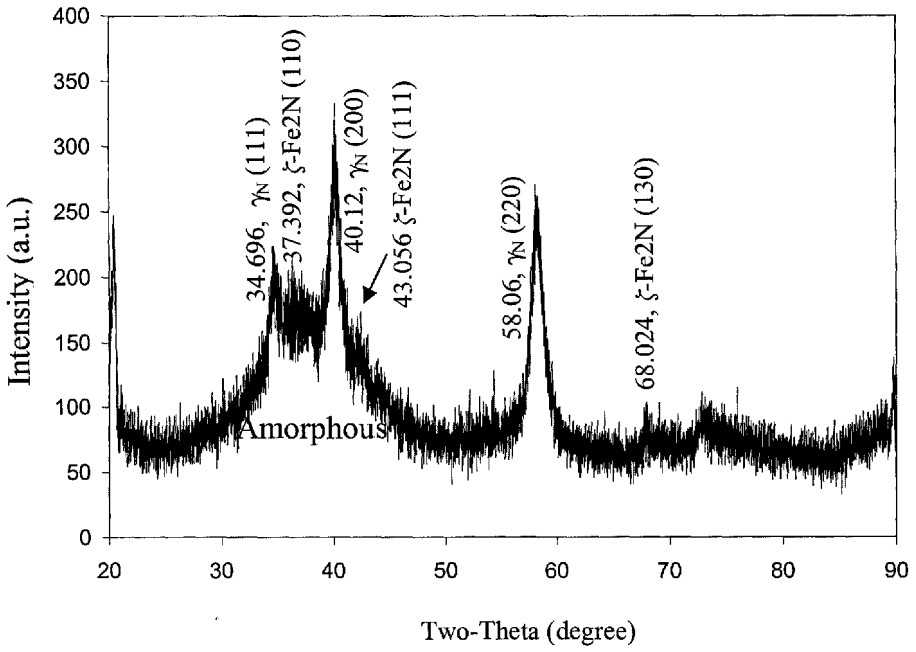


Figure 4.10: GIXD pattern of SS-N film deposited on unheated substrate with 40% N_2 2.2Wcm^{-2} and 7 cm target-substrate distance

Further increasing the nitrogen gas composition to 50% N_2, the resultant film formed is completely crystalline with mainly the single phase of γ_N with a lattice parameter of 4.32 Å (Figure 4.11).

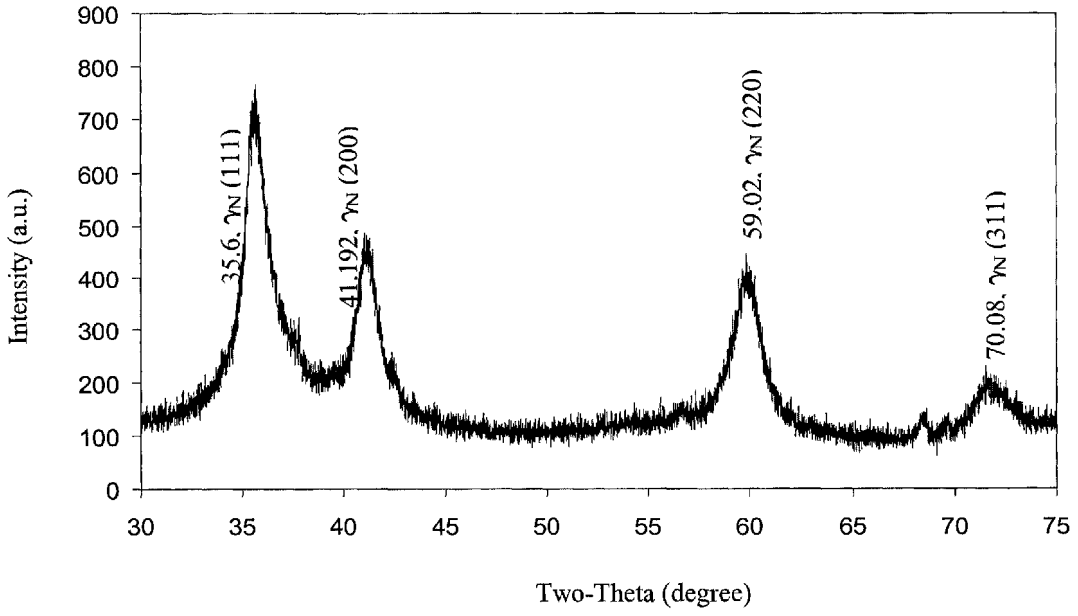


Figure 4.11: GIXD pattern of SS-N film deposited on unheated substrate with 50% N_2 2.2Wcm^{-2} and 7 cm target-substrate distance

ATTENTION: The Singapore Copyright Act applies to the use of this document. Nanyang Technological University Library

The nitrogen concentration in the film is about 50 at.% (Figure 4.2), indicating that the γ_N phase indeed has equiatomic composition. The broadness of the peaks suggests that the γ_N phase in the film is nanocrystalline and highly strained microscopically.

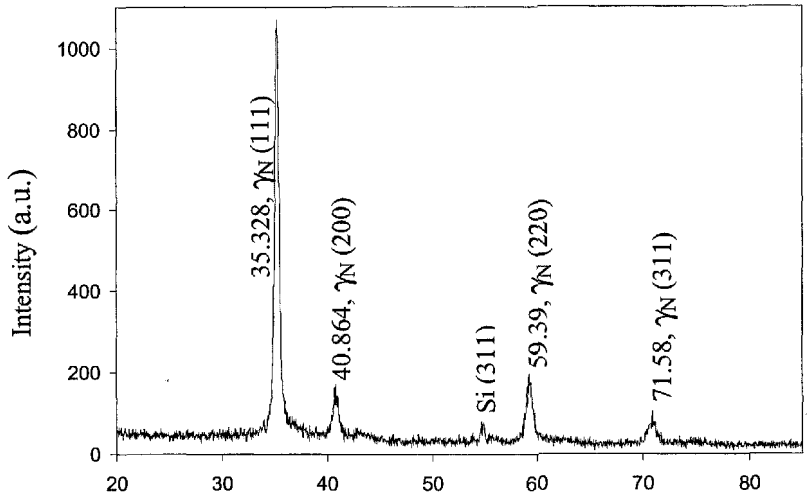


Figure 4.12: GIXD pattern of SS-N film deposited on unheated substrate with 100% N_2 2.2Wcm^{-2} and 7 cm target-substrate distance

In summary, four types of films were produced on the unheated substrates. These include: (1) α-ferrite films formed with N_2 below 10%;

(2) expanded austenite, γ_N, films formed with % N_2 between 10% and 20%,

(3) amorphous + crystalline phases formed with % N_2 between 25% and 40%, and

(4) Again single γ_N phase films formed with N_2 above 40%.

4.2.2 SS-N Films Deposited on Substrates Heated to 300 °C

Ferrite films with BCC structure formed when pure Argon gas was introduced into the sputtering chamber. Figure 4.13(a) shows the GIXD pattern of the pure stainless steel film deposited at 300 °C with pure Ar sputtering. The electron diffraction pattern (shown in Figure 4.14b), obtained from transmission electron microscope (TEM), constitutes polycrystalline rings due to the grain-orientation distribution across the whole range of angles with respect to the electron beam. Even with the introduction of 4% nitrogen gas into the chamber, the phase constitution of the film did not change as can be seen from Figure 4.13(b). However, the relative peak intensity corresponding to the (211) plane decreased suggesting reduction in the degree of texture.

ATTENTION: The Singapore Copyright Act applies to the use of this document. Nanyang Technological University Library

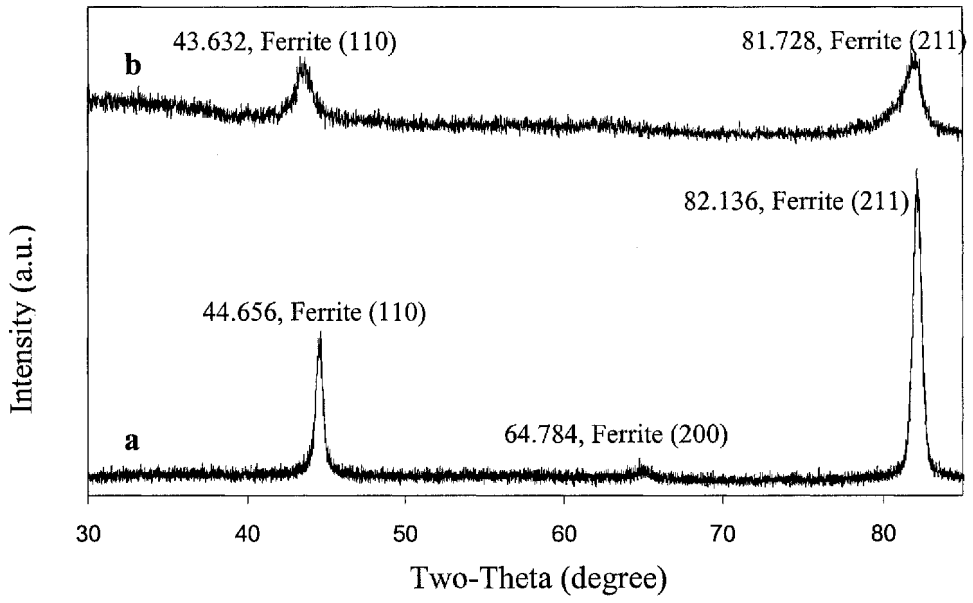


Figure 4.13: GIXD pattern with 2° glancing angle of incidence obtained for stainless steel films deposited with (a) 0% and (b) 4% N_2 at 300 °C with 2.2Wcm^{-2} and 7 cm target-substrate distance

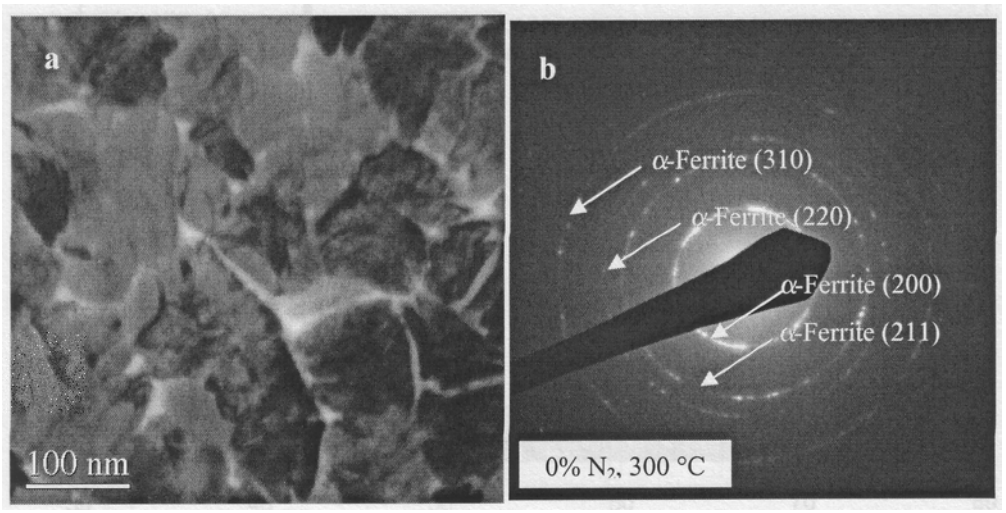


Figure 4.14: (a) Plan view bright field image and (b) Electron Diffraction Pattern of the SS film deposited at 300 °C with 0% N_2, 2.2Wcm^{-2} and 7 cm target-substrate distance

This corresponds to region I in Figure 4.3, where no nitrogen incorporation in the film was detected. However, it is interesting to note the sudden change in the as-deposited phase from ferrite to austenite when % N_2 in the atmosphere was increased to 10% N_2 (Figure 4.15). The GIXD pattern shown in Figure 4.15 suggests polycrystalline austenitic phase whose lattice parameter (3.66 Å) is about 2% larger than that of the bulk austenite phase (3.59 Å). Similar sudden change in

ATTENTION: The Singapore Copyright Act applies to the use of this document. Nanyang Technological University Library

phase formation was also observed in the films deposited on unheated substrate, as described in section 4.2.1. The lattice expansion in the austenite phase again can be attributed to the dissolution of nitrogen, as measured by EDS (Figure 4.3).

Although only a single γ_N phase was detected by XRD in the films, deposited with such low nitrogen gas compositions (10%), traces of BCC ferrite phase were also found by electron diffraction. This indicates that the γ_N films formed with relatively low % N_2 (less than 10%) contain a small amount of BCC ferrite phase. Figure 4.16 (a) and (b), showing the plan view bright field image and electron diffraction pattern of the film deposited with 10% N_2, confirming the identified phases and the polycrystalline structure.

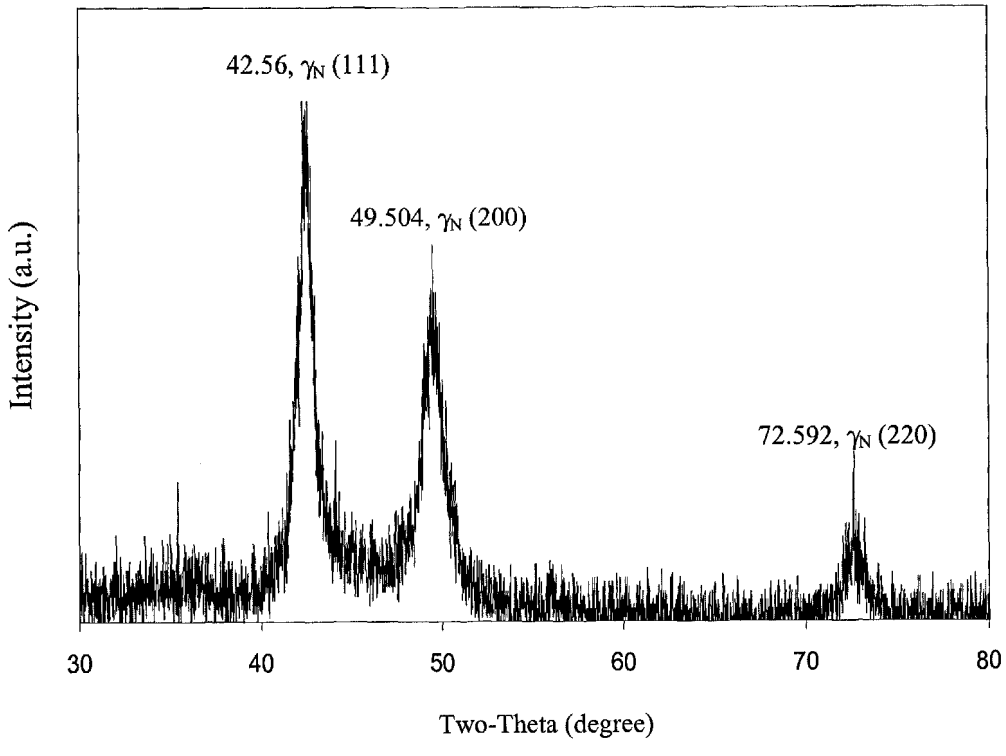


Figure 4.15: GIXD pattern of SS-N film deposited at 300 °C, 2.2Wcm^{-2}, 7 cm target-substrate distance and with 10% N_2

ATTENTION: The Singapore Copyright Act applies to the use of this document. Nanyang Technological University Library

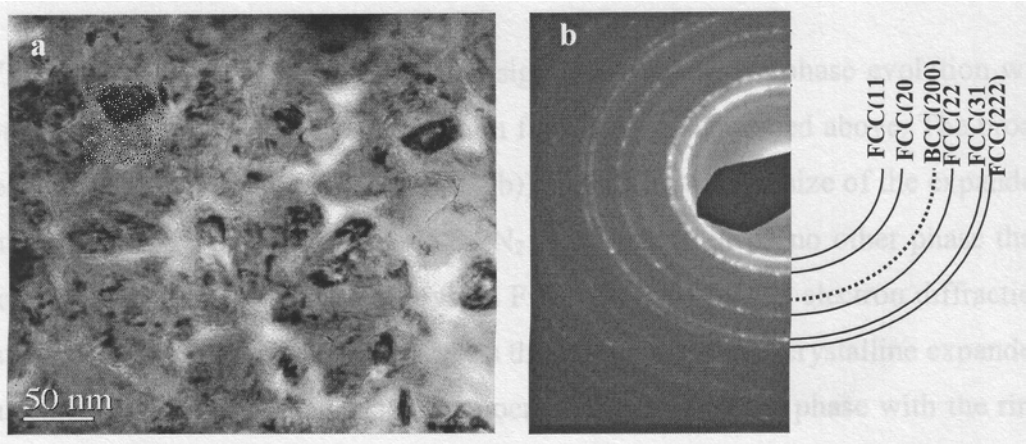


Figure 4.16: TEM bright field image (a) and SAD pattern (b) from the γ_N film produced with 10%N_2 in the gas mixture at 300 °C, 2.2 Wcm^{-2} and 7 cm target-substrate distance

When the nitrogen gas composition was increased to 25%, 30%, 37%, single polycrystalline expanded austenite (γ_N) phase formed in the SS-N films, in accordance with the increased nitrogen concentration in the film and increased lattice parameter (Figure 4.17 a, b & c). For the SS-N films deposited with high %N_2, the lattice parameter found for the γ_N phase is about 4.02 Å, corresponding to about 40 at.% N incorporated in the film deposited with 37% N_2. This maximum lattice parameter value is in agreement with γ_N films produced by sputtering by other investigators [50, 52 and 90] and is larger than that found in low temperature

ATTENTION: The Singapore Copyright Act applies to the use of this document. Nanyang Technological University Library

With the increase in % N_2 to 30%, no significant change in phase evolution was found, except for the observed change in film texture mentioned above. The broad peaks in the GIXD pattern (Figure 4.17(b)) suggest fine grain size of the expanded austenite phase. Further increase in % N_2 to 37 also showed no other phase than expanded austenite, as can be seen from Figure 4.17(c). While electron diffraction pattern shown in Figure 4.19(b) supports the formation of polycrystalline expanded austenite, Figure 4.19(c) shows the nanocrystallite size of the phase with the ring pattern obtained even with the nano electron beam. The nanobeam electron diffraction analysis proved to be more sensitive than GIXD because MN phase, which is identified by XRD only in the film deposited with next higher %N_2, could also be detected by the former.

ATTENTION: The Singapore Copyright Act applies to the use of this document. Nanyang Technological University Library

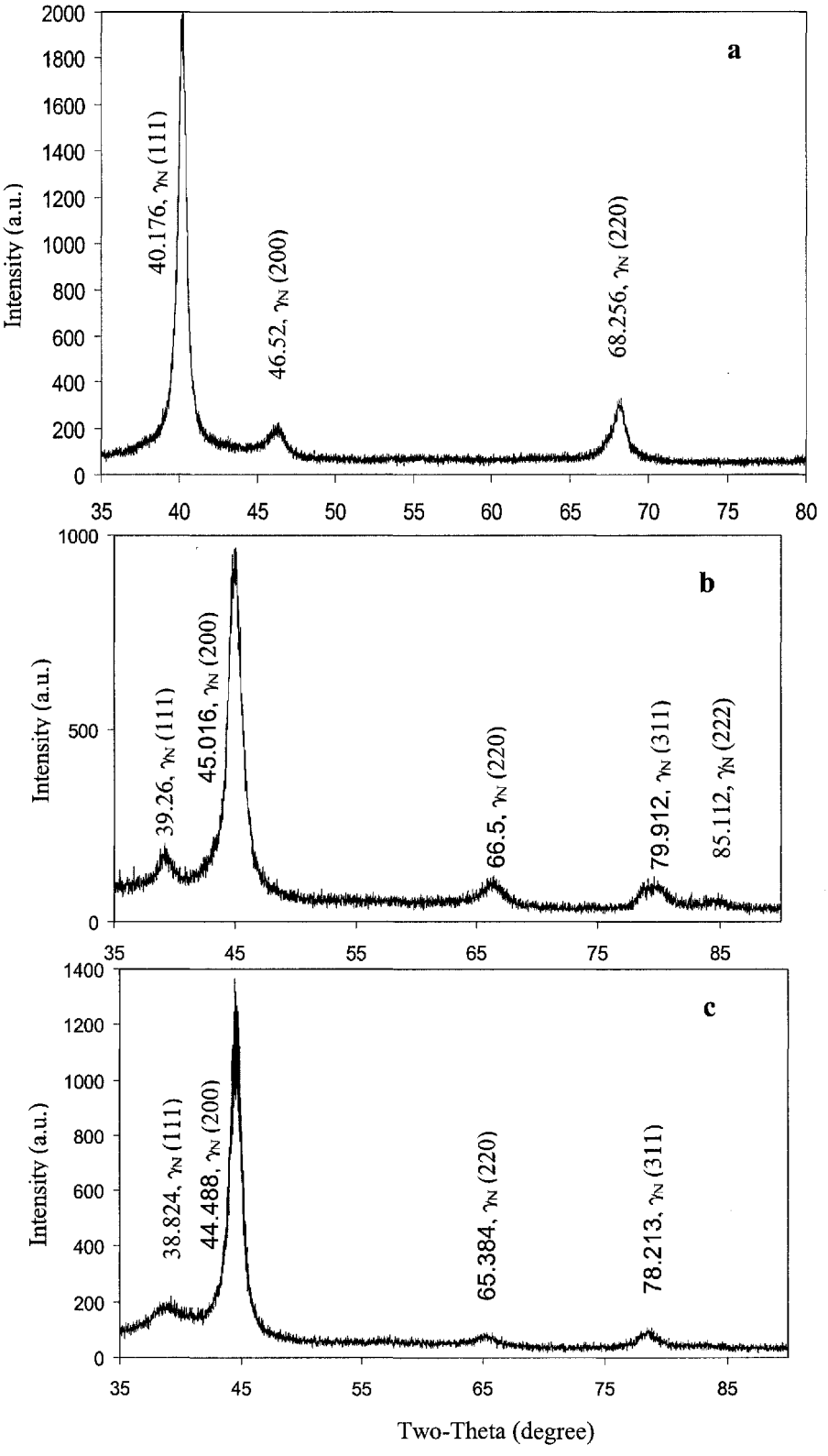


Figure 4.17: GIXD pattern of SS-N film deposited at 300 °C & 2.2Wcm^{-2}, 7 cm target-substrate distance and with (a) 25% N_2, (b) 30% N_2 and (c) 37% N_2

With further increase in nitrogen content through increasing nitrogen proportion to 45% N_2 during the sputter deposition, two FCC phases resulted in the SS-N films,

ATTENTION: The Singapore Copyright Act applies to the use of this document. Nanyang Technological University Library

with different lattice parameters, one corresponding to γ_N phase with lattice parameter 4.04 Å and other corresponding to the MN phase with lattice parameter 4.3 Å. The broad amorphous-like peaks, as can be seen in Figure 4.20, of both the phases suggest nanocrystallinity in the film. The presence of these two nanocrystalline phases is also confirmed by TEM electron diffraction analysis in Figure 4.21. The MN phase in the film is referred to as the minor phase with less number of diffracting peaks and with lower intensities. The diffraction rings corresponding to this secondary minor phase are less. This suggests formation of the MN phase only in smaller fraction.

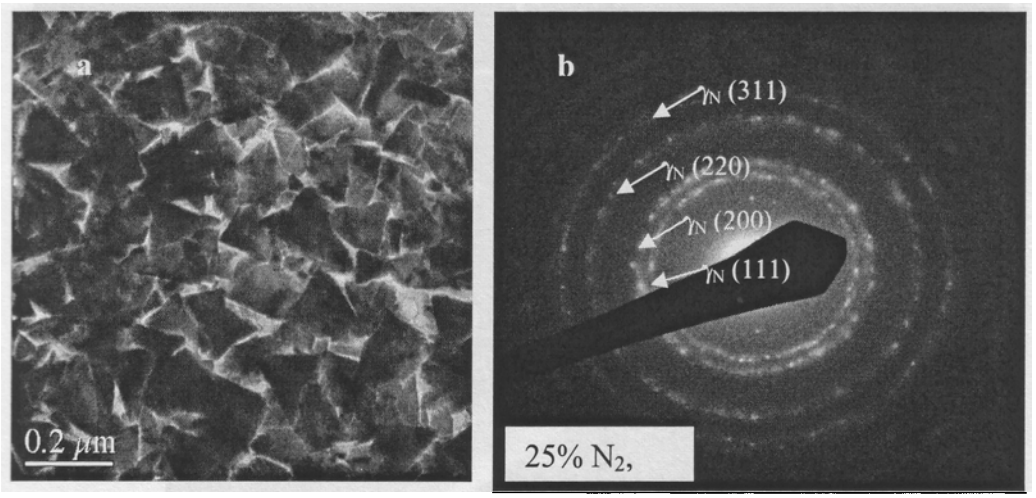


Figure 4.18 (a) Bright field image and (b) Electron Diffraction Pattern of the SS-N film deposited at 300 °C with 25% N_2, 2.2Wcm^{-2} and 7 cm target-substrate distance

In the case of the film deposited with 37% N_2, it has been shown by nanobeam electron diffraction that traces of MN phase were formed (Figure 4.19c). The proportion of MN phase increases (Figure 4.20 & 21) when % N_2 was increased to 45% N_2 such that this phase was detected by XRD. Now by changing the sputter gas composition to 50% N_2, the γ_N phase disappeared from the film. Instead a single MN phase was formed with ideal FCC lattice, as can be seen from the characteristic FCC diffraction patterns shown in Figure 4.22 & 23. A further increase in nitrogen gas composition to 75% did not lead to any significant change in the XRD pattern (Figure 4.24). Thus, the two films produced with 50% and 75% N_2 have similar structure and similar nitrogen concentration. The four reflection peaks from each of these two films correspond well to the ideal FCC structure with

ATTENTION: The Singapore Copyright Act applies to the use of this document. Nanyang Technological University Library

minimal distortion, because the lattice parameter calculated from each peak coincides with one another.

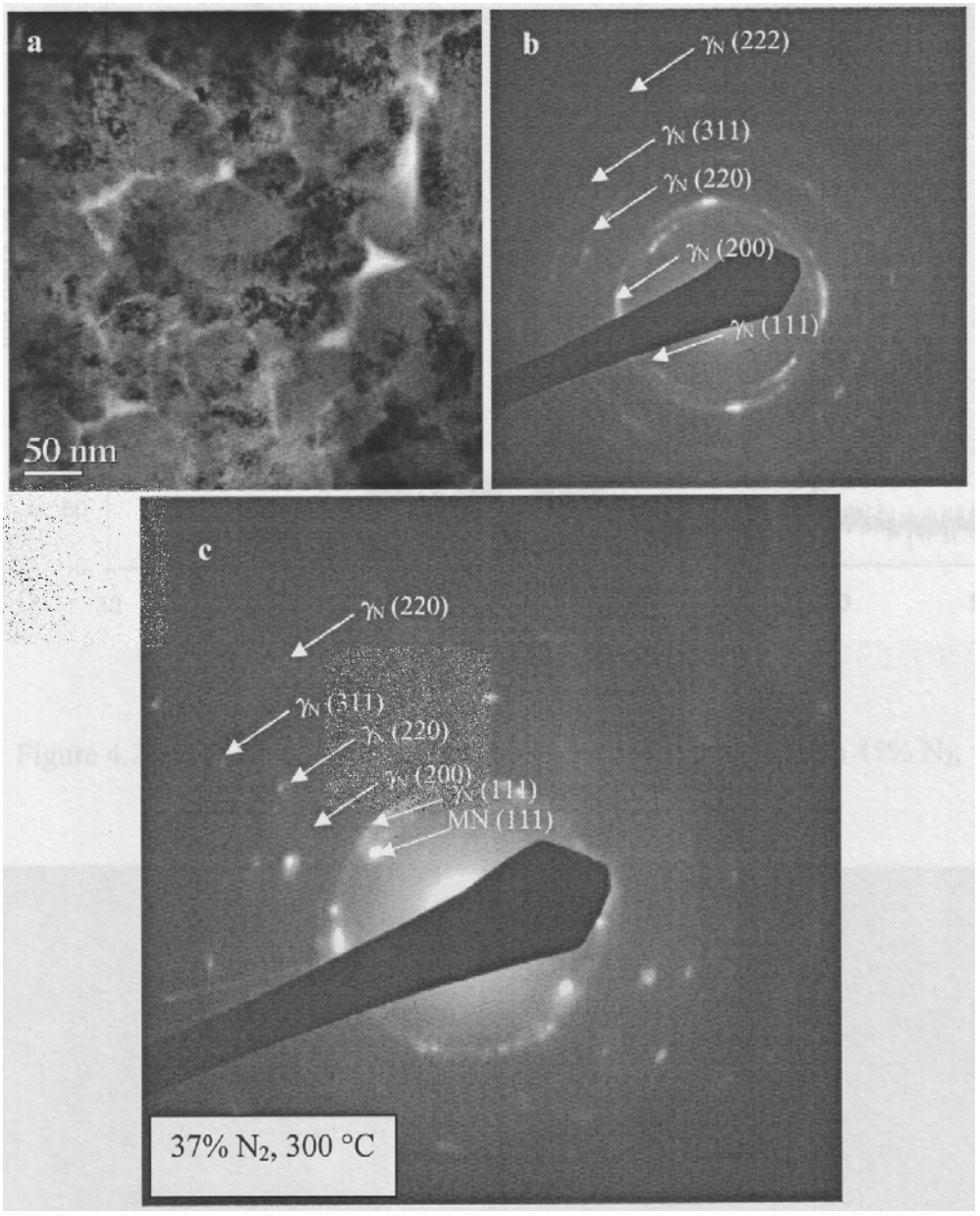


Figure 4.19: (a) Plan view bright field image, (b) Electron Diffraction and (c) Nanobeam electron diffraction patterns obtained from the same SS-N film deposited at 300 °C with 37% N_2, 2.2Wcm^{-2} and 7 cm target-substrate distance

ATTENTION: The Singapore Copyright Act applies to the use of this document. Nanyang Technological University Library

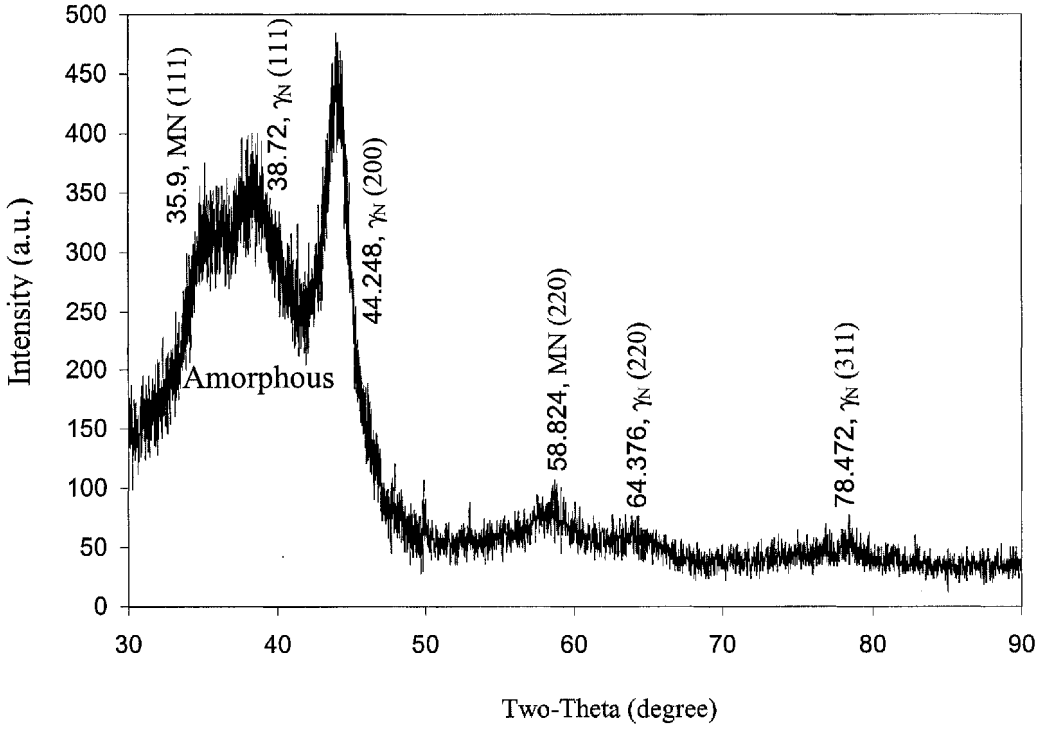


Figure 4.20: GIXD pattern of SS-N film deposited at 300 °C with 45% N_2, 2.2Wcm^{-2} and 7 cm target-substrate distance

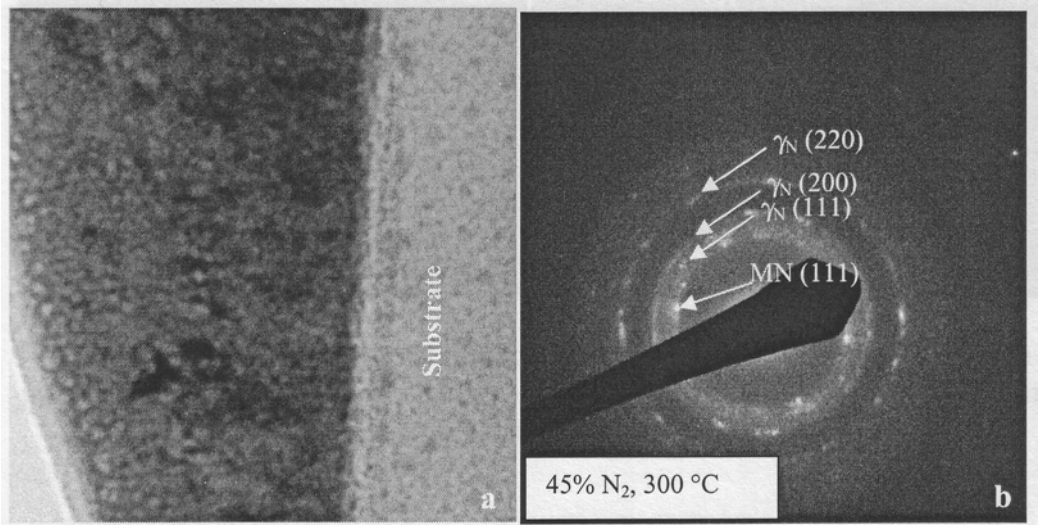


Figure 4.21: (a) Cross sectional bright field image and (b) Electron Diffraction Pattern of the SS-N film deposited at 300 °C with 45% N_2, 2.2Wcm^{-2} and 7 cm target-substrate distance

ATTENTION: The Singapore Copyright Act applies to the use of this document. Nanyang Technological University Library

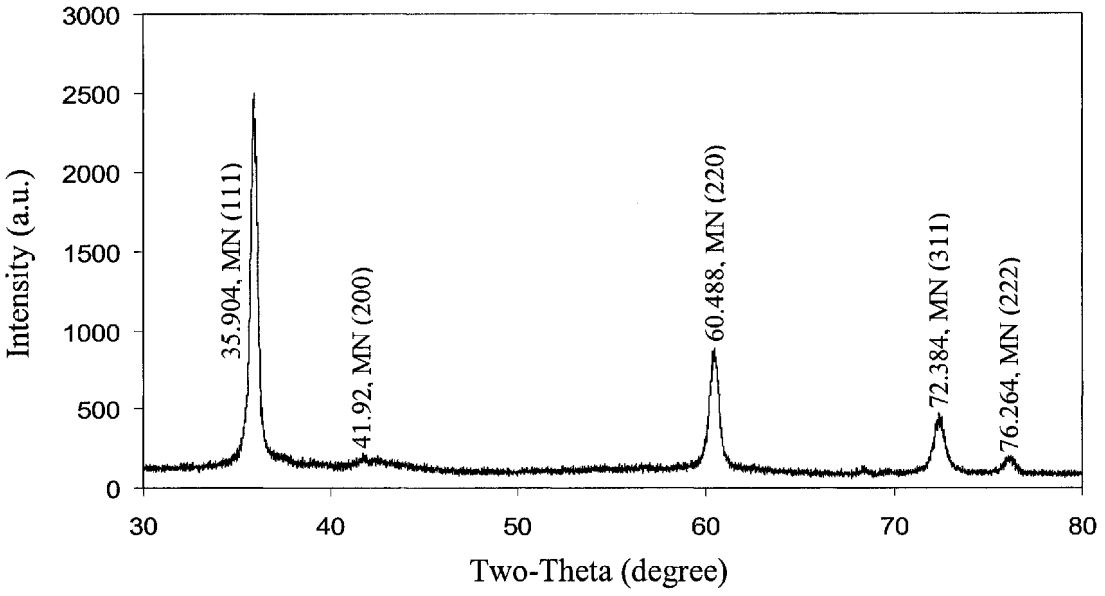


Figure 4.22: GIXD pattern of SS-N film deposited at 300 °C with 50% N_2, 2.2Wcm^{-2} and 7 cm target-substrate distance

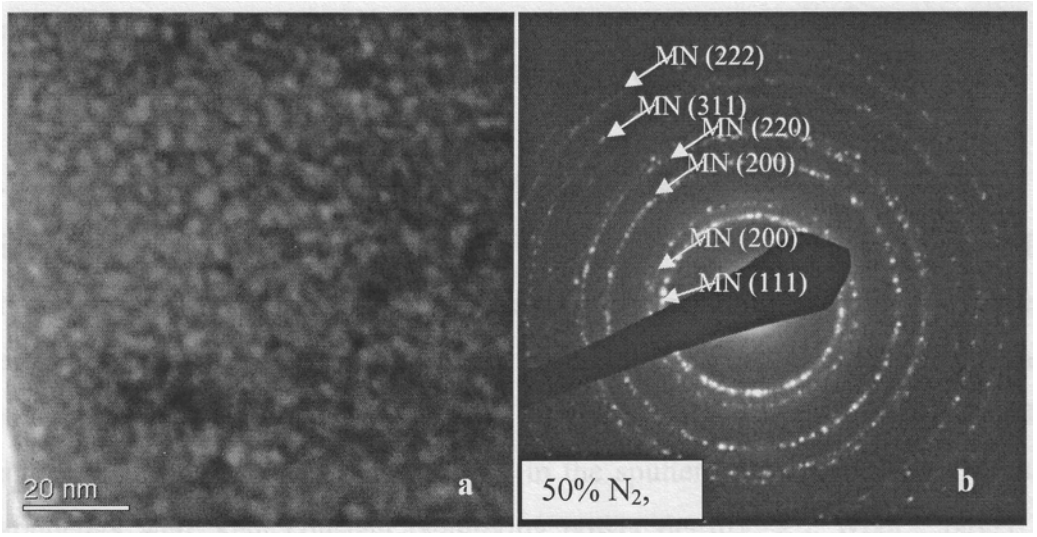


Figure 4.23: (a) Cross sectional bright field image and (b) electron diffraction pattern of the SS-N film deposited at 300 °C with 50% N_2, 2.2Wcm^{-2} and 7 cm target-substrate distance

ATTENTION: The Singapore Copyright Act applies to the use of this document. Nanyang Technological University Library

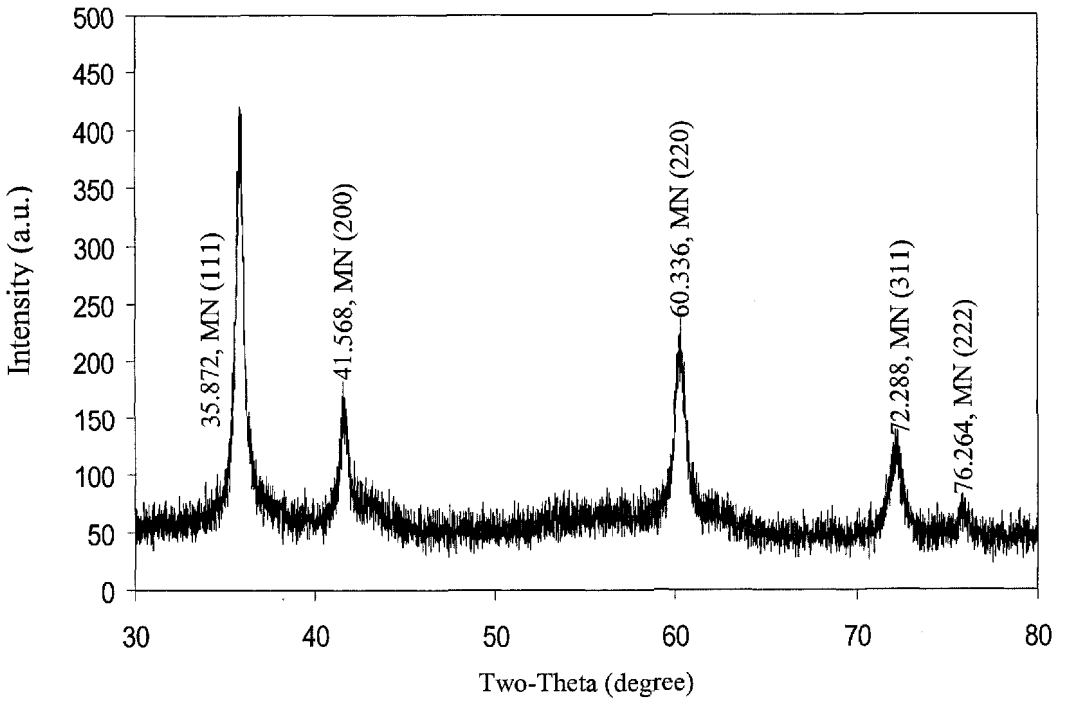


Figure 4.24: GIXD pattern of SS-N film deposited at 300 °C with 75%, 2.2Wcm^{-2} and 7 cm target-substrate distance

4.2.3 Effect of Substrate Temperature on γ_N Phase Formation

Since the two most interesting phases found in SS-N films are the γ_N and MN phases, further experiments were conducted to investigate the effect of varying deposition parameters in the formation of these two phases. Influence of substrate temperature on the formation of the γ_N phase was studied by varying the temperatures upto 500° C with 25% N_2 in the sputtering gas mixture. All other parameters were kept constant (sputtering power density: 2.2 Wcm^{-2}, target to substrate distance: 7 cm). Figure 4.25 shows the GIXD patterns of the resultant films. It can be seen that on unheated substrates, the film is predominantly amorphous with traces of ferrite. Increasing the temperature to 150 °C, the amorphous structure is persistent but with traces of γ_N phase as further confirmed by TEM elctron diffraction (Figure 4.26). With further increasing temperature to 300 °C and 400°C, crystalline γ_N phase formed. But at 500 °C, CrN starts to form together with nitrogen-free austenite (γ). This suggests that the γ_N phase is atleast stable up to 400 °C, above which it decomposes to CrN and austenite and is thus unstable.

ATTENTION: The Singapore Copyright Act applies to the use of this document. Nanyang Technological University Library

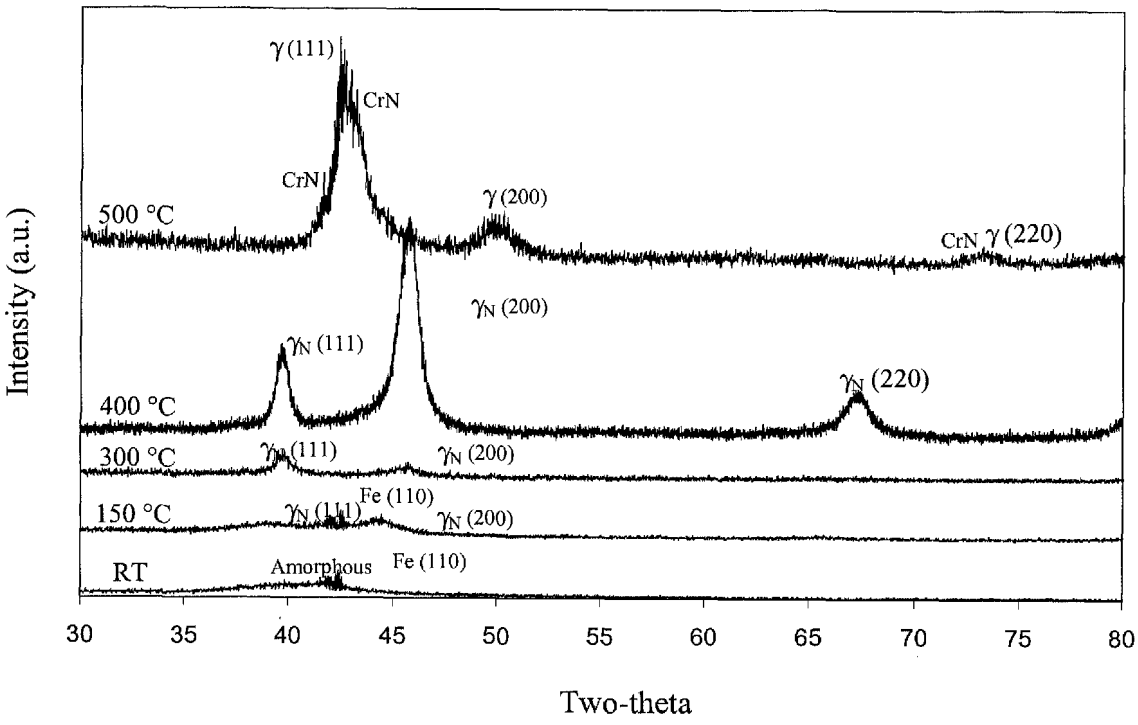
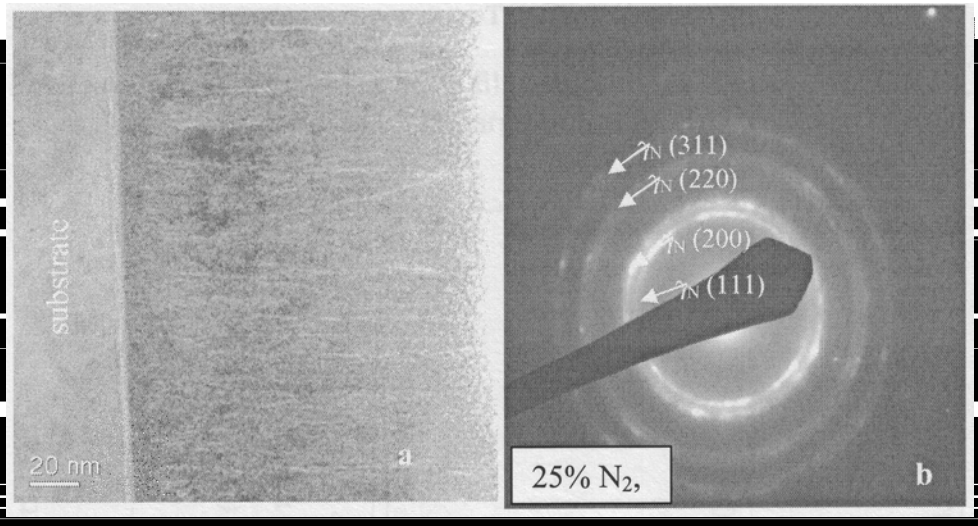


Figure 4.25: GIXD pattern of various γ_N films deposited with different substrate temperatures, 2.2Wcm^{-2} and 7 cm target-substrate distance



ATTENTION: The Singapore Copyright Act applies to the use of this document. Nanyang Technological University Library

°C. From the results, it can be seen that the MN phase formed in the SS-N films deposited with 50% N_2 upto the temperature as high as 400 °C. But a broad weak peak corresponding to ferrite (110) can also be seen from the GIXD pattern. This is reflected in the decreased nitrogen content (Figure 4.31) in the film.

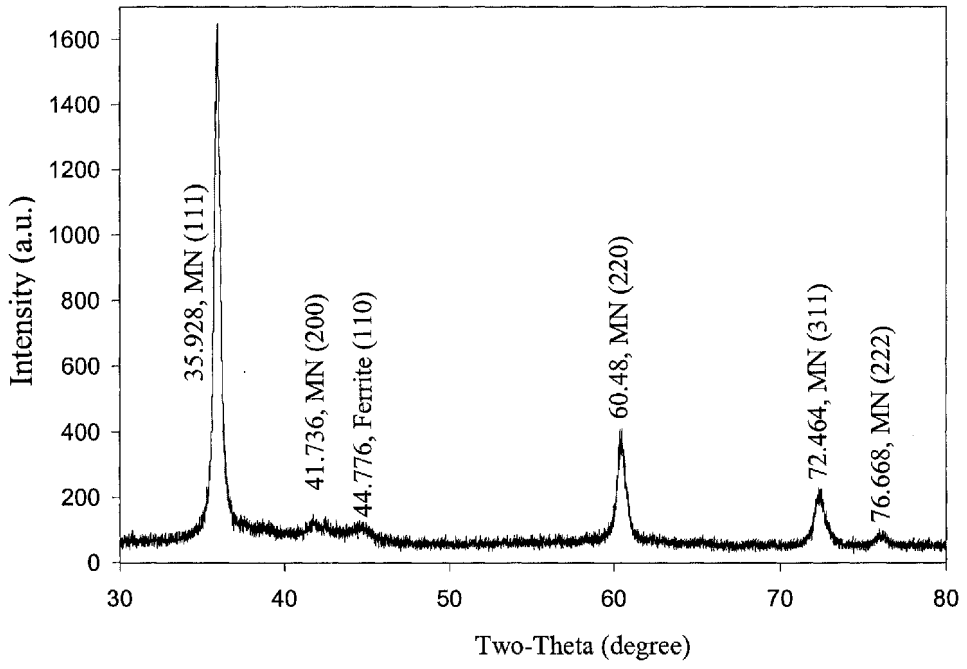


Figure 4.27: GIXD pattern of SS-N film deposited at 400 °C with 50% N_2, 2.2Wcm^{-2} and 7 cm target-substrate distance

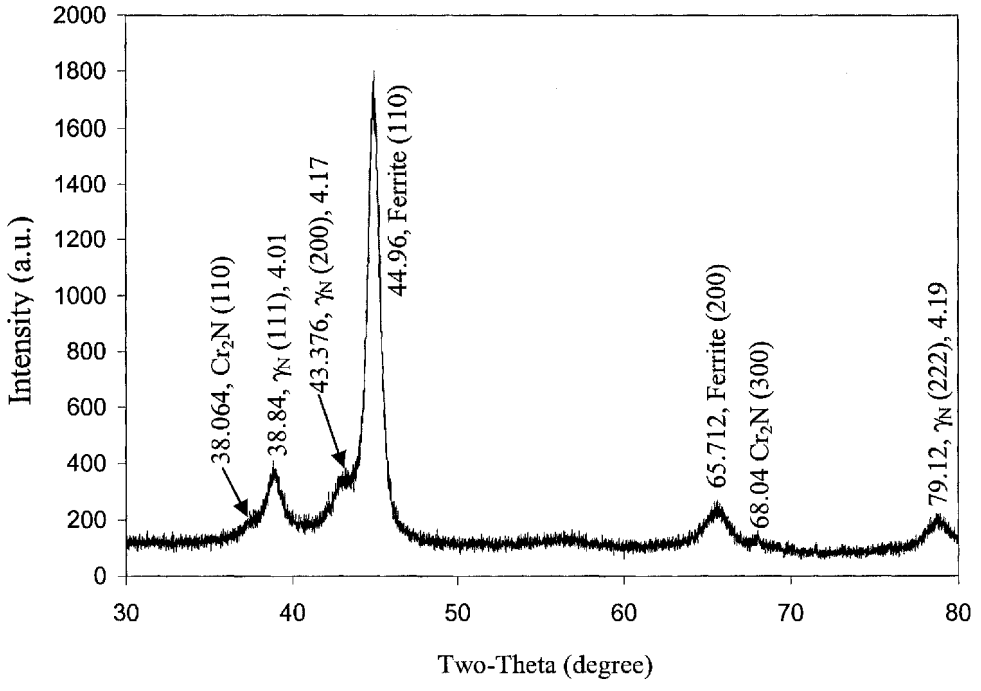


Figure 4.28: GIXD pattern of SS-N film deposited at 450 °C with 50% N_2, 2.2Wcm^{-2} and 7 cm target-substrate distance

ATTENTION: The Singapore Copyright Act applies to the use of this document. Nanyang Technological University Library

With increasing temperature to 500 °C, the MN phase is unstable and thus more stable Cr_2N phase formed together with ferrite and expanded austenite.

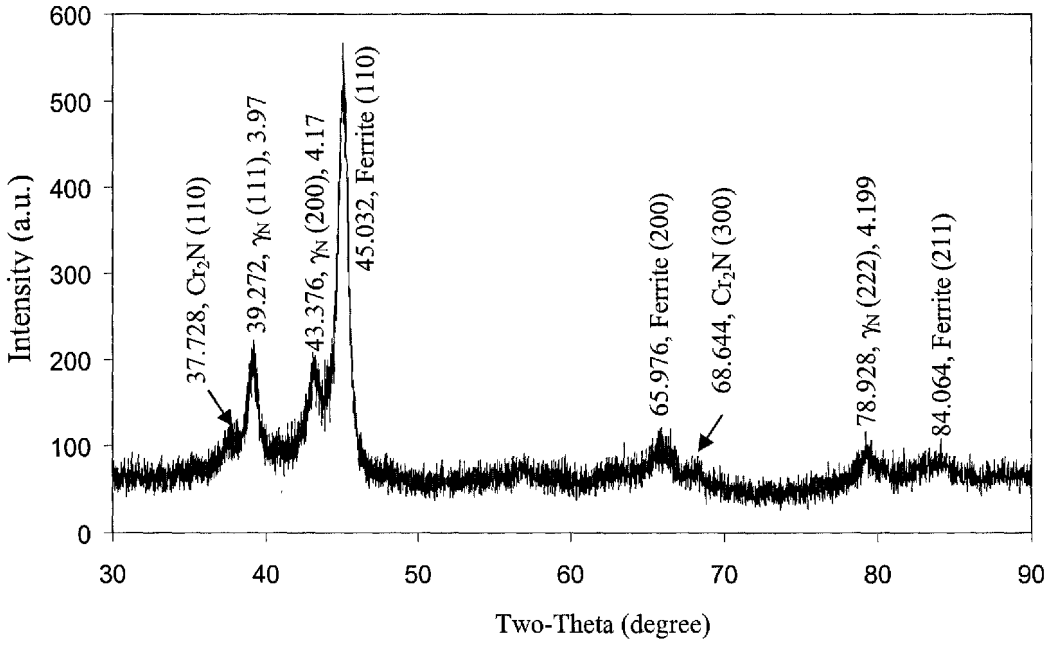


Figure 4.29: GIXD pattern of SS-N film deposited at 500 °C with 50% N_2 2.2Wcm^{-2} and 7 cm target-substrate distance

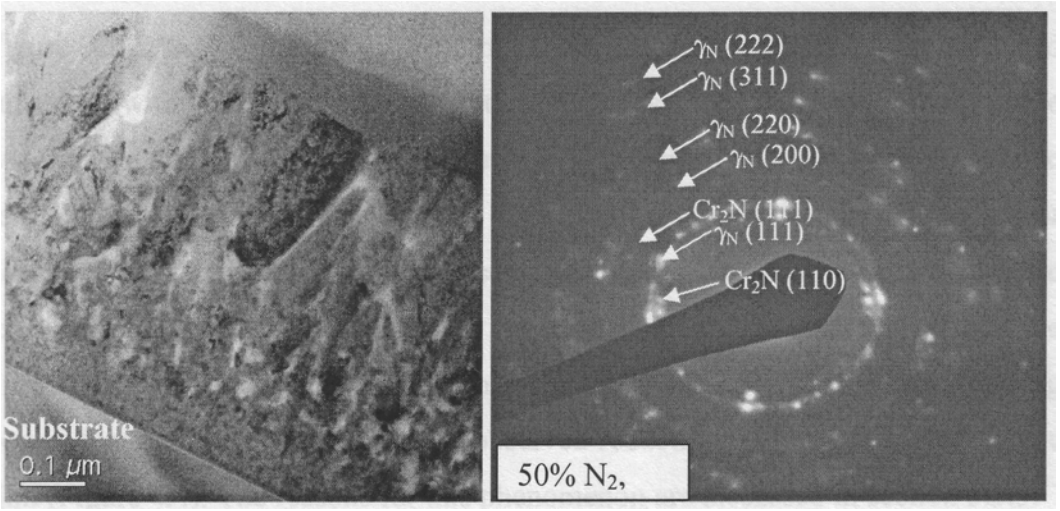


Figure 4.30: (a) Cross sectional bright field image and (b) Electron Diffraction Pattern of the SS-N film deposited at 500 °C with 50% N_2, 2.2Wcm^{-2} and 7 cm target-substrate distance

ATTENTION: The Singapore Copyright Act applies to the use of this document. Nanyang Technological University Library

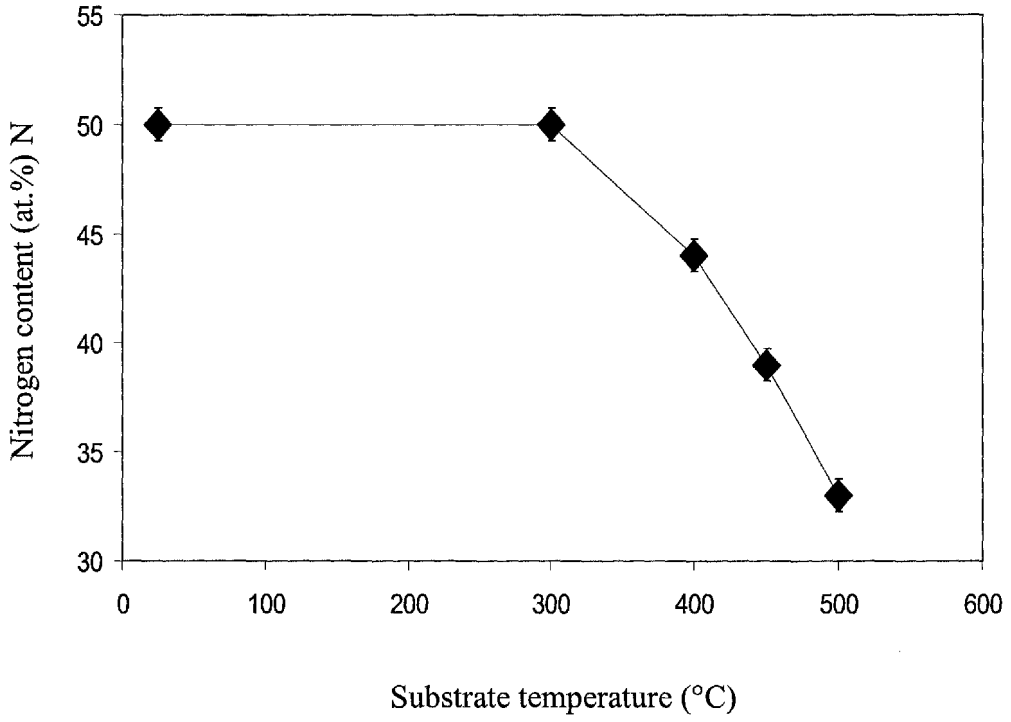


Figure 4.31: Plots of nitrogen content versus substrate temperature of the films deposited with 50% N_2, 2.2Wcm^{-2} and 7 cm target-substrate distance

4.2.5 Effect of Deposition Power Density on γ_N Phase Formation

Figure 4.32 shows the GIXD patterns from the films deposited on unheated substrates with 25% N_2 in the gas mixture. It can be seen that an amorphous phase was formed for the lowest power density (2.2 Wcm^{-2}) together with crystalline ferrite phase. The constituent phases depended greatly on the deposition power density. Amorphous and ferrite phases formed for low power densities while expanded austenite formed for higher power densities. It is also evident that the diffraction peaks from the γ_N phase are shifted to higher angles with increasing power density in agreement with the observed reduction in nitrogen content in the film (Figure 4.4). The reasons for this phenomenon are discussed in section 5.3.3.

ATTENTION: The Singapore Copyright Act applies to the use of this document. Nanyang Technological University Library

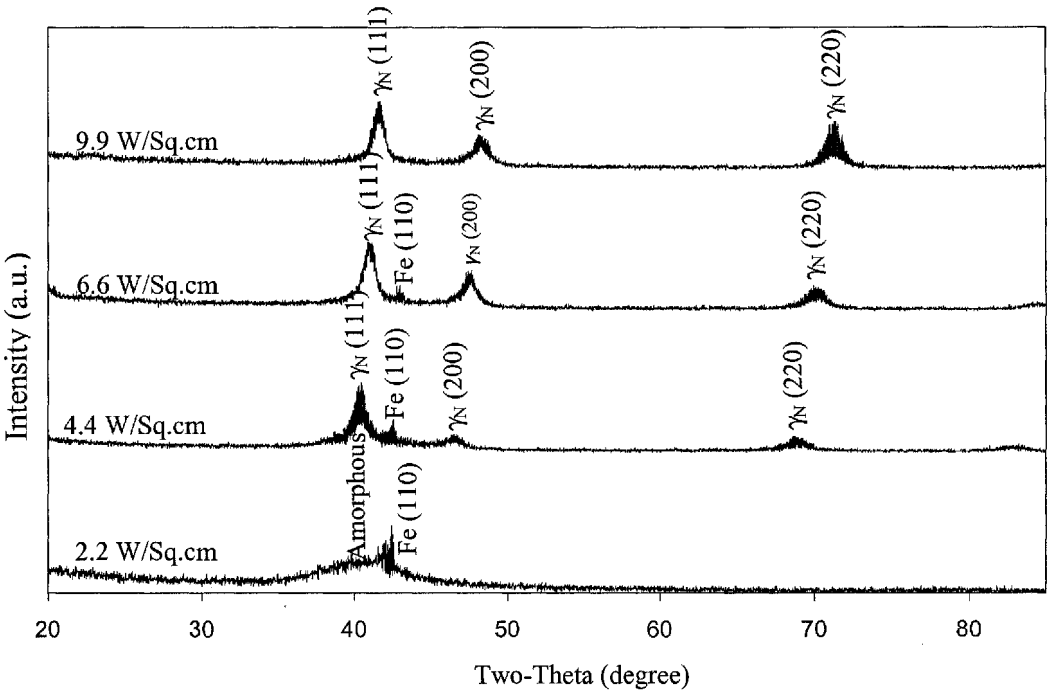


Figure 4.32: GIXD patterns of SS-N films deposited on unheated substrate with 25% N_2, 7 cm target-substrate distance & various power densities

4.2.6 Effect of Deposition Power Density on MN Phase Formation

Figure 4.33 shows the GIXD patterns from the films deposited on unheated substrates with 100% N_2 gas and varying power density.

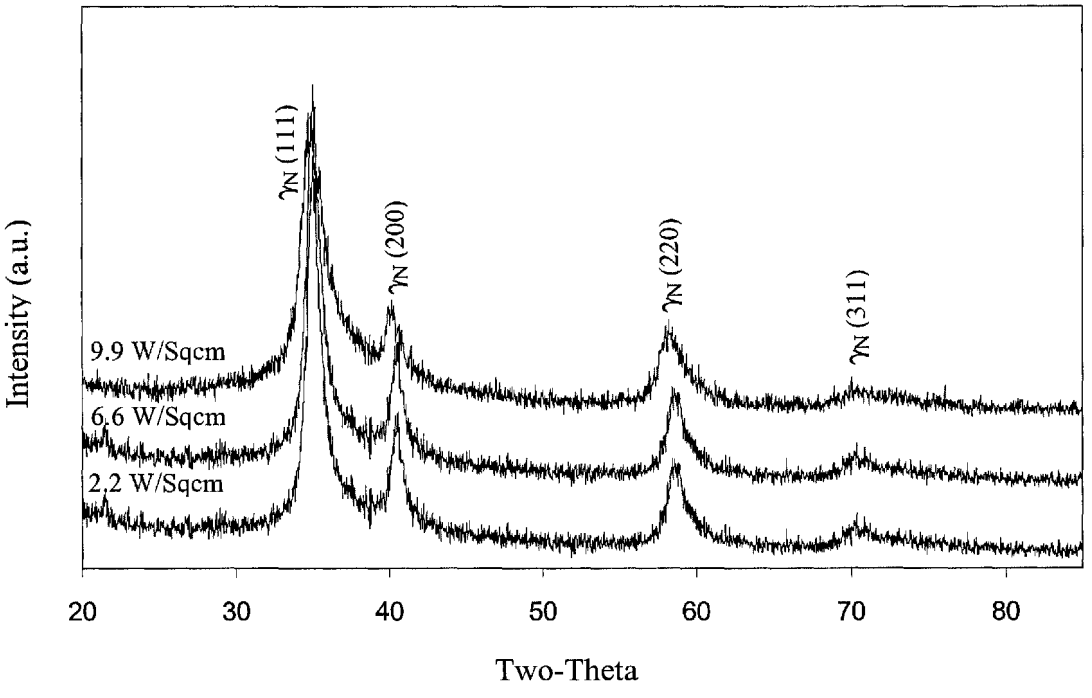


Figure 4.33: GIXD patterns of SS-N films deposited on unheated substrate with 100% N_2, 7 cm target-substrate distance & various power densities

ATTENTION: The Singapore Copyright Act applies to the use of this document. Nanyang Technological University Library

It can be seen that the cubic γ_N phase formed consistently in all the films.

4.2.7 Effect of Target-Substrate Distance on Phase Evolution

In order to study the effect of target-substrate distance on phase evolution, the target-substrate distance was reduced from 7 cm to 4 cm for the depositions on substrates heated to 300 °C. Figure 4.34 shows the GIXD patterns of the resultant SS-N films. In the film deposited with 25% N_2 γ_N phase along formed while for the 40% N_2 mixture of γ_N and MN phases formed. The formation of the cubic MN phase also did not seem to depend on target-substrate distance, as confirmed by GIXD shown in Figure 4.35 for the films deposited with 50% and 75% N_2 and with reduced (4 cm) target-substrate distance. It can be seen that the relative peak intensities of both the γ_N and MN phases are different from that of the phases formed for target-substrate distance of 7 cm. This is due to the effect of target-substrate distance on texture development in the film which is discussed in section 5.3.2.

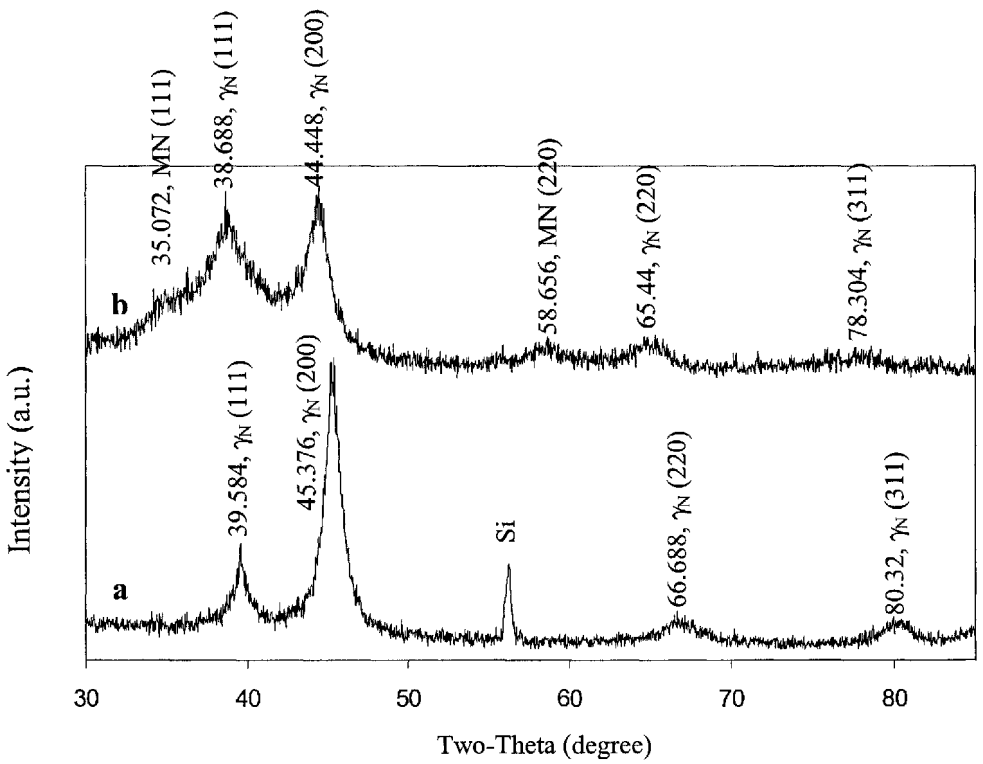


Figure 4.34: GIXD patterns of SS-N films deposited with (a) 25% & (b) 40% N_2 at 300 °C, 2.2Wcm^{-2} & 4 cm target-substrate distance

ATTENTION: The Singapore Copyright Act applies to the use of this document. Nanyang Technological University Library

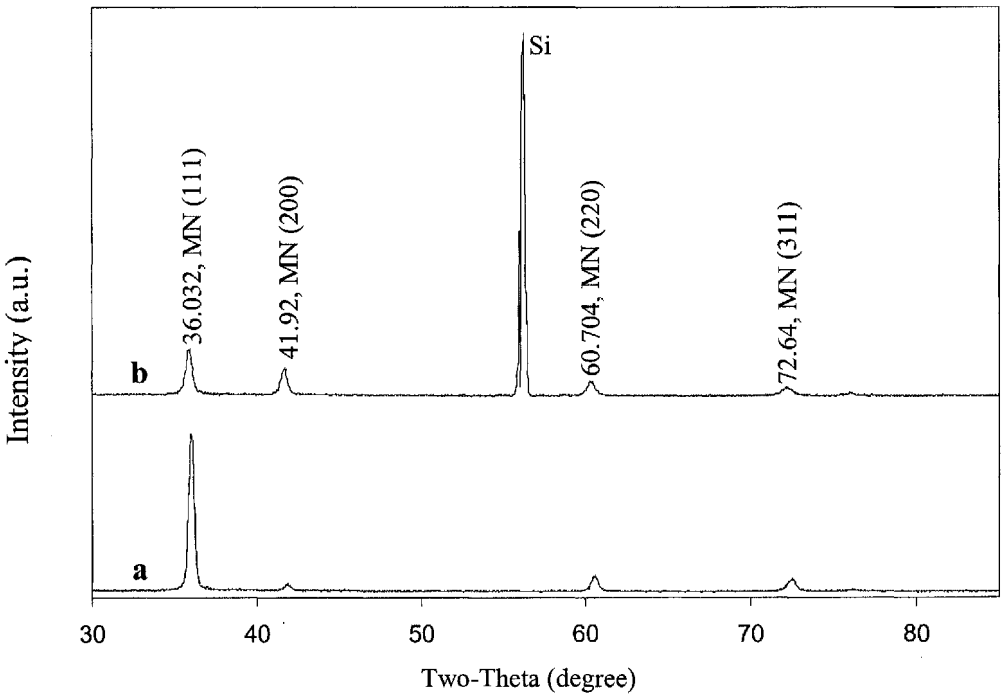


Figure 4.35: GIXD patterns of SS-N films deposited with (a) 50% & (b) 75% N_2 at 300 °C, 2.2Wcm^{-2} & 4 cm target-substrate distance

4.2.8 Effect of Substrate Bias on MN Phase Formation

The effect of substrate bias on MN phase formation was studied by applying RF bias of power from 2.2Wcm^{-2} to 300W during the sputter deposition process. Figure 4.36 shows GIXD patterns of the SS-N films deposited at 300 °C and with 50% N_2 with varying RF substrate bias power. In comparison to the diffraction pattern (Figure 4.22) obtained for the film deposited with 50% N_2 at 300 °C without bias, it can be seen that MN phase did not form at all for the highest substrate bias power and the decomposition products γ_N and Cr_2N appeared instead.

ATTENTION: The Singapore Copyright Act applies to the use of this document. Nanyang Technological University Library

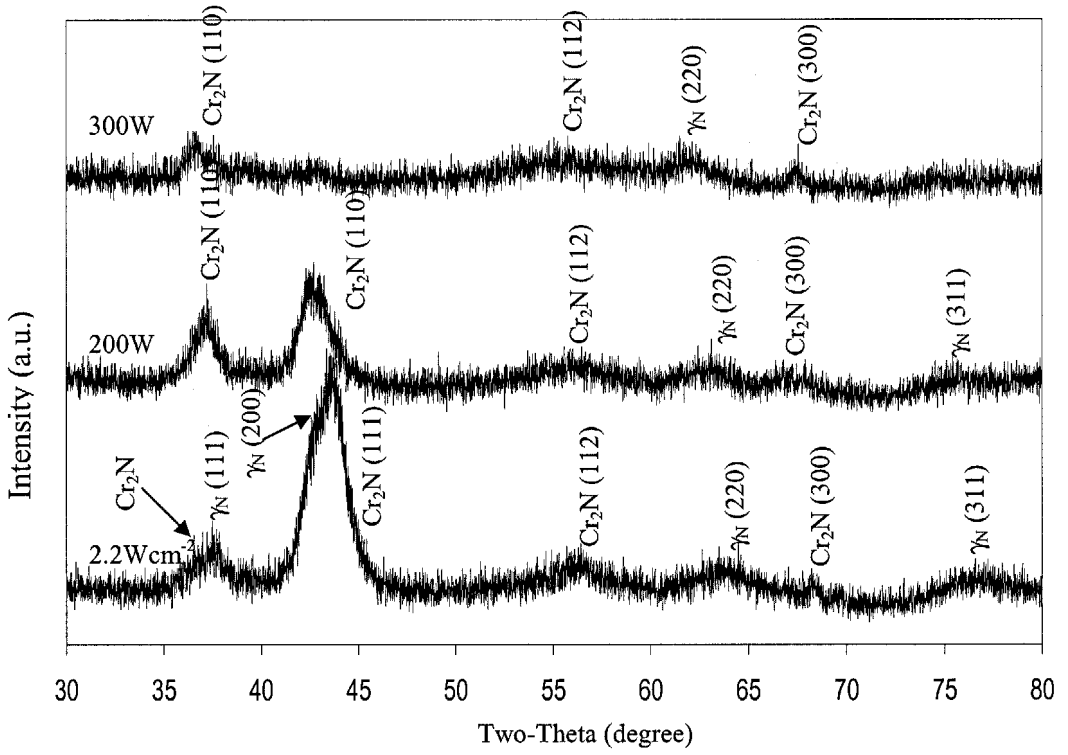


Figure 4.36: GIXD patterns of SS-N films deposited at 300 °C with 50% N_2, 2.2Wcm^{-2}, 7 cm target-substrate distance and various RF substrate bias powers

4.2.9 Phase Evolution in the Annealed Films

Annealing of selected SS-N films was conducted in vacuum at 500 °C to study the thermal stability of the phases. Figures 4.37 to 4.40 show the GIXD Patterns of the films after annealing of selected MN and expanded austenite films with the conditions similar to that of the above depositions. When all the films with different at.% N and constituent phases were annealed at 500 °C, ferrite, expanded austenite, austenite and Cr_2N phases formed due to the decomposition of expanded austenite phases with high at.% N and MN phase.

ATTENTION: The Singapore Copyright Act applies to the use of this document. Nanyang Technological University Library

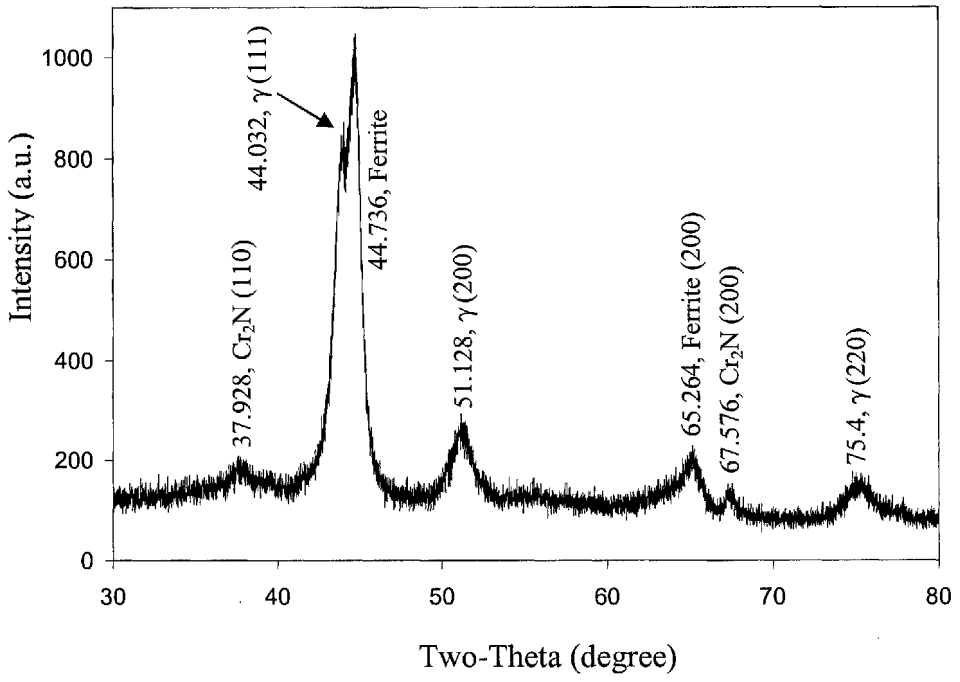


Figure 4.37: GIXD pattern of MN film annealed for 500 °C-3 hours after depositing on unheated substrate with 50 % N_2, 2.2Wcm^{-2} and 7 cm target-substrate distance

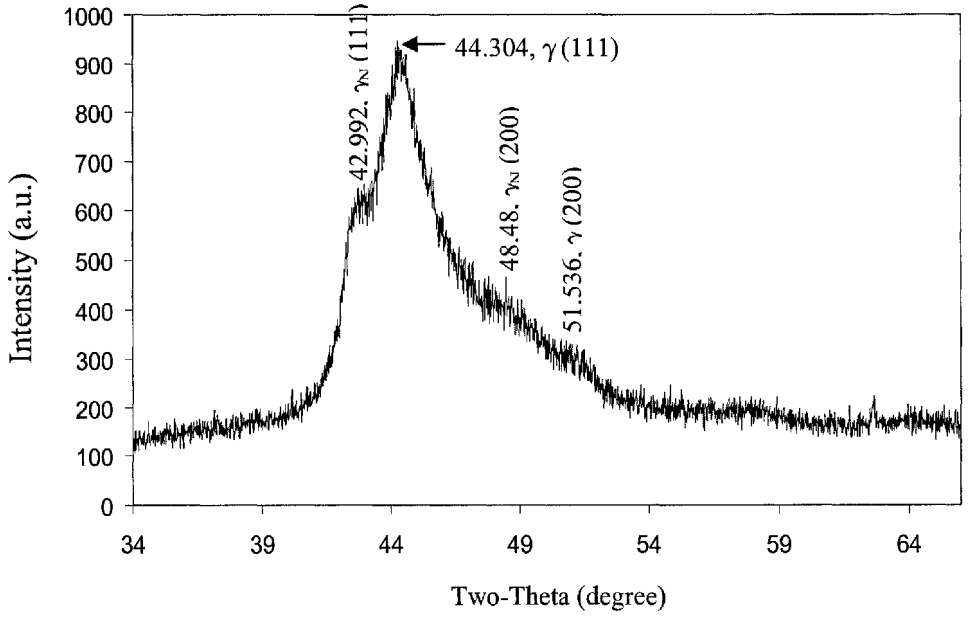


Figure 4.38: GIXD pattern of SS-N film deposited on unheated substrate with 9.9Wcm^{-2}, 7 cm target-substrate distance power, and 25% N_2 and annealed for 500 °C-3 hours. The film contains pure γ_N phase with nitrogen content insufficient for Cr_2N precipitation

ATTENTION: The Singapore Copyright Act applies to the use of this document. Nanyang Technological University Library

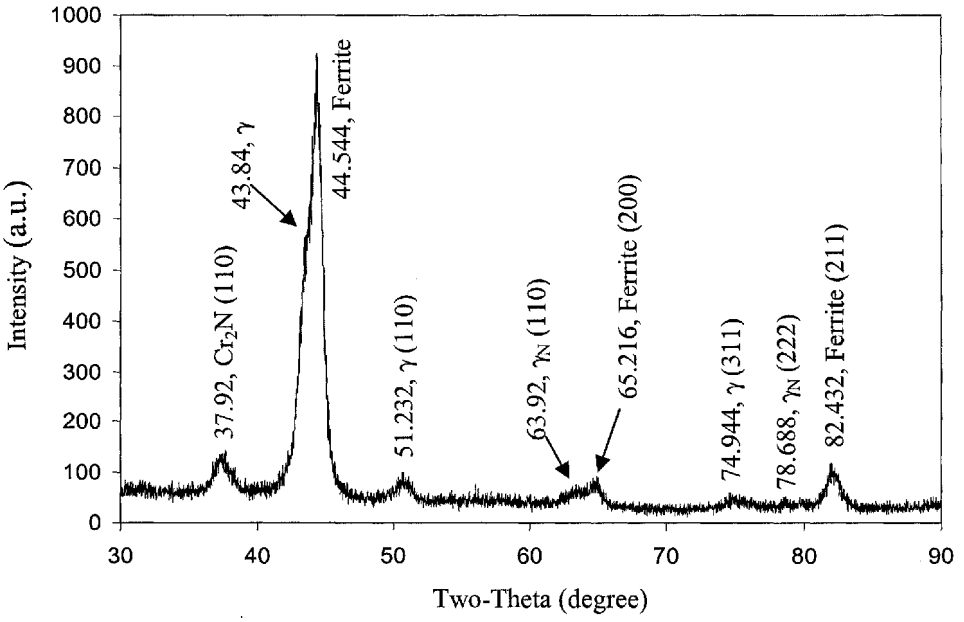


Figure 4.39: GIXD pattern of SS-N film annealed for 500 °C-3 hours after depositing on unheated substrate with 100 % N_2 & 6.6Wcm^{-2} and 7 cm target-substrate distance

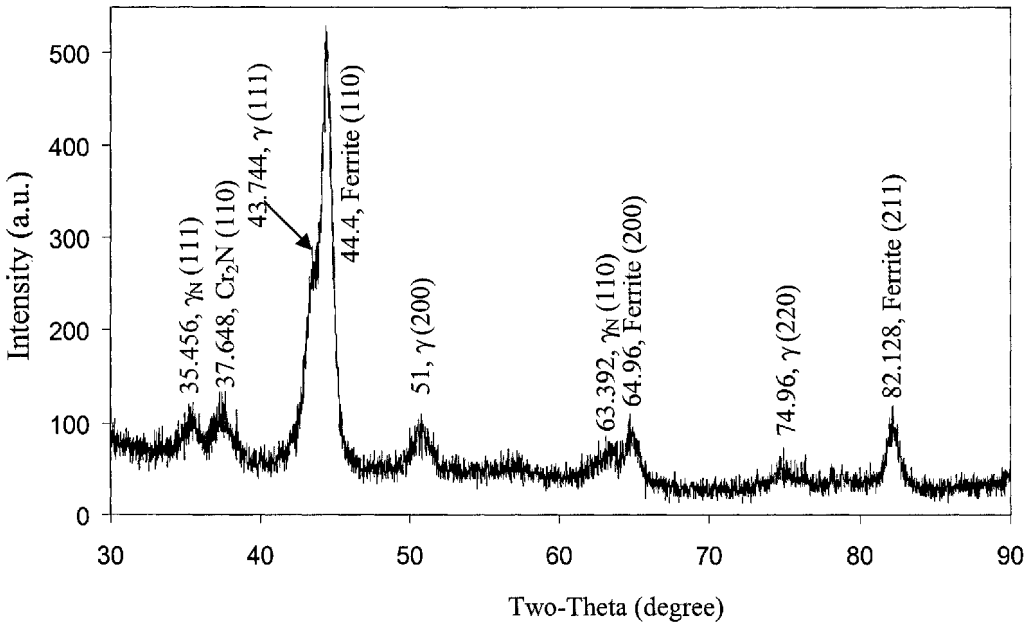


Figure 4.40: GIXD pattern of SS-N film annealed for 500 °C-3 hours after deposited at 300 °C with 75% N_2 & 2.2Wcm^{-2}

4.3 DEPOSITION RATE

All the films studied in this work have thickness value varying from 0.5 μm to 1.3 μm. The deposition rate depends on deposition conditions and affects the phase evolution and morphology of the films. Figure 4.41 shows the deposition rate (in

ATTENTION: The Singapore Copyright Act applies to the use of this document. Nanyang Technological University Library

nm/minute) as a function of nitrogen gas composition for the films deposited on unheated substrates and at 300 °C. It can be seen that the deposition rate increased slightly with the increase in nitrogen composition up to 10% N_2. But further increase in nitrogen gas composition above 10% led to gradual reduction in deposition rate. Increasing the substrate temperature slightly reduced the deposition rate.

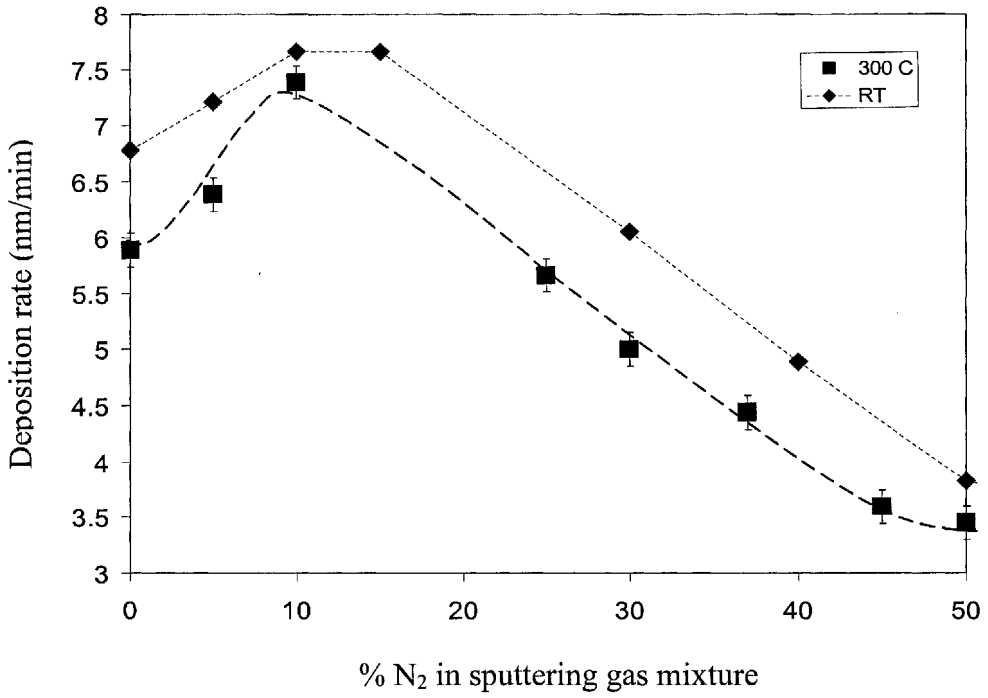


Figure 4.41: Deposition rate as a function of nitrogen gas composition in the gas mixture, on unheated substrates, 2.2Wcm^{-2} and 7 cm target-substrate distance

The effect of deposition power density on deposition rate is illustrated in Figure 4.42. As the deposition power density was gradually increased from 2.2 to 9.9 Wcm^{-2}, deposition rate increased gradually. The deposition rate can be seen to be fairly changing linearly with the increasing power density. In addition, decreasing the target-substrate distance from 7 cm to 4 cm is found to be effective in increasing deposition rate from 6 nm/min to 7.4 nm/min with a power density of 2.2Wcm^{-2}. It will be discussed later that deposition rate has a significant effect on the incorporation of nitrogen in the SS-N films, in particular the γ_N films during the deposition process.

ATTENTION: The Singapore Copyright Act applies to the use of this document. Nanyang Technological University Library

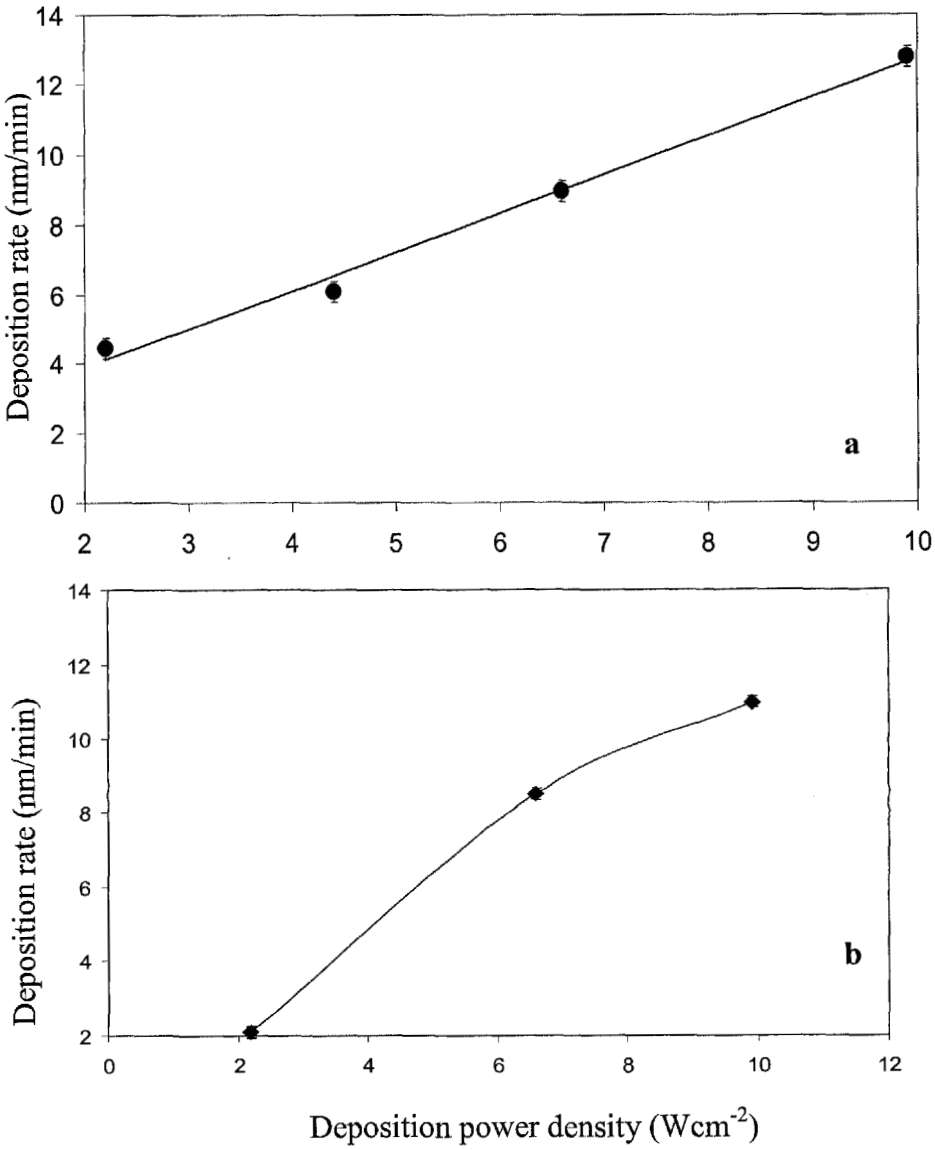


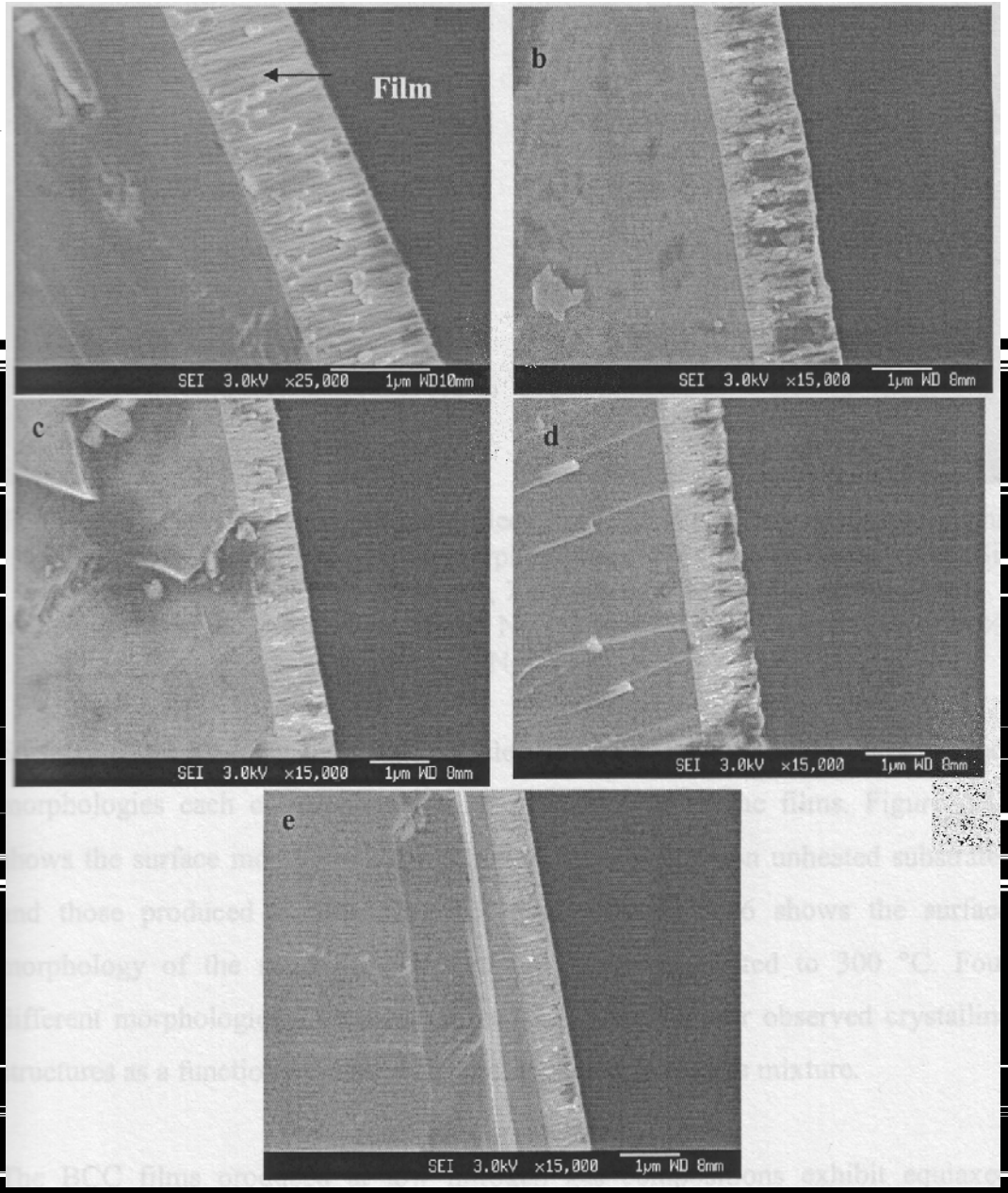
Figure 4.42: Deposition rate versus power density, of pure γ_N films deposited with (a) 25% N_2 and (b) 50% N_2 on unheated substrate, 2.2Wcm^{-2} and 7 cm target-substrate distance

4.4 FILM MORPHOLOGIES DETERMINED BY ELECTRON MICROSCOPY

Figure 4.43 are FESEM micrographs showing fractured cross section of the films deposited on unheated substrates with various % N_2 in the atmosphere. The morphology of these films is similar to those deposited at 300 °C, shown in Figure 4.44. It can be seen that majority of the films show fibrous growth excepting the expanded austenite films (Figure 4.44b and c) deposited at 300 °C with 10 % and 25% N_2. In this film, fractured surface did not show columnar morphology

ATTENTION: The Singapore Copyright Act applies to the use of this document. Nanyang Technological University Library

properly due to the predominant deformation of the ductile austenite films. It will be shown in section 4.5 that the TEM cross section examination of the SS-N films showed equiaxed grains close to the substrate-film interface similar to the previous reported [53] observation.



ATTENTION: The Singapore Copyright Act applies to the use of this document. Nanyang Technological University Library

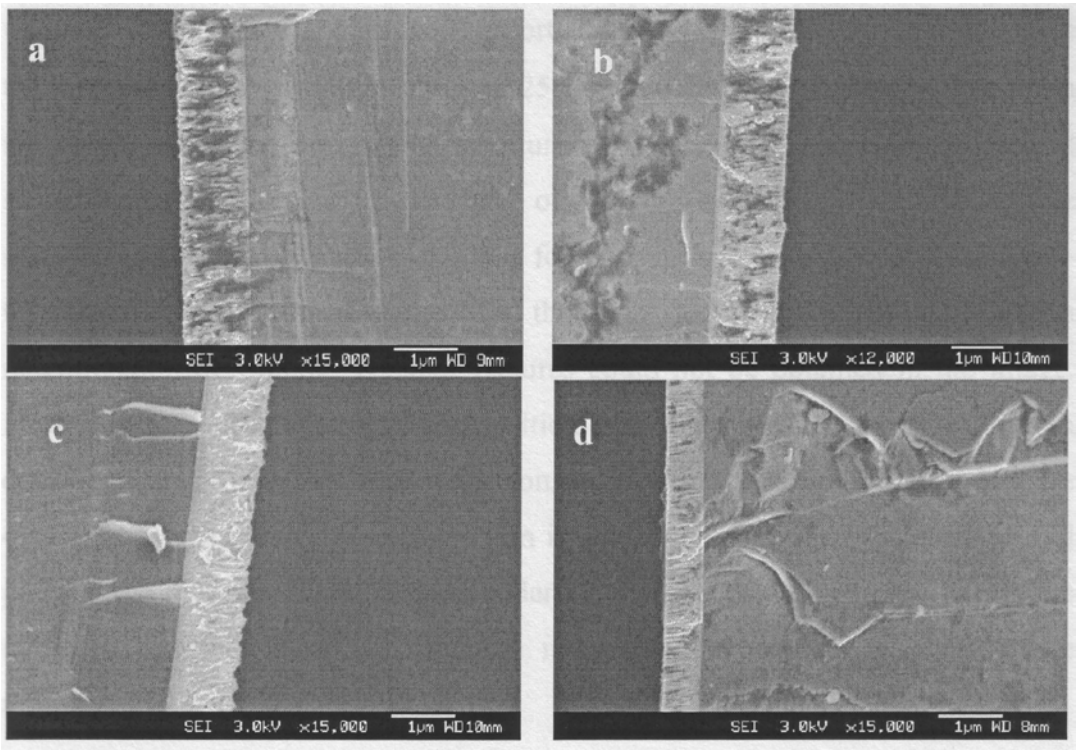


Figure 4.44: Field Emission Scanning Electron (FESEM) Microscope micrographs showing the fractured cross section morphologies of the films deposited on the Si substrates heated to 300°C, 2.2Wcm^{-2}, 7 cm target-substrate distance and with various % N_2 in the gas mixture. (a) 0% N_2; (b) 10% N_2; (c) 25% N_2; and (d) 50% N_2

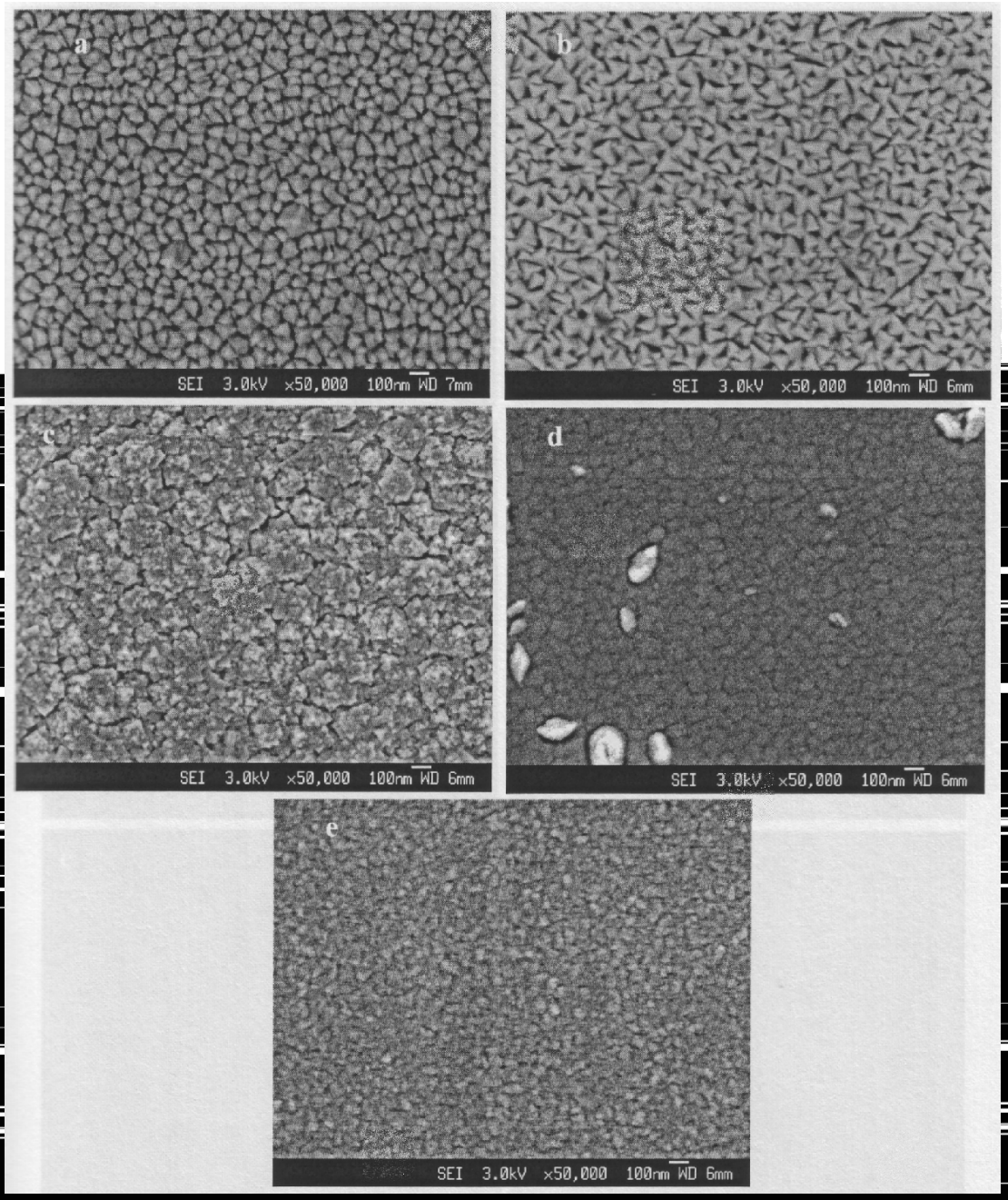
Surfaces of the as-deposited films, revealed by FESEM examination, show distinct morphologies each corresponding to a different type of the films. Figure 4.45 shows the surface morphologies of various types of films on unheated substrates and those produced at 300 °C, respectively. Figure 4.46 shows the surface morphology of the films produced on the substrates heated to 300 °C. Four different morphologies are noted, corresponding to the four observed crystalline structures as a function of nitrogen gas composition in the gas mixture.

The BCC films produced at low nitrogen gas compositions exhibit equiaxed pyramidal surface morphology. The base of the pyramids is polygonal with 0% N_2 (Figure 4.45a and 4.46a), and then changes to triangular-based with increasing nitrogen gas composition upto 5% (Figure 4.45b). The γ_N films produced with 10% N_2 in the gas mixture are populated with clusters of triangular based asperitic grain structure of very small sizes, with voids and cracks at the cluster boundaries (Figure 4.46c). It should be noted that the word asperities is used in the place of grain only to refer to the point that the grains are with relatively sharp pyramidal

ATTENTION: The Singapore Copyright Act applies to the use of this document. Nanyang Technological University Library

tips and that similar shape has been reported [53] already in the SS-N films. With the increase in nitrogen composition to 25% such that the γ_N phase was formed on the heated substrate, the granular structure attained angular asperitic and faceted shapes with varying sizes. In the case of the film deposited with 45% N_2, the surface morphology (Figure 4.46e) was found to be similar to characteristic low-temperature deposition. Despite the thorough focusing of the SEM at a magnification of 15000x, granular features could not be obtained in the image. Further increase in the nitrogen composition to 50% resulted in the formation of a dense and crack-free MN film with elongated "worm"-like morphology (Figure 4.46f). The high density of the MN film is evidenced from the lack of voids and pores at the intersections of grain boundaries. Film deposited with 50% N_2 on the unheated substrate showed irregular mound-like structures in the surface morphology.

ATTENTION: The Singapore Copyright Act applies to the use of this document. Nanyang Technological University Library



ATTENTION: The Singapore Copyright Act applies to the use of this document. Nanyang Technological University Library

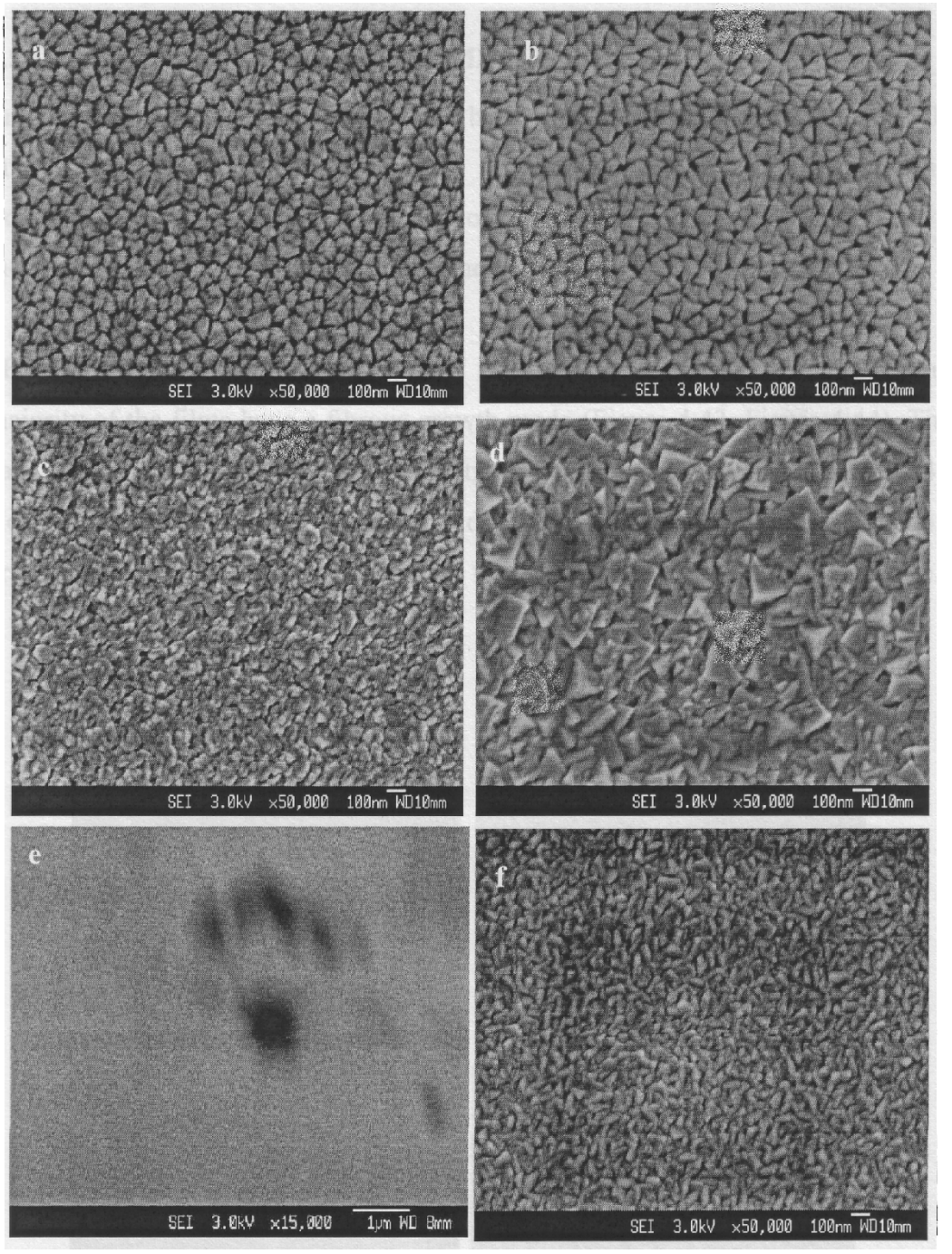


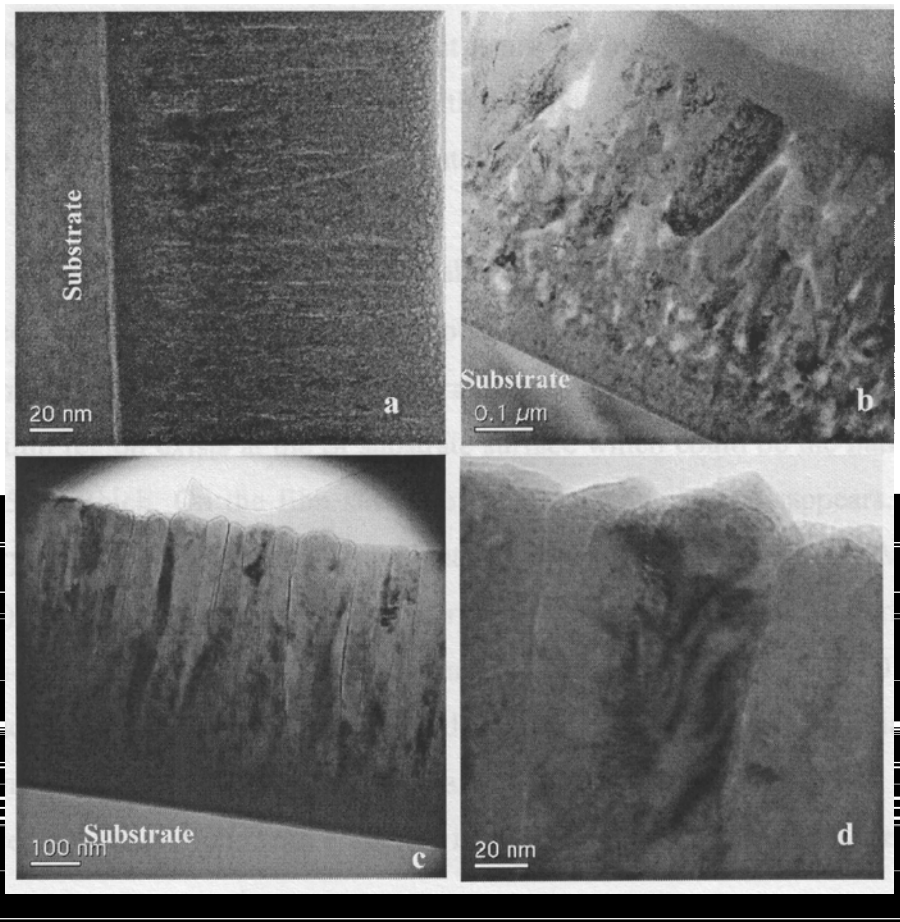
Figure 4.46: FIELD EMISSION SEM micrographs showing the surface morphologies of the films deposited on the Si substrates heated to 300°C with 2.2Wcm^{-2}, 7 cm target-substrate distance and various % N_2 in the gas mixture. (a) 0% N_2; (b) 5% N_2; (c) 10% N_2; (d) 25% N_2; (e) 45% N_2 and (f) 50% N_2

ATTENTION: The Singapore Copyright Act applies to the use of this document. Nanyang Technological University Library

4.5 CROSS SECTIONAL TEM EXAMINATION

Transmission electron microscopy has been used in this work to examine the microstructural features and the phase constituents of selected films. Further examination was made on cross section by TEM to study the film growth morphology and the film-substrate interfacial region.

FESEM morphological examination of fractured cross section has shown that majority of the films have a fibrous growth mode (Figure 4.43, Figure 4.44). This has been further confirmed by cross sectional examination shown in Figure 4.47. However, fractured surface morphology does not necessarily restore the columnar grain morphology in the present case due to the ductile nature of the film fracture.



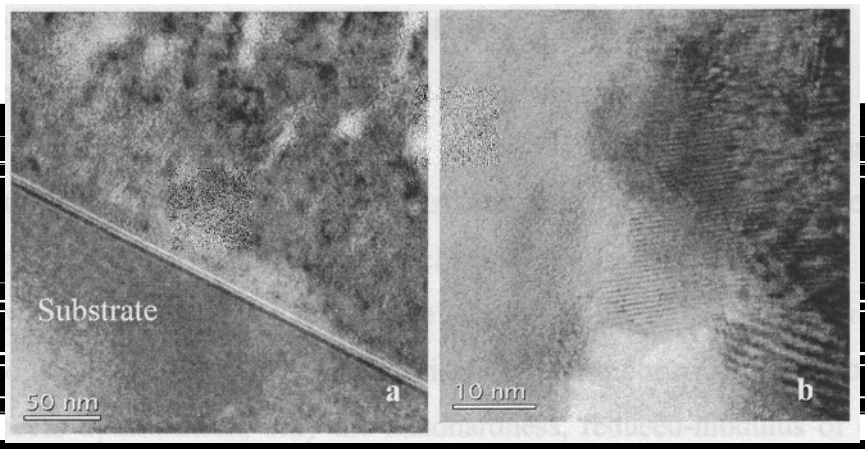
ATTENTION: The Singapore Copyright Act applies to the use of this document. Nanyang Technological University Library

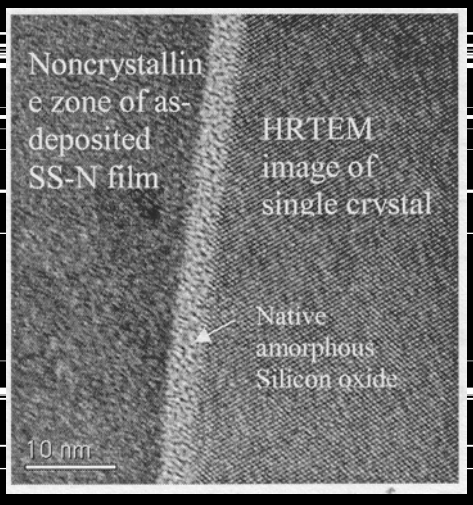
temperature (Figure 4.47b). From Figures 4.47a & c, it can be clearly seen that the film growth is a columnar mode with clear column boundaries. However, the SS-N film with mixture of phases (Figure 4.47 b) did not show the columnar growth. Surface morphology observed in Figure 4.47 c & d is similar to that observed by FESEM. The measured column diameters agree quite well with the grain sizes measured by FESEM. Therefore, the asperity size measurement based on FESEM surface morphological features (discussed later in section 5.5.3) seems valid. Another observation is that there is a variation in column size with distance from the film substrate surface. For all the films examined, the column size increases from the interface towards the film surface. Thus, the asperity size measured by FESEM surface morphology only represent the maximum size of the grain feature in the two dimensional view.

A further observation is that two distinct zones are observed in the film substrate interface region, one on the film side with amorphous-like or extremely fine grain feature and another on the silicon substrate side. These are discussed below.

Figure 4.48 shows the TEM images taken at the interface region of the films produced at 500 °C with 50% N_2. It should be recalled that under this condition, the film produced has a mixture of several phases (Figure 4.29). The images show that a thin region exists at the Si substrate surface which could be the native SiO_2 about 5 nm thick. On the film side, the column morphology disappears, instead nanocrystalline equiaxial grains dominate in the interface region. HREM image (4.48b) clearly reveals that SiO_2 is amorphous while the film at the interface has periodic atomic arrangement and crystalline nature with size about 20 nm. In conjunction with Figure 4.47, it can be deduced that the film formed initially into ultrafine grain (20 nm) on the native amorphous SiO_2, and then grew into the observed columnar mode with gradually increased column size towards the surface.

ATTENTION: The Singapore Copyright Act applies to the use of this document. Nanyang Technological University Library





ATTENTION: The Singapore Copyright Act applies to the use of this document. Nanyang Technological University Library

4.6 MECHANICAL PROPERTIES OF SS-N FILMS

From the previous sections of this chapter it is clear that the SS-N films produced under various conditions are composed of various phases. One of the anticipated applications for these films is wear resistance and tribological applications which are very much determined by the mechanical properties of the films and their integrity with the substrate. Due to time constraints in this project, where most of the time has been devoted to film fabrication, phase constituent characterization and process optimization, only the nanohardness, reduced-modulus of elasticity, and the film-substrate adhesion have been evaluated by nanoindentation and microscratch, respectively. Interpretation and discussion of these results is given in section 5.6.

4.6.1 Hardness & Reduced-Modulus Values of SS-N Films

Nanoindentation was done on SS-N films deposited at 300 °C with different % N_2 in the sputtering gas mixture. Table 4.2 shows the hardness values of the SS-N films. Interpretation and discussion of these results is given in section 5.6.

Table 4.2: Hardness & Reduced-Modulus values of various SS-N films deposited with varying % N_2 in sputtering gas mixture at 300 °C

Sample (%N_2)	At.% N	Hardness (GPa)	Reduced-Modulus (GPa)
0	0	7.7	202.4
5	0	8.3	216
10	20	8.9	174
25	33	8.5	195
50	50	9.3	159.3

In order to further study the mechanical properties of these films, another series of films were deposited on mild steel substrates and then tested by nanoindentation. Figure 4.50 shows the hardness plot of the SS-N films deposited on mild steel substrates at 300 °C with varying % N_2 in gas mixture. Figure 4.51 shows the load versus displacement curves of the indentation experiments done on the SS-N films.

ATTENTION: The Singapore Copyright Act applies to the use of this document. Nanyang Technological University Library

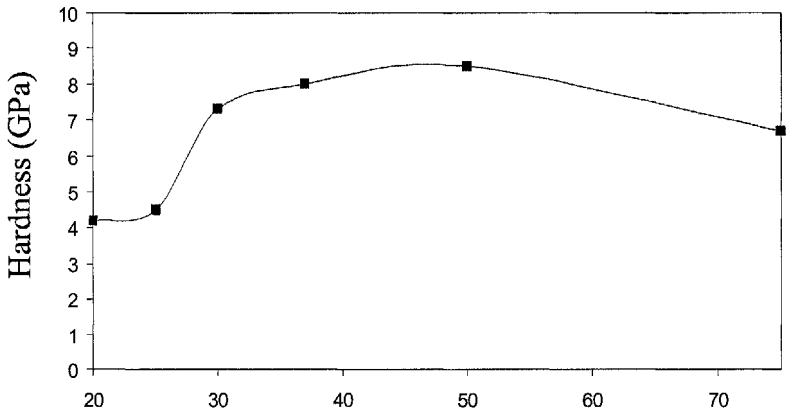


Figure 4.50: Hardness of the SS-N films deposited on mild steel substrates with different % N_2 in the sputtering gas mixture at 300 °C & with 2.2 Wcm^{-2}, 7 cm target-substrate distance

4.6.2 Mechanical Properties of MN Phase

As discussed in previous sections of this chapter, the films deposited at 300 °C with 50% N_2 and 75% N_2, constitute pure MN phases. Thus, these films were chosen for comparative studies on MN films formed under different conditions. The depth of penetration, for measuring hardness of all the samples, was fixed at 50 nm irrespective of the film thickness. Figure 5.51 shows the load versus depth curves of the MN films characterized by Nanoindentation and Table 4.3 summarizes the hardness values.

Table 4.3: Hardness values of various SS-N films

Sample	Phase Constituents	Hardness (GPa)
300° C-50% N_2	MN	9.3
300° C-75% N_2	MN	7.38

ATTENTION: The Singapore Copyright Act applies to the use of this document. Nanyang Technological University Library

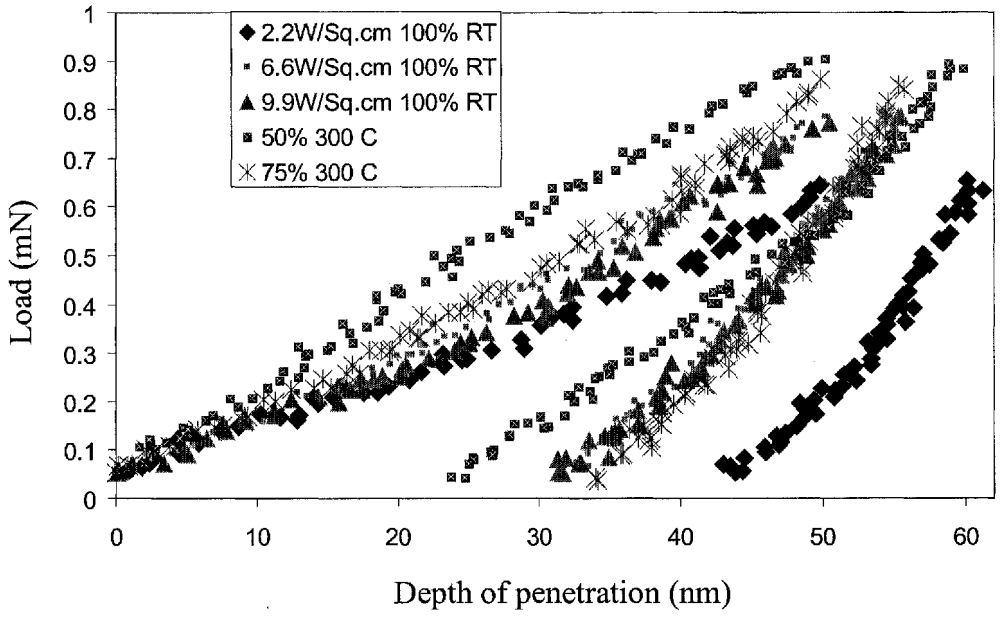


Figure 4.51: Load versus depth of indentation done on various MN films

4.6.3 Adhesion Properties of SS-N Films

Typical friction vs displacement plots from the scratch tests are shown in Figure 4.52, plotted against a secondary axis of linearly increasing load. The sharp increase in friction is due to the film failure which imposed resistance during crushing of the delaminated film. The critical load, (L_c) was determined from the friction curve as indicated by the arrows in Figure 4.52.

ATTENTION: The Singapore Copyright Act applies to the use of this document. Nanyang Technological University Library

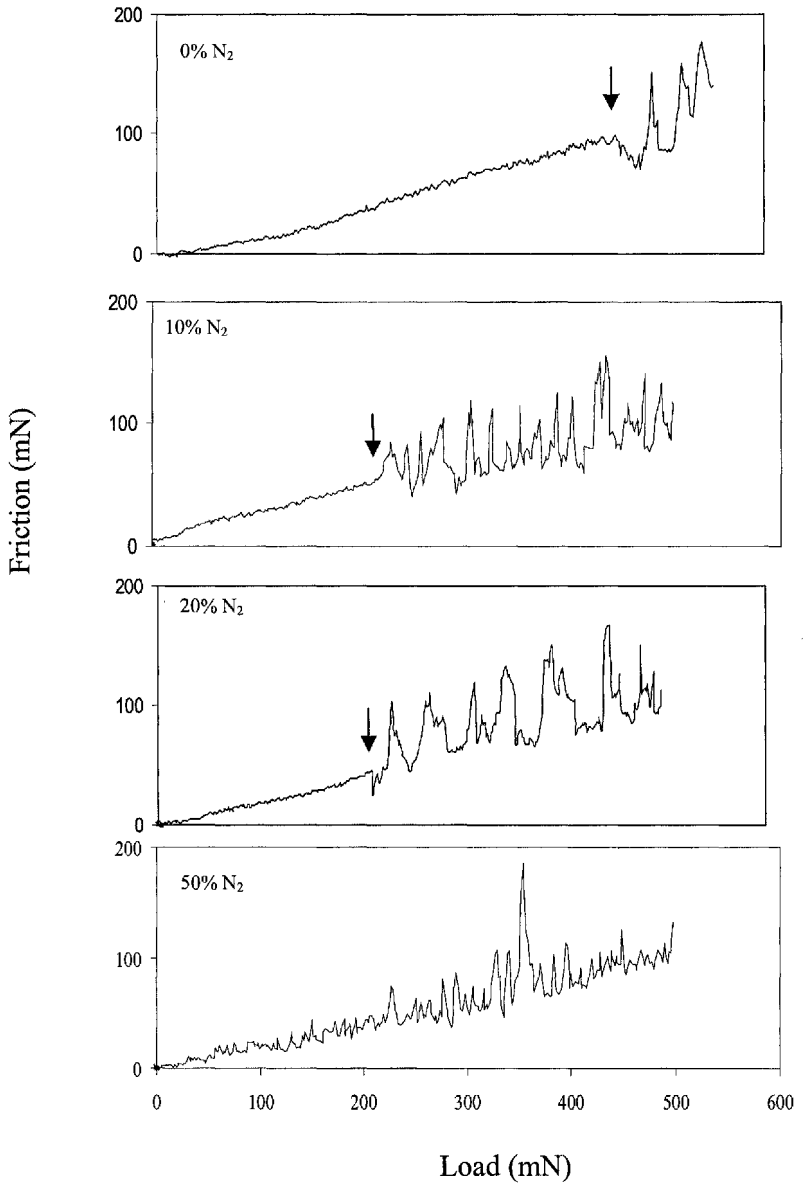


Figure 4.52: Friction versus load curves of the microscratch tests performed on various SS-N films

ATTENTION: The Singapore Copyright Act applies to the use of this document. Nanyang Technological University Library

4.7 MAGNETIZATION VALUES OF SS-N FILMS AT ROOM TEMPERATURE

To the best of our knowledge, no efforts have been made so far to investigate the magnetic behavior of sputter deposited SS-N films and the influence of nitrogen doping on magnetic behavior of iron based films with the help of vibrating sample magnetometer (VSM). Figure 4.53 shows the hysteresis plots of bare sample holder (Figure 4.53a) and various SS-N films (Figure 4.53b to f), deposited at 300 °C with various % N_2 in gas mixture and the films (Figure 4.53g and 4.53h) deposited on unheated substrates with 10% and 50% N_2 in gas mixture. Except the films corresponding to Figure 4.53b, c and g, all other films did not show magnetic moment higher than that of the sample holder. These magnetic films can be recalled from sections 4.2.1 and 4.2.2 to constitute at least traces of ferritic phase, while the other films constitute either pure expanded austenite or MN phase. This suggests that the γ_N phase and the MN phase are non magnetic at room temperature. Figure 4.54 (a) and (b) shows initial permeability curves, of the SS-N films deposited with 4 and 8 % N_2 respectively, plotted with an external magnetic field of 2000 Oe.

ATTENTION: The Singapore Copyright Act applies to the use of this document. Nanyang Technological University Library

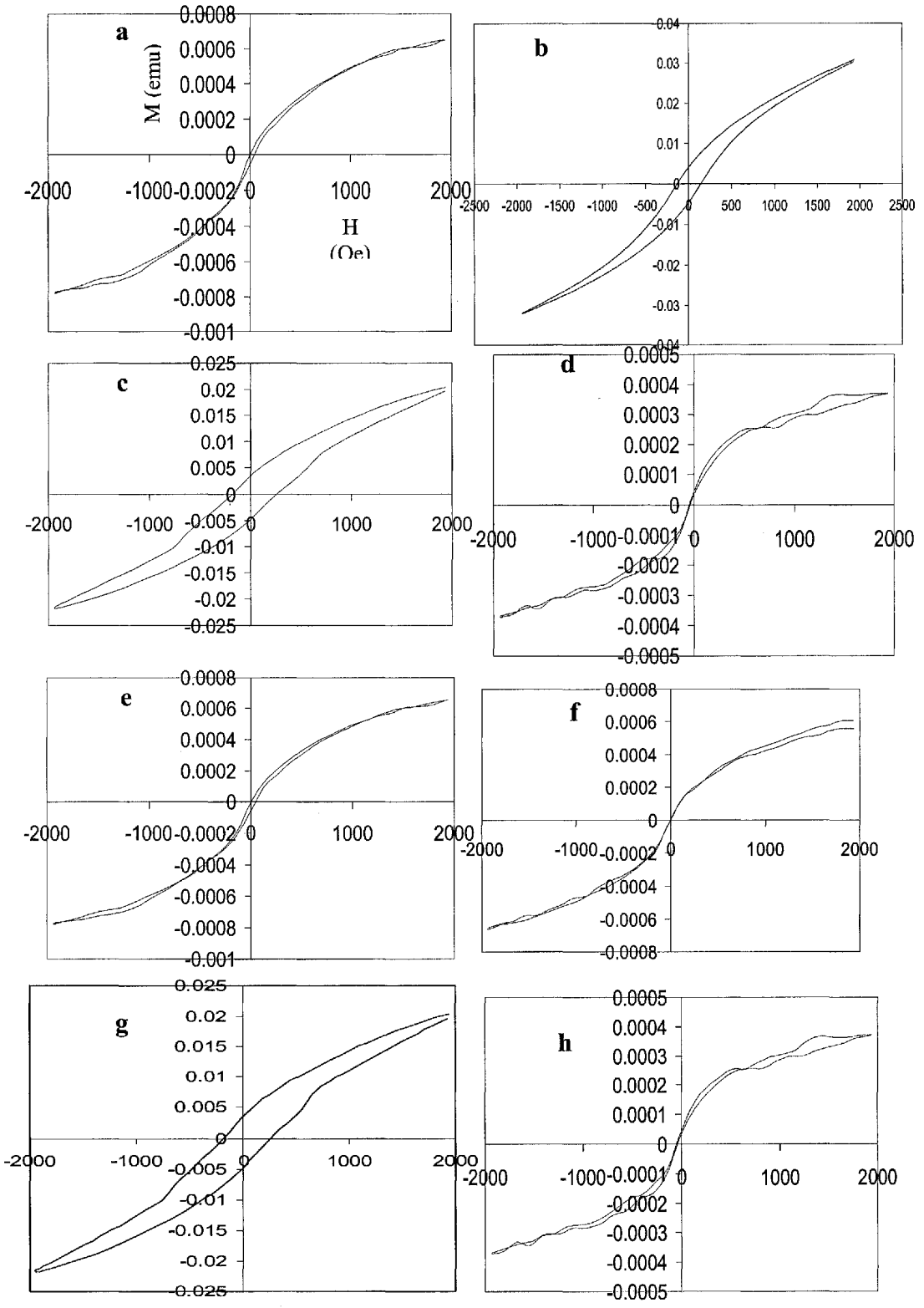


Figure 4.53: Magnetic moment (emu) vs magnetic Field (Oe) curves measured at room temperature for (a) Bare Holder, (b) 0, (c) 8, (d) 37, (e) 45, (f) 50, and on unheated substrates with % N_2 of (g) 10, and (h) 50

ATTENTION: The Singapore Copyright Act applies to the use of this document. Nanyang Technological University Library

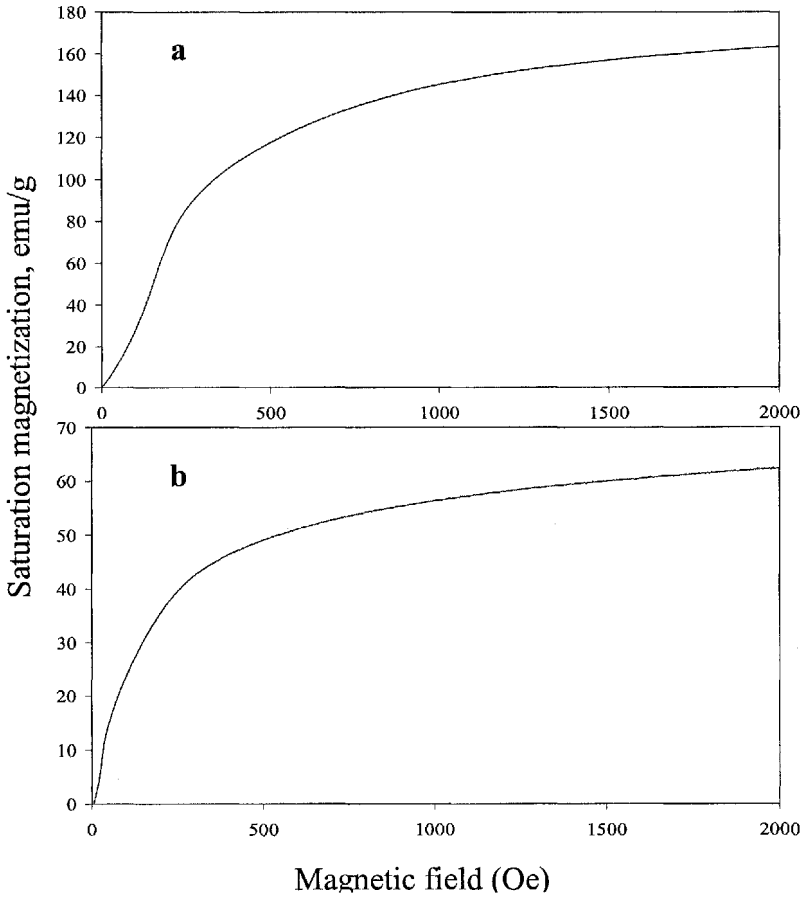


Figure 4.54: Initial permeability plot of the SS-N films deposited with (a) 4% N_2 and (b) 8% N_2 in gas mixture

ATTENTION: The Singapore Copyright Act applies to the use of this document. Nanyang Technological University Library

Chapter 5

DISCUSSION

5.1 NITROGEN INCORPORATION AND PHASE EVOLUTION

5.1.1 Nitrogen Incorporation

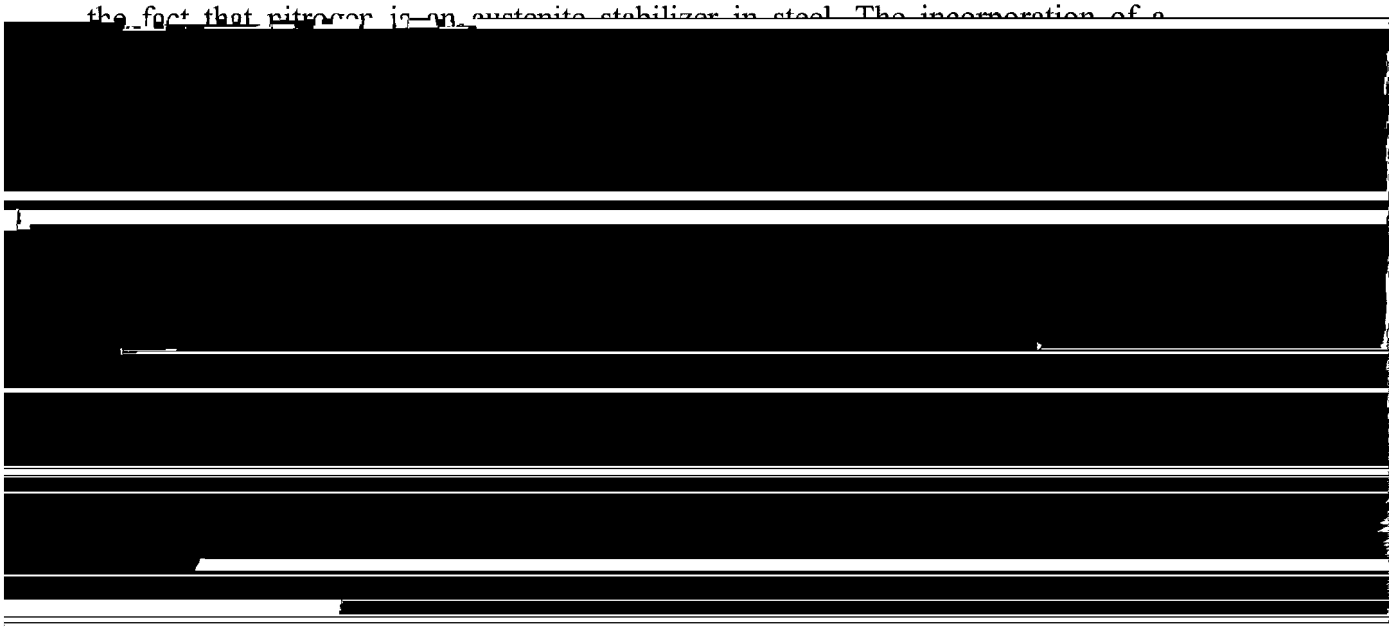
Formation of pure SS film with composition identical to that of the target agrees with the results of other investigators [50 and 52] that the multi element compositions of the bulk stainless steel can be successfully transferred to the substrate to form a film without dramatic stoichiometric changes. The incorporation of nitrogen in the film as a result of introduction of nitrogen gas to the sputtering atmosphere is influenced by several factors, including 1) available amount of nitrogen species in the atmosphere, 2) ratio of nitrogen and metal species arriving the film surface and 3) phase evolution and structural development in the film. As expected, in general nitrogen content incorporated in the film increases with $\%N_2$ in the atmosphere upto saturation value of 50 at.% in the MN film. But incorporation of nitrogen was detected only when a critical $\%\ N_2$ was exceeded such that the γ_N phase starts to form. This is obviously due to the fact that the BCC ferrite film formed with low $\%\ N_2$ could not dissolve too much of nitrogen. The reduction (Figure 4.4) in nitrogen content in the films with increasing power density could be explained by the increased flux of sputtered species, which resulted in the increased deposition rate, and the decreased time for the incorporation of nitrogen into the growing film before the arrival of another layer of atoms, in the gas mixture containing a constant nitrogen gas composition of 25% which favors the formation of γ_N. Such a trend was maintained in the films deposited with 100% N_2.

5.1.2 Phase Evolution

Several phases have been observed to evolve in the SS-N films depending on deposition conditions. These include ferrite phase, amorphous phase, the γ_N and the MN phases and the ζ-Fe_2N phase. The phase that is stable at room temperature for the same stainless steel elemental composition is austenite and thus the ferritic phase formed in the film is metastable. Formation of such a metastable ferrite is

ATTENTION: The Singapore Copyright Act applies to the use of this document. Nanyang Technological University Library

similar to the observations of other investigators and is the major stimulus for the investigation into stainless steel films for potential magnetic applications [88, 93-97]. The phenomenon of the formation of a BCC phase sputter deposited from an austenite target of similar elemental composition, can be explained by the high 'quenching rate' of the sputtered adatoms and the highly non-equilibrium nature of the deposition processes involved. Nevertheless, the exact reasons for the formation of such a metastable phase have been dealt with [33 and 98] but not conclusively. Nitrogen could not be efficiently incorporated in the film for $\%N_2$ as high as 8. Accordingly the constituent phase and the texture of the film also did not change. However, as nitrogen is efficiently incorporated in the SS-N film for $\%N_2$ of about 10, austenite starts to form and the lattice parameter of the austenite lattice was found to be 3.66 Å, which is about 2% larger than that of the bulk austenite phase (3.59 °A). This means that some amount of nitrogen atoms have been incorporated in the film, as evident from Figure 4.1 and that sufficient amount of nitrogen atom population is required to be in contact with the growing film for nitrogen incorporation. This phase transition from BCC to FCC is obviously due to the fact that nitrogen is an austenite stabilizer in steel. The incorporation of a



sufficient amount of nitrogen in the film not only stabilizes the FCC structure but also leads to the expansion of the FCC lattice.

When the $\%N_2$ is increased to as high as 25, three phases, i.e. amorphous phase, γ_N, and α-ferrite, were formed in the film deposited on unheated substrate. For a better understanding on the nature of the film growth it is necessary to determine the distribution of these phases across the thickness of the film. This was done by phase profiling across the film thickness by analyzing the GIXD patterns generated at different glancing angles of incidence. The depth of X-ray penetration ζ, across

ATTENTION: The Singapore Copyright Act applies to the use of this document. Nanyang Technological University Library

phase > ferrite phase > expanded austenite phase, with the increase in X-ray penetration depth. Based on the results in Figure 5.1, the distribution of the three phases in the film produced with 25% N_2 can be qualitatively depicted in Figure 5.2. The film can be divided into three zones i.e. amorphous rich at the film substrate interface, expanded austenite rich zone at the surface and the ferrite zone in between.

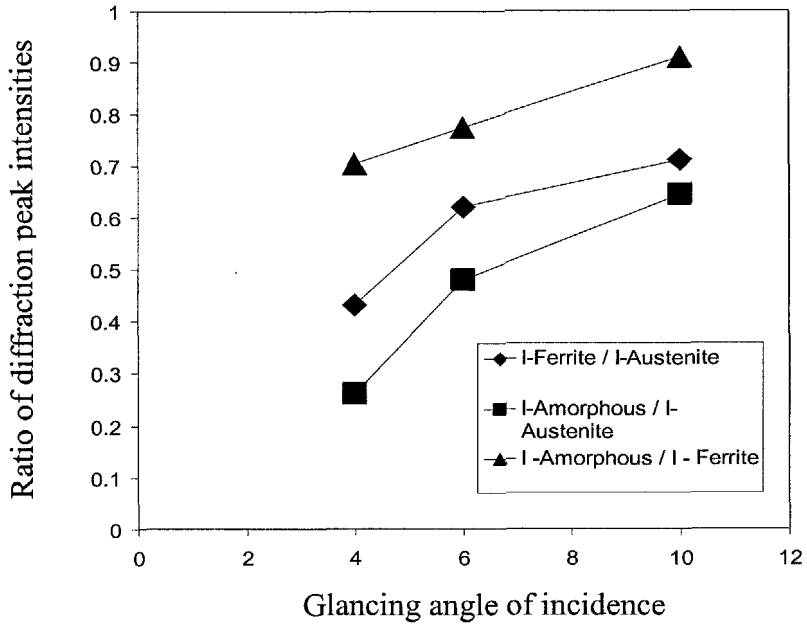


Figure 5.1: Relative XRD peak intensities of various constituent phases in the film deposited with 25% N_2 on unheated substrates

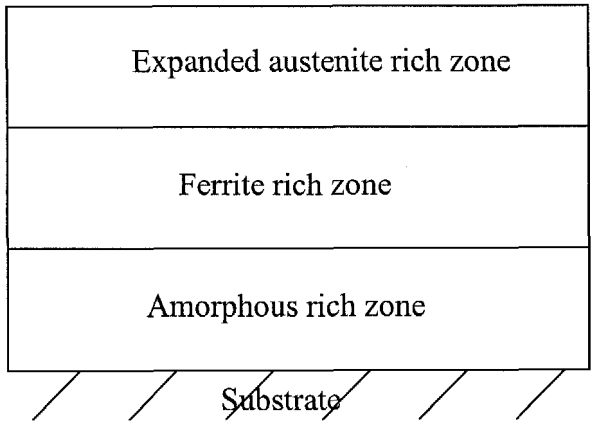


Figure 5.2: Schematic showing qualitatively the relative positions of various zones in the film deposited with 25% N_2 on unheated substrates

In connection to the formation of ζ-Fe_2N in the SS-N film deposited with 30% N_2 on unheated substrate, it should be recalled that the ζ-Fe_2N phase is an intermediate phase formed in the bulk nitrided sample due to poor solid state

ATTENTION: The Singapore Copyright Act applies to the use of this document. Nanyang Technological University Library

diffusion [2, 63]. The reason for the formation of such a phase is that it is a low temperature intermediate compound phase which does not require high thermal energy for its formation. In the present case the mobility of the adatoms should be sufficient for the crystalline phase formation while the deposition rate is low (Figure 4.40), allowing more time for atomic diffusion and arrangement before the next layer of deposition of atoms. In the film deposited with 40% N_2 on unheated substrate, along with the formation of crystalline ζ-Fe_2N phase, γ_N phase with characteristic FCC diffraction peaks was found. GIXD analysis of the as-deposited SS-N films showed consistently that the films with more than one crystalline phase showed relatively broad diffraction peaks. It can be inferred from this observation that the crystallinity of the phases formed and the film as a while is influenced by the phase constitution which is again dependent on the deposition process. The formation of the MN phase is evident with 50% N_2 and above in the gas mixture and on heated (300 °C) substrates (Figure 4.23). Table 5.1 summarizes the phase constituents formed in the films produced on unheated substrate and deposited at 300 °C with various nitrogen gas compositions in the atmosphere.

ATTENTION: The Singapore Copyright Act applies to the use of this document. Nanyang Technological University Library

Table 5.1: Phase constituents in various SS-N films deposited on Si (100) with varying % N_2, with 100W on unheated substrates

	Unheated substrate		Heated to 300 °C	
% N_2	Phases	'a' Å)	Phases	'a' (Å)
0	Ferrite		Ferrite	
5	Ferrite		Ferrite	
8	Ferrite		γ_N	3.61
10	γ_N	3.66 (γ_N)	γ_N	3.68
15	γ_N	3.67 (γ_N)	γ_N	3.68
25	γ_N + Ferrite + Amorphous	4.2 (γ_N)	γ_N	3.88
30	ζ-Fe_2N + Amorphous		γ_N + MN-trace	3.97
40/45	γ_N + ζ-Fe_2N + Amorphous (40% N_2)	4.32 (γ_N)	γ_N (major) + MN (minor) (45% N_2)	4.04 (γ_N)
50	γ_N	4.31	MN	4.32
100	γ_N	4.41	MN	4.32

5.2 NATURE OF THE γ_N AND MN PHASES

The MN nitride phase certainly possesses different characteristics from the expanded austenite phase. The MN phase is characterized in the present analysis by a characteristic GIXD pattern with consistent peak positions. The same MN phase was found to form with the increase in % N_2 to 75, as can be seen from Figure 4.23. The GIXD pattern can be seen to be identical as that of the film deposited with 50% N_2. The diffraction peak positions and the relative peak intensities did not change. Such consistency in the diffraction pattern of the SS-N films, deposited with % N_2 greater than 45, lead to the interpretation of the phase as a new Metal-Nitride type of stoichiometric phase rather than as extension of lattice in austenitic stainless steel – nitrogen solid solution. As mentioned earlier, such a phase has also been observed by Bourjot [48] and Dahm [33] earlier. On the other hand, expanded austenite, γ_N, gives different patterns owing to different at.% N, texture, and lattice distortion. Figure 4.24 shows the bright field TEM image and the electron diffraction pattern of the MN phase of the film deposited with 50% N_2. The electron diffraction pattern is characterized by sharp bright rings,

ATTENTION: The Singapore Copyright Act applies to the use of this document. Nanyang Technological University Library

which are characteristic of fine-sized strain-free, randomly oriented crystalline phase.

MN phase is a stoichiometric nitride phase unlike γ_N, as can be supported in the following way. There is a striking difference between the diffraction profile of MN and nitrogen expanded austenite. It can be seen from the Table 5.2 that unlike the peak positions of those of the γ_N phase, MN phase did not vary (within the experimental error of 0.032°, step of the diffractometer) from one deposition condition to the other. In disregard to the deposition conditions, all the identified MN phases showed identical diffraction profiles in terms of peak positions, relative degrees of line width (full width at half maxima).

Table 5.2: Bragg angles diffraction peaks corresponding to γ_N and the MN phases

	Deposition Condition	**Bragg angle (111)**	**Bragg angle (200)**	**Bragg angle (220)**
	100W, 100% N_2, RT	35.2	40.8	59.2
	300W, 100% N_2, RT	35.0	40.5	58.7

ATTENTION: The Singapore Copyright Act applies to the use of this document. Nanyang Technological University Library

the γN phase where the M:N ratio is fixed at 1:1. Due to this reason the interplanar spacing of γ_N cannot be the same as that of MN phase for all the planes. Further since the nitrogen dissolution is reported to occur preferably between certain crystal planes [12] the lattice dilation is not symmetric in all directions. Because of this reason, some Bragg angles of γ_N may perfectly match with those of MN phase but others may be shifted. Thus, there is no systematic change in all peak positions with increasing N dissolution, as is generally expected in random solid solution formation. The difference between Bragg angles of γ_N and MN phase is however small which makes it possible to use the diffraction data of γ_N to identify to identify MN phase too.

In order to gain a better understanding of the nature of the γ_N and the MN phase, further analysis is made in this section by examining the variation of the lattice parameter with nitrogen content in the films, lattice distortion, film texture and chemical states of nitrogen in the films evaluated by XPS.

5.2.1 Lattice parameter and Nitrogen Concentration

In order to have a clearer picture of the lattice parameter of the FCC γ_N phase and the FCC MN phase, the lattice parameter data collected for various γ_N and MN films produced under various conditions were plotted against the measured nitrogen concentrations in the films, as shown in Figure 5.3. The lattice parameter of bulk FCC austenite dissolved with nitrogen was calculated using Equation (2-2) present in section 2.2.1 [4].

$$a\ (Å) = a\ (Å) + 0.000861\ \text{at.\%}\ N \text{------(2.2)}$$

by extrapolating to higher nitrogen concentration. The calculated straight line is also plotted in Figure 5.3. It can be seen that the lattice parameter of the γ_N phase increases with increasing nitrogen concentration and almost follows the trend predicted by equation 4.2 for bulk nitrogen containing austenite. This strongly indicates that the γ_N phase is indeed a solid solution phase formed based on the original FCC austenite of the target material as solid solution supersaturated with nitrogen. The lattice parameter of the FCC γ_N phase is expected to increase linearly with increasing nitrogen concentration. This not only agrees with the prediction for stress-free bulk austenite which can dissolve up to 8.7 at.%N, but also agrees with

ATTENTION: The Singapore Copyright Act applies to the use of this document. Nanyang Technological University Library

the experimental results of other investigators [49 and 52]. However, the slight deviation of the a vs at.% N relationship from linearity at larger at.% N and the scattering of the data points may arise from existence of residual stresses in the films. Due to nitrogen incorporation and lattice expansion, large stresses inevitably develop in the γ_N films which would cause XRD peaks shifting and a change in lattice parameter measured by this technique. Nevertheless, the positive deviation of the lattice parameter suggests presence of tensile stresses in the expanded austenite and the MN phases unlike the results reported [33] previously. While it is typical of sputter deposition process to cause compressive stresses, the exact reasons for the tensile stresses in the phases encountered in the present case are unclear.

Another important observation that can be made from Figure 5.3 is that the lattice parameter of the cubic MN phase with around 50 at.% N does not follow the trend of the γ_N phase, but increases abruptly. This suggests that the MN phase is not a solid solution phase and that the MN phase is indeed different from the γ_N phase by nature.

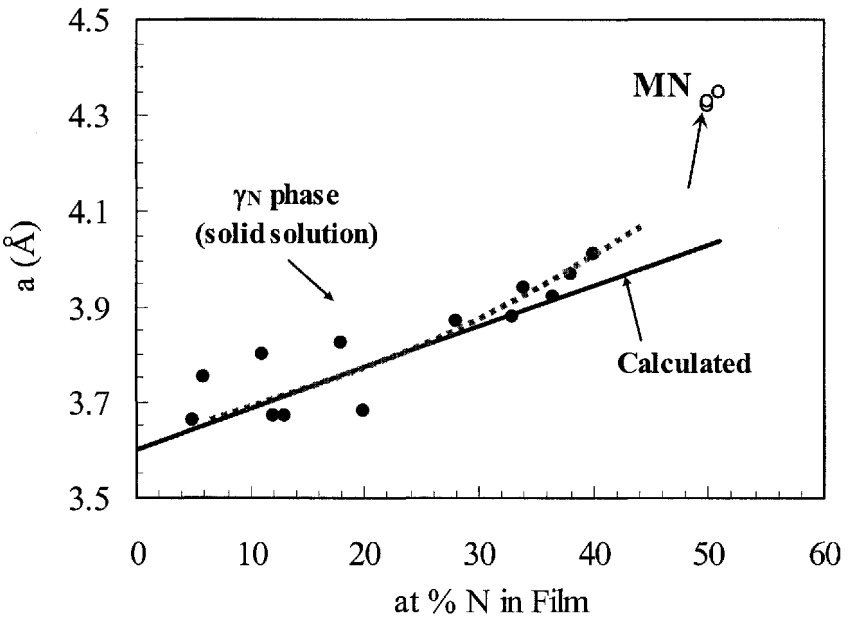


Figure 5.3: Variation of lattice parameter with nitrogen concentration in the FCC γ_N and MN phases formed in the SS-N films deposited at 300 °C, 100W and 7 cm target-substrate distance

ATTENTION: The Singapore Copyright Act applies to the use of this document. Nanyang Technological University Library

5.2.2 Lattice Distortion

It has been well documented that the nitrogen expanded austenite phase (γ_N) produced by low temperature nitriding processes has a FCC structure, but with distorted lattice [40]. It was frequently observed that the shift of the XRD peaks to lower Bragg angles is more significant along the (200) peak than for the (111) peak, suggesting that lattice expansion is more significant in the direction perpendicular to (200) planes than to the (111) planes. Such a phenomenon has also been observed in the present study for the γ_N films. Attempts have been made to characterize the lattice distortion by plotting a_{hkl} versus $\cos^2\theta/\sin\theta$ for each γ_N and MN films, where a_{hkl} is the lattice parameter calculated from each individual (hkl) reflection peaks, and 2θ is Bragg angle. The a_{hkl} values were plotted against $\cos^2\theta/\sin\theta$ because a_{hkl} values vary with a gradient of $\cos\theta.\cot\theta$ due to the linear increase in error in the determination of diffraction peak position ($2\theta_B$) with respect to 2θ. For a distortion-free cubic phase, such a plot should be linear with all data points neatly falling on a straight line. Scattering of the data points around the square-root fitted line indicates lattice distortion [40].

Figure 5.4 shows such plots for selected γ_N and MN films. It can be seen that the MN phase is nearly distortion-free since all data points neatly fall on the straight line, whilst the γ_N phase exhibits some lattice distortion, particularly along the (111) and (200) planes.

ATTENTION: The Singapore Copyright Act applies to the use of this document. Nanyang Technological University Library

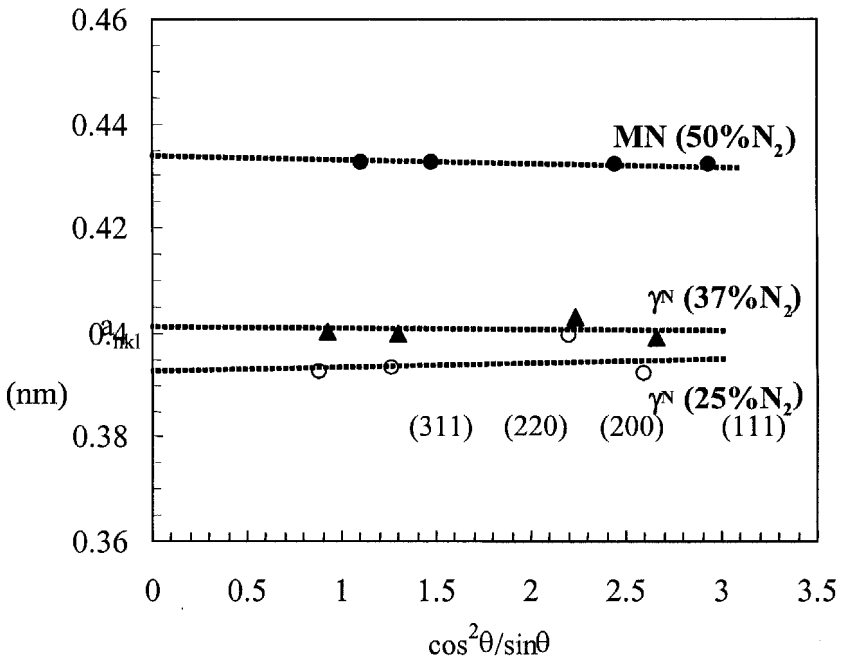


Figure 5.4: Plot of a_{hkl} versus $\cos^2\theta/\sin\theta$ of γ_N and MN phases from selected films

Unfortunately, the XRD patterns from most of the γ_N films in this work do not show enough number of peaks for the analysis, shown in Figure 5.4. Thus, another parameter was used as the lattice distortion index (LDI) which is determined by subtracting the ratio of interplanar spacing of (111) to that of (200) plane of distortion-free FCC sample from that of the γ_N phase and MN phases produced in this work. i.e.

$$\text{Lattice Distortion Index (LDI)} = [d_{(111)}/d_{(200)}]_{\gamma N \text{ or MN}} - [d_{(111)}/d_{(200)}]_{\text{standard}}$$
$$= [d_{(111)}/d_{(200)}]_{\gamma N \text{ or MN}} - 2/\sqrt{3} \quad \text{----------(4-3)}$$

A positive LDI value refers to larger lattice expansion perpendicular to (111) planes than to the (200) planes. Table 5.3 summarizes the calculated LDI values from the XRD patterns of the γ_N and MN phases. It can be seen that almost all LDI values are negative, thus the (200) planes are expanded more than the (111) plane in the γ_N and MN phases. But the absolute LDI values found for the MN phase are extremely small, indicating the distortion-free nature of this phase, in agreement with the result shown in Figure 5.4. On the other hand, the absolute LDI values for the γ_N phase can be an order of magnitude larger than those for the MN phase. This

ATTENTION: The Singapore Copyright Act applies to the use of this document. Nanyang Technological University Library

proves again that the expanded austenite (γ_N) phase can have a distorted FCC lattice where the degree of distortion seems to be affected to some extent by process conditions, as shown in Table 5.3, whereas the MN phase always keeps up a distortion free FCC lattice.

Lattice distortion of the γ_N phase produced by low temperature nitriding has been analyzed and explained by several investigators [12, 39 40, 41 and 99]. Two origins have been considered, including residual stress and lattice disorder such as formation of stacking faults in FCC structure. In general, in XRD analysis, lattice strains and nanograins (microstresses) would lead to broadening of XRD peaks while internal macrostresses would lead to shift of positions of the XRD peaks. The direction and degree of peak shift depend on the sense and magnitude of the stress, as well as the elastic constant of the crystal in the lattice direction concerned. For example, compressive internal stresses will shift all the diffraction peaks to lower angles, leading to lattice expansion. However, if the crystal is elastically anisotropic, then the degree of shift of each individual peak will be different. This will result in the scatter of the data points around the corrected line in the $a_{(hkl)}$ against $\cos^2\theta/\sin\theta$ plot, as shown in Figure 5.4 and increased absolute value of LDI .

Similarly, the formation of lattice defects, such as stacking faults or residual internal elastic microstresses may lead to the modifications of the normal stacking of matrix planes and thus influences not only the profiles (peak broadening) but also the position (peak shift) of XRD peaks. This will result in the shift of the FCC (111) peak towards a higher angle and the (200) peak towards a lower angle, and thus larger lattice expansion along the (200) planes. Unfortunately, the lack of sufficient reflection peaks from most γ_N films prevented further detailed analysis as to which of these factors contribute to lattice distortion in the present case.

ATTENTION: The Singapore Copyright Act applies to the use of this document. Nanyang Technological University Library

Table 5.3: Lattice Distortion Index for various SS-N films

Sample		LDI	Phase
RT	% N_2		
	40	-0.00438	Expanded austenite
	50	-0.00399	Expanded austenite
	100	-0.00425	Expanded austenite
300 °C			
7 cm			4 cm
50	0.005859	MN	25	-0.01561	Expanded austenite
100	-0.00246	MN			
25	0.00495	Expanded austenite	40	-0.00712	MN
30	-0.01522	Expanded austenite	50	0.001872	MN
37	-0.01574	Expanded austenite	75	-0.00021	MN

5.2.3 Analysis of Chemical States by XPS

In order to study further the nature of the γ_N and MN phases, selected samples were analyzed by XPS. Due to the limitations on the working conditions of the XPS instrument, the analyses were done on the as-deposited surface without any sputter cleaning. Figure 5.5 shows the obtained Cr2p and N1s spectra for the pure stainless steel films, the γ_N and MN films produced at 300 °C with 25% N_2 and 50% N_2 respectively. Whilst, Table 5.4 summarizes the binding energies for Cr2p 2/3 and N1s.

XPS analysis not only gives information on chemical compositions of the analyzed surface, but also provides information on chemical binding states of the constituent elements in the form of the binding energies. In general, elements in the free (metallic or solid solutions) states have lower binding energies, whilst the same element in a compound state such as nitride and oxide has higher specific binding energies. From Figure 5.5a and Table 5.4, it can be seen that the Cr2p in pure SS film and γ_N film has very similar spectra and binding energies. The binding energy of 576.1eV could be attributed to chromium oxide state, obviously due to the native oxide film on the film surface which was not sputter cleaned during the XPS

ATTENTION: The Singapore Copyright Act applies to the use of this document. Nanyang Technological University Library

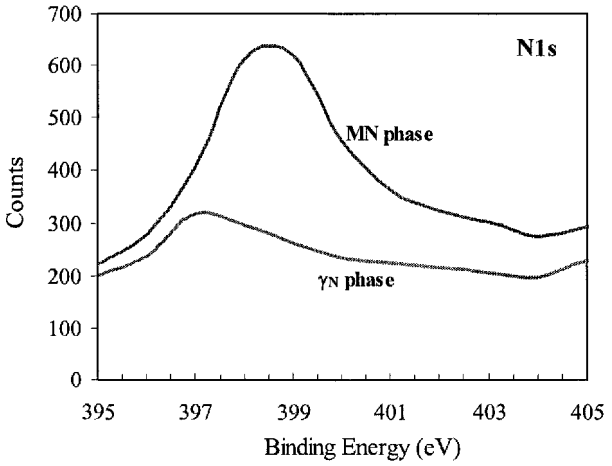
analysis. Difference in the Cr2p spectrum was noticed in the MN film where the spectrum shows two peaks, one corresponding to the oxide state (576.2 eV), similar to that found for the other two films. The peak with higher energy (577.19 eV) could thus be attributed to the chemical state of chromium in MN phase, which is obviously in a strongly bonded compound state i.e. nitride state.

Table 5.4: Summary of binding energy or Cr2p 2/3 and N1s, and possible bonding state Cr and N in pure SS, γ_N and MN phases

Phases	**Cr2p 2/3 (eV)**	**Cr bonding**	**N1s (eV)**	**N bonding**
Pure SS	576.1	Cr-O	N/A	N/A
γ_N	576.1	Cr-O	397.2	In solid solution
MN	576.2, 577.9	Cr-O, Cr-N	398.3	Cr-N

From the N1s spectra shown in Figure 5.5b, it can be seen that binding energy of N in the γ_N phase is lower than that in the MN phase. This suggests that N in the γ_N phase is indeed in a free-state (with low energy), i.e. in solid solution of the FCC lattice. On the hand, the higher binding energy of N in the MN phase strongly suggests that N is in the nitride-state. The XPS results thus further support previous

ATTENTION: The Singapore Copyright Act applies to the use of this document. Nanyang Technological University Library



(b)

Figure 5.5: XPS spectra of (a) Cr2p 2/3 and (b) N1s from various phases indicated. The pure SS film was produced on unheated substrates with pure argon, and the γ_N and MN phases were produced at 300 °C with 25%N_2 and 50%N_2, respectively

5.2.4 Summary

From the results and discussion presented, it can be summarized that the γ_N phase has the following characteristics:

(a) It is a solid solution phase supersaturated with nitrogen

(b) It has a distorted FCC structure

(c) It can dissolve various amounts of nitrogen upto 40 at.%

(d) Its lattice parameter increases with increasing nitrogen content.

(e) Its lattice is expanded along the directions perpendicular to (200) plane more than the (111) plane.

It is also clear that the MN phase has the following characteristics:

(a) It has an ideal FCC crystal structure, with a characteristic XRD pattern

(b) It is a nitride compound phase, with M = Fe + Cr + Ni + Mo.

(c) It has a equiatomic composition, i.e. confining to the MN stoichiometry and thus the cation to anion ratio is approximately one.

Such a MN type nitride with FCC structure can have two possible cation–anion coordination configurations: they are either octahedrally coordinated in the NaCl-type structure or tetrahedrally coordinated in the zine blende (ZnS)-type structure [100]. From the information gathered so far from XRD and TEM, it is difficult to

ATTENTION: The Singapore Copyright Act applies to the use of this document. Nanyang Technological University Library

distinguish unambiguously whether the new MN phase has NaCl- or ZnS-type lattice structure. However, further discussion can be made with reference to the new cubic FeN iron nitride phase discovered in sputtered Fe–N films [68, 70 and 101].

As discussed in section 2.4, the Fe–N system has been well known for a long time, particularly at the nitrogen-poor side, where many nitride compounds exist [102], but phases at the nitrogen-rich side are less well known. However, the Fe–N phase diagram has recently been extended and there are indications of a cubic FeN phase with equiatomic composition, which was found in reactively sputtered Fe–N films [68 and 70]. Although many transition metal nitrides such as CrN and TiN have NaCl-type lattice structure, based on Conversion Mossbauer spectra analysis [68 and 70] and theoretical lattice parameter calculation [103], the FeN phase was found to have two sublattices, one belongs to the ZnS-type (γ'-FeN) with a lattice parameter around 0.435 nm, and the other belongs to the NaCl-type (γ''-FeN) with a lattice parameter around 0.452 nm. In the MN phase found in this work, although the cation (M) has a mixed composition corresponding to that of the bulk stainless steel (FeCrNiMo), based on the lattice parameter (0.432 – 0.435 nm) measured from XRD and electron diffraction, it is believed that the (FeCrNMo)N phase should have the ZnS-type lattice structure, similar to the ZnS-type γ'-FeN phase formed in sputtered Fe–N films. This also suggests that structural similarity exists between the cubic FeN phase discovered previously and the cubic MN phase. It is thermodynamically viable that some of the Fe cations in FeN can be substituted by other cations like Cr, Ni and Mo to form the MN phase. The fact that the same MN phase was formed at both 300 °C and on unheated substrates suggests that the thermal activation required for this phase formation is minimal. It seems that sufficient amount of % N_2 in the atmosphere to ensure incorporation of 50 at.% N in the film is the most essential requirement for the MN phase formation. It should be noted that the MN phase formed consistently disregard of the surface characteristic of the substrate. To prove this, two types of Si substrates, Si (100) and Si (111) were used for further deposition with 50% N_2, substrates being sputter cleaned before deposition. Figure 5.6 shows the GIXD patterns of the films formed on these substrates. On the basis of these results it can be understood that nature of

ATTENTION: The Singapore Copyright Act applies to the use of this document. Nanyang Technological University Library

substrate does not influence the MN phase evolution in the SS-N films. In general, such independence on the nature of substrate allows for flexibility in process optimization in favor of the phase of interest.

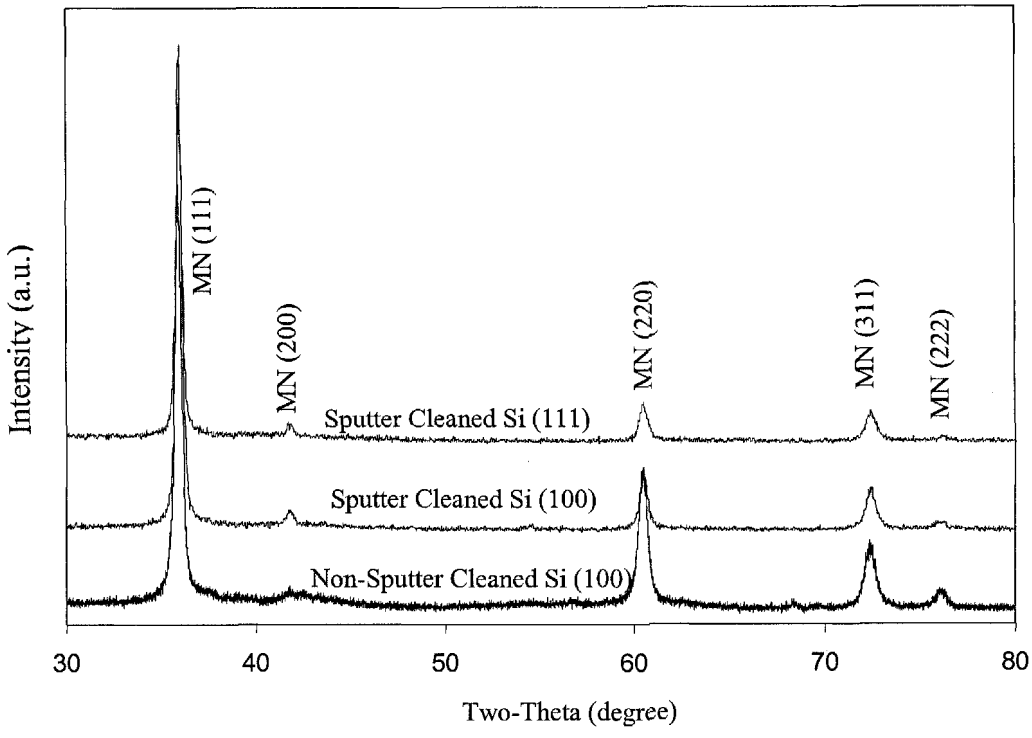


Figure 5.6: GIXD patterns of SS-N films deposited on various substrates at 300 °C with 50% N_2 & 100W

5.3 FACTORS AFFECTING THE FORMATION OF γ_N AND MN PHASES

Amongst the phases of the SS-N system, the expanded austenite phase (γ_N), provides a range of attractive properties as discussed in detail in chapter 2. The properties of the films depend on nitrogen content and microstructure, which in turn depend on the deposition process conditions [79]. However, negligible efforts have been made previously to understand the influence of reactive sputter deposition conditions on the expanded austenite phase formed in the SS-N films. In addition, the formation of the cubic MN nitride phase also deserves further studies in relation to various deposition parameters. Further studies have thus been made in this work to investigate the influence of other processing parameters on the formation of the γ_N and MN phases. The combined understanding on the influences of each of the deposition process parameters provides improved insight into the nature of the formation of the γ_N and MN phases and the film growth.

ATTENTION: The Singapore Copyright Act applies to the use of this document. Nanyang Technological University Library

5.3.1 Influence of Substrate Temperature on γ_N Phase Formation

As discussed in section 5.3.1, despite the availability of nitrogen in the sputtering gas mixture with 25% N_2, crystalline γ_N phase did not form in the film produced on unheated substrate. Instead, an amorphous-like phase together with a small amount of crystalline metastable ferrite phase formed in the film. The bcc ferrite (110) peak shifted to lower Bragg angle, suggesting some amount of nitrogen incorporation, causing lattice expansion of the ferrite phase (Figure 4.8). Figure 5.7 shows the variation of nitrogen concentration in film and the lattice parameter of the γ_N phase, as a function of deposition temperature. The amount of nitrogen incorporated in this film is the largest (~ 40%) amongst all the films of this set, most of which must be trapped in the metastable amorphous phase, since the crystalline ferrite phase can dissolve only a small amount of nitrogen.

When the temperature is increased to 150°C, broad peaks corresponding to the γ_N phase appeared along with the ferrite peak. The amount of nitrogen incorporated in the film was reduced to 36 at%. The thermal energy provided by the increased substrate temperature obviously caused easier dissolution of nitrogen into the austenite lattice. The broadness of the reflection peaks from the γ_N phase indicates the nanocrystalline nature of this film, suggesting that the thermal energy was not sufficient for grain growth in the γ_N phase. The fine grain microstructure of the expanded austenite in this film is also supported by TEM examination shown in Figure 4.26.

A single γ_N phase film formed when the temperature was increased to 300°C, as evidenced by both XRD analysis (Figure 4.17a) and TEM analysis (Figure 4.18). The nitrogen concentration in this single γ_N phase film further reduced to 34 at%, which is also reflected in the reduced lattice parameter (Figure 5.7) as compared to that of the γ_N phase formed at 150 °C. When the substrate temperature was further increased to 400 °C, the single γ_N phase film resulted. The peaks corresponding to the expanded austenite became narrower suggesting growth in the crystallite size. But the nitrogen concentration in this single phase γ_N phase film is similar to that produced at 300 °C (34 at%), in agreement with the similar lattice parameter of the γ_N phase for these two films. It is to be noted that no other phase formed in the

ATTENTION: The Singapore Copyright Act applies to the use of this document. Nanyang Technological University Library

films at 400 °C, undermining the possibility of annealing effect, which otherwise would cause decomposition or precipitation into product phases. When the substrate temperature was further increased to 500 °C, CrN was found in the film, together with the γ_N phase which contains much reduced nitrogen content, as evident by the shift of the γ_N phase peaks to higher Bragg angles. The overall nitrogen concentration in this film is further reduced to 29 at%. Thus the stability temperature of the metastable γ_N phase must be around 450 °C, similar to that found for low temperature nitriding of stainless steels [36].

It can be seen that with a constant % N_2 in the atmosphere, the concentration of nitrogen incorporated in the film decreases with increasing temperature. The amorphous-like film on unheated substrates has the highest nitrogen concentration, while the predominant CrN film at 500 °C has the lowest nitrogen concentration. It should be noted that the two single γ_N phase film at 300 °C and 400 °C have similar nitrogen concentration. As expected, the variation of γ_N phase lattice parameter with temperature is similar to that of nitrogen concentration.

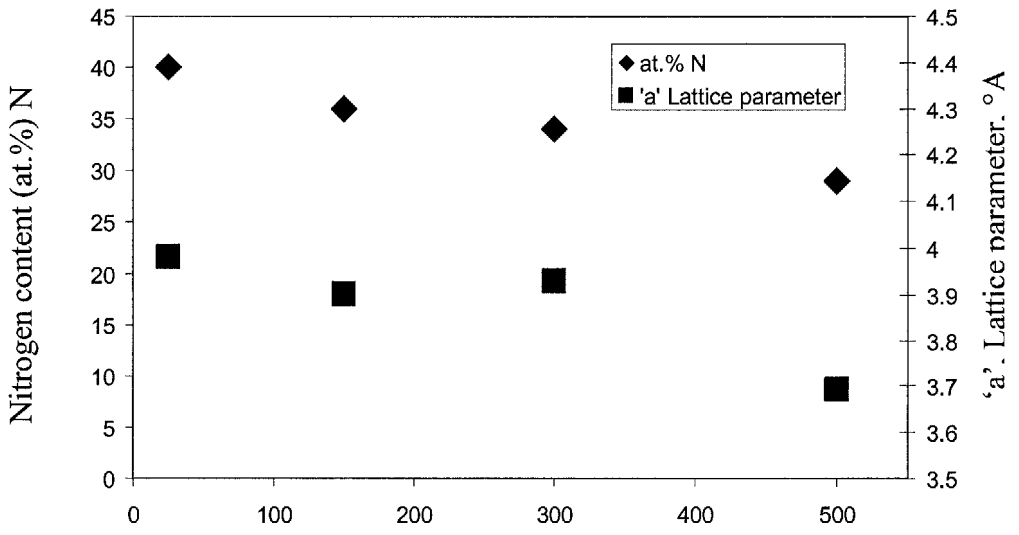


Figure 5.7: Nitrogen contents and lattice parameters plotted for various substrate temperatures of the films deposited with 25% N_2

5.3.2 Influence of Target-substrate Distance on Phase Formation

Several noticeable effects arising from the shortened target-substrate distance were observed. Firstly, the deposition rate increased obviously due to the decreased

ATTENTION: The Singapore Copyright Act applies to the use of this document. Nanyang Technological University Library

number of scattering events of sputtered species with the gaseous species. Secondly, both the films showed nanocrystalline, expanded austenite phase with different nitrogen content. The shift in the diffraction peaks of the film deposited with 40% N_2, towards lower Bragg angles in comparison to the film deposited with 25% N_2, suggests greater lattice expansion of expanded austenite in the former. While the absence of ζ-Fe_2N can be attributed to the increased adatom-mobility with decreasing target-substrate distance, it is interesting to note that nitrogen content in the film did not decrease with the increase in deposition rate. It should be recalled that the extent of nitrogen incorporation depends on % N_2 and deposition rate, as discussed in section 5.1. However, in the present case the increase in exposure of the growing film to N_2 gas compensated for the effect of increase in deposition rate, thus favoring the maximum possible nitrogen incorporation in the film. The nitrogen dissolution in the expanded austenite phase is about 40 at.% in the film deposited with 40% N_2, irrespective of target-substrate distance and deposition rate. Thirdly, the resultant γ_N phase film became textured with strong (200) orientation as can be seen from the XRD patterns which show that the (200) peak is the strongest (Figure 4.34. However, this texture in the γ_N phase decreases with increasing nitrogen gas composition from 25% to 40%. This is probably due to the decrease in energy of sputtered species as a result of the increase in nitrogen gas composition in the gas mixture.

5.3.3 Influence of Deposition Power Density on γ_N Phase Formation

Power density has a significant effect on the evolution of the γ_N phase. At a low power density of 2.2 Wcm^{-2}, the film deposited on unheated substrate with 25% N_2 is predominantly amorphous (Figure 4.8), but increasing the power density to 4.4 Wcm^{-2} and 6.6 Wcm^{-2}, the γ_N phase became crystalline and the amount of ferrite phase was reduced. Further increasing the power density to 9.9 Wcm^{-2}, the film produced contains a single crystalline γ_N phase. From Figure 4.31, it is also clear that the reflection peaks from the crystalline γ_N phase are shifted to higher Bragg angles with increasing power density, indicating reduced lattice parameter. Chemical composition analysis indeed confirmed that the amount of nitrogen incorporated in the film decreases with increasing power density. Figure 4.4a shows the variation of nitrogen concentration of the γ_N phase with power density. The reason for the reduction in at.% N in film has been discussed in section 5.1.1.

ATTENTION: The Singapore Copyright Act applies to the use of this document. Nanyang Technological University Library

From the above results, it is clear that the crystallinity of the film depends not only on substrate temperature, but also on sputtering power density. Low temperature and low power density deposition favors the formation of amorphous γ_N phase in the film, but in all cases, the ferrite phase formed (if any) is always crystalline. In general, the crystallinity of deposited thin films depends on adatom mobility which depends on substrate temperature and the kinetic energy of the sputtered species. In addition, the incorporation of nitrogen is known to decrease the energy and mobility of iron adatoms [20, 104, 105 and 106]. The formation of amorphous γ_N phase on unheated substrate at low power density can thus be explained by the combined effect of low thermal energy, low adatom energy and mobility arising from the low sputtering power and more importantly the incorporation of large amount of nitrogen in the film. Increasing substrate temperature and sputtering power increases the thermal energy and kinetic energy of the adatoms respectively and thus favors the evolution of crystalline γ_N phase. On the other hand, formation of crystalline ferrite, even at room temperature and with low sputtering power density, is not hindered due to the low solubility of nitrogen in ferrite.

In addition to the studies on power density for depositions with 25% N_2, deposition with 100% N_2, which favors the formation of γ_N phase, was also chosen for similar studies. Figure 4.33 shows the GIXD patterns of the films deposited with different power densities for 100% N_2. The cubic γ_N phase with similar diffraction peaks, was found consistently with all the films. This indicates that although the deposition rate increased with increase in power density as shown in Figure 4.4b, it only slightly affected the amount of nitrogen incorporated in the film produced in pure nitrogen atmosphere, in contrast to the films produced with 25% N_2 in the atmosphere, discussed above. However, from Figure 4.32 it can also be seen that the peaks shifted slightly to lower Bragg angles with the increase in power density, although the nitrogen content in the film slightly decrease with increasing power density.

5.3.4 Influence of Substrate Temperature on MN Phase Formation

From section 4.2.1 and 4.2.2, it is clearly seen that MN phase films are formed at both room temperature and 300 °C with 50-100% N_2 in the sputtering atmosphere.

ATTENTION: The Singapore Copyright Act applies to the use of this document. Nanyang Technological University Library

Further studies have been carried out at higher substrate temperatures (400 °C to 500 °C), keeping all other parameters unchanged. It can be seen that the MN phase formed in the SS-N film deposited with 50% N_2 up to the temperature as high as 400 °C as evident from the GIXD pattern shown in Figure 4.27 This temperature is the maximum deposition temperature for the formation of the MN phase. It should be noted that the maximum deposition temperature need not be the same as decomposition temperature, as discussed later. The lattice parameter of MN phase is about 4.33 °A, similar to that produced at 300 °C discussed previously. However, a small amount of nitrogen-free ferrite phase in the film leads to a reduction in nitrogen concentration in the film (Figure 5.9). The maximum deposition temperature of 610 K [66] for 1:1 stoichiometric cubic FeN phase, reported in sputter deposited FeN films, is much lower than the present destabilizing temperature of 673 K for the MN phase. When the substrate temperature was increased to 450° C, expanded austenite (γ_N) formed in the film together with Cr_2N and ferrite. This indicates that the MN phase is unstable above 400 °C. With further increasing temperature to 500 °C, the formation of ferrite and Cr_2N is more obvious. This is accompanied with a further decrease in nitrogen concentration in the film (Figure 5.9), obviously due to the increase in the amount of nitrogen-free ferrite. It is interesting to note that the expanded austenite (γ_N) was found in the films produced at 450 °C and 500 °C. This indicates that the γ_N phase has a better thermal stability than the MN phase. However, it is unlikely to produce a single γ_N phase film at temperatures above 400 °C because the thermodynamically more stable phases such as Cr_2N and ferrite also form in the film. The precipitation of Cr_2N in the films produced at 450 °C and 500 °C was also confirmed by electron diffraction analysis, shown in Figure 4.33. By reducing the X-ray glancing angle, i.e. reducing the X-ray penetration depth, it was found that the Cr_2N precipitation actually occurred close to the film – substrate interface as can be understood from the absence of the diffraction peak (corresponding to Cr_2N at Bragg angle of 37.728) in the GIXD pattern of 3.5° glancing angle, as shown in Figure 5.8. Figure 4.31 shows the variation of nitrogen concentration with temperature.

ATTENTION: The Singapore Copyright Act applies to the use of this document. Nanyang Technological University Library

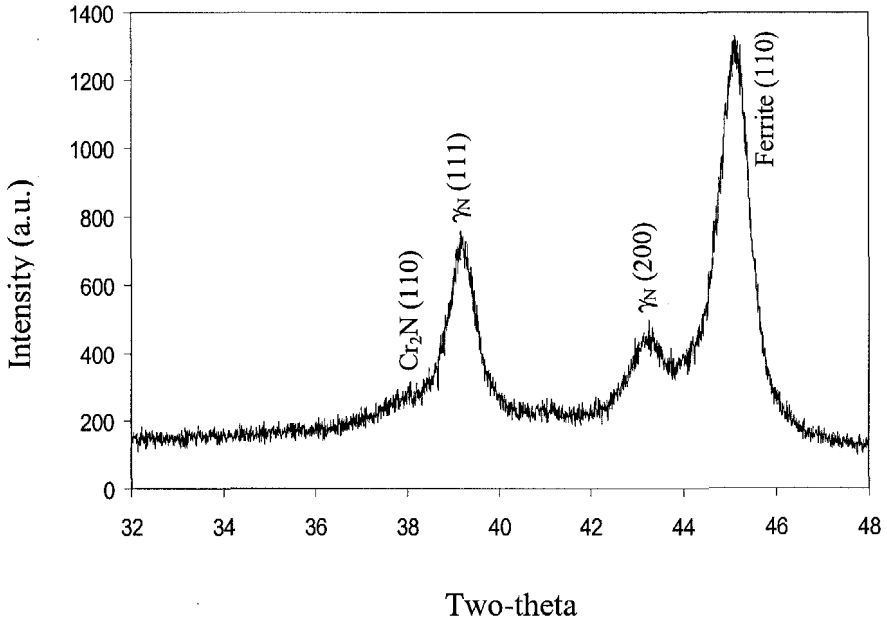


Figure 5.8: GIXD patter obtained with 3.5° glancing angle for the film deposited at 500° C with 50% N_2, 2.2Wcm^{-2} and 7 cm target-substrate distance. The film shows very shallow diffraction peak corresponding to Cr_2N

5.3.5 Influence of Substrate Bias on the MN Phase Formation

Figure 5.39 shows that with the application of substrate bias during deposition under similar conditions that favor MN phase formation without bias, the phase constituent of the films changed significantly. Surprisingly, no MN phase was found in the film under the biasing conditions. Instead, Cr_2N became the major

[redacted]

constituent in the film, together with a small amount of γ_N phase. The intensity of the strongest peak, corresponding to (111) plane of expanded austenite, decreased with increasing bias power from 100 to 300 W. With the increase in bias power, the peak intensity of the crystalline Cr_2N phase in the films is reduced probably due to the interruption of nucleation and growth of the phase by energetic bombarding ions. The results suggest that under the present experimental conditions, increasing the adatom energy by biasing and sputtering of the growing film prevent the formation of the MN phase and favors the formation of the more stable Cr_2N and γ_N phase. This also suggests that the MN phase is indeed metastable, as it decomposes with increasing adatom energy and at increased temperatures, as discussed in the next section.

ATTENTION: The Singapore Copyright Act applies to the use of this document. Nanyang Technological University Library

5.4 THERMAL STABILITY OF THE γ_N AND MN PHASES

The effect of deposition temperature on γ_N phase and MN phase evolution has been discussed in the previous section. The stability of these two phases was further studied annealing the film in vacuum at 500 °C for 180 minutes. The results were presented in section 4.2.9. In the case of the γ_N phase film, deposited on unheated substrates and with 50% N_2, vacuum annealing at 500 °C resulted in the decomposition of the austenite phase into Cr_2N and ferrite. The decomposition products are accompanied by austenite phase with lattice parameter reduced to that of expansion-free (i.e. nitrogen-free) austenite, as can be seen from Figure 4.37.

In the case of γ_N films, it is interesting to find that the precipitation of Cr_2N phase probably needs certain critical nitrogen content in the film, as evident from the absence of Cr_2N in GIXD pattern (Figure 4.38) of the annealed film, deposited with 450W power and 25% N_2 on unheated substrates, which contains the lowest nitrogen content amongst all the films that were subjected to annealing studies. Such a requirement of critical amount of nitrogen for Cr_2N precipitation was also found in the case of aging of nitrided austenitic stainless steel [107]. However, during the annealing of the reactively sputter deposited SS-N films, Cr_2N precipitated within a short period of 180 minutes. This is due to the ultrafine grained microstructure with very high grain boundary volume, which helps in easy solid state diffusion. However, the same precipitation did not take place (despite the affinity of nitrogen towards chromium [37, 43 and 108]) in the annealed film shown in Figure 4.38, as sufficient nitrogen could not diffuse towards the chromium in the lattice due to lower nitrogen content in the as-deposited film.

The formation of Cr_2N phase, ferrite and nitrogen-free austenite in the annealed MN films is similar to the case of the as-deposited film deposited at 500° C and with 50% N_2 (Figure 4.29). The Cr_2N precipitation was also supported by the electron diffraction pattern shown in Figure 4.30. But nitrogen-free austenite did not form in the as-deposited film, deposited at 500 °C and with 50% N_2. Such an absence of austenite phase amongst the decomposition products was also found in the case of plasma nitriding austenitic stainless steel performed by Menthe et al

ATTENTION: The Singapore Copyright Act applies to the use of this document. Nanyang Technological University Library

[16]. This is due to the continuous availability of nitrogen on the growing film, which hindered the out diffusion of nitrogen from the lattice of expanded austenite.

Based on the above results and analysis, it can be deduced that during annealing of the MN phase film at temperatures of around 500 °C, the following reaction takes place:

$$MN \xrightarrow{500\ ^{\circ}C} Cr2N + \alpha\text{-Ferrite} + (\gamma\text{-austenite or } \gamma_N\text{-expanded austenite})$$

5.5 DEPOSITION RATE, TEXTURE AND MORPHOLOGY OF SS-N FILMS

5.5.1 Deposition Rate

The effect of reactive nitrogen gas on the deposition rate of the reactively sputtered films is known to be two folds. First, it reduces the sputtering rate of the target material due to the lower sputtering yield of nitrogen ions as compared to that of heavier Ar ions [18]. Second, the reactive gas ions may react with the target surface to change its chemical and physical nature, a phenomenon known as target poisoning, which normally causes a drastic drop in deposition rate [18]. However, the initial increase (Figure 4.40) in the deposition rate with upto 10% N_2 in the present case could not be explained by these two effects. Even the lattice expansion arising from the incorporation of nitrogen in the films need not counterbalance the first effect, i.e. the reduction in sputtering rate. It was initially thought to be probable that the films produced with up to 10%N_2 in the gas mixture are more porous than pure stainless steel bcc films, which might account for the observed increase in film thickness and deposition rate. However, a more plausible explanation for the observed deposition rate peaked at 10%N_2 is given below.

It is a well established fact that under the same sputtering power density, the amount of material sputtered from the target, i.e. the flux of adatoms generated from the target, increases with increasing ion energy and number of ions in the system. Argon ions are heavier than nitrogen ions and thus have higher kinetic

ATTENTION: The Singapore Copyright Act applies to the use of this document. Nanyang Technological University Library

energy and higher sputtering rate. It is generally true that sputtering in pure argon atmosphere generates larger flux of adatoms than sputtering in pure nitrogen atmosphere. However, because nitrogen has a lower ionization potential (14.6 eV) than argon (15.8 eV), the addition of a small amount of nitrogen to argon is expected to increase the ionization efficiency of the atmosphere and thus increase the number of ions, including argon ions and nitrogen ions, in the system. Although nitrogen ions do not have sputtering rate as high as argon ions, if the contribution arising from the increased ionization efficiency is more significant than the reduced sputtering rate, then the addition of a small amount of nitrogen would result in increased flux of adatoms generated from the target, and thus increased deposition rate. In other word, sputtering of the target by a large number of ions with slightly reduced energy should knock out a larger amount of material than sputtering by a smaller number of ions with slightly higher energy. Accordingly, the deposition rate initially increases with increasing nitrogen gas composition until a peak value at certain critical nitrogen gas composition (10% N_2 in this case), after which the contribution of the reduced sputtering rate towards the overall flux of adatoms becomes more significant than the increased ionization efficiency, and the flux of adatoms generated from the target decreases, i.e. deposition rate decreases with further increase in nitrogen gas composition. In other word, too much nitrogen added to the atmosphere results in increased ionization efficiency dominated by nitrogen ions with much reduced energy and sputtering rate. This would reduce the flux of adatoms from the target and the deposition rate.

The gradual decrease in deposition rate with nitrogen above 10% suggests that the reduction in sputtering rate due to the introduction of nitrogen gas with lighter atomic weight became dominant, while target poisoning could be ruled out otherwise a sudden drop in the deposition rate at certain critical nitrogen composition would be observed. This observation agrees with other investigators [50 and 52] who claimed that target poisoning was avoided in sputtering of a stainless steel target with various amounts of nitrogen in the sputtering gas mixture.

As expected the deposition rate increases with increasing sputtering power density (Figure 4.42) and decreased target-substrate distance (section 4.3). The latter effect

ATTENTION: The Singapore Copyright Act applies to the use of this document. Nanyang Technological University Library

could be explained by the reduced scattering events between the sputtering species and the gas species with reduced target-substrate distance.

5.5.2 Texture in SS-N Films

Apart from lattice distortion, properties and performance of the as-deposited films also depend on the texture of the phases formed in the films [79]. However, determination and analysis on film texture by the help of GIXD is complex and needs careful understanding of the procedure. Details of texture analysis of the films are given below.

In the GIXD pattern (Figure 4.6) glancing angle of incidence of 10°, the (110) planes corresponding to the diffraction peak are inclined at an angle of about 58° with respect to the surface. Also it should be recalled that within the same grains (100) planes are inclined at 45° about (110) planes. Accordingly it can be inferred from the single diffraction peak of (110) in the GIXD pattern (at glancing angle of 10°) that grains with the (100) planes are preferentially orientation at an angle of 13° about the surface of the substrate. This information does not carry any significance unless it can be deduced that the highest population is for the grains within which the (100) planes are parallel to the surface. Such a conclusion is based on the continuum distribution of the grain orientations, with the most probable number for the orientation of 0°.

Figure 5.9 shows the schematic of GIXD analysis with the help of which texture determination can be visualized properly. The maximum scanning range employed in terms of Bragg angle is from 30° to 90°. Accordingly, the planes with orientation range of 35° to 65° with respect to the surface of the sample can only give diffraction peaks for 10° glancing angle GIXD, when Bragg's law is satisfied. The widest Bragg angle for which diffracting peak was obtained in the GIXD mode is 89° while the smallest Bragg angle is 35°. It can be understood that the planes of the analyses are oriented with respect to the surface of the sample with angles 35.5° (90°-[(θ_B/2) + glancing angle of incidence]) and 62.5°, respectively. Thus, in the present GIXD analysis, planes diffracting at higher Bragg angles are always less tilted about the surface of the film compared to that of lower Bragg angles. While a perfect randomly-oriented polycrystalline sample gives GIXD

ATTENTION: The Singapore Copyright Act applies to the use of this document. Nanyang Technological University Library

pattern similar to that of Bragg-Brentano, perfectly textured sample gives different patterns for these two of the scanning geometries. Based on this discussion, inferences on the microstructure analysis by GIXD are drawn in the following paragraphs.

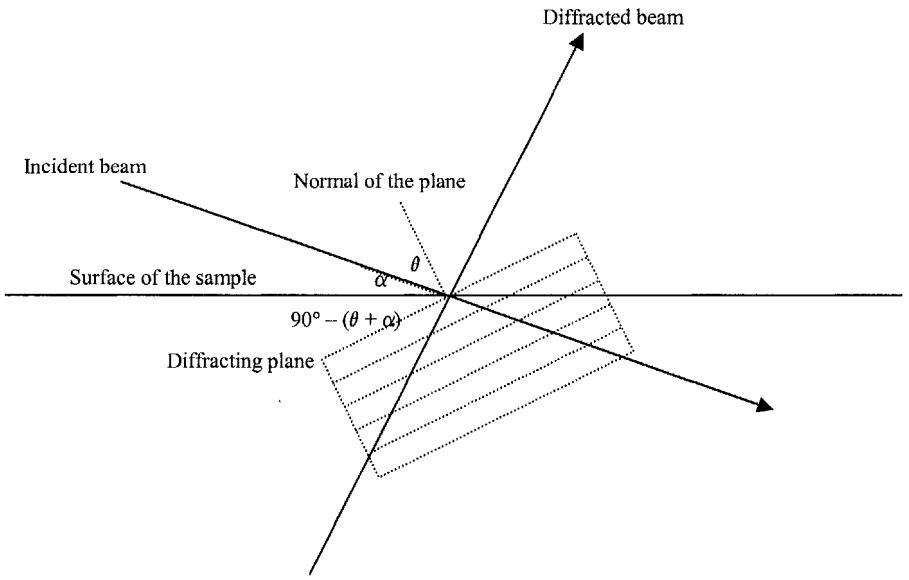


Figure 5.9: Schematic showing angle between the diffracting plane and the surface of the sample as $90° - (\theta + \alpha)$

The tilt in the (111) plane, giving a diffraction peak at Bragg angle of 43.5°, should be 58.25° while that of (200) should be 54.65°. However, the included angle between the (111) planes and the (200) planes of austenitic stainless steel within the same grain is typically 54.7°. Based on this information we can conclude that in a given GIXD pattern the planes giving diffracting peaks corresponding to the planes (111) and (200) should not be from the same grains. And the relative intensity ratio between the two peaks should give only statistical grain-orientation distribution with respect to the perfect randomly oriented sample. Based on the above discussion it can be inferred that care should be taken while determining the texture by GIXD especially when the GIXD pattern contains only one peak. However, the fixed glancing angle of incidence scanning can be used similar to Bragg-Brentano mode in the case of nanocrystalline grains with perfect random orientation. Grain-orientation, distributed continuously but statistically across 0° - 180°, gives all the diffraction peaks but with relative intensities different from that of the standard. In such cases the basis for texture analysis can be devised in the following manner. From Figure 4.17b it can be seen that a typical SS-N film (30%-300 °C-7 cm-100W) shows GIXD pattern different from that of the standard

ATTENTION: The Singapore Copyright Act applies to the use of this document. Nanyang Technological University Library

pattern. The ratio of peak intensity of (111) and (200) planes decreases with the increase in glancing angle of incidence as can be seen from Figure 5.10. This means that for the grains whose (111) and (200) planes are less tilted about the surface, $I_{(111)}$ / $I_{(200)}$ is less. This suggests preferred orientation of (200) plane parallel to the surface in comparison to the (111) plane. However, determination of actual plane, which is parallel to the surface, is not as much straightforward. Thus, in the case of statistical orientation distribution of the grains, GIXD can still be used for qualitative texture analysis, by comparing relative intensity ratios of two specific peaks for a given glancing angle of incidence.

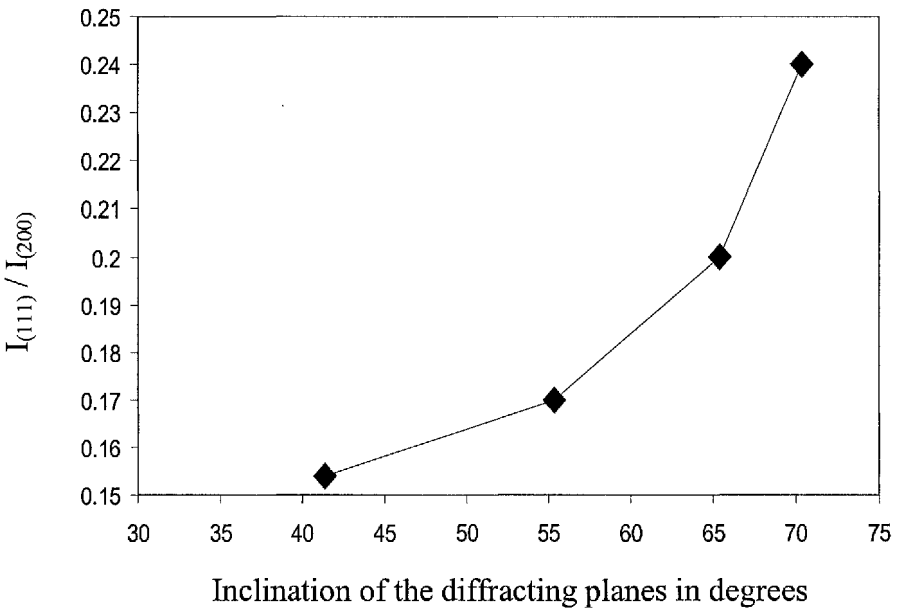


Figure 5.10: Tilt of (111) plane about the surface (degree) in the SS-N film containing expanded austenite deposited with 30% N_2 at 300 °C

Table 5.4 shows the trend in variation of the texture index, calculated by subtracting the ratio of peak intensity of (111) to that of (200) planes of standard sample from that of the γ_N and MN phase in various films. A positive value suggests preferred orientation of (111) plane parallel to the surface of the substrate while a negative value suggests the orientation of (200) plane. From Table 5.4, it can be seen that all MN films exhibit strong (111) orientation corresponding to the strongest (111) peak in the GIXD patterns in all the MN films. While most γ_N films exhibit (200) orientation, some do exhibit (111) orientation. It seems that deposition with 10% N_2 to 25% N_2 at relatively low power densities favor the formation of (111) orientation while the other conditions favor (200) orientation.

ATTENTION: The Singapore Copyright Act applies to the use of this document. Nanyang Technological University Library

Table 5.5: Texture Index in terms of (111) plane parallel to the surface for SS-N Films

Sample	Texture Index in terms of orientation of (111) plane parallel to the surface
RT varying % N_2	
10% N_2	2.398
15% N_2	3.452
40% N_2	-0.580
300 °C varying % N_2	
6% N_2	-0.330
10% N_2	0.093
25% N_2	8.418
30% N_2	-1.055
37% N_2	-1.101
45% N_2	-0.520
25% RT varying powers	
100W	0.078
300W	-0.147
450W	-0.181

The ferritic stainless steel film gave only a diffracting peak corresponding to (110) plane. Such single peak pattern of the film is characteristic of well-defined texture in the film. The only one peak, obtained in the GIXD within the Bragg angle range, predicates the absence of random orientation of grains. In the GIXD pattern obtained for glancing angle of incidence of 10°, the (110) planes corresponding to the diffraction peak are inclined at an angle of about 58° with respect to the surface. Also it should be recalled that within the same grains (100) planes are inclined at 45° about (110) planes. Accordingly it can be inferred from the single diffraction peak of (110) in the GIXD pattern (at glancing angle of 10°) that grains with the (100) planes are preferentially orientation at an angle of 13° about the surface of the substrate. This information does not carry any significance unless it is deduced that the highest population is for the grains within which the (100) planes are parallel to the surface. Such a conclusion is based on the continuum distribution of the grain orientations, with the most probable number for the orientation of 0°.

ATTENTION: The Singapore Copyright Act applies to the use of this document. Nanyang Technological University Library

Plane (110) is the densest atomic plane for the bcc phase and the film accordingly would attain (110) texture if sufficient time could be allowed for crystalline arrangement for the close packing. Nevertheless, the (100) texture (Figure 4.5) in the present case could be due to (1) the deposition rate being greater than that would allow sufficient time for crystalline arrangement, and (2) the substrate temperature being too low, restricts the motion of adatoms required for the crystalline growth in a thermodynamically favorable orientation.

However, pure stainless steel film deposited at 300 °C is strikingly different. Plane (211) gave the strongest peak (Figure 4.13a). It should be recalled that the tilt of the diffracting planes in the GIXD pattern, with respect to the surface of the film, changes with the glancing angle of incidence. Figure 5.9 shows the GIXD pattern of the same sample obtained with a glancing angle of incidence of 44°. In this case, the diffracting peak at 82.288° corresponds to the (211) plane oriented at an angle of 5° about the surface parallel. While the glancing angle of incidence of 10° in Figure 4.13(a) suggests statistical distribution of the grain orientation with preferred orientation of (211) plane parallel to the surface. This is confirmed by GIXD patterns of both 10° and 2° glancing angles. Such a preferred orientation suggests positive surface tension at the SS/Si interface as the (211) plane has the lowest atomic density. It should be recalled that the atomic density of the plane (211) is lower than that of (100) plane, which is the preferentially oriented plane in the films deposited on unheated substrate. The thermal activation due to substrate heating in the present case increased adatom-mobility for greater reduction in surface tension at the interface and thus favored the (211) plane preferred orientation. However, it can be seen that the introduction of small amounts of nitrogen (4% N_2) into the sputtering gas mixture reduced (Figure 4.13b) this surface tension effect probably due to change in the chemical nature of the interface between the surface of the substrate and the growing film.

ATTENTION: The Singapore Copyright Act applies to the use of this document. Nanyang Technological University Library

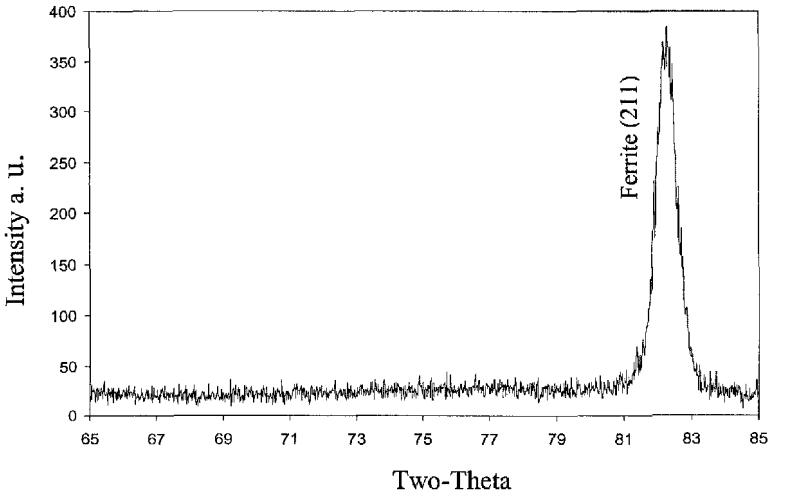


Figure 5.11: GIXD pattern, of pure stainless steel film deposited at 300 °C & with 100W, obtained with glancing angle of incidence of 44°

5.5.3 Surface Morphological Features

The well-defined boundaries between the granular structures on ferrite film (Figure 4.45a) suggest that surface diffusion and overlapped growth is only limited on both the heated and unheated substrates. The transition from polygonal base to triangular base of the pyramids with increase in $\%N_2$ suggests the important role of nitrogen in determining the surface morphology. Nitrogen in the sputtering atmosphere is known to reduce the kinetic energy and mobility of adatoms due to the affinity of nitrogen with the metallic adatoms [22]. It is thus understandable that the crystallites in the nitrogen-doped bcc film would preferentially take the triangular-based shape which has the least surface area for an as-grown pyramidal crystalline film.

The average size of the granular structures, as measured from the surface morphology by FESEM, is given in Figure 5.12, for the films deposited on unheated substrate at 300 °C. The measurements were done on the fractured surfaces because of the potential error that can be derived due to the ductile nature of the film fracture. It shows that heating the substrate to 300 °C indeed increases the asperity size in the films. An increase in asperity size is evident in the γ_N phase film produced with 25% N_2 (40 at.% N). The nucleation density of the γ_N phase must be low and since this film is relatively dense (Figure 4.46d), surface diffusion of adatoms required for grain growth and film densification must be enhanced,

ATTENTION: The Singapore Copyright Act applies to the use of this document. Nanyang Technological University Library

rate (Figure 4.41), led to the densification of the film, while grain growth was restricted due to the high density of nuclei. Indeed, the average diameter of the columnar grains increased (Figure 5.13) slowly from 25 nm for 45 minutes to 55 nm for 75 minutes and to 65 nm for 180 minutes deposition.

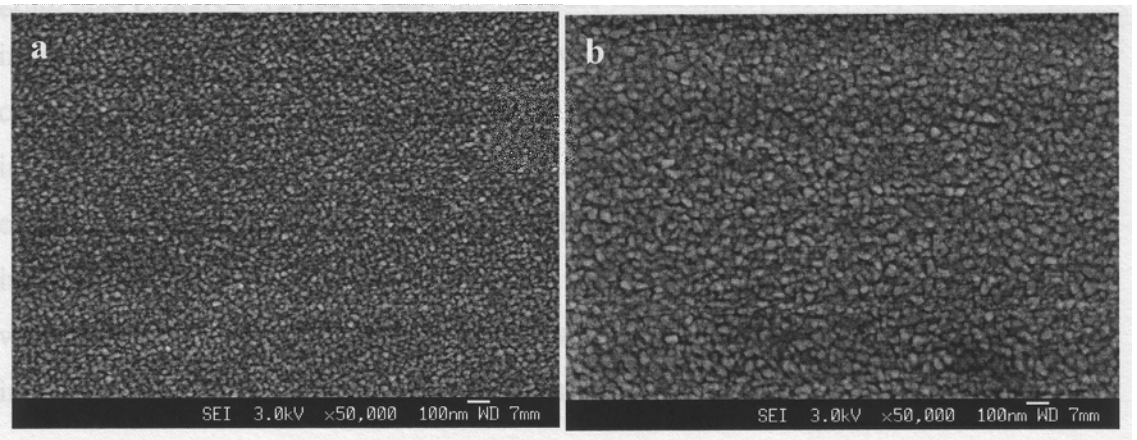


Figure 5.13: FIELD EMISSION SEM micrographs showing the surface morphology of the films deposited at 300 °C with 50% N_2 in the gas mixture, for (a) 45 minutes (135 nm thick) and (b) 75 minutes (225 nm thick)

5.6 PROPERTY – STRUCTRE RELATIONSHIP

5.6.1 Hardness and Reduced-Modulus of SS-N Films

Figure 5.14 can be divided into 4 segments of trend in the variation. In segment I, both the films constitute single ferrite phase but the hardness and reduced-modulus were found to increase with increase in % N_2 in the sputtering gas mixture. This can be due to the incorporation of a small amount of nitrogen in the ferrite film and the increased film thickness with the increase in ion-density and flux of sputtered atoms reaching the growing film (discussed in section 5.1). The reduced-modulus found for the ferrite film is similar to that of the bulk ferrite, 200-220 GPa. But the hardness of the ferrite films (~ 8 GPa) is much higher than the expected bulk ferrite (200-300 MPa). This increased hardness could be attributed to the nanograin size nature of the film structure and possibly to evolution of residual stresses in the films.

With a further increase in the nitrogen gas composition to as high as 10% (segment II) expanded austenite phase formed in the SS-N film and the film showed

ATTENTION: The Singapore Copyright Act applies to the use of this document. Nanyang Technological University Library

increased hardness but decreased reduced-modulus. It should be recalled that the austenite phase has lower hardness compared to the ferrite phase [109]. Nevertheless, the incorporation of nitrogen in the γ_N phase and possible duplex microstructure in the film as well as further increased film thickness and reduced grain size (Figure 5.12) can cause the increase in hardness. However, this trend of increase in hardness did not continue with further increase in nitrogen gas composition to 25 % (segment III). The hardness decreased but reduced-modulus increased for the pure expanded austenite film in comparison to the relatively less expanded austenite in the film deposited with 10% N_2 in gas mixture. The decrease in hardness, despite the incorporation of a large amount of nitrogen in γ_N phase, which should lead to increased hardness, can be explained by the observed increased grain size and reduced film thickness.

The hardness values obtained for the expanded austenite films are lower by an order compared to the values reported [33] previously. While the coatings were produced in the previous studies by unbalanced magnetron sputtering, the films characterized in the present study were deposited without the application of substrate bias. The bombardment of the growing film with the energetic ionic species caused compressive residual stresses in the film and decreases the grain size. The relative higher values of the hardness for the previous studies should be attributed to the deposition process technique.

In segment IV the formation of MN phase increased the hardness of the SS-N film to the highest value while the reduced-modulus value is the lowest, amongst all the SS-N films. It is noted that the increase in hardness occurred against the contribution of lowest deposition rate and thus the smallest film thickness. This again clearly suggests the change in nature of the iron – nitrogen bond in this MN phase.

ATTENTION: The Singapore Copyright Act applies to the use of this document. Nanyang Technological University Library

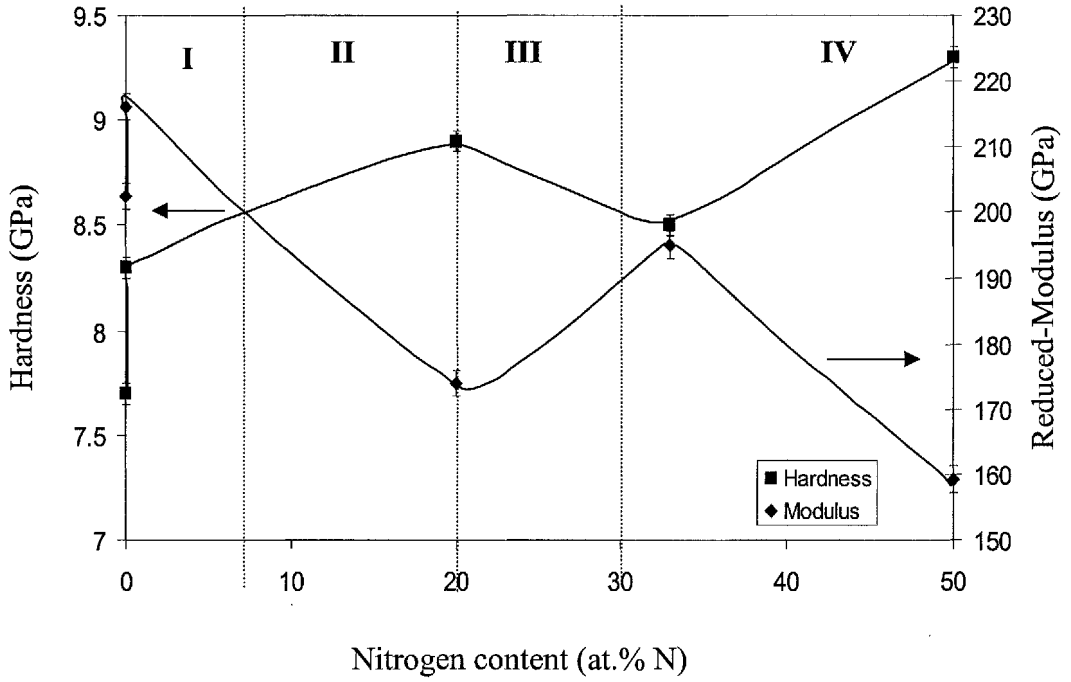


Figure 5.14: Variation of hardness and reduced-modulus of the SS-N films deposited with at.% N in the SS-N films deposited at 300 °C & with 100W

It can be seen that the hardness values of the films, deposited on mild steel substrates, increased with increasing % N_2 in gas mixture until 50%. The hardness of the expanded austenite increased with increase in nitrogen content in the phase, while the MN phase (formed with 50% N_2) showed hardness value higher than all the expanded austenite films. However, the MN phase did not show the same highest hardness values when deposited with 75% N_2 in the gas mixture. This could be due to the much reduced film thickness and the increased contribution from the softer mild steel substrate during nanoindentation.

It can be seen that the hardness of the MN films is not constant but varies with deposition conditions. The highest hardness was obtained for the film deposited at 300 C with 50 % N_2. Depositions at room temperature led to reduced film hardness. This could be due to reduced crystallinity and density of the MN films deposited on unheated substrates. Another observation that can be made is the MN film hardness increases with increasing deposition power density, i.e. increasing film thickness.

ATTENTION: The Singapore Copyright Act applies to the use of this document. Nanyang Technological University Library

5.6.2 Adhesion Properties

Table 5.6 summarizes the measured critical loads for film failure (L_c) from which it can be seen that L_c of the films decreased with increase in nitrogen content, excepting for the sample deposited with 25 $\%N_2$ in the gas mixture. The nature of film failure and plastic deformation in the film can also be seen for selected samples from optical micrographs in Figure 5.15. The magnitude and distribution of delaminations, throughout the tracks, are noticeably different from the gross-spallations that are typical of hard coatings on soft/hard substrates. Scratch width, measured at a particular value of the load, decreased with increase in $\%N_2$ in gas mixture, due to the increase in hardness. Absence of cracks consistently in all the samples is due to the ductile nature of the films as well as negligible film-growth defects.

Table 5.6: Critical loads of adhesive failure of the SS-N films deposited with various $\%N_2$ in gas mixture at 300 °C

Sample (at.%)	L_{c2}, Critical load (mN)
0 (0 $\%N_2$)	413
0 (5 $\%N_2$)	263
5 (10 $\%N_2$)	212
40 (25 $\%N_2$)	221

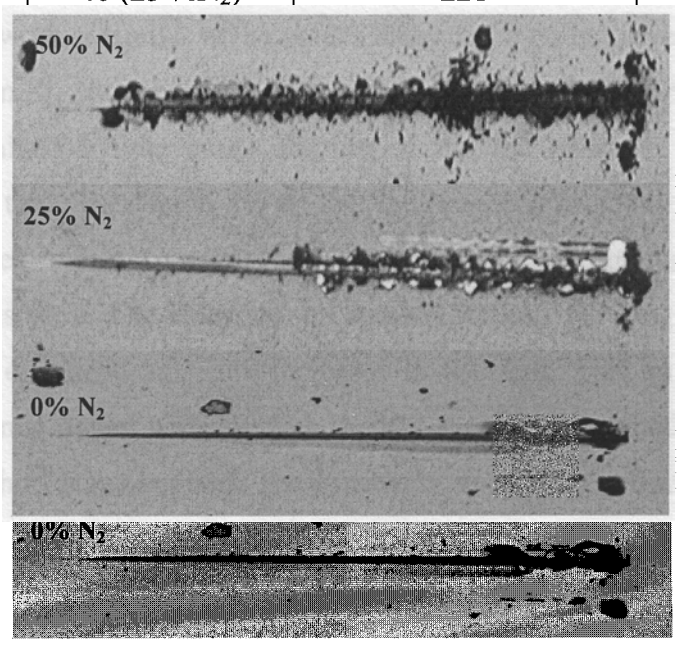


Figure 5.15: Optical micrographs of micro scratch tracks on various SS-N films

ATTENTION: The Singapore Copyright Act applies to the use of this document. Nanyang Technological University Library

It is interesting to notice that the critical load decreased drastically from 413 mN to 263 mN for the ferrite films deposited increasing % N_2 from 0 to 5. It has been established already during the discussion in the previous sections, even though phase constitution of the film does not change, deposition rate, amount of residual stresses and the nature of the substrate/film interface change with the introduction of nitrogen in the sputtering gas mixture. Similar drastic change in the microstructure of the ferrite film can be seen when the (211) preferred orientation of the ferrite film reduced with the introduction of small amounts of nitrogen. While the gradual increase in the at.% nitrogen in the expanded austenite decreased the critical load monotonically, the MN phase film deposited with 50% N_2 showed plummeting of the critical to as low as 27 mN. The change from the metallic nature of the expanded austenite to the ionic nature of the MN phase is the reason for the sudden decrease in the adhesion property. This suggests that the adhesion strength of the MN phase is low which has to be addressed for their potential use in wear resistant coatings.

5.7 SATURATION MAGNETIZATION OF SS-N FILMS

The saturation magnetization (M_s), at room temperature, of the films decreased with increasing % N_2 during deposition. As can be seen from Figure 5.16, the decrease in M_s follows three stages. In the first stage for the films deposited with less than 4% N_2, where the major phase is ferrite, the M_s value decreased slowly with increase in % N_2. The Ms value of 130 emu/g found for the pure SS films (ferrite) in this work is similar to the values measured by other investigators [110]. No increment in M_s was observed with nitrogen doping in the ferrite films. This could be explained by the small amount of the fcc phase in the film. The significance of this observation lies in that the magnetic moment of ferrite films

ATTENTION: The Singapore Copyright Act applies to the use of this document. Nanyang Technological University Library

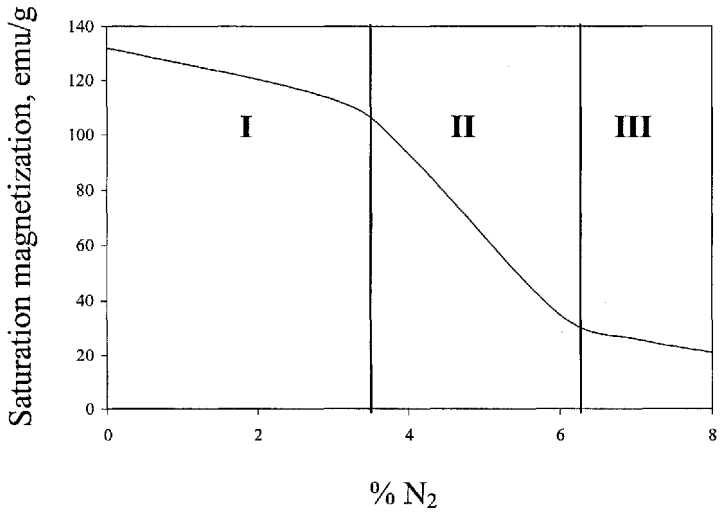


Figure 5.16: Saturation magnetization on unheated substrates of SS-N films with varying % N_2

The present VSM results of the γ_N phase did not agree with the magnetic force microscope results of the expanded austenite already reported [110]. One of the sources of ferromagnetic behavior of the nitrogen incorporated austenite is the defect density in the films [11] and iron nitrides formed during the nitridation or coating process [110]. Despite the decrease of M_s, a better understanding of the chemical state of the iron and nitrogen atoms will help in a better correlation of magnetic properties with the microstructure. From the VSM magnetic property measurement it can be concluded that:

1. The pure stainless steel film with bcc ferrite structure is ferromagnetic with a saturation magnetization (Ms) 130 emu/g.
2. The Ms values of the predominant ferrite films can be controlled and altered by adding a small amount of nitrogen gas to the sputtering atmosphere which reduces gradually the Ms of the films.
3. The expanded austenite, γ_N film is non magnetic.
4. The MN phase is non magnetic which is similar to that of FeN phase in the

ATTENTION: The Singapore Copyright Act applies to the use of this document. Nanyang Technological University Library

Chapter 6

CONCLUSIONS AND SUGGESTIONS FOR FUTURE WORK

6.1 CONCLUSIONS

1. It was realized that surface modifications for improved anti-wear and anti-corrosion properties by reactive sputter deposition of stainless steel target yields several advantages over other nitriding techniques. These include low temperature processing, process flexibility and range of tailorable microstructures and combinations of properties. A range of nitrogen contents and phases could be developed in reactively sputter-deposited stainless steel films in nitrogen-containing atmosphere.
2. It was found that the nitrogen content in the film increases gradually with increasing % N_2 in the sputtering gas mixture, irrespective of the substrate temperature. However, abrupt transitions in the constituent phases in the as-deposited SS-N films occurred at specific temperatures due to the change in chemical activity of nitrogen with respect to the metallic adatoms, with increasing % N_2. The phase evolution was found to follow through α, $\gamma + \alpha$, then to γ_N, and finally to MN phase.
3. In the as-deposited SS-N films in which more than two crystalline phases formed, the XRD diffraction peaks were broad, suggesting amorphous-like nature of the phases.
4. Stability of MN phase was studied and found that it forms at substrate temperatures below 450 °C in gas mixture containing sufficient amount of nitrogen (>45% N_2) which ensures the incorporation of about 50% nitrogen in the film.
5. While the lattice distortion of the MN phase did not vary with % N_2 the lattice distortion of expanded austenite was dependent on the at.% N in the film.
6. Further, structural difference between expanded austenite and MN phase was proved by X-ray photoelectron spectroscopic studies which showed

ATTENTION: The Singapore Copyright Act applies to the use of this document. Nanyang Technological University Library

Cr-N bond unlike the absence of such a spectrum in the case of expanded austenite.

7. The MN phase is unstable at temperatures above 500 °C as the maximum substrate temperature for its formation in as-deposited films is 450 °C. This is about 50 °C higher than the maximum substrate temperature for the formation of the FeN phase, discovered by others by reactive sputtering.
8. Deposition power density was found to have similar influences on expanded austenite and MN phases. With the increasing power density, nitrogen content in the films was found to decrease for expanded austenite and MN phases.
9. Decomposition of the MN phase was favored by increased substrate bias power. Single MN phase could not be produced by deposition with substrate biasing, which favors the formation of nanocrystalline Cr_2N phase in the films.
10. Texture developed in the as-deposited expanded austenite (γ_N) films was influenced by % N_2. GIXD studies at various glancing angles of incidence showed that the population of the grains with (200) planes parallel to the surface is more than that of (111) planes.
11. Deposition power density influences the texture of the γ_N films the most. The preferred orientation of (200) planes parallel to the surface was found to increase with increasing power density.
12. Bright field cross sectional TEM micrograph corresponding to MN phase showed morphology characteristic of nitride phase with defect-free growth, while that of the films with expanded austenite phase showed greater defect density.
13. Observations made with the help of HREM showed that the non-crystalline phases were found to form on an amorphous interface with substrate temperatures of 300 °C, while deposition at 500 °C showed growth of film with crystalline atomic order on the silicon native oxide interface.
14. Trends in variation of deposition rates of SS-N films for different substrate temperatures were found to be similar. The deposition rate increased gradually with increase in proportion of nitrogen in sputtering gas mixture

ATTENTION: The Singapore Copyright Act applies to the use of this document. Nanyang Technological University Library

due to increased ionization efficiency and started decreasing after 10% N_2 due to the decreased sputtering efficiency.

15. Surface morphology of the SS-N films undertook transformations across range of granular shapes and sizes. It was found that the grain shapes were characteristic of crystallinity and consistent disregard of the substrate temperature.
16. Nanoindenation studies on the films showed that the hardness of the ferrite phase in film is much higher than that in bulk form. It was interesting to find that the hardness of the γ_N phase increases with increasing at.% N. The MN phase has the highest hardness among all the films tested.
17. The film-substrate adhesion was found to decrease with increasing nitrogen content in the film and thus with increasing film hardness. The MN films showed the worst film-substrate adhesion among all the films produced.
18. Vibrating sample magnetometer characterization of SS-N films for room temperature magnetization was done for the first time. It was found that the metastable ferrite phase in the films is ferromagnetic while the expanded austenite and the MN phases are non-magnetic. Thus, the reasons for the manifestation of ferromagnetism in nitrided austenitic phase in bulk stainless steels are different from the role of nitrogen, defect density, volume expansion of the austenite lattice.

6.2 SUGGESTIONS FOR FUTURE WORKS

Even though the maximum deposition temperature for MN phase formation in reactively sputtered SS-N films was found to be higher than that of previous reports on FeN phase, decomposition temperature of the phase is yet to be determined by aging the SS-N films at various temperatures below 500 °C.

Hardness of the SS-N films was found to increase with increase in at.% N. The hardness of MN phase was found to be the largest amongst all the SS-N films. However, the adhesion strength of the film was found to be the lowest. Efforts to enhance and optimize the adhesion of MN phase can be thus made for further pursuit for enhanced performance and properties. Based on the present results in hand, future works may include depositions of SS-N films with graded nitrogen

ATTENTION: The Singapore Copyright Act applies to the use of this document. Nanyang Technological University Library

content on stainless steel underlayer and under conditions that yield minimal compressive residual stresses.

In the present studies, increase in magnetization by incorporation of nitrogen could not be achieved. However, it is worth studying the magnetic properties with the help of vibrating sample magnetometer and magnetic force microscope. So far the ferromagnetic behavior of bulk nitrided austenite was interpreted in terms of Mossbauer spectroscopy, but negligible efforts were made to establish the magnetism with the help of vibrating sample magnetometer. Similarly, magnetic force microscope was used for the bulk nitrided surfaces but was not used to characterize the films produced by reactive sputter deposition. The microstructure, strain distribution of these nitride layers can be different from that of the bulk nitrided surfaces. Thus, it holds the significance for dedicated systematic studies on magnetic behavior of the SS-N films deposited by reactive sputter deposition.

A further study can be made to investigate in more details the tribological and corrosion properties of the new MN phase and explore its potentials for industrial applications. Efforts should be made to produce thick and adherent γ_N films and MN films intended for engineering applications.

ATTENTION: The Singapore Copyright Act applies to the use of this document. Nanyang Technological University Library

Appendix

OTHER RELATED STUDIES ON FE–N FILMS

Several sets of Fe-N films have been fabricated under various RF sputtering techniques, which allow for the evaluation of the effect of substrate temperature; nitrogen partial pressure, and RF power, on the phase evolution, morphology, and nature of the films, by XRD, SEM, and AFM analyses. In this chapter, various structural and phase constitutional features of the film are presented and discussed.

A.1 XRD STUDIES ON PHASE EVOLUTION

Standard XRD data has been collected from the database given with the Shimadzu X-ray diffractometer [111 and 112], and from other research articles [11, 113, 114, and 115].

A.1.1 Pure Fe Film

For comparison purpose, pure iron film was first deposited by using pure argon as the working gas at 100°C for 180 minutes and at 200 W (4.52 Wcm^{-2}) The deposition rate was estimated to be 5.5 nm/min, such that an iron film about 1.0 μm thick was produced under these conditions. Figure A.1 shows the XRD pattern generated, from which it can be seen that in addition to the strong diffraction peaks from the Si substrate, two peaks from the film were generated, corresponding to pure iron.

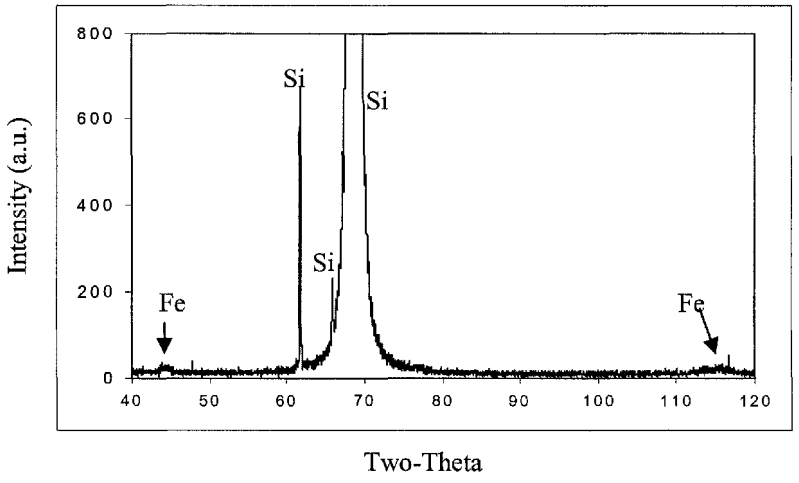


Figure A.1: XRD plot of the film deposited with 0% N_2 gas mixture and at 100° C

ATTENTION: The Singapore Copyright Act applies to the use of this document. Nanyang Technological University Library

In addition, the broadness of the peaks suggests that the film has a very fine grain size. This agrees with AFM results and FESEM observation of the as-deposited surface and fractured cross section discussed later, which revealed grains of nanometer size in the films.

A.1.2 Fe-N Films Produced at Various N_2/Ar Flow Rates

At the same deposition temperature (100 °C), the introduction of nitrogen gas significantly changed the phase constituents of the film. Figures A.2-A.4 show selected XRD patterns of the films, illustrating the influence of nitrogen-argon flow rate ratio.

The introduction of 5% N_2 in the sputtering gas mixture led to the formation of α''-$Fe_{16}N_2$ phase in the film, as confirmed by the small α'' (200) peak, which is characteristic of this ordered phase, and two other peaks possibly overlapping with other phases (Fig. A.2a). The mixture of two phases, i.e. α-Fe and α'', in the film indicates that the nitrogen content is not sufficient for the formation of a single α''-$Fe_{16}N_2$ phase, which has a nominal nitrogen content of 11.1 at. %.

Increasing the nitrogen-argon ratio to 0.11 at the same deposition temperature of 100 °C, however, did not increase the tendency for the formation of the α'' phase. The N_2/Ar flow rate of 11.1 is equivalent to at. % N content in the single phase α''-$Fe_{16}N_2$. So a single phase α''-$Fe_{16}N_2$ would be expected to form in the film. But, γ'-Fe_4N phase, which is richer in nitrogen (20 at. %), was formed in the film (Fig. 5.2b).

Compared to the film deposited with 0.05 N_2/Ar flow rate, the peak of α''-$Fe_{16}N_2$ is prominent. This proves that the contact of the substrate with the plasma (or) glow discharge did not necessarily prevent the formation of metastable phases like α''-$Fe_{16}N_2$. Thus, other kinetic factors of phase formation like rate of deposition and substrate temperature have their roles in the metastable phase formation, in spite of the chemical activation of the reacting species by the plasma, which favors the formation of the stable phases. Possibly, prolonged deposition at 100 °C as well as poor thermal stability of α''-$Fe_{16}N_2$ rendered the formation of γ'-Fe_4N. Thus,

ATTENTION: The Singapore Copyright Act applies to the use of this document. Nanyang Technological University Library

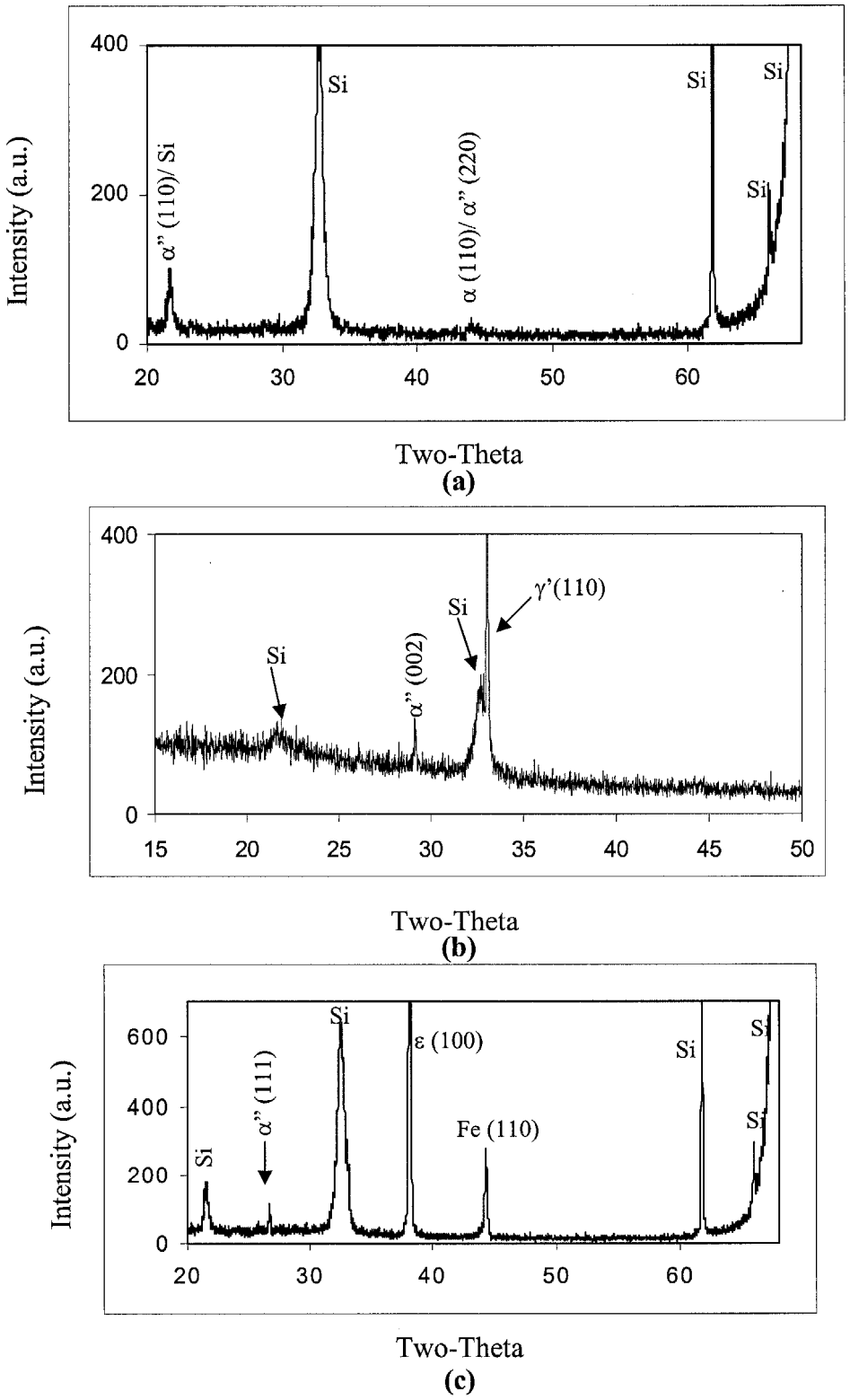


Figure A.2: XRD plot of the film deposited with (a) 0.05%, (b) 0.11% &, and (c) 0.33% N_2 in gas mixture and at 100° C

ATTENTION: The Singapore Copyright Act applies to the use of this document. Nanyang Technological University Library

A.1.3 Fe-N Films Produced at Various Temperatures

Phase evolution in the film was also strongly influenced by the substrate temperature. Formation of oxides, especially due to the dissociation of native SiO_2 and subsequent diffusion into the Fe-N film can be overruled as the deposition temperatures were much below 900 °C [129]. Figure A.3 shows the XRD plot of the film deposited with a nitrogen partial pressure of 0.5 on an unheated substrate. It suggests that the temperature was not sufficient for any crystalline phase to form. With such a high nitrogen content in the gas, complete ordering of the nitrogen atoms in the film to form α''-$Fe_{16}N_2$ was difficult, but the thermal energy at room temperature was not sufficient to form other nitride compound phases. For obtaining stronger peaks of α''-$Fe_{16}N_2$, substrate heating during deposition was tried.

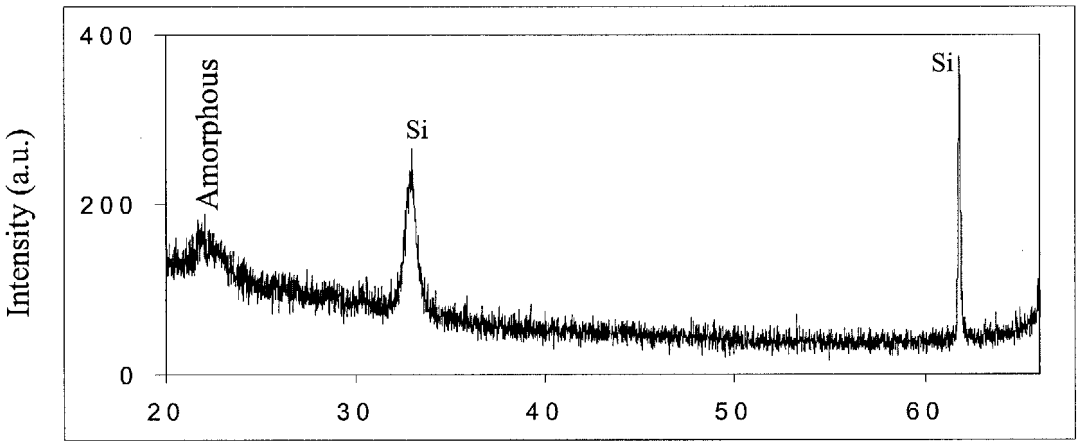


Figure A.3: XRD plot of the film deposited on unheated substrate and with 50% N_2 gas mixture

Increasing the substrate temperature to 100°C, γ' and ε nitrides started to form in the film at 0.5 N_2/Ar flow rate. At 150°C and 300°C, the films produced were dominated by the γ' nitride, as confirmed by the strong diffraction peak from this phase, shown in Figure A.4, 5.5. It therefore appears that increased substrate temperature favors the formation of the more stable nitride phases, γ'-Fe_4N and ε-Fe_3N, in the Fe-N film. This is counter to our expectation of obtaining greater proportion of ordered phase (α''-$Fe_{16}N_2$) for higher substrate temperatures. It should be understood that for nitrogen partial pressure of 0.5, the activity of nitrogen is enough to form relatively more stable phases like γ'-Fe_4N and ε-Fe_3N.

ATTENTION: The Singapore Copyright Act applies to the use of this document. Nanyang Technological University Library

Thus, conditions favorable for mobility of adatoms like heated substrates form stable compounds easily, for such high nitrogen activities. This emphasizes the need for controlling the chemical activity of nitrogen along with allowing proper mobility of adatoms, for optimal formation of α''-$Fe_{16}N_2$. Further studies to confirm the nitrogen incorporation in the film are required.

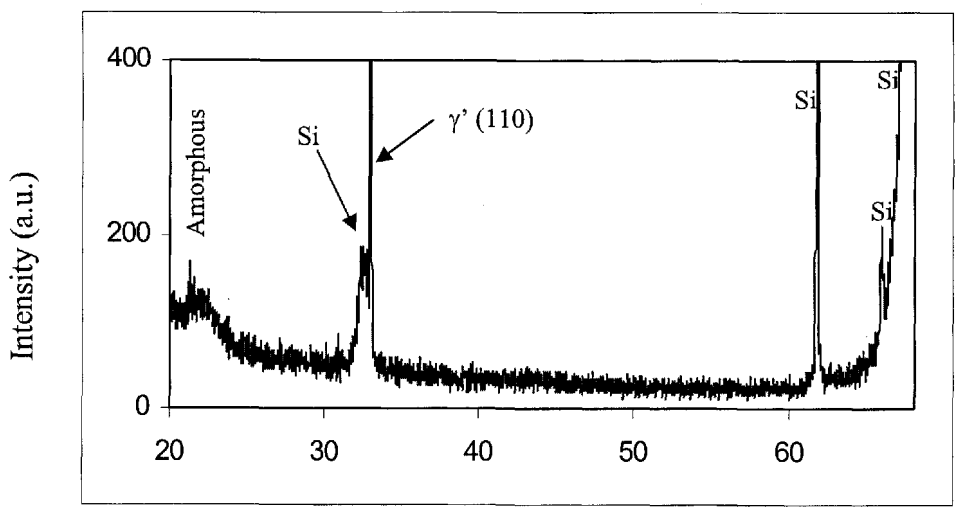
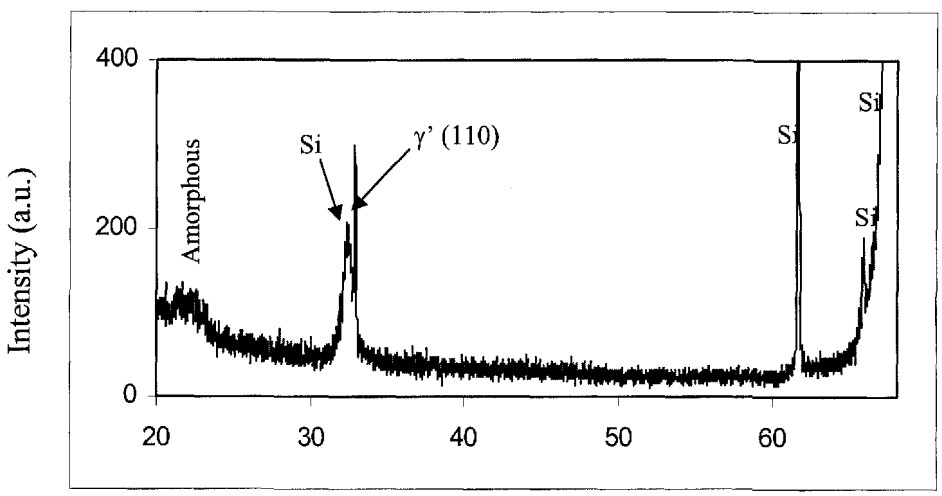


Figure A.4: XRD plot of the film deposited with 50% N_2 in gas mixture and at 150 °C



ATTENTION: The Singapore Copyright Act applies to the use of this document. Nanyang Technological University Library

A.2 DISCUSSION

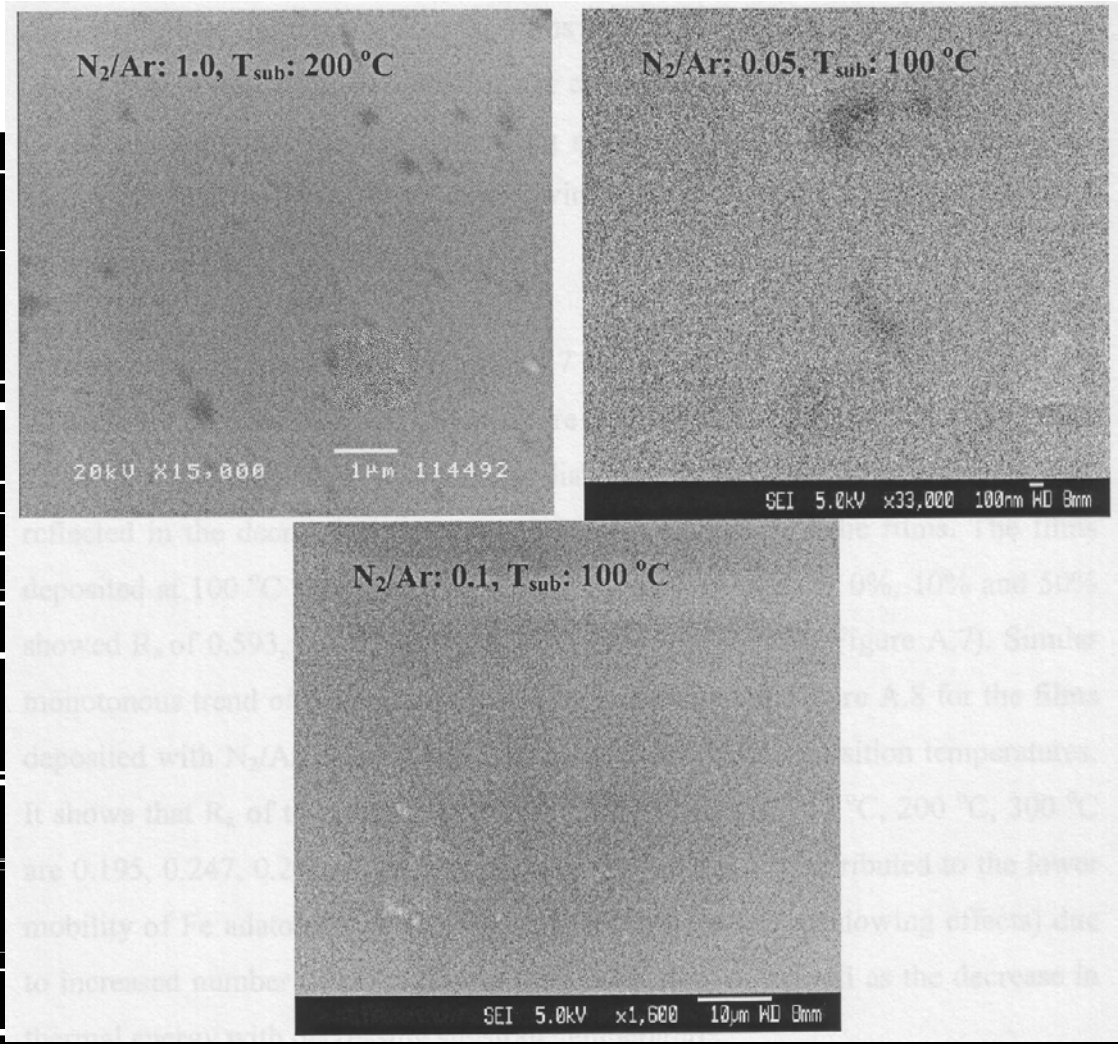
Earlier reports [60, 130 and 131] on reactive sputter deposition of Fe-N films, on Si (100) substrates, at varying nitrogen partial pressures and substrate temperatures, could not form α''-$Fe_{16}N_2$. Films prepared by sputtering with a power of 500 W (11.32 Wcm^{-2} and with a working pressure of 2.25 mTorr did not form α''-$Fe_{16}N_2$ [62, 69], whereas films prepared in our experiments formed α''-$Fe_{16}N_2$. The conditions chosen in our experiments contributed individually to lower deposition rate of Fe atoms. This suggests that greater deposition rate cannot incorporate sufficient number of nitrogen ion/atom species into the interstitial sites of Fe lattice, for the formation of metastable α''-$Fe_{16}N_2$, whereas it can form nitrogen rich phases at higher substrate temperatures and nitrogen partial pressures. This supposition leads to the idea of investigating the effects of increase in deposition rate and increase in mobility of adatoms, on the formation of α''-$Fe_{16}N_2$ (by varying the target-substrate distance, at constant lower powers).

Films prepared at a working pressure of 30 mTorr could not yield α''-$Fe_{16}N_2$ [114], as the nitrogen activity (even for % N_2 in sputtering gas mixture as high as 10) could be sufficient for the formation of more stable phases. It has been reported that the temperatures of the substrate increased to as high as 300 °C during the deposition of Fe-N films [131] by RF diode sputtering (non-magnetron), could have prevented the formation of α''-$Fe_{16}N_2$.

A.3 FESEM OF FE-N FILMS

Figure A.6 shows some of the FESEM micrographs of the Fe-N films, deposited at various conditions, on glass and Si (100) substrates. Details on morphology of the films, at a magnification appropriate for the nano-sized grains to appear could not be obtained. It was assumed that the gold coating on the samples prevents the view of prospective nano-sized grains. But, electrical conductivities of the uncoated films and substrates were not sufficient for obtaining the pictures at higher magnifications needed for viewing the grains.

ATTENTION: The Singapore Copyright Act applies to the use of this document. Nanyang Technological University Library



ATTENTION: The Singapore Copyright Act applies to the use of this document. Nanyang Technological University Library

Another feature observed is that the films appear to be very dense and free from open pores. Deep voids surrounding the columns as well as the conical shape of the columns suggest the self-shadowing mode of grain growth. Self-shadowing occurs because high points on the growing film receive more flux of sputtered atoms than the surroundings.

It can be clearly seen from the Figures 5.7 and 5.8 that as nitrogen partial pressure increases and as the substrate temperature decreases, the average diameter of the columns decreased. This decrease in diameter of the columnar grains is also reflected in the decreasing R_a (average roughness) value of the films. The films deposited at 100 °C temperature and with N_2/Ar flow rates of 0%, 10% and 50% showed R_a of 0.593, 0.577, and 0.204 nm respectively (from Figure A.7). Similar monotonous trend of decrease in R_a can be noticed in the Figure A.8 for the films deposited with N_2/Ar flow rate of 50%, with decrease in deposition temperatures. It shows that R_a of the films deposited at RT (unheated), 150 °C, 200 °C, 300 °C are 0.195, 0.247, 0.286, 0.583 nm respectively. This can be attributed to the lower mobility of Fe adatoms (which can not overcome the self shadowing effects) due to increased number of collisions with nitrogen species as well as the decrease in thermal energy with decreasing substrate temperature.

A.5 PROBLEMS ENCOUNTERED WITH FE-N FILMS

Although initial efforts have been made to fabricate α''-$Fe_{16}N_2$ phase in Fe-N films with the help of magnetron sputtering of iron target in reactive atmosphere of nitrogen, due to time constraint, no further efforts have been continued in this work. DC sputter deposition of the target caused uncontrollable arcing in the chamber. The arcing caused macro particulates of iron on the substrates thus burning the latter. Destabilization of the glow discharge was a common hindrance to the experiments caused by the arcing. The arcing took place over a considerable range of nitrogen proportion in the sputtering gas mixture and deposition power densities. This hindered broader study on the influence of deposition parameters on the Fe-N films.

The magnetic field is required for capturing the electrons to move in helical path thereby increasing the collision events between the electrons and the sputter gas atoms. This increased ionization generated more electrons and positive ions for

ATTENTION: The Singapore Copyright Act applies to the use of this document. Nanyang Technological University Library

easy sustenance of plasma. Further, sputtering events on the surface of the target increase there by increasing the deposition rate. In the case of a ferromagnetic target, iron target in the present case, the magnetic field lines, from the permanent magnets of planar magnetron behind the target, can not penetrate the target material to form efficient trapping of electrons for the above described purpose. Thus, deposition rate of ferromagnetic materials is very low despite the presence of magnetron behind the target.

While the phase of interest, α"-$Fe_{16}N_2$, forms preferably for low deposition rates, inefficient functioning of magnetron due to the ferromagnetic properties of iron target could not yield sufficient thickness of the Fe-N films for convenient characterization of the latter. The depositions were further done for durations as long as 6 hours but in vein. Decreased thickness of the iron target from 6 mm to 0.5 mm did not improve the deposition rate to a favorable extent.

The base pressure of 5-9 x 10^{-6} Torr in the sputtering chamber worsened the situation by supplying oxygen gas molecules for potential arcing on the target even at minimal nitrogen proportions (10-11 percentage of Ar + N_2). This is due to the relative easiness of oxygen to form non-conducting iron oxide in comparison to the nitrides [148]. Surface morphology studies of the films by scanning electron microscopy characterization was found to be difficult as clear micrographs could not be obtained due to the insufficient electric conduction in the films.

ATTENTION: The Singapore Copyright Act applies to the use of this document. Nanyang Technological University Library

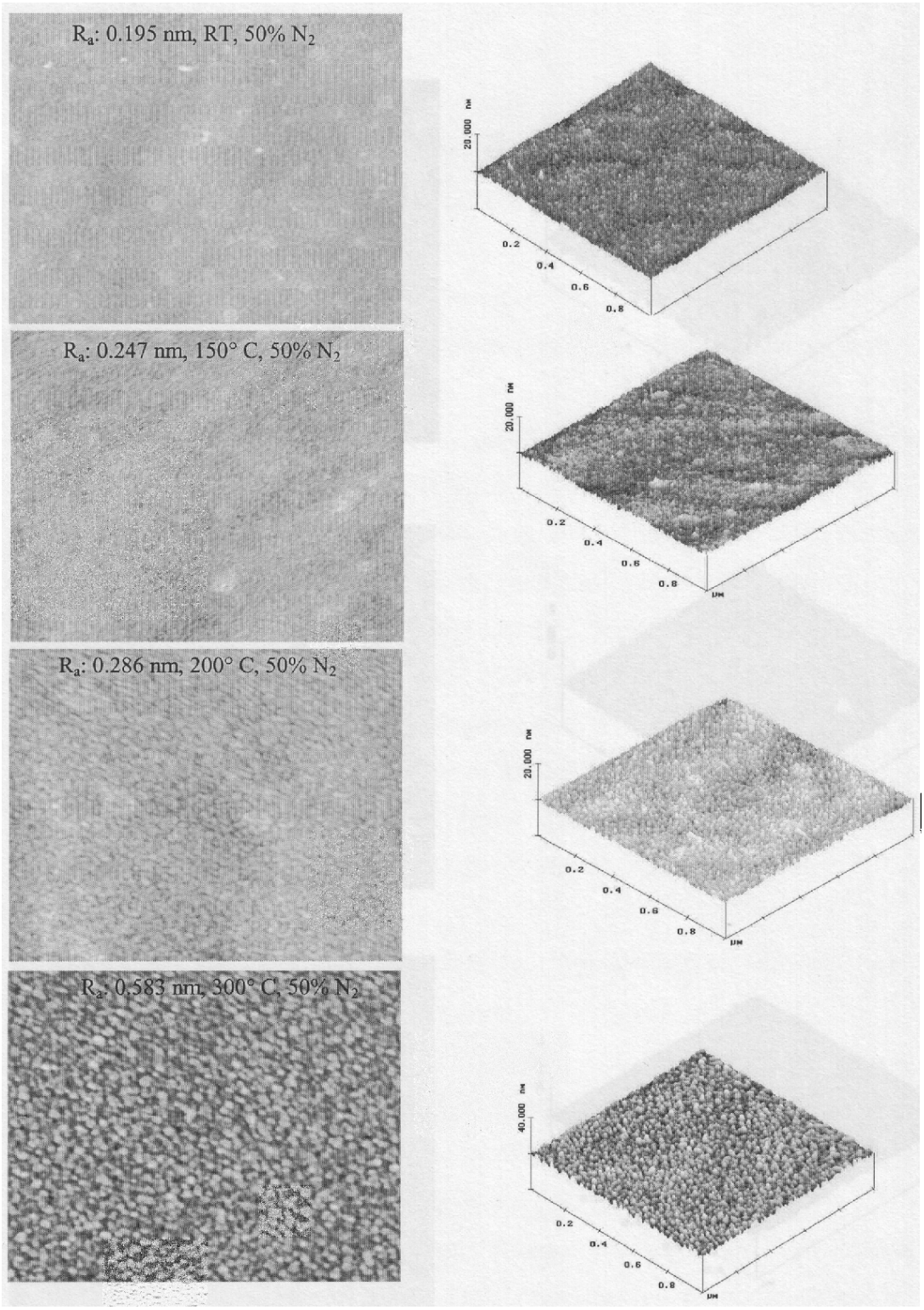
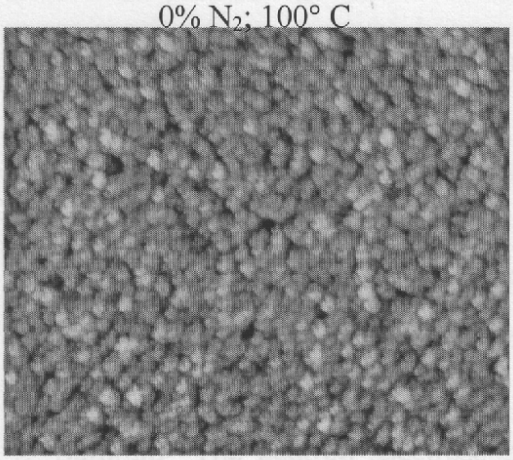
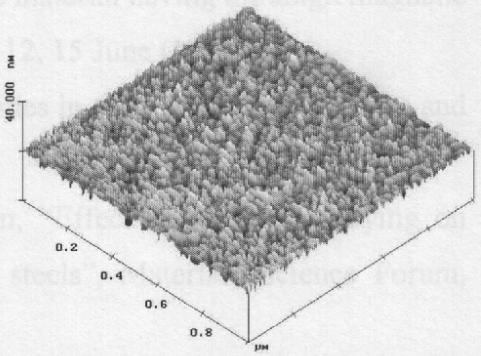


Figure A.7 AFM pictures of films deposited at temperatures with 50% N_2 in sputtering gas mixture, along with the respective R_a values in nm

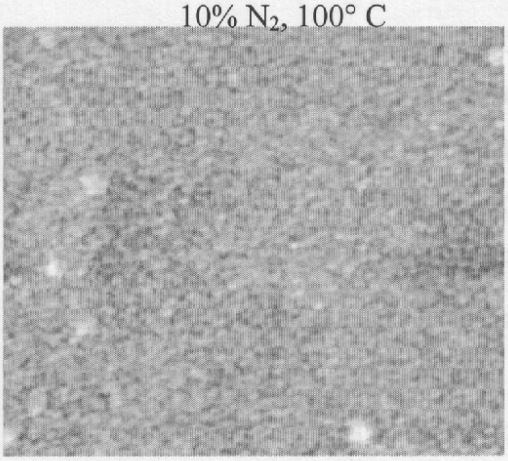
ATTENTION: The Singapore Copyright Act applies to the use of this document. Nanyang Technological University Library

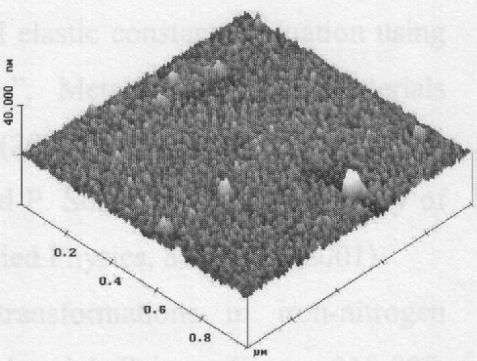
R_a: 0.593 nm
0% N_2; 100° C



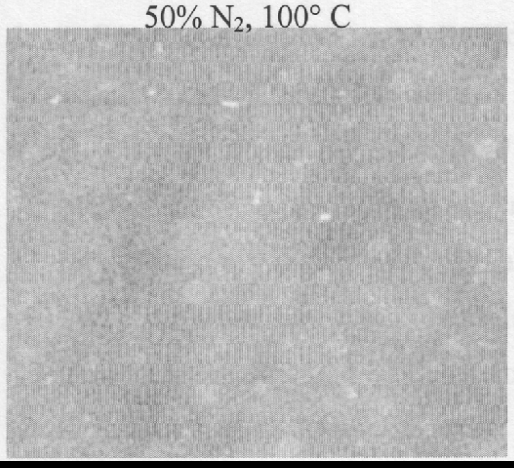


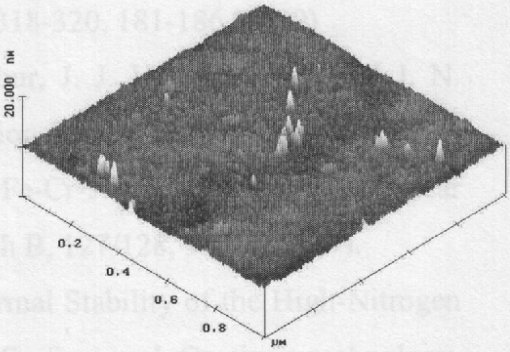
R_a: 0.577 nm
10% N_2, 100° C





R_a: 0.204 nm
50% N_2, 100° C





ATTENTION: The Singapore Copyright Act applies to the use of this document. Nanyang Technological University Library

REFERENCES

1. T.K.Kim and M.Takahashi, "New magnetic material having ultrahigh magnetic moment", Applied Physics Letters, 20, No. 12, 15 June (1972)
2. D.H.Jack and K.H.Jack, "Carbides and nitrides in steel", Materials Science and Engineering, 11, 1-27 (1973)
3. J. Tervo, A. Tarasenko, and H. Hanninen, "Effect of nitrogen alloying on elastic coefficients of austenitic stainless steels", Materials Science Forum, 318-320, 318-320 (1999)
4. Summin "The neutron spectroscopy proof of the strong Cr-N interaction in nitrogen stainless steels", Materials Science Forum, 318-320, 31-40 (1999)
5. P.Shankar, P. Palanichamy, T. Jayakumar, Baldev raj, and S. Ranganathan, "Nitrogen redistribution, microstructure, and elastic constant evaluation using ultrasonics in aged 316L stainless steels", Metallurgical and Materials Transactions A, 32A, December, 2001-2959 (2000)
6. M.Han, E.Carpene, F.Landry, K.-P.Lieb, and P. Schaaf, "Thermal stability of laser-produced iron nitrides", Journal of Apllied Physics, 89, No. 8 (2001)
7. A.Bottger and E.J.Mittemeijer, "Phase transformations in iron-nitrogen martensites, role of elastic strain energies", Materials Science Forum, 318-320, 61-70 (1999)
8. J. Sundvall, J. Olsson, and B. Holmberg, "Applications of nitrogen-alloyed stainless steels", Materials Science Forum, 318-320, 181-186 (1999)
9. D. L. Williamson, J. A. Davis, P. J. Wilbur, J. J. Vajo, R. Wei, and J. N. Matossian, "Relative roles of ion energies, ion flux, and sample temperature in low-energy nitrogen ion implantation of Fe-Cr-Ni stainless steel", Nuclear Instruments and Methods in Physcis research B, 127/128, 930-4 (1997).
10. Orhan Ozturk and D. L. Williamson, "Thermal Stability of the High-Nitrogen Solid-Solution layer on Stainless Steel", Surface and Coatings technology, 158-159, 288-294 (2002).
11. C. Blawert, B. L. Mordike, G. A. Collins, K. T. Short, Y. Jiraskova, O. Schneeweiss, and V. Perina, "Characterization of duplex layer structures produced by simultaneous implantation of nitrogen and carbon into austenitic stainless steel X5CrNi89", Surface and Coatings Technology, 128-129, 219-225, (2000).

ATTENTION: The Singapore Copyright Act applies to the use of this document. Nanyang Technological University Library

12. M.P.Fewell, D. R. G. Mitchell, J. M. Priest, K. T. Shorrt and G. A. Collins, "The Nature of Expanded Austenite", Surface and Coatings Technology, 131, 300-306 (2000).
13. A.L.Sozinov, A.G. Balanyuk, and V.G.Gavriljuk, "Atomic interaction and distribution of nitrogen and carbon atoms in binary Fe-N alloys", Materials Science Forum, 318-320, 13-18 (1999)
14. A J Sedriks, Corrosion of Stainless Steels, John Wiley & Sons (1979)
15. Jerzy Piekoszewski, Bożena Sartowska, Lech Waliś, Zbigniew Werner, Michał Kopcewicz, Friedrich Prokert, Jacek Stanisławski, Justyna Kalinowska, Władysław Szymczyk, "Interaction of nitrogen atoms in expanded austenite formed in pure iron by intense nitrogen plasma pulses", NUKLEONIKA, 49 (2), 57–60 (2004)
16. Menthe E, Rie K-T, Schultze JW, Simon S, "Structure and properties of plasma-nitrided stainless steel", Surface and Coatings Technology, 74/75, 412–416, (1995)
17. S. Mukherjee, "Plasma-based nitrogen incorporation techniques for surface modification", CURRENT SCIENCE, 83, NO. 3, 10 AUGUST (2002)
18. Leon I. Maissel, "The deposition of thin films by cathode sputtering", Physics of thin films, 3, Academic press.
19. Kiyotaka Wasa, Shigeru Hayakawa, "Handbook of sputter deposition and technology; principles, Technology & Applications", Noyes publication, (1992)
20. John L. Vossen and Werner Kern, "Thin film processes", Academic press, Inc. (1978)
21. Maissel Leon I and Glang Richard, "Handbook of thin film technology", Mc Graw Hill company.
22. John A.Thornton, "Sputtering", Metallic coating processes.
23. I.Safi, "Recent aspects concerning DC reactive magnetron sputtering of thin films: a review", Surface Coatings and Technology, 127, 203-219, (2000)
24. I.Safi, "A novel reactive magnetron sputtering technique for producing insulating oxides of metal alloys and other compound thin films", Surface Coatings and Technology, 135, 48-59, (2000)
25. J.Schulte and G. Sobe, "Magnetron sputtering of aluminium using oxygen or nitrogen as reactive gas", This Solid Films, 324, 19-24, (1998)

ATTENTION: The Singapore Copyright Act applies to the use of this document. Nanyang Technological University Library

26. A.Billiard, D. Mercs, F. Perry, and C. Frantz, "Influence of the target temperature on a reactive sputtering process", Surface and Coatings technology, 116-119, 721-726, (1999)
27. H. Barankova, S. Berg, P. Carlsson, and C. Nender, "Hysteresis effects in the sputtering process using two reactive gases", Thin Solid Films, 260, 181-186, (1995).
28. R. F. Bunshah, "PAVD process and some applications", Surface and Coatings Technology, 27, 1-21, (1986)
29. L.Le Brizoual, A. Granier, F. Clenet, P. Briaud, G. Lemperiere, G. Turban, "Experimental study of Ti-Si-N films obtained by radio frequency magnetron sputtering", Surface and Coatings technology, 116-119, 922-926, (1999)
30. ASM Handbook
31. Zhang, Z.L. and Bell.T, Surface Engineering, 1, 131-136 (1985)
32. K. Ichii, K. Fujimura and T. Takase, Techn. Rep. Kansai University 27, 135 (1986)
33. K.L.Dahm and P.A.Dearnley, "On the nature, properties and wear response of S-phase (nitrogen-alloyed stainless steel) coatings on AISI 316L", Proceedings of Institute of Mechanical Engineers, 214 part L (2000)
34. Orhan Ozturk and D. L. Williamson, "Phase and Composition Depth Distribution Analyses of Lowe Energy High Flux N implanted Stainless Steel", Journal of Applied Physics, 77 (8), 15 April (1995)
35. T. Bell and Y. Sun, "Low Temperature Plasma Nitriding and Carburising of Austenitic Stainless Steels", Stainless Steel, 275-288 (2000)
36. Sun Y, Li XY, Bell T., Journal of Materials Science, 34, 4793 (1999)
37. J. C. Jiang and E. I. Meletis, "Microstructure of the nitride layer of AISI 316 stainless steel produced by intensified plasma assisted processing", Journal of Applied Physics, 88, issue 7, 4026-4031 (2000)
38. K. Marchev, M. Landis, R. Vallerio, C. V. Cooper, and B. C. Giessen, "The m phase layer on ion nitrided austenitic stainless steel (III): an epitaxial relationship between the m phase and the γ parent phase and a review of structural identifications of this phase", Surface and Coatings Technology, 116-119, 184-188 (1999)
39. Y. Sun, X. Y. Li and T Bell, "The formation and decomposition of nitrogen and carbon fct austenitic stainless steel", Stainless steel (2000)

ATTENTION: The Singapore Copyright Act applies to the use of this document. Nanyang Technological University Library

40. Y.Sun, X.Y.Li, and T.Bell, "X-ray diffraction characterisation of low temperature plasma nitrided austenitic stainless steels", Journal of Materials Science, 34, 4793-4802 (1999)
41. Thomas Christiansen and Marcel A. J. Somera, "On the crystallographic structure of S-phase", Scripta Materialia, 50, 35-37, (2004)
42. D. L. Williamson, J. A. Davis, P. J. Wilbur, J. J. Vajo, R. Wei, and J. N. Matossian, "Relative roles of ion energies, ion flux, and sample temperature in low-energy nitrogen ion implantation of Fe-Cr-Ni stainless steel", Nuclear Instruments and Methods in Physcis research B, 127/128, 930-4 (1997)
43. Orhan Ozturk and D. L. Williamson, "Thermal Stability of the High-Nitrogen Solid-Solution layer on Stainless Steel", Surface and Coatings technology, 158-159, 288-294 (2002)
44. M.P.Fewell, D. R. G. Mitchell, J. M. Priest, K. T. Shorrt and G. A. Collins, "The Nature of Expanded Austenite", Surface and Coatings Technology, 131, 300-306 (2000)
45. D. L. Williamson, O. Ozturk, R. Wei, P. J. Wilbur, Surface and Coatings Technology, 65, 15 (1994)
46. Seiki Takahashi, Junichi Echigoya, Terushige Ueda, Xingguo Li and Hiroshi Hatafuku, "Martensitic Transformation Due to Plastic Deformation and magnetic Properties in SUS 304 Stainless Steel", Journal of Materials Processing Technology, 108, 213-216 (2001)
47. H. Ishigaki, Y. Konishi, K. Kondo, and K. Koterazawa, "Possibility as a Magnetic Recording Media of Austenitic Stainless Steel Using Stress-Induced Phase Transformation", Journal of Magnetism and Magnetic Materials, 193, 466-469 (1999)
48. A. Bourjot, M. Foos, and C. Frantz, "Basic properties of sputtered 310 stainless steel-nitrogen coatings", Surface and Coatings Technology, 43/44, 533-542 (1990)
49. J.von Stebut, A. Darbeida, A. Saker, A. Billard, and R. Rezakhanlou, "Optimization of the contact mechanical strength of magnetron-sputtered nitrogen-doped AISI 316L physically vapor deposited coatings", Surface and Coatings Technology, 57, 31-42, (1993)

ATTENTION: The Singapore Copyright Act applies to the use of this document. Nanyang Technological University Library

50. B.A.Shedden, F. N. Kaul, M. Samandi, and B. Window, "The role of energetic neutrals in reactive magnetron sputtering of nitrogen-doped austenitic stainless steel coatings", Surface and Coatings Technology, 97, 102-108, (1997)
51. Shozo Inoue, Toshiaki Saeki, Hitoshi Uchida, Keiji Koterazawa, and Mikio Iwasa, "Effects of ion flux on the properties of dc magnetron-sputtered stainless steel films", Vacuum, 66, 257-261, (2002)
52. A. Bourjot, M. Foos, and C. Frantz, "Basic properties of sputtered 310 stainless steel-nitrogen coatings", Surface and Coatings Technology, 43/44, 533-542 (1990)
53. K. L. Dahm and P.A. Dearnley, "S phase coatings produced by unbalanced magnetron sputtering", Surface Engineering, 12, No. 1, 61-67 (1996)
54. P. Gutier, A. Darbeida, A. Billard, C. Frantz and J. von Stebut, "Tribological behaviour of N- or O- doped austenitic stainless-steel magnetron sputter-deposited coatings", Surface and Coatings Technology, 114, 148-155, (1999)
55. Peter A. Dearnley "Corrosin-wear mechanisms of hard coated austenitic 316L stainless steels", Wear 256, 491-99 (2004)
56. A.Saker et al, "Properties of sputtered stainless steel-nitrogen coatings and structural analogy with low temperature plasma nitrided layers of austenitic steels", Materials Science and Engineering, A 140, 702-708, (1991)
57. J. Koskinen, P. Torri, J.-P. Hirvonen, A. mahiout, and, A. Stanishevsky, "Arc discharge deposition of stainless steel coatings at different nitrogen pressures", Surface and Coatings Technology, 80, 57-60, (1996)
58. M. Idiri, B. Boubekar, R. Sabot, Ph. Goudeau, J-F. Dinhut, J-L. Grosseau-Poussard, "Structure and related corrosion behaviour in 1 M H_2SO_4 of bcc 304L films prepared by ion sputtering", Surface and Coatings Technology, 122, 230-234 (1999)
59. H. Baba, T. Kodama, and Y. Katada, "Role of nitrogen on the corrosion behaviour of austenitic stainless steels", Corrosion Science, 44, 2393-2407 (2002)
60. P. Schaaf, Progress in Materials Science, 47, 1 (2002)
61. Gotoh Y, Tsuji H, Ishikawa J , "Measurement of work function of transition metal nitride and carbide thin films", Journal of Vacuum Science and Technology, B 21 (4): 1607-1611, JUL-AUG (2003)

ATTENTION: The Singapore Copyright Act applies to the use of this document. Nanyang Technological University Library

62. C. Gao, W. D. Doyle, M. Shamsuzzoha, "Quantitative correlation of phase structure with the magnetic moment in RF sputtered Fe-N films", Journal of Applied Physics, 73 (10), 15 May, (1993)
63. S. Maliniv, A. J. Bottger, E. J. Mittemeijer, M. I. Pekelharing, and M. A. J. Somers, "Phase Transformations and Phase Equilibria in the Fe-N System at temperatures below 573 K", Metallurgical and materials Transactions A, 32A, January, 50-73 (2001)
64. Y.K.Kim and P.B.Narayan, "Magnetic, microstructural, and compositional characterization of Fe-N thin films for recording sensor applications", Journal of Vacuum Science and Technology A, 13 (3), May/June, (1995)
65. C. Chang, J. M. Siversten, and J. H. Judy, "Structure and magnetic properties of RF reactively sputtered iron nitride thin films", IEEE Tansactions on Magnetics, MAG-23, No.5, September, (1987)
66. Leena Rissanen, Klaus-Peter Lieb, Matthias Nieder Drenk, Olaf Schulte, and Peter Schaaf, "Structure and stability of the new cubic FeN phase produced by magnetron sputtering", Proceedings of ICAME'95, Rimini, (1995)
67. A. Oueldennaaoua, E. Bauer-Grosse, M. Foos and C. Frantz, "Formation D'un Nitrure metastable FeN Structure NaCl Par Pulverisation Cathodique", Scripta Maetallurgica, 19, 1503-1506 (1985)
68. L. Rissanen, P. Schaaf, M. Neubauer, K. P. Lieb, J. Keinonen, and T. Sajavaara, "The production of the new cubic FeN phase by reactive magnetron sputtering", Applied Surface science, 138-9, 261-5, (1999)
69. Shinichi Kikkawa, Mitsushi Fujiki, Massao Takahashi, Fumikazu Kanamaru, Hideki Yoshioka, Tohru Hinomura, Sabura Nasu and Iwao Watanabe, "Interface of Iron Metal/Aluminum Interface Nitride Multilayered Composite Film", Applied Physics Letters, 68 (19), 6 May (1996)
70. L. Rissanen, M. Neubauer, K. P. Lieb and P. chaaf, "The new cubic iron-nitride phase FeN prepared by reactive magnetron sputtering", Journal of Alloys and Compounds, 274, 74-82 (1998)
71. D. L. Peng, T. Hihara and K. Sumiyama, "Formation and Magnetic Propoerties of the fcc-FeN Compound Clusters Prepared by by Plasm-gas-condenseation", Journal of Alloys and Compounds, (2004)
72. H. Shimmizu, M. Shirai, N. Suzki, Journal of Physical Society of Japan, 66, 3147, (1997)

ATTENTION: The Singapore Copyright Act applies to the use of this document. Nanyang Technological University Library

73. H. Shimmizu, M. Shirai, N. Suzki, Journal of Physical Society of Japan, 67, 922, (1998)] and experimental results [refe- T.Hinnomura, S. Nasu, Physics B 237-238, 557 (1997)
74. T.Hinnomura, S. Nasu, Physics B 237-238, 557, (1997)
75. H. Nakagawa, S. Nasu, M. Takahashi, Kanamaru, Hyperfine Interact, 69, 455 (1991)
76. H.Jiang, Q. L. Wu, K. Tao, and H. Li, "Structure and magnetic properties of Fe-N films prepared by ion-beam-assisted deposition", Journal of Applied Physics, 78 (5), 1 September, (1995)
77. "Elements of X-ray Diffraction", BD Cullity and SR Stock, 3'nd Edition (2001)
78. "Encyclopedia of materials characterization", C.Richrard, Manning publications Co.
79. Milton. Ohring, "Materials science of thin films", Academic press Inc. (1992)
80. Manual of Surface profiler-alpha-step 500 type.
81. David Williams and C.Barry Carter, "Transmission Electron Microscopy", Plenum Press (1996)
82. Manual of VSM 736
83. "Getting the Most From Your Vibrating Sample Magnetometer", Dennis Speliotis, ADE Technologies, Inc., Newton, MA, USA
84. N.Huber, D. Munz, and Ch. Tsakmakis, "Determination of Young's modulus by spherical indentation", Journal of Materials Research, 12, No.9, Sep. (1997)
85. T. J. Bell, J.S. Field, and M.V. Swain, "Precision hardness and elastic modulus measurements of thin films and cross sections", Materials Forum, 17, 127-138, (1993)
86. Deok-Hyung Lee, Hyukjae Lee, Byungwoo Park, "Hardness of modulus properties in ion-beam modified amorphous carbon: Temperature and dose rate dependences", Journal of Materials Research, 12, No.8, August (1997)
87. W.C.Oliver and G.M.Pharr, "An improved technique for determining hardness and elastic modulus using load and displacement sensing indentation experiments", Journal of Matarials Research, 7, No.6, June (1992)
88. J.P. Eymery and G. Laplanche, Journal of Magnetism and Magnetic Materials 93, 179 (1991)
89. X-RAY ANALYSIS OF PROTECTIVE COATINGS, Edzo Zoestbergen. Thesis, ISBN 90 367 1327 7 (2001)

ATTENTION: The Singapore Copyright Act applies to the use of this document. Nanyang Technological University Library

90. Sanjeev Aggarwal, Peter J.Goodhew, and R.T.Murray, "Scanning transmission electron microscopy (STEM)-transmission electron microscopy (TEM) analysis of nitrogen ion implanted austenitic 302 stainless steel", Thin Solid Films, 446, 12-17 (2004)

91. Xiao-Ying Li, Yong Sun and Tom Bell, "The thermal stability of the nitrogen S-phase in austenitic stainless steel", Z.Metallkd, 90 (1999)

92. H.Takahashi, H. Shoji, and Migaku Takahashi, "Structure and magnetic moment of $Fe_{16}N_2$ sputtered film", Journal of Magnetism and Magnetic Materials, 174, 57-69, (1997)

93. J.P. Eymery, G. Laplanche, M. Cahoreau, M.F. Denanot, Thin Solid Films 217, 1 (1992)

94. B. Boubeker, Ph. Goudeau, A. Serrari, J.P. Eymery, Nuclear Instrumental Methods B 155, 289 (1999)

95. Shozo Inoue, Tishiaki Saeki, Hitoshi Uchida, Keiji Koterazawa, Mikio Iwasa, Vacuum 66, 257 (2002)

96. J. Koskinen, P. Torri, J-P. Hirvonen, A. Mahiout, A.Stanishevsky, Surface Coatings and Technology, 80, 57 (1996)

97. J.P. Eymery, N. Merakeb, Ph. Goudeau, A. Fnidiki, B.Bouzabata, Journal of Magnetism and Magnetic Materials, 256, 227 (2003)

98. X.Zhang, A.Misra, R.K.Schulze, C.J.Wetteland, H.Wang, and M.Nastasi, "Critical factors that determine face-centered cubic to body-centered cubic phase transformation in sputter-deposited austenitic stainless steel films", Journal of Materials Research, volume 19, No.6, June (2004)

99. Orhan Ozturk and D. L. Williamson, "Thermal Stability of the High-Nitrogen Solid-Solution layer on Stainless Steel", Surface and Coatings technology, 158-159, 288-294 (2002)

100. W.D. Callister, Materials Science and Engineering, 6th Edition, Wiley, USA (2003)

101. Mukul Gupta, Ajay Gupta, P. Bhattacharya, P. Misra, L. M. Kukreja, "Study of Iron nitride thin films deposited by pulsed laser deposition", Journal of Alloy and Compounds, 326, 265-269, (2001)

102. K.H. Jack, J. Appl. Phys. 76, 6632 (1994)

103. H. Shimizu, M. Shirai, N. Suzuki, Physica B 237–238, 546 (1997)

ATTENTION: The Singapore Copyright Act applies to the use of this document. Nanyang Technological University Library

104. J.-F. Bobo, H. Chatbi, M. Vergnat, L. Hennet, O. Lenoble, Ph. Vauer, and M. Piecuch, Journal of Applied Physics, 77 (10), 5309-5313 (1995)

105. Tsuyoshi Yoshita and Masatoshi Ohkoshi, "Structural characterization of Fe-N films prepared by laser ablation", IEEE Transactions on Magnetics, 31, No.6, 3850-3852, November (1995)

106. D. C. Sun, C Lin, and E. Y. Jiang, Journal of Physics: Condensed Matter, 7, 3667-3674, (1995)

107. P. Shankar, D. Sundararaman and S. Ranganathan, "Clustering and ordering of Nitrogen in Nuclear grade 316LN austenitic stainless steel", Journal of Nuclear materials, 254, 1-8 (1998)

108. J.P.Riviere, M.Cahoreau, and P.Meheust, "Chemical bonding of nitrogen in low energy high flux implanted austenitic stainless steel", Journal of Applied Physics, volume 91, No.10, 15 May (2002)

109. H.Nordberg, K. Fernheden (ed.), Nordic Symposium on Mechanical Properties of Stainless Steels, Avesta Research Foundation (1990)

110. F.M.El-Hossary, "Effect of rf plasma nitriding density on microhardness, structure, and magnetic properties of 304 austenite stainless steel", Surface Engineering, 16 (6), 491-494 (2000)

111. Powder Diffraction File, Hanawalt Inorganic Phases Index, JCPDS-ICDD, USA, (1995)

112. Powder diffraction Database of XRD-6000 v2.5

113. Robert M. Metzger, Xiaohua Bao, and Massimo Carbucicchio, "Magnetism of α"-$Fe_{16}N_2$", Journal of Applied Physics, 76 (10), 15 November, (1994)

114. Tian, E. Y. Jiang, and D. C. Sun, "Fe-N gradient films and epitaxial $Fe_{16}N_2$ single-crystal films", Journal of Vacuum Science and Technology A, 15 (4), Jul/Aug, (1997)

115. T. J. Bell, J.S. Field, and M.V. Swain, "Precision hardness and elastic modulus measurements of thin films and cross sections", Materials Forum, 17, 127-138, (1993)

116. C. Gao and M. Shamsuzzoha, "The annealing effect on magnetic moment density and phase formations in Fe-N films", IEEE Transactions on Magnetics, 29, No.6, November, (1993)

ATTENTION: The Singapore Copyright Act applies to the use of this document. Nanyang Technological University Library

117. Satoshi Okamoto, Osamu Kitakami, and Yutaka Shimada, "α"-$Fe_{16}N_2$ phase epitaxially grown by sputter beam method", Journal of Applied Physics, 79 (8), 15 April, (1996)

118. N. Takahashi, Y. Toda, Ishibashi, and T. Nakamura, "Growth mechanism of FeN films by means of an atmospheric pressure halide chemical vapor deposition", Materials Chemistry and Physics, 65, 113-116, (2000)

119. J.Schulte and G. Sobe, "Magnetron sputtering of aluminum using oxygen or nitrogen as reactive gas", This Solid Films, 324, 19-24, (1998)

120. J.-F. Bobo, H. Chatbi, M. Vergnat, L. Hennet, O. Lenoble, Ph. Vauer, and M. Piecuch, Journal of Applied Physics, 77 (10), 5309-5313 (1995)

121. Kyusik Sin and Shan X. Wang, "Stress and magnetic properties in high moment FeN thin films", Journal of Applied Physics, 79 (8), 15 April, (1996)

122. H.Jiang, Q. L. Wu, K. Tao, and H. Li, "Structure and magnetic properties of Fe-N films prepared by ion-beam-assisted deposition", Journal of Applied Physics, 78 (5), 1 September, (1995)

123. H.Jiang, K. Tao, and H. D. Li, "Structure and magnetic properties of Fe-N films deposited on heated substrates by ion-beam assited-deposition", Journal of Magnetism and Magnetic Materials, 149, 358-62, (1995)

124. Trevor E. Clark, Mark R. Visoka, Nanchang Zhu, and Robert Sinclair, "Growth of α' nitrogen martensite and $Fe_{16}N_2$ films using (001) Silicon substrates", IEEE Transactions on Magnetics, 3503-5, (1996)

125. C. Chang, J. M. Siversten, and J. H. Judy, "Structure and magnetic properties of RF reactively sputtered iron nitride thin films", IEEE Tansactions on Magnetics, MAG-23, No.5, September, (1987)

126. Milton. Ohring, "Materials science of thin films", Academic press Inc. (1992)

127. Y.K.Kim and P.B.Narayan, "Magnetic, microstructural, and compositional characterization of Fe-N thin films for recording sensor applications", Journal of Vacuum Science and Technology A, 13 (3), May/June, (1995)

128. Tsuyoshi Yoshita and Masatoshi Ohkoshi, "Structural characterization of Fe-N films prepared by laser ablation", IEEE Transactions on Magnetics, 31, No.6, November, (1995)

ATTENTION: The Singapore Copyright Act applies to the use of this document. Nanyang Technological University Library

129. Bing-Hwai Hwang, Chi-Shan Chen, Hong-Yong Lu, and Tzu-Chien Hsu, "Growth mechanism of reactively sputtered aluminum nitride thin films", Materials Science and engineering, A 325, 380-380, (2002)

130. Oda and Tetsuo Hoshio, "Preparation of Fe-N films by RF sputtering", Journal of Materials science, 25, 2557-61, (1990)

131. C. Lo, S. V. Krishnaswamy, R. Messier, K. R. P. M. Rao, L. N. Mualy, "Mossbauer characterization of reactively sputtered Iron nitride films", Journal of Vacuum Science and Technology, 18 (1), March, (1981)